

**Multifunctional PNIPAM-based Copolymer  
Microgels: From Structural Inhomogeneities to  
Nanoreactors for Hybrid Microgels**

Inaugural-Dissertation

zur Erlangung des Doktorgrades  
der Mathematischen-Naturwissenschaftlichen Fakultät  
der Heinrich-Heine-Universität Düsseldorf

vorgelegt von

**Marius Otten**

aus Duisburg

Düsseldorf, August 2023

aus dem Institut für Physikalische Chemie I – Kolloide & Nanooptik  
der Heinrich-Heine-Universität Düsseldorf

Gedruckt mit der Genehmigung der  
Mathematisch-Naturwissenschaftlichen Fakultät der  
Heinrich-Heine-Universität Düsseldorf

Berichtersteller:

1. Prof. Dr. Matthias Karg
2. Prof. Dr. Thomas Hellweg

Tag der mündlichen Prüfung: 30.11.2023

## Eidesstattliche Erklärung

Die vorliegende Arbeit wurde in der Zeit von Februar 2019 bis August 2023 am Lehrstuhl für Physikalische Chemie I an der Heinrich-Heine-Universität Düsseldorf unter Betreuung von Herrn Prof. Dr. Matthias Karg angefertigt.

Ich, Marius Otten, versichere an Eides statt, dass die Dissertation von mir selbständig und ohne unzulässige fremde Hilfe unter Beachtung der „Grundsätze zur Sicherung guter wissenschaftlicher Praxis an der Heinrich-Heine-Universität Düsseldorf“ erstellt worden ist. Alle verwendeten Quellen und Hilfsmittel sind als solche gekennzeichnet und im Literaturverzeichnis aufgelistet.

---

*Ort, Datum*

---

*Unterschrift*



# Table of Contents

<b>Danksagung</b> .....	<b>I</b>
<b>List of Publications</b> .....	<b>III</b>
<b>Presentations at Scientific Conferences</b> .....	<b>V</b>
<b>List of Abbreviations and Symbols</b> .....	<b>VII</b>
<b>Abstract</b> .....	<b>1</b>
<b>1. Introduction</b> .....	<b>3</b>
<b>2. Theoretical Background</b> .....	<b>19</b>
<b>2.1 Microgels – “Smart” Materials</b> .....	<b>19</b>
2.1.1 Synthesis and Formation of Microgels .....	20
2.1.2 Temperature-responsive Behavior .....	22
2.1.3 Influence of Crosslinker Density on the Swelling Behavior and Structure .....	25
2.1.4 Copolymer Microgels .....	27
<b>2.2 Hybrid Microgels – The Combination of Microgels and Inorganic Nanoparticles</b> .....	<b>31</b>
2.2.1 Loading or Decoration by Diffusion .....	31
2.2.2 Encapsulation of Nanoparticles .....	33
2.2.3 Loading by In Situ Reduction.....	34
<b>2.3 Characterization of Microgel Systems</b> .....	<b>36</b>
2.3.1 Dynamic Light Scattering .....	36
2.3.2 Ultraviolet-visible Absorbance Spectroscopy .....	41
2.3.3 Transmission Electron Microscopy.....	46
<b>3. Synopsis</b> .....	<b>59</b>
3.1 Contributions to Joint Publications .....	65
<b>4. PNIPAM-based copolymer microgels as nanoreactors for the in situ synthesis of gold nanoparticles</b> .....	<b>67</b>
<b>4.1 Abstract</b> .....	<b>68</b>
<b>4.2 Introduction</b> .....	<b>69</b>
<b>4.3 Experimental Section</b> .....	<b>71</b>
4.3.1 Materials.....	71
4.3.2 Synthesis.....	72
4.3.3 Methods .....	75

<b>4.4 Results and Discussion .....</b>	<b>76</b>
4.4.1 $\mu$ gel-AAEM .....	76
4.4.2 $\mu$ gel-AAEM-AAc .....	79
4.4.3 One-Step Gold Overgrowth.....	84
4.4.4 Characterization via small-angle X-ray scattering (SAXS) .....	86
<b>4.5 Conclusion.....</b>	<b>89</b>
<b>4.6 Supporting Information.....</b>	<b>91</b>
<b><i>5. Following the volume phase transition of thermoresponsive microgels by dynamic light scattering and turbidity: Correlations depend on microgel homogeneity.....</i></b>	<b><i>107</i></b>
<b>5.1 Abstract.....</b>	<b>108</b>
<b>5.2 Introduction .....</b>	<b>109</b>
<b>5.3 Experimental Section .....</b>	<b>111</b>
5.3.1 Materials .....	111
5.3.2 Synthesis .....	112
5.3.3 Methods.....	118
<b>5.4 Results .....</b>	<b>119</b>
5.4.1 PNIPAM microgels .....	119
5.4.2 Copolymer Microgels .....	123
5.4.3 Core-shell microgels .....	125
<b>5.5 Discussion .....</b>	<b>127</b>
<b>5.6 Conclusion.....</b>	<b>131</b>
<b>5.7 Supporting Information.....</b>	<b>134</b>
<b><i>6. Conclusion and Perspectives.....</i></b>	<b><i>177</i></b>
<b><i>7. References.....</i></b>	<b><i>183</i></b>

## Danksagung

Zuerst möchte ich meinem Doktorvater Matthias Karg danken, welcher mich vor mittlerweile fast 6 Jahren in seinen Arbeitskreis aufgenommen hat und mir über die Zeit meines HiWi-Jobs, der Masterarbeit und nun auch während der Promotion die Möglichkeit gegeben hat mich an einem breiten Spektrum an Themen zu erproben und meine eigenen Stärken und Schwächen über die Jahre hinweg kennenzulernen. Des Weiteren möchte ich mich für die Unterstützung bei jeglichen Problemen und Fragen bedanken und werde das Vertrauen was mir bezüglich meiner Projekte und Aufgaben entgegengebracht wurde immer zu schätzen wissen.

Herrn Prof. Dr. Thomas Hellweg danke ich für die Übernahme des Korreferats dieser Arbeit.

Ein weiterer Dank soll an Saskia Mölders, Diana Hildebrandt, Viktoria Voigt und den Matheprofi Ben Pfeffing gehen, welche im Rahmen ihrer Bachelorarbeiten und im Rahmen von Forschungspraktika geholfen haben neue Impulse für die Projekte dieser Arbeit einzubringen. Abgesehen von dem fachlichen Beitrag zu dieser Arbeit, möchte ich mich besonders für die spaßige und lehrreiche Zeit, die wir zusammen hatten, bedanken.

Ein großer Dank geht auch an alle Leute, welche ich durch die unzähligen Stunden am Elektronenmikroskop näher kennenlernen durfte. Als erstes ist hierbei natürlich meine Elektronenmikroskopie-Leidensgenossin Miriam Bäumers zu nennen, mit der ich immer stundenlang über den Sinn und Unsinn von TEMs philosophieren konnte. Aber auch Alexander Banger, Andreas Neusch, Iuliia Novoselova und Nicolaas van der Voort sind zu erwähnen, welche mir mithilfe der Elektronenmikroskopie ermöglichten etwas über den eigenen Tellerrand hinauszuschauen, zusammen über die Projekte und neue Ideen für Messungen zu tüfteln und allgemein tolle Gespräche zu führen.

Nicht unerwähnt bleiben dürfen natürlich auch Alessa Lappe, Wiebke Haselbach, Oliver Nolden, Julian Ringling, Sonja Coors und Sebastian Hölzel mit denen ich jedes Jahr aufs Neue eine unglaubliche und witzige Zeit im Mediziner-Praktikum hatte. Die chaotische Zeit im Praktikum hat für unglaublich viele Momente gesorgt, welche ich wahrscheinlich nie vergessen werde!

Meine Zeit im Arbeitskreis wurde stark durch die verschiedenen Charaktere bereichert, welche über die Jahre in die Arbeitsgruppe gekommen sind und diese auch wieder verlassen haben. Neben den Doktorranden der ersten Stunde: Kirsten Volk, Kristina Strohmiegl (geb. Wagner), Julian Sindram und Arne Lerch, welche mich besonders in der Zeit der Masterarbeit und am Anfang der Promotion geprägt haben, hat auch jedes andere Mitglied des Arbeitskreises auf seine eigene Weise zu meinem Weg beigetragen. Besonders hervorzuheben sind hierbei natürlich Kollegen, welche sich im Laufe der Zeit zu guten Freunden entwickelt und so für unvergessliche Momente in den letzten Jahren gesorgt haben. Hierbei seien Déborah Feller, Jonathan Garthe, Caspar Croonenbrock und Philipp Hammers hervorzuheben. Neben den ganzen fachlichen Diskussionen habe ich die Zeit mit euch in Restaurants, auf Konzerten, Festivals oder bei euch Zuhause immer sehr genossen.

Meinen Eltern möchte ich für die ganze emotionale und finanzielle Unterstützung danken ohne den mein Werdegang nicht möglich gewesen wäre.

Mein abschließender und besonderer Dank geht an Marco Hildebrandt (den besten Laborabschnittgefährten den man sich wünschen kann!), welcher mich die letzten 10 Jahre durch alle Höhen und Tiefen des Studiums, die Abschlussarbeiten und durch die Promotion begleitet hat! Ohne dich wäre ich wahrscheinlich nicht an diesen Punkt gekommen und dafür werde ich immer dankbar sein!

## List of Publications

1. Déborah Feller, **Marius Otten**, Marco Hildebrandt, Marcel Krüsmann, Gary Bryant and Matthias Karg  
Translational and rotational diffusion coefficients of gold nanorods functionalized with a high molecular weight, thermoresponsive ligand: a depolarized dynamic light scattering study  
  
*Published in Soft Matter, 2021, 17, 4019-4026*
2. Alexander Banger, Julian Sindram, **Marius Otten**, Jessica Kania, Dimitri Wilms, Alexander Strzelczyk, Sean Miletic, Thomas C Marlovits, Matthias Karg and Laura Hartmann  
Synthesis and self-assembly of amphiphilic precision glycomacromolecules  
  
*Published in Polymer Chemistry, 2021, 12, 4795-4802*
3. Julian Sindram, Marcel Krüsmann, **Marius Otten**, Thomas Pauly, Luitgard Nagel-Steger and Matthias Karg  
Versatile Route toward Hydrophobically Polymer-Grafted Gold Nanoparticles from Aqueous Dispersions  
  
*Published in J. Phys. Chem. B, 2021, 125, (29), 8225-8237*
4. Iuliia P. Novoselova, Andreas Neusch, Julia-Sarita Brand, **Marius Otten**, Mohammed Reza Safari, Nina Bartels, Matthias Karg, Michael Farle, Ulf Wiedwald and Cornelia Monzel  
Magnetic Nanoprobes for Spatio-Mechanical Manipulation in Single Cells  
  
*Published in Nanomaterials, 2021, 11, (9), 2267*
5. **Marius Otten**, Marco Hildebrandt, Ralf Kühnemuth, and Matthias Karg  
Pyrolysis and Solvothermal Synthesis for Carbon Dots: Role of Purification and Molecular Fluorophores  
  
*Published in Langmuir, 2022, 38, (19), 6148-6157*
6. Alexander Banger, Peter Pasch, Luca-Ceasre Blawitzki, Simon Weber, **Marius Otten**, Cornelia Monzel, Stephan Schmidt, Jens Voskuhl and Laura Hartmann  
Detection of Lectin Clustering in Self-Assembled, Glycan-Functionalized Amphiphiles by Aggregation-Induced Emission Luminophores  
*Published in Macromolecular Chemistry and Physics, 2022, 224, 220314*

7. Jan-Hendrik Budde, Nicolaas van der Voort, Suren Felekyan, Julian Folz, Ralf Kühnemuth, Paul Lauterjung, Markus Köhler, Andreas Schönle, Julian Sindram, **Marius Otten**, Matthias Karg, Christian Hermann, Anders Barth and Claus. A. M. Seidel  
FRET nanoscopy enables seamless imaging of molecular assemblies with sub-nanometer resolution

*Manuscript submitted and under revision in Nat. Commun.*

8. **Marius Otten**, Marco Hildebrandt, Ben Pfeffing, Victoria Voigt, Thomas Hellweg and Matthias Karg  
Following the volume phase transition of thermoresponsive microgels by dynamic light scattering and turbidity: Correlations depend on microgel homogeneity

*Manuscript in preparation for submission*

9. **Marius Otten**, Diana Hildebrandt, Saskia Mölders, Marco Hildebrandt, Andrij Pich and Matthias Karg  
PNIPAM-based copolymer microgels as nanoreactors for the in situ synthesis of gold nanoparticles

*Manuscript in preparation for submission*

10. Déborah Feller, **Marius Otten** and Matthias Karg  
Long-ranging Bravais lattices of soft core-shell microgels via interface assisted self-assembly: Structural characteristics and optical response

*Manuscript in preparation for submission*

11. Arne-Lerch, **Marius Otten** and Matthias Karg  
Synthesis and pH-responsive properties of core-shell-particles and hollow microgels from poly-2-vinylpyridine

*Manuscript in preparation for submission*

12. Laura E. Goodwin, Manuel Escobedo, **Marius Otten**, Stefan U. Egelhaaf and Matthias Karg  
Asymmetrically loaded gold-PNIPAM hybrid microgels through an interface-assisted loading strategy

*Manuscript in preparation for submission*

## Presentations at Scientific Conferences

1. **Marius Otten**, Marco Hildebrandt and Matthias Karg  
Poster presentation: Synthesis, Characterization and Nanocomposite Film of High Quantum Yield Carbon Dots

*17<sup>th</sup> European Student Colloid Conference (2019), Varna, Bulgaria*

2. **Marius Otten**, Marco Hildebrandt and Matthias Karg  
Poster presentation: Synthesis, Characterization and Nanocomposite Film of High Quantum Yield Carbon Dots

*33<sup>rd</sup> Conference of the European Colloid and Interface Society (2019), Leuven, Belgium*

3. **Marius Otten** and Matthias Karg  
Poster presentation (online participation): In situ formation and growth of inorganic nanoparticles in copolymer microgels

*35<sup>th</sup> Conference of the European Colloid and Interface Society (2021), Athens, Greece*

4. **Marius Otten** and Matthias Karg  
Oral presentation: Optical characterization of complex-shell copolymer microgels

*36<sup>th</sup> Conference of the European Colloid and Interface Society (2022), Crete, Greece*



## List of Abbreviations and Symbols

$\alpha$	De-swelling ratio
$\beta$	Swelling ratio
$\Gamma$	Relaxation rate
$\Delta E$	Change in energy
$\Delta H$	Change in enthalpy
$\Delta S$	Change in entropy
$\epsilon_0$	Permittivity
$\epsilon_\lambda$	Molar attenuation coefficient
$\eta$	Viscosity
$\theta$	Scattering angle
$\lambda$	Wavelength
$\mu gel$	Microgel
$v$	Velocity
$v_m$	Mean velocity
$\Pi$	Osmotic pressure
$\sigma_{el.}$	Probability of an electron being elastically scattered
$\tau$	Correlation time
$v$	Molar volume of the solvent
$\phi$	Polymer volume fraction
$\chi$	Flory-Huggins interaction parameter
$\Omega$	Solid angle segment
2-VP	2-Vinylpyridine
A	Absorbance
a.u.	Arbitrary units
AAc	Acrylic acid
ACMA	2,2'-Azobis(N-(2-carboxyethyl)-2-methylpropionamide) tetrahydrate
AAEM	Acetoacetoxy ethyl methacrylate
AFM	Atomic force microscopy
AMPS	2-Acrylamido-2-methylpropane sulfonic acid
APTAC	(3-Acrylamidopropyl) trimethylammoniumchlorid
BIS	N,N'-methylenebisacrylamide
$c$	Light velocity
$c$	Concentration
$C_{Scat.}$	Scattering cross section
$C_{Ext.}$	Extinction cross section
CCD	Charge-coupled device
CMOS	Complementary metal oxide semiconductor
d	Pathlength
$D_H$	Hydrodynamic diameter
$D_T$	Translational diffusion constant
$D_{TEM}$	Diameter determined by transmission electron microscopy
DLS	Dynamic light scattering
dSTORM	Direct stochastic optical reconstruction microscopy
$e$	Unit charge
e.g.	Exempli gratia (for example)
$E_0$	Energy of a single electron

$E_{\text{Elast.}}$	Elastic energy
$E_{\text{Gel}}$	Free energy of a microgel network
$E_{\text{Ion.}}$	Electrostatic energy
$E_{\text{Mix}}$	Mixing energy
EDX	Energy-dispersive X-ray spectroscopy
EELS	Electron energy loss spectroscopy
EM	Electron microscopy
EtOH	Ethanol
et al.	Et alii (and others)
$f$	Number of counter ions per chain
FEG	Field emission gun
FWHM	Full width at half maximum
g	Gramm
$g_1(\tau)$	Field time autocorrelation function
$g_2(\tau)$	Intensity time autocorrelation function
$h$	Planck constant
h	Hour(s)
$\text{HAuCl}_4 \cdot 3\text{H}_2\text{O}$	Tetrachloroauric(III) acid trihydrate
HPLC	High pressure liquid chromatography
i.e.	Id est (that is)
$I$	Intensity of transmitted light
$I_0$	Intensity of incident light
$k_B$	Boltzmann constant
$\vec{k}_{\text{in}}$	Incident wave vector
$\vec{k}_{\text{out}}$	Scattered wave vector
KPS	Potassium persulfate
$\text{LaB}_6$	Lanthanum hexaboride
LCST	Lower critical solution temperature
LPR	Surface plasmon resonance
LSPR	Localized surface plasmon resonance
$m_0$	Effective electron mass
m	Mass
M	Mol
mg	Milligram
min	Minute(s)
MPS	3-(Trimethoxysilyl)propyl methacrylate
$n$	Refractive index
n	Amount of substance
$N$	Number concentration
$N_A$	Avogadro constant
NaOH	Sodium hydroxide
$\text{NH}_3$	Ammonia
NIPAM	<i>N</i> -isopropylacrylamide
nm	nanometer
$p$	Momentum
PDI	Polydispersity index
pm	picometer
PNIPAM	Poly- <i>N</i> -isopropylacrylamide
PNIPMAM	Poly- <i>N</i> -isopropylmethacrylamide
PVCL	Polyvinyl chloride
$\vec{q}$	Scattering vector

$R$	Radius/Distance to the center of mass
$R_c$	Radius of the core
$R_H$	Hydrodynamic radius
RDG	Rayleigh-Debye-Gans
RPM	Revolutions per minute
RITC	Rhodamine b isothiocyanate
s	Second(s)
SANS	Small-angle neutron scattering
SAXS	Small-angle X-ray scattering
SDS	Sodium dodecyl sulfate
SiO <sub>2</sub>	Silicon dioxide
SLS	Static light scattering
STEM	Scanning transmission electron microscopy
t	Time
$T$	Temperature
TEM	Transmission electron microscope/microscopy
TEOS	Tetraethyl orthosilicate
$U_A$	Acceleration voltage
UV-Vis	Ultraviolet-visible
V	Volume
$V_0$	Volume of a relaxed gaussian geld network
V50	2,2'-Azobis(2-methylpripionamide) dihydrochloride
VOU	3,9-Divinyl-2,4,8,10-tetraoxaspiro[5.5]undecane
VPT	Volume phase transition
VPTT	Volume phase transition temperature
Z	Atomic number of the nucleus



## **Abstract**

Chemical and/or physical crosslinking of polymer chains can lead to the formation of micro- or nanometer sized gel-like networks that are known as micro- and nanogels. These soft, deformable objects can react to external stimuli like pH or temperature, which enable microgels to either take up, hold or release solvent resulting in a change of the effective size. These “smart” characteristics make microgels interesting for various applications such as drug delivery or as responsive coatings. The combination of soft microgels with inorganic nanoparticles can further extend the properties of such systems which therefore gain increased interest in research fields like sensing or catalysis. Furthermore, the incorporation of multiple different monomers into microgel networks can result in systems with a more complex architecture and enhanced properties. This increased complexity can be interesting for applications as well as fundamental research. For certain applications, the introduction of functional groups that can bind enzymes or complex ions can be useful while fundamental research is interested in the potential to mimic more complex (bio)molecules using soft particles with specific structures and properties. The characterization of those systems with scattering and microscopic techniques plays an important role to understand the morphology of those systems. Resolving the inner structure of microgel is challenging due to the complex architecture. Results from small-angle neutron scattering revealed a fuzzy sphere model for microgels where the core of the network is rather densely crosslinked and the outer periphery consists of loosely crosslinked polymer chains.

In this thesis, complex copolymer microgels were synthesized as nanoreactors for the in situ formation of gold nanoparticles. In the past, only few studies revolved around the controlled in situ synthesis of nanoparticles within microgels, as seeded precipitation polymerization is typically a reliable strategy to introduce single nanoparticles into microgel networks. In this work, the influence of comonomers on the in situ synthesis has been systematically studied to open a new synthesis route for hybrid microgels. A successful formation of a single gold nanoparticle in each individual microgel could be achieved by incorporation of two functional comonomers.

The characterization of the complex microgels via scattering techniques, including dynamic light scattering and small-angle X-ray scattering but also imaging via transmission electron microscopy indicated a domain-like structure of the networks that favors the localized accumulation of gold ions and thereby allows for the controlled in situ synthesis.

Typically, X-ray and neutron scattering experiments are used to address the structure on a local scale but come with the disadvantage of being complex and costly. In this thesis, the correlation of data from dynamic light scattering and absorbance spectroscopy was evaluated as an alternative approach that can provide insights into structural inhomogeneities and deviation from the established fuzzy sphere morphology. Therefore, a systematic study of three different types of microgels was carried out to prove the significance of this analytical methodology. The comparison of “classical” PNIPAM microgels, copolymer microgels and core-shell microgels revealed a dependency between the swelling behavior and the inner structure. As a consequence, the combination of temperature-dependent dynamic light scattering and temperature-dependent ultraviolet-visible absorbance spectroscopy was identified as promising towards an accessible and fast characterization of microgels that can potentially be automatized to study and categorize larger numbers of systems.

# 1. Introduction

Microgels are three-dimensional networks formed by the crosslinking of polymer chains in the sizes between 100 nm<sup>1</sup> and several micrometers.<sup>2</sup> In a good solvent, microgels are swollen whereby the solvent can make up over 90% of the total volume of the particle. Because of solvent dynamics within a three-dimensional polymer scaffold, microgels can be attributed with liquid and solid characteristics. Most microgels are made from stimuli-responsive polymers that react to external stimuli including changes in temperature,<sup>3-8</sup> pH,<sup>9-13</sup> ionic strength,<sup>14-17</sup> solvent composition,<sup>18, 19</sup> electric field,<sup>20, 21</sup> pressure<sup>22-24</sup> or even light of certain wavelengths.<sup>25-29</sup> The response to changes in the environment often results in the release of solvent from the microgel network and consequently a decrease in the effective size.

Ease of synthesis and scalability, low dispersity, colloidal stability and convenient functionalization but first and foremost the responsiveness of the polymer networks make microgels interesting for a multitude of applications but also for fundamental studies.<sup>30, 31</sup> Multiple works show that microgels are suitable for applications in drug delivery,<sup>32-36</sup> sensing<sup>37, 38</sup> or as responsive coatings<sup>39, 40</sup>. For fundamental studies microgels can act as model systems for globular proteins<sup>41</sup> or for concentrated colloidal suspensions.<sup>42</sup> Hybrid microgel systems that combine the properties of microgels with inorganic nanoparticles noticeably extend the range of applications.<sup>43</sup> Depending on the material, size, position and quantity of inorganic nanoparticles, catalytic,<sup>44-46</sup> optical<sup>47-50</sup> or magnetic<sup>51-55</sup> properties can be observed which can further be controlled and modified by the responsiveness of the surrounding microgel.

Properties of microgels, including the swelling behavior, porosity and the elasticity are strongly dependent on the crosslinking density, overall composition of the microgel and the distribution of components within the network.<sup>56-60</sup> For example, the swelling behavior can not only be influenced by incorporation of comonomers or the crosslinking degree but also the distribution of crosslinker in the microgel network. It was found that a homogenous distribution of crosslinker (and monomers) leads to an increased potential degree of swelling, whereby the homogeneity is again strongly affected by the synthesis route.<sup>61, 62</sup>

To understand all processes, dynamics and interactions of complex microgels and thereby further improve potential applications, the detailed and complete characterization of the internal structure are of great importance.<sup>63</sup>

The picture of the internal architecture of microgel networks has been drastically changed over the past 30 years of investigations due to the ever-increasing improvements of existing measurement techniques and the introduction of new methods into the research field. Pelton and Chibante were the first to report of water-swollen microgels obtained by precipitation polymerization in 1986.<sup>64</sup> Since then, “classical” microgels based on poly-*N*-isopropylacrylamide (PNIPAM) crosslinked with *N,N*-methylenebisacrylamide (BIS) rank among the most studied microgels that show a responsiveness to temperature. Similar to typical macrogels, the simplest model to describe the inner structure of microgels is a network with a statistical but homogenous distribution of all components (**Figure 1.1 (a)**).

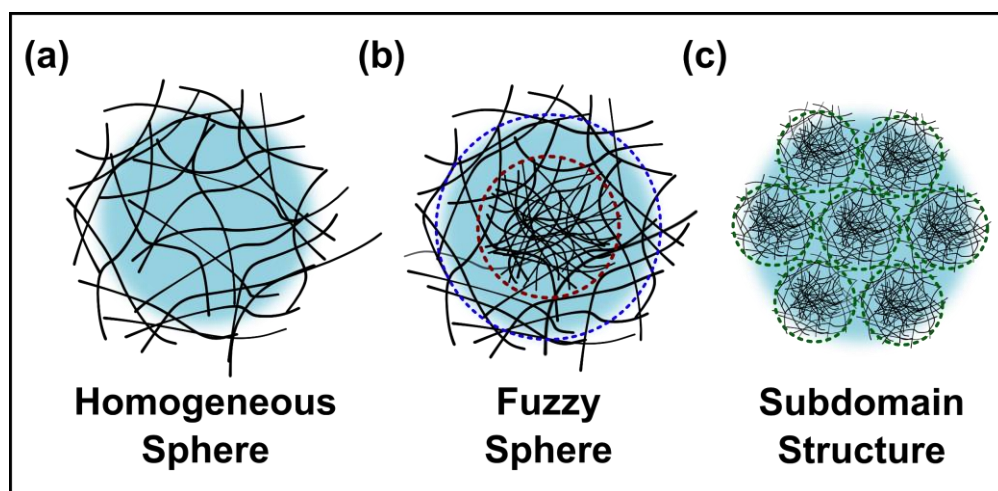


**Figure 1.1:** Overview of postulated structural models of “classical” microgels. **(a)** Model of a sphere with a statistical, homogeneous distribution of all components. **(b)** Fuzzy sphere model with high crosslinked core (red circle) and a radial decaying crosslinked shell with a fuzzy morphology in the periphery (blue circle). **(c)** Subdomain structure where the microgel network is made from smaller interconnected domains (green circles).

Already in 1994, Wu et al. brought up first evidence of variations in the polymer and crosslinker density by detailed investigations of the conversion of monomers during a microgel synthesis using dynamic light scattering (DLS) and high-pressure liquid chromatography (HPLC).<sup>65</sup> Ever since, the formation kinetics and final conformation of the microgels were extensively studied and an inhomogeneous distribution of monomers in the network was confirmed. Microgels with a rather homogenous distribution of components still can be achieved but demand different polymerization

techniques like feed-batch or semi-batch methods.<sup>62, 66</sup> As one example, the group of Yodh showed the successful synthesis and characterization of micrometer-sized PNIPAM microgels with a homogeneous crosslinker density distribution by use of a semi-batch method which results in different optical properties e.g., weaker scattering of light compared to microgels synthesized by a regular one-pot precipitation polymerization.<sup>67</sup>

Just like for typical polymer systems the reactivities of the individual monomers play an important role in the formation of the (inner) structure of microgels. Moreover, gradients as well as other inhomogeneities in the distribution of components need to be considered. Over the past decades, small-angle neutron scattering (SANS) has been established as the most promising method to gain information about the inner architecture by investigation of the microgel form factor.<sup>68</sup> SANS measurements are especially favorable due to the adjustable contrast by using heavy water mixtures as well as the wide  $q$ -range that can be investigated.

Stieger et al. were the first to use the form factors measured by SANS to derive a model for the radial polymer-density profile in 2004.<sup>69</sup> Initiated by the findings, the model that has been established and continues to be the most relevant for research in the field of microgels, is the so-called fuzzy sphere model. Multiple SANS studies suggest that the radial density profile of a neutral microgel can be described as:

$$\rho(R) = \frac{\rho(0)}{2} \operatorname{erfc} \left[ \frac{(r - R_c)}{\sqrt{2}\sigma} \right] \quad (1.1)$$

Here,  $\rho(R)$  describes the polymer-density as a function of the distance  $R$  from the center of mass of the microgel.  $\rho(0)$  is the polymer-density at the center of mass,  $R_c$  is the radius of the “homogenous” core with a high crosslinking density and  $\sigma$  is the “fuzziness” parameter which quantifies the width of the fuzzy corona.

The fuzzy sphere model (**Figure 1.1 (b)**) considers the different reactivities of monomers and the crosslinker molecules (e.g., NIPAM and BIS) resulting in a scenario where synthesized microgels contain a highly crosslinked polymer core with a radially decaying crosslinking density in the periphery. Thus, in the swollen state the microgels have dangling ends that reach into the surrounding medium while in the collapsed state the microgels resemble compact, homogenous spheres. Approximations like the fuzzy sphere model were also used for numerical modeling to

simulate interactions and processes within and between microgels in dispersion. Numerical modeling of microgels is challenging due to the complexity of the microgel architecture. Nonetheless, the group of Zaccarelli was able to derive an atomistic model of a microgel which is in agreement with experiments and therewith potentially help to understand the dynamics and structure of the microgel networks.<sup>70, 71</sup>

Recently, Kyrey et al. presented data of SANS and neutron spin echo measurements for “classical” microgels based on PNIPAM and BIS. The results indicated that the prominent fuzzy sphere model may not be a completely accurate representation of the inner structure. Therefore, the authors suggested that the network could be described more precisely by an inhomogeneous domain-like structure (**Figure 1.1 (c)**).<sup>61</sup>

Similar structures were found by the group of Richtering for copolymer microgels. The group proposed a “dirty snowball” structure for the description of the nanophase separated structure of copolymer microgels consisting of PNIPAM and poly-*N*-isopropylmethacrylamide (PNIPMAM). The VPTT of the investigated copolymer microgel was determined at 38 °C which is in between the VPTTs of microgels based only on PNIPAM ( $VPTT_{PNIPAM} = 32 \text{ °C}$ ) and PNIPMAM ( $VPTT_{PNIPMAM} = 44 \text{ °C}$ ) respectively. An accurate form factor model could be derived based on SANS measurements during the volume phase transition of the copolymer microgel. Under these conditions, the group found that the copolymer network consists of collapsed PNIPAM domains (“dirt”) and swollen PNIPMAM regions (“snowball”).<sup>72</sup>

The work of the group of Richtering underlines the increasing complexity when multiple monomers are incorporated in a microgel. **Figure 1.2** presents an overview of possible structural models of copolymer microgels. The models are similar to those illustrated in **Figure 1.1** for “classical” microgels based only on a single monomer and crosslinker molecules. For the presented copolymers, both the distribution of the crosslinker as well as an exemplary comonomer are depicted. Here, orange coloring represents the existence of comonomers within the polymer chains in the respective model.

Compared to “classical” microgels the realization of a statistical, homogeneous distribution of components (**Figure 1.1 (a)**) in copolymer microgels is challenging even when using semi-batch or feed-batch methods. This challenge arises from the addition of multiple monomers during the copolymerization, each showing a distinct reactivity. The differences in the reactivities of the individual components during polymerization can lead to a scenario where a less reactive comonomer is preferentially incorporated in the periphery of the microgel. Simultaneously a higher reactivity of the crosslinker causes the formation of the fuzzy sphere morphology known from “classical” microgels (**Figure 1.2 (b)**).

The “dirty snowball” structure reported by Richtering is a first indication that the fuzzy sphere model needs to be carefully evaluated when multiple monomers are incorporated in a microgel, potentially leading to more complex architectures with nanophase separated domains (**Figure 1.2 (c)**).

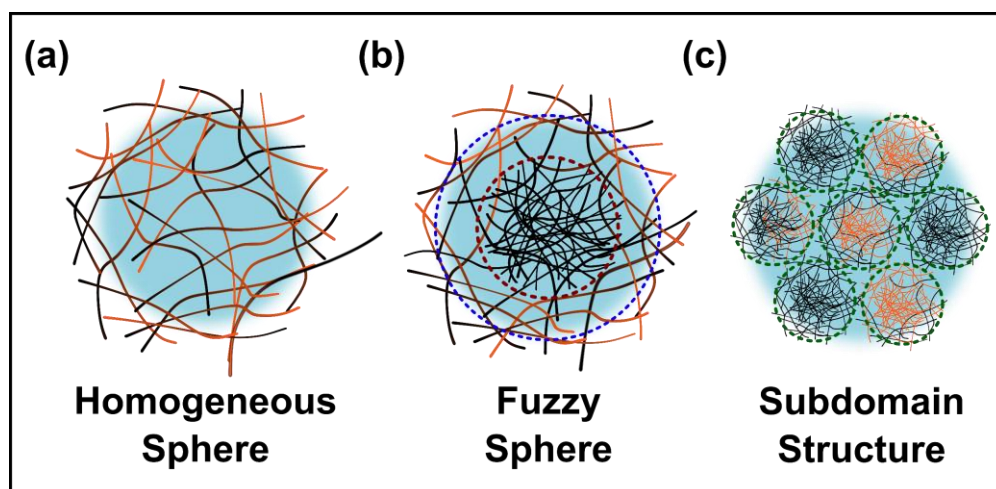


**Figure 1.2:** Overview of possible structural models of copolymer microgels. Orange colored polymer chains represent the incorporation of comonomers. **(a)** Model of a sphere with a statistical, homogeneous distribution of the main monomer, a comonomer and the crosslinker. **(b)** Fuzzy sphere model with high crosslinked core (red circle) and a radial decaying crosslinked shell with a fuzzy morphology in the periphery (blue circle). In the presented example the comonomer is incorporated in the periphery of the microgel **(c)** Subdomain structure where the microgel network is made from smaller interconnected domains (green circles). The comonomer is accumulated in some domains or part of the domains.

For core-shell microgels not only the reactivity of the monomers and crosslinker molecules need to be considered regarding the final internal architecture but also the difference in the polymerization technique itself since both have an influence on the formation mechanism of the microgel shell surrounding the inorganic core. During a regular seeded precipitation polymerization, inorganic cores act as seeds whereby the precipitating polymer chains adsorb onto the surface of the seeds and form the

surrounding microgel shell. Hence, again different scenarios like the formation of a shell with a homogeneous, statistical distribution of monomers and crosslinker molecules (**Figure 1.3 (a)**) or a fuzzy shell morphology could be considered. Reports in the past indicate that seeded precipitation polymerization also leads to the formation of a fuzzy architecture of the shell (**Figure 1.3 (b)**).<sup>73</sup> Nevertheless, more detailed investigations are needed to understand the potential differences between the inner structures resulting from the various polymerization techniques. In order to achieve this, the introduction of new analytical instrumentation or the combination of well-established scattering, spectroscopy or microscopy techniques could be essential to allow for the faster and more efficient investigation of larger numbers of microgel systems.

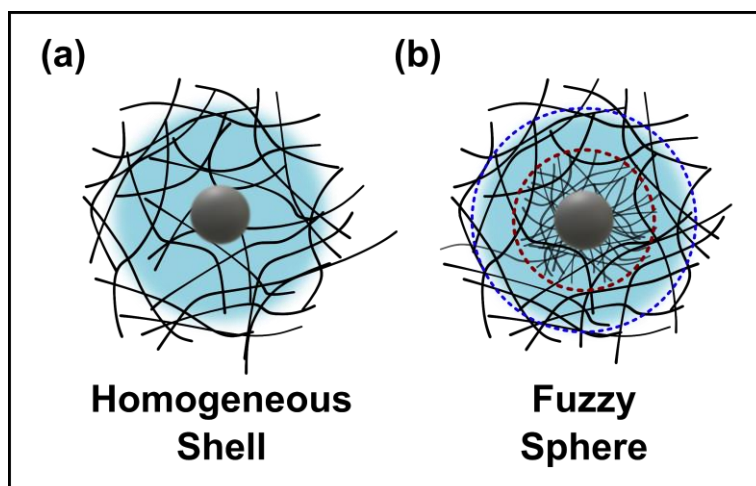


**Figure 1.3:** Overview of possible structural models of core-shell microgels synthesized by seeded precipitation polymerization. The inorganic core (grey) can consist of various materials e.g., silicon dioxide or gold. **(a)** Model of a core-shell microgel with a statistical, homogeneous distribution of all components in the shell. **(b)** Fuzzy sphere model with high a degree of crosslinking near the core (red circle) and a radial decaying crosslinked shell with a fuzzy morphology in the periphery (blue circle).

By now, the characterization via state-of-the-art nanoscopic imaging methods can be used to confirm and supplement data acquired by scattering techniques. Karanastasis et al. recently used a modified super-resolution fluorescence microscopy technique to evaluate the crosslinker distribution in microgel networks with a 20 nm isotropic resolution.<sup>74</sup> The authors chemically attached a dye to crosslinker molecules and thereby found that the crosslinking density in the core-like regions is not homogeneous but rather clustered. The individual clusters are embedded in a polymer scaffold with a lower crosslinking density. The observations have been validated by the group of Wöll who introduced a photoswitchable

crosslinker into polymer networks to visualize crosslinker points and quantify them by the means of in situ nanoscopic imaging.<sup>75</sup> Bergmann et al. and Otto et al. used an alternative approach, where dye molecules were added during the measurement to observe the diffusion behavior and resulting distribution of dye molecules in the network. Direct stochastic optical reconstruction microscopy (dSTORM) studies thereby suggested that the fuzzy sphere model still sufficiently describes the network morphology.<sup>76, 77</sup> Electron microscopy also plays an integral part in the characterization of microgels by allowing for the estimation of the dispersity and size range through visualization of the particles.

Obtained information have to be carefully considered due to drying of the microgels and resulting changes in the morphology and arrangement when investigated with an electron microscope. To circumvent the change in morphology during the drying process, cryo-techniques have gained in importance as they allow the imaging of single particles in the swollen state without ongoing liquid dynamics.<sup>78</sup> One example was recently presented by Gelissen et al. The authors combined dSTORM and (cryo-) in situ transmission electron microscopy (TEM) to study the structural details of hybrid microgels. It was demonstrated that labeling of microgel networks with nanoparticles and fluorophores allows for the tracking of structural changes (e.g., response to changes in temperature) with both methods.<sup>79</sup>

Investigations of microgel using TEM imaging showed that electron microscopy can extend the characterization of microgels over spectroscopy methods in two ways:

- I. Determination of the number of inorganic particles and distribution position in hybrid microgels
- II. Staining of the microgels to provide additional information about the morphology and structure

Typically, absorbance spectroscopy can be used to detect the existence of inorganic nanoparticles which exhibit discrete absorbance e.g., gold- and silver nanoparticles within hybrid microgels. In the past, it was also shown that optical properties like the local surface plasmon resonance (LSPR) can be used to estimate the size and dispersity of gold and silver nanoparticles within the microgels based on the linear correlation between the size and the position of the LSPR signal.<sup>80-83</sup> Nevertheless, absorbance spectroscopy does not allow to locate the exact position of the gold nanoparticles within the microgel or at the microgels surface.

This limitation can be overcome by using electron microscopy that allows for the characterization of microgel particles and determination of the number, size, shape and position of nanoparticles in hybrid microgel systems.

As an example, TEM imaging acted as the essential characterization method in an upcoming publication by Goodwin et al. (*manuscript in preparation*). For the study, an interface-assisted loading strategy to asymmetrically load PNIPAM-based microgels with gold nanoparticles was established. By floating microgels at the air/water interface, gold nanoparticles can only approach the microgels from the bulk water phase and therefore lead to an asymmetrical, one-sided loading at the periphery of the microgels. To verify the successful, one-sided loading of the microgels TEM tomography was performed to not only get a statistical overview of the amount of gold nanoparticles that got attached to the microgels but also to visualize the spatial position of the particles. In **Figure 1.4 (a) – (e)**, a series of exemplary bright-field TEM images is presented for the loaded microgel particles at five different tilting angles including  $-70^\circ$ ,  $-35^\circ$ ,  $0^\circ$ ,  $35^\circ$  and  $70^\circ$ . The images show that all microgels have been successfully loaded on one side by at least one but up to 15 gold nanoparticles with diameter  $D_{\text{TEM}}$  of  $13 \pm 1$  nm. Thus, it could be proven that the loading strategy at the air/water is applicable but there is no control about the amount of gold nanoparticles that attach to the microgels. In **Figure 1.4 (f)** a corresponding three-dimensional reconstruction of the microgel particles based on the tilting series is presented. Gold nanoparticles can be identified as white spheres with high contrast. Columnar image artifacts can be identified next to all gold nanoparticles which are caused by electron scattering. The softness of the microgels becomes apparent from the three-dimensional reconstruction as the microgels are deformed on the surface and appear rather as hemispheres with lower contrast compared to the gold nanoparticles.

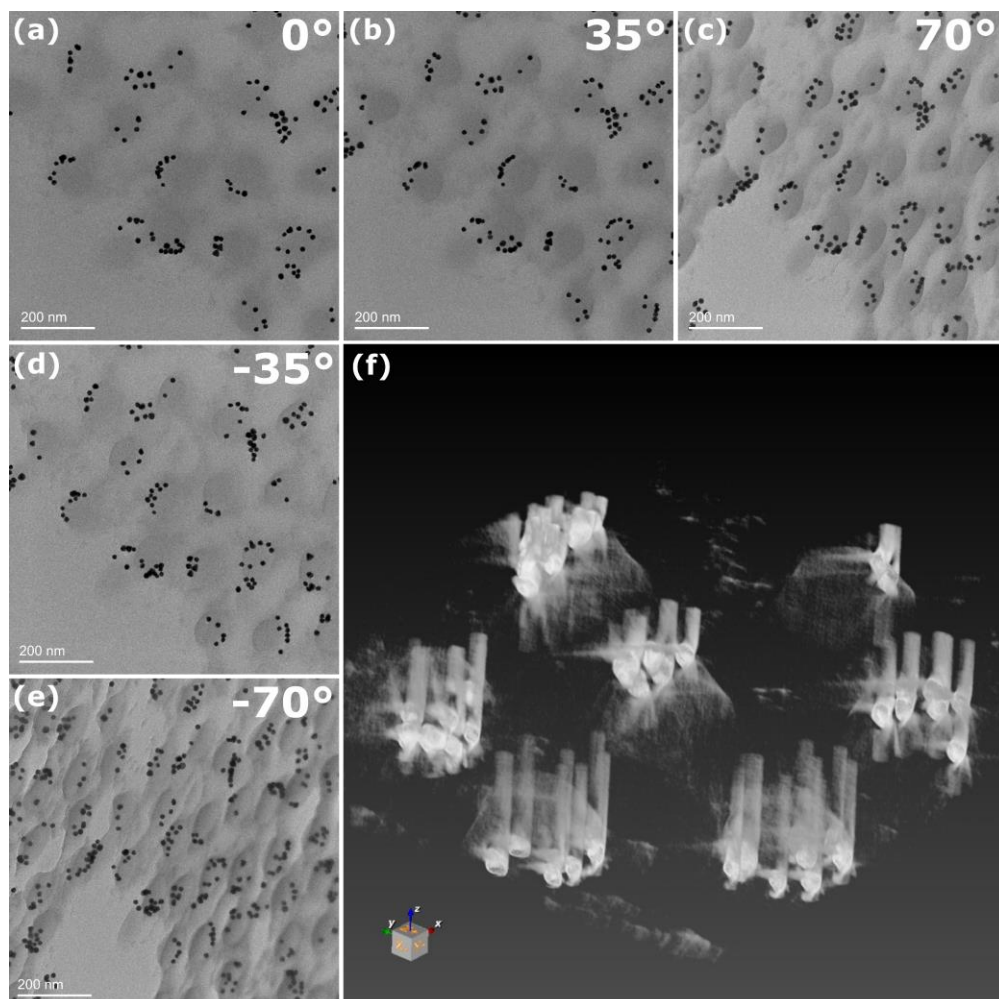


**Figure 1.4:** Example of TEM images of asymmetrical loaded PNIPAM-based microgels with gold nanoparticles. **(a) – (e)** Brightfield images of the particles at 20.000x magnification at five different tilting angles ( $-70^\circ$ ,  $-35^\circ$ ,  $0^\circ$ ,  $35^\circ$ ,  $70^\circ$ ) **(f)** Three-dimensional reconstruction of the hybrid microgel system. The reconstruction was carried out by using images from a tilting series from  $-70^\circ$  to  $70^\circ$  in steps of  $1^\circ$ . The brightfield images and the reconstruction do not show the same position on the TEM grid.

For another study that was carried out by Lerch et. al (*manuscript in preparation*), TEM imaging was used to validate the removal of silicon dioxide cores from microgel scaffolds using strong basic conditions. **Figure 1.5 (a)** and **(b)** show TEM images of the initial core-shell microgels based on poly-2-vinylpyridine. The images confirm the core-shell morphology with single nanoparticle cores homogeneously surrounded by polymer shells with a low dispersity. The pronounced contrast of the silicon dioxide cores with a size  $D_{\text{TEM}}$  of  $96 \pm 4$  nm arises from the high atomic number of silicon and the volume of the cores (see **Chapter 2.3.3**). The cores are surrounded by a poly-2-vinylpyridine shell with a shell thickness  $R_{\text{TEM}}$  of  $25 \pm 6$  nm. The images in **(c)** and **(d)** present the same batch of microgels after etching of the  $\text{SiO}_2$ -cores under

harsh basic conditions. The removal of the cores can be identified by cavities in the center of the microgels. A schematic in (e) illustrates the collapse of the hollow sphere microgels when dried on the TEM grids after the etching process. Moreover, the sketch emphasizes the lower density of polymer chains in the center after drying, resulting in lower contrast compared to the former shell of the core-shell microgels. The absence of the hard silica cores also causes the hollow microgels to be prone to deformation upon drying which is also evident by the TEM images.

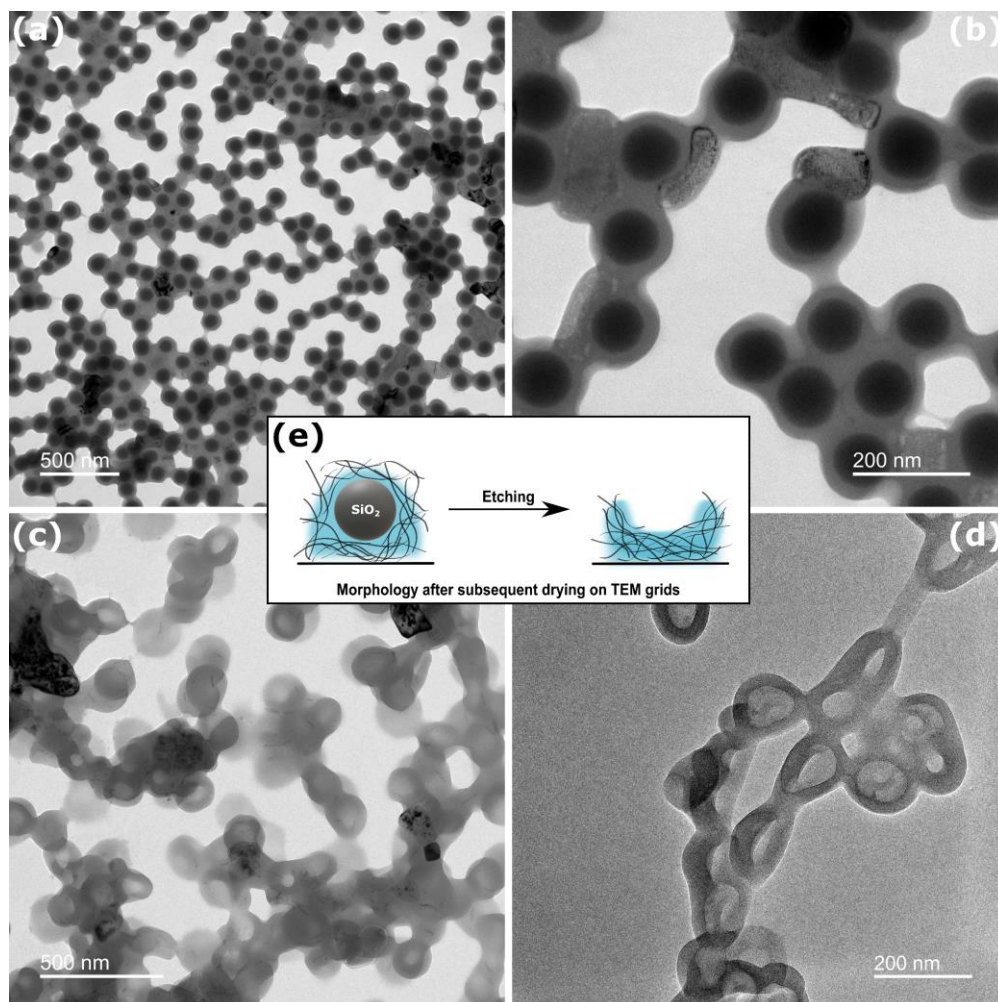


**Figure 1.5:** Exemplary TEM images of SiO<sub>2</sub> core-shell and hollow sphere microgels. (a) and (b) The core-shell particles prior to treatment with sodium hydroxide (NaOH) at 12.000x and 50.000x magnification respectively. (c) and (d) present exemplary hollow sphere particles after the alkaline treatment at 20.000x and 50.000x magnification respectively. (e) Sketch of the morphology of microgel systems prior and after the etching process when dried on a TEM grid.

While the investigation of hybrid microgels using TEM is well established, staining of microgels to gain further insight into the internal structure and morphology is rarely addressed in the literature.<sup>84</sup> Recent studies that were performed alongside the work presented in **Chapter 5** included negative staining of PNIPAM microgels dependent on the degree of crosslinking. These investigations give a first indication of the potential of negative staining in the field of microgel characterization with electron microscopy methods.

As the mesh size of microgel networks exceed the size of heavy metal ions used for negative staining by far, in theory, the metal ions should be able to diffuse into the microgel network and stain individual polymer chains of the microgels.

In **Figure 1.6**, exemplary TEM images of PNIPAM microgels recorded in the dried state in bright-field mode are presented. The images allow for the comparison of microgels with three different crosslinker densities of 1 mol% BIS in **(a)** and **(b)**, 5.4 mol% BIS in **(c)** and **(d)** and 16.3 mol% BIS in **(e)** and **(f)**. The pairs of images show the unstained particles in **(a)**, **(c)**, **(e)** and stained with a solution of 1 wt% uranyl acetate in **(b)**, **(d)** and **(f)** respectively. A significant difference of the imaged microgels for both, unstained and stained particles can be found, dependent on the crosslinker density. For the unstained particles two observations can be made when increasing the amount of crosslinker incorporated into the microgel network. On the one hand the contrast drastically increases especially when comparing microgels with crosslinker contents of 1 mol% in **(a)** to 5.4 mol% in **(c)**. On the other hand, the periphery of the microgels shows a more distinct outline with increasing degree of crosslinking. A higher degree of crosslinking leads to higher density of the polymer chains and thus a lower amount of dangling polymer chains in the periphery causing the microgels to appear more homogeneously. On the contrary, at a lower degree of crosslinking the transition of contrast between the particles and the background is less pronounced.

Staining of the microgels revealed new information about the structure and morphology. Microgels with a degree of crosslinking of 16.3 mol% BIS (**f**) show almost no difference compared to the unstained particles (**e**) due to the high density of polymer chains and the smaller mesh size that potentially prevent uranyl ions from entering the microgel. By lowering the crosslinking density, metal ions have a higher chance to diffuse into the microgel and thus allow to stain parts of the internal structure of the polymer network. The images in (**b**) and (**d**) show the loose network structure with very low homogeneity. The particles in (**b**) suggest that the microgels are made from smaller, interconnected domains or particles although a change in morphology due to drying always has to be considered which could be circumvented by cryo-EM measurements.

The investigation of microgels with transmission electron microscopy in combination with staining techniques underline the potential when scattering techniques like DLS, SAXS or SANS and spectroscopy methods like ultraviolet-visible (UV-Vis) absorbance spectroscopy are supplemented by EM imaging techniques.

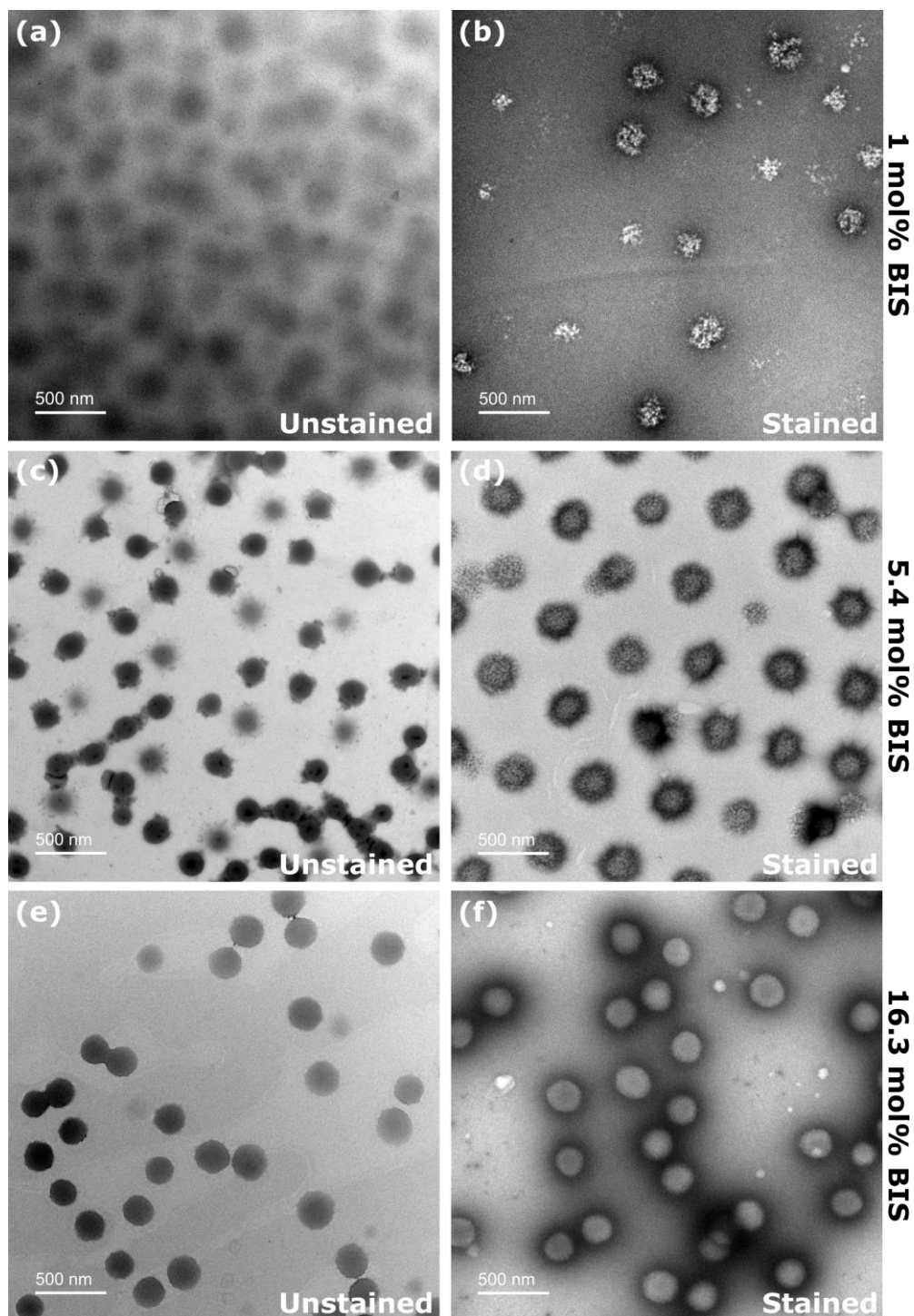


**Figure 1.6:** Comparison of TEM images of unstained and stained PNIPAM-based microgels with three different crosslinker densities. (a) and (b) Microgels with an amount of crosslinking of 1 mol% (BIS) without staining and after negative staining with uranyl acetate respectively. (c) and (d) Microgels with a crosslinking degree of 5.4 mol% unstained and stained. (e) and (f) Microgels without and with negative staining which have a crosslinking degree of 16.3 mol% BIS.

The main objective of this thesis was the preparation and systematic characterization of multifunctional copolymer microgels based on the temperature-responsive polymer PNIPAM to investigate structure-property relations. Furthermore, the synthesized microgels were used to introduce a synthesis route for core-shell hybrid microgels with a single gold nanoparticle core by an in situ formation approach (**Chapter 4**). Compared to established protocols for the encapsulation of gold nanoparticles by seeded precipitation polymerization, the in situ approach is based on the controlled accumulation and reduction of gold ions within the microgels by incorporation of comonomers with  $\beta$ -diketone functionalization. The characterization via scattering techniques like DLS and small-angle X-ray scattering (SAXS), UV-Vis absorbance measurements and (TEM) imaging of the complex microgels suggested the existence of inhomogeneous, domain-like distribution of the monomers within the network which affect the in situ formation of single gold nanoparticles in the microgels.

Driven by the questions about the inner structure of the synthesized complex copolymer microgels, a fast, accessible analytical methodology was introduced to gain deeper insights into structural inhomogeneities and potential differences between the global volume phase transition and local structural changes. By use of a combination of temperature-dependent DLS and temperature-dependent absorbance measurements, microgels with different complexities and synthesis routes have been investigated. Ponomareva et al. recently reported a linear dependency when normalized data of temperature-dependent absorbance measurements is plotted against normalized data of temperature-dependent DLS measurements for core-shell microgels with a gold core.<sup>73</sup> This correlation allows to follow the relative swelling behavior of the core-shell microgels almost interchangeable for DLS and UV-Vis absorbance measurements. Further, the study clarified that the fuzzy sphere morphology is the reason for the observed absorbance properties of the microgels during the volume phase transition. The decrease in hydrodynamic radius during the volume phase transition would suggest a decrease in absorbance or, to be more precise, scattering which cannot be explained by scattering theories like the Rayleigh-Debye-Gans (RDG) theory for spheres with a homogeneous refractive index. For a fuzzy sphere structure, the largest radius and lowest average, effective refractive index can be observed when the microgel is in the swollen state. In this state, the fuzzy shell mostly does not contribute to the visible wavelength scattering. During the volume phase transition, polymer chains from the fuzzy shell collapse onto the denser

crosslinked microgel core and thereby cause for increase in polymer volume fraction. Hence, the size as well as the refractive index contrast of the inner, homogeneous core region increase which consequently leads to an increase in the scattering intensity and detected absorbance.

In this thesis, the method presented by Ponomareva et al. was used to investigate “classical” PNIPAM microgels, various complex copolymer microgels and core-shell microgels with silicon dioxide cores with different degrees of crosslinking in the shell. **(Chapter 5)** It was shown that the correlation of data for the absolute change in size and the absolute change in absorbance acts as an indicator of the inhomogeneous distribution of monomers in the microgel network. The systematic comparison between the different types of microgels suggested the existence of differences in the internal architecture depending on the synthesis route. Furthermore, the temperature-dependent data from UV-Vis absorbance measurements could be used to calculate theoretical swelling curves, if a linear dependency exists for the correlation of DLS and UV-Vis data of the microgel system.

This highlights the potential of combining DLS and UV-Vis absorbance spectroscopy, both of which are cost-effective, readily accessible and fast techniques, as an analytical methodology to evaluate larger numbers of microgels with various compositions obtained by different synthesis routes. The approach could be particularly valuable as preliminary step before utilizing more time-consuming and costly methods like SANS.



## 2. Theoretical Background

### 2.1 Microgels – “Smart” Materials

Microgels are three-dimensional, chemically and/or physically crosslinked polymer networks that are swollen in a good solvent and can also show colloidal stability. In response to various environmental stimuli such as temperature,<sup>3-8</sup> pH,<sup>9-12</sup> or ionic strength,<sup>14, 15</sup> the crosslinked polymer networks can uptake and release solvent which results in an increase or decrease in the effective size. The term “microgel” is often treated as equivalent to terms such as hydrogel or nanogel. While a hydrogel is strictly defined by water as the surrounding medium, nanogels are defined by their size range in the nanometer range.<sup>85</sup> However, a hydrogel can still be a micro- or nanogel and vice versa which causes for the interchangeable use of the terms in the literature.

All microgels discussed in this work are based on the monomer *N*-isopropylacrylamide (NIPAM) which is one of the most intensely studied monomers that shows thermosensitive behavior when incorporated in a microgel or in a linear polymer. The surfactant-free precipitation polymerization of temperature-responsive NIPAM-based microgels was first established by Robert Pelton and Philip Chibante in 1986.<sup>64</sup> A simplified representation of a crosslinked poly-*N*-isopropylacrylamide (PNIPAM) network and a closer look at the chemical structure is shown in **Figure 2.1**. Exemplary the PNIPAM backbone is presented in red while the bifunctional crosslinker *N,N'*-methylenebisacrylamide (BIS) is colored in blue. For simplicity, the schematic does not consider the gradient in crosslinking within the network which is to be expected.

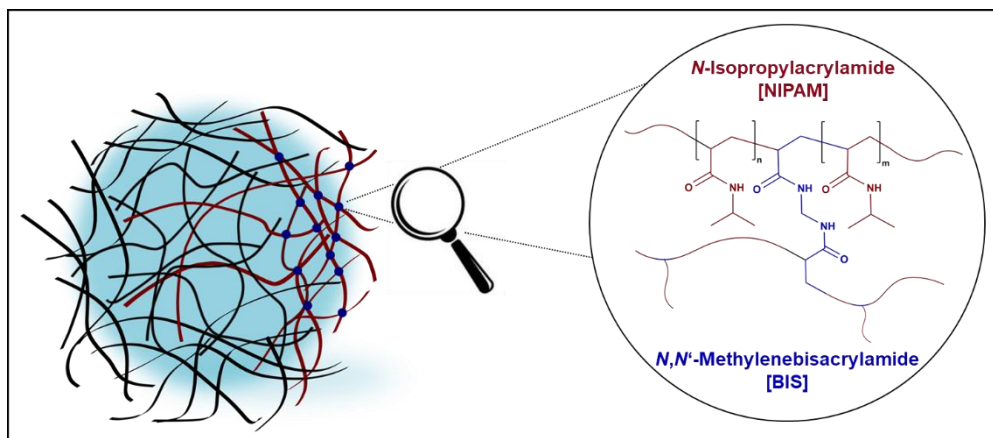


**Figure 2.1:** Sketch of a microgel network swollen in a good solvent (blue background). The magnified part shows the chemical structure of polymer chains within the microgel. *N*-isopropylacrylamide (NIPAM) is depicted in red and the crosslinker *N,N'*-methylenebisacrylamide (BIS) is presented in blue. Points of crosslinking and polymer chains are also shown in the respective color in the sketch.

### 2.1.1 Synthesis and Formation of Microgels

Microgels can be synthesized through various methods, including precipitation polymerization,<sup>64</sup> microfluidics<sup>86, 87</sup> and self-assembly<sup>88</sup> using natural and synthetic polymers. The most common methods to synthesize microgels are surfactant-supported and surfactant-free precipitation polymerizations as they provide flexible control over multiple physical and chemical properties like size distribution, surface charge, chemical composition and microstructure.

For a typical precipitation polymerization, all components including monomers, potential comonomers, crosslinkers and initiators are solved in the respective solvent. For most syntheses presented in the literature, thermal initiators like potassium persulfate (KPS) or 2,2'-azobis(2-methylpropionamide) dihydrochloride (V50) are used. A schematic representation of a precipitation polymerization is shown in **Figure 2.2**. As all microgels synthesized and evaluated in this work are based on PNIPAM, an exemplary reaction of NIPAM and the crosslinker BIS, initiated with KPS is presented in the following (**Figure 2.2 (a)**). Upon reaching reaction temperatures between 50 °C to 90 °C, the formation of free, water-soluble radicals can be observed in **(b)** and **(c)**. The free radicals react with available monomer in the solution and form oligoradicals in **(d)**. When the oligoradicals reach a certain chain length, they become insoluble, collapse and form so-called precursor particles (**Figure 2.2 (e)**).

The behavior is based on the reaction temperature exceeding the volume phase transition temperature (VPTT) of the forming polymer networks. Due to the increased polymer-polymer interactions above the VPTT, the precursor-particles are more likely to grow either by addition of singular monomers or oligoradicals or by aggregation of smaller precursor-particles to form larger particles in **(f)**. Microgels, that reach a critical size, gain colloidal stabilization by electrostatic- and steric effects. The charge that causes the electrostatic stabilization can be introduced by the (co)monomers or charge of the initiator that are incorporated into the polymer chains. Therefore, the choice and amount of the used initiator can also essentially change the properties of the formed microgels. When cooled to room temperature to finish the polymerization, the microgels swell and increase in size as the temperature falls below the VPTT. Below the VPTT, microgels resemble the fuzzy sphere model where the periphery of the microgels is formed by loose polymer chains that stabilize the microgels by steric hinderance. This can be observed in **(g)**. After the synthesis, microgels can be purified depending on the application or further functionalization. Typically, microgels are be centrifuged multiple times and/or dialyzed against water. In any case, purification will remove leftovers of unreacted monomers, short oligomers and initiator molecules.<sup>89</sup>

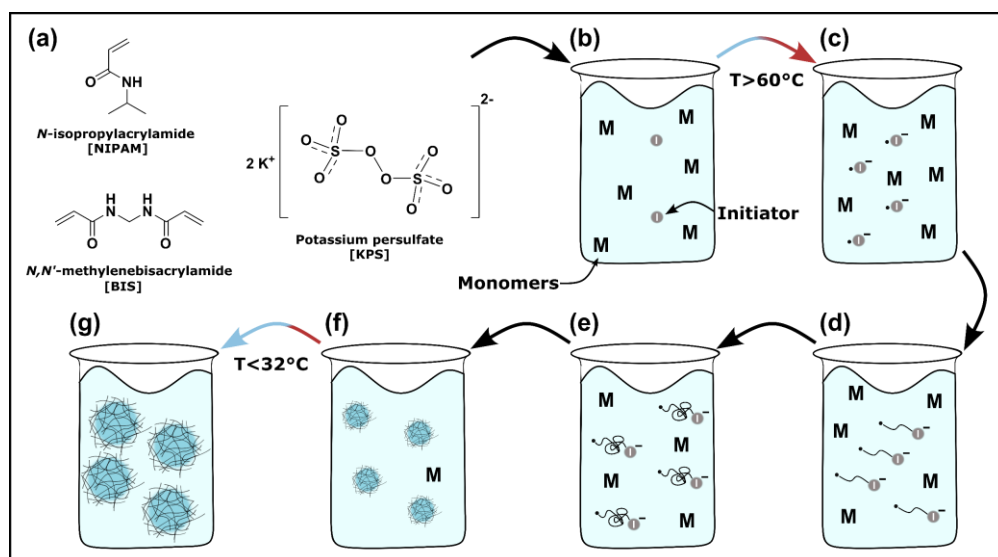


**Figure 2.2:** Schematic representation of a precipitation polymerization of microgels. **(a)** Components for a “classical” microgel synthesis including the main monomer *N*-isopropylacrylamide (NIPAM), the bifunctional crosslinker *N,N'*-methylenebisacrylamide (BIS) and the initiator potassium persulfate (KPS). **(b)** Homogeneous solution with all components **(c)** Thermic decomposition of initiator molecules and formation of initiator radicals **(d)** Formation of oligoradicals **(e)** Generation of precursor particles **(f)** Particle growth due to further consumption of monomers or aggregation **(g)** Swollen microgels after cooling to room temperature and purification.

One drawback associated with surfactant-free precipitation polymerization is the lack of control over the size of the formed microgels. To circumvent the restriction, techniques like selective quenching of the polymerization process or semi-batch and feeding methods can be used. Furthermore, a surfactant like sodium dodecyl sulfate (SDS) can be added during the polymerization to decrease the size of the microgels. Surfactants can stabilize small precursor particles with a high surface-area-to-volume ratio and thus minimize the growth by aggregation. Thereby, the overall particle size can be drastically reduced.<sup>90</sup>

### 2.1.2 Temperature-responsive Behavior

Polymers like PNIPAM possess a lower critical solution temperature (LCST) at which the polymer chains prefer the interactions with other polymer chains over the interaction with the surrounding solvent.<sup>91</sup> Linear PNIPAM exhibits a LCST of about 32 °C in water which translates to a volume phase transition temperature (VPTT) when the monomer is incorporated in PNIPAM-based microgel network. The swelling behavior of microgels can be modelled by the Flory-Rehner theory. The theory describes the free energy of a microgel  $E_{Gel}$  by a combination of the mixing energy  $E_{Mix}$ , the elastic energy due to deformations of the network  $E_{Elast.}$  and electrostatic energy  $E_{Ion.}$  in case of charged microgels and thus the presence of counter ions:<sup>92, 93</sup>

$$E_{Gel} = E_{Mix} + E_{Elast.} + E_{Ion.} \quad (2.1)$$

As a change in volume also causes a change in the internal osmotic pressure  $\Pi_{Gel}$ , a connection between the energy and the osmotic pressure  $\Pi$  can be made:

$$-\left(\frac{\partial E}{\partial V}\right) = \Pi_{Gel} = \Pi_{Mix} + \Pi_{Elast.} + \Pi_{Ion.} \quad (2.2)$$

Each contribution can be defined individually as:

$$\Pi_{Mix} = -\frac{N_A k_B T}{v} (\phi + \ln(1 - \phi) + \chi \phi^2) \quad (2.3)$$

$$\Pi_{Elast.} = -\frac{N k_B T}{V_0} \left( \left( \frac{\phi}{2\phi_0} \right) - \left( \frac{\phi}{\phi_0} \right)^{\frac{1}{3}} \right) \quad (2.4)$$

$$\Pi_{Elec.} = -\frac{fNk_B T}{V_0} \frac{\phi}{\phi_0} \quad (2.5)$$

With the volume  $V$ , the Avogadro constant  $N_A$ , the Boltzmann constant  $k_B$ , the temperature  $T$ , the molar volume of the solvent  $v$ , the volume fraction of the polymer  $\phi$ , the Flory-Huggins parameter  $\chi$  which indicates the polymer/solvent interaction, the number of chains in the network  $N$ , the volume of the relaxed Gaussian gel network  $V_0$  (reference conditions), the volume fraction of polymer  $\phi_0$  at reference conditions and the number of counter ions per chains  $f$ .

Upon collision of polymer chains in a microgel with molecules of the surrounding solvent, energy is transferred. The resulting change in energy  $\Delta E$  can be described by the product of the Flory-Huggins parameter and thermal energy  $k_B T$ . The change in energy is also directly correlated to the change in enthalpy  $\Delta H$  and entropy  $\Delta S$ :

$$\chi = \frac{\Delta E}{k_B T} = \frac{\Delta H - T\Delta S}{k_B T} = \frac{1}{2} - \frac{2\Delta S + k_B}{2k_B} \left( 1 - \frac{2\Delta H}{2\Delta S + k_B} \right) \quad (2.6)$$

The temperature-responsive swelling behavior of PNIPAM microgels is based on polymer-polymer, polymer-solvent and solvent-solvent interactions. In the swollen state, at temperatures below the VPTT, the formation of hydrogen-bonds between the amide-groups of the polymer and the solvent can be observed as they are enthalpically favored compared to polymer-polymer interactions. Additionally, water reorganizes around the hydrophobic isopropyl-groups of NIPAM in the polymer chains. If the temperature is increased (above the VPTT), the hydrogen-bonds start to break, eventually resulting in the exclusion of water from the polymer network. At the same time, the hydrophobic interactions between the isopropyl groups also increase. A phase separation of polymer and solvent can be observed as a result of the transition to a state where polymer-polymer interactions exceed the polymer-solvent interactions. Even in the collapsed state, when water is repressed, microgels still contain high amounts of water within the network. In **Figure 2.3**, exemplary data of temperature-dependent DLS measurements are presented for a PNIPAM-based microgel. The swelling curve shows the hydrodynamic radius of the microgel dependent on the temperature of the surrounding medium. Typically, the swelling curve can be adequately described by a sigmoidal function (solid red line). It can be observed, that the size of the microgel slightly decreases starting with a hydrodynamic

radius of about 275 nm at 20 °C until an abrupt strong decrease can be identified when reaching the VPTT at around 32 °C. After the collapse of the microgel, the hydrodynamic radius of the microgel approaches a plateau at about 170 nm with increasing temperature. A schematic representation of the swelling and collapse is depicted in the inset. The schematic is accompanied by digital photographs of a microgel dispersion below and above the VPTT. Upon collapse of the microgels, the turbidity significantly increases causing the dispersion to change from almost transparent to a turbid and “milk-like” appearance.

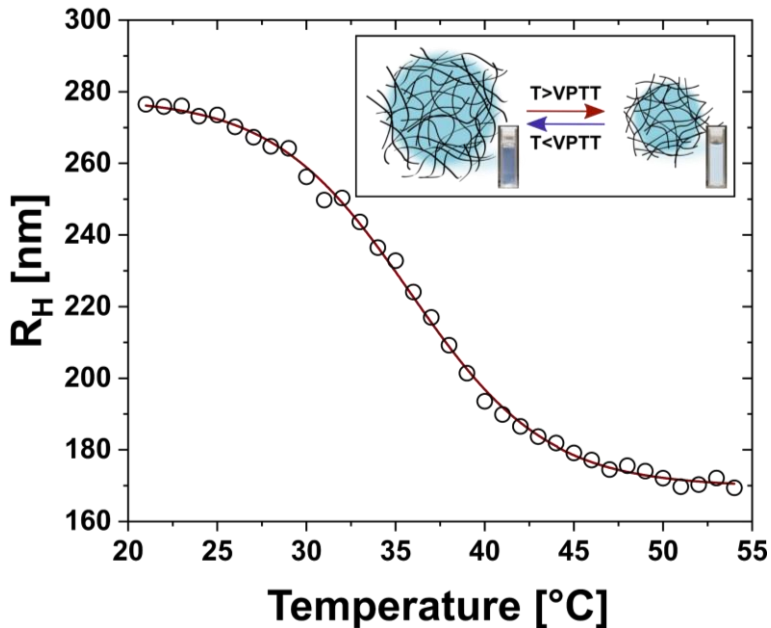


**Figure 2.3:** Exemplary data for the temperature-dependent size measurements via DLS (swelling curve). The volume phase transition is presented for a PNIPAM microgel crosslinked with 16.3 mol% BIS content. The solid red line corresponds to a sigmoidal Boltzmann fit-function. The inset shows a sketch that visualizes the change in volume below and above the VPTT. Digital photographs in the inset show the respective appearance of the microgel dispersions in the swollen and collapsed state.

The volume (de-)swelling ratios  $\alpha$  and  $\beta$  can be used to simplify the characterization of the swelling behavior of a microgel. The de-swelling ratio  $\alpha$  is defined as the ratio of the hydrodynamic volume  $V_H(T)$  of the microgel at a given temperature  $T$  to the hydrodynamic volume in the swollen state  $V_{H,swollen}$ .<sup>94</sup>

$$\alpha = \frac{V_H(T)}{V_{H,swollen}} = \left( \frac{R_H(T)}{R_{H,swollen}} \right)^3 \quad (2.7)$$

Alternatively, the swelling ratio  $\beta$  can be used which describes the hydrodynamic volume at any temperature in relation to the hydrodynamic volume in the collapsed state  $V_{H,\text{collapsed}}$ :

$$\beta = \frac{V_H(T)}{V_{H,\text{collapsed}}} = \left( \frac{R_H(T)}{R_{H,\text{collapsed}}} \right)^3 \quad (2.8)$$

As microgels are assumed as spherical objects the hydrodynamic radii can be used instead of the volume. The amount of solvent that a microgel can take up and release is strongly dependent on the degree of crosslinking. The following section will provide a more comprehensive explanation about this relationship.

### 2.1.3 Influence of Crosslinker Density on the Swelling Behavior and Structure

The potential temperature-responsive behavior of a microgel network is primarily attributed to polymers such as PNIPAM. However, it is important to note that the crosslinking of the polymer chains also has a significant impact on the physicochemical properties and architecture of the microgel. Microgels with a higher degree of crosslinking are rigid and more compact and hence show a lower swelling capacity and thus a lower de-swelling ratio  $\alpha$  compared to microgels with a lower degree of crosslinking.<sup>95</sup> To clarify the influence on the swelling capacity and the volume phase transition, **Figure 2.4** shows the data of temperature-dependent DLS measurements for three PNIPAM microgels with different degrees of crosslinking. Vertical dashed lines mark the respective VPTTs. The comparison reveals that the investigated microgels with crosslinker amounts of 1 mol% BIS (black), 5.4 mol% BIS (blue) and 16.3 mol% (red) show hydrodynamic radii between 275 nm and 380 nm below the VPTT at 20°C. In the collapsed state above the VPTT, the difference in size to the swollen state increases with decreasing amount of incorporated crosslinker. Also, for the system with a lower degree of crosslinking, the microgels show a sharp volume phase transition at about 32 °C. In comparison, for microgels with a degree of crosslinking of 16.3 mol% BIS, the volume phase transition continuously extends over a temperature range from 27 °C to about 40 °C with a determined VPTT of 34 °C. Finally, the microgel with a degree of crosslinking of 5.4 mol% BIS shows a VPTT of

33 °C and a size in the collapsed state which levels off between the microgels with lower and higher amounts of incorporated crosslinker respectively. The observations can be attributed to the rigidity of the crosslinked polymer networks. Microgels are synthesized in the collapsed state where they typically exhibit similar dimensions independent of the degree of crosslinking. Upon swelling when cooled down to room temperature, the swelling capacity of microgels differs dependent on the rigidity of the network. The degree of crosslinking hereby defines the possibilities of conformational changes and amount of water that the network can take up. At the same time, comparison of the data underlines the influence of the composition of polymer chains within the microgel network on the VPTT.

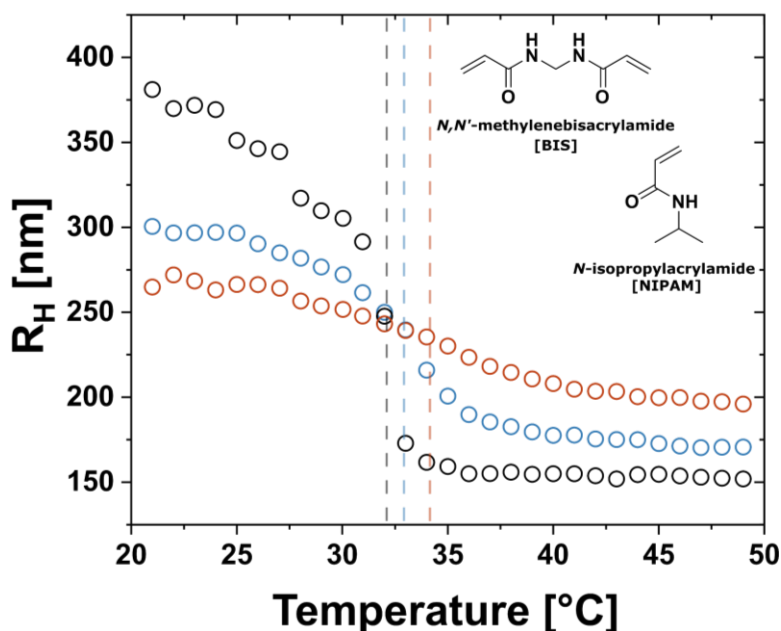


**Figure 2.4:** Data for temperature-dependent DLS measurements for three PNIPAM microgels with different amounts of crosslinker. Microgels with 1 mol% (black), 5.4 mol% (blue) and 16.3 mol% (red) of BIS content are compared. Vertical dashed lines label the respective VPTT.

Different studies showed that the distribution of the crosslinker in the microgels is not homogeneous but shows a gradient where the amount of crosslinker decreases towards the outer parts of the microgel.<sup>65, 69, 95, 96</sup> The outer periphery of microgels shows loose polymer chains often referred to as “dangling ends”. At the same time, the microgels possess a highly crosslinked core. The reason for the gradient of crosslinking within the microgels is the ratio of reactivity between monomers and crosslinker. For PNIPAM-based microgels, often the bifunctional crosslinker BIS is used, as both molecules show similarities in the chemical structure. Despite the

structural similarities, the reactivity of BIS is higher when compared to the reactivity of NIPAM, resulting in a faster incorporation at the beginning of the polymerization.

While NIPAM-based microgels are complex systems due to the interplay of the temperature-responsive polymer chains, crosslinker as well as initiator contents, the complexity and functionality can be further modified by incorporation of additional monomers into the crosslinked polymer networks resulting in the formation of copolymer microgels.

### 2.1.4 Copolymer Microgels

By definition, the addition of a crosslinker during a microgel synthesis already results in the formation of a copolymer microgel since the polymerized units contain two different monomers. As the crosslinker is a necessity for most microgel syntheses to form covalently crosslinked polymer networks (although there are microgel which are not covalently crosslinked), most of the time copolymer microgels are defined by the addition of yet another monomer. The synthesis of responsive copolymer microgels usually does not differ from the synthesis of homopolymers in terms of the reaction conditions or procedure. The comonomers can be added prior to the initiation leading to the formation of copolymers with either a statistical distribution of all components or the incorporation of additional monomers preferably in the center or periphery of the microgels due to different reaction kinetics e.g., reaction times and conversion speeds. Alternatively, the comonomers can be added during the polymerization process to affect the time of the incorporation in the polymer chains and therefore the final spatial distribution in the microgel. Usually, comonomers can be incorporated into the microgel network as long as the copolymer chains are still solvophobic enough under the preparation conditions. The composition and combination of multiple monomers can alter the properties of the microgel including the size, shape and mechanical but also physicochemical properties like the VPTT. As the volume phase transition behavior of microgels is dependent on the hydrophilic and hydrophobic interactions between individual polymer chains as well polymer chains and the solvent respectively, functional groups introduced by comonomers strongly affect the swelling properties of the network. Generally, the copolymerization with hydrophilic

comonomers leads to an increase in the VPTT,<sup>11</sup> while comonomers with an hydrophobic character decrease the VPTT.<sup>17, 97</sup>

One common example for the change of the properties is the introduction of charges to microgel systems by adding additional anionic or cationic comonomers. In 1996, Snowden et al. were the first to synthesize a PNIPAM-based microgel with statistical distribution of negative charges.<sup>17</sup> Acrylic acid (AAc), which was used for the experiments, does not only provide a negative charge which alters the swelling behavior, but also introduces an additional responsiveness to pH. In the case of acrylic acid and similar comonomers with carboxyl groups like methacrylic acid,<sup>98</sup> vinylacetic acid<sup>10, 99</sup> or allylacetic acid,<sup>14</sup> the negative charge of the carboxyl group introduces an additional repulsive electrostatic contribution to the osmotic pressure which needs to be considered regarding to the volume phase behavior. As a result, higher temperatures are needed to overcome the electrostatic repulsion and promote the polymer-polymer interactions resulting in an increase of the VPTT.<sup>17, 100</sup> Also, by incorporating higher amount of charged comonomers into the microgels network, specific changes to the swelling behavior can be observed for example the occurrence of a two-step de-swelling behavior. This behavior was also extensively studied for PNIPAM-co-AAc microgels with comonomer contents above 10 mol% of AAc. After the expected collapse of the PNIPAM contents of the network at 32 °C, a second de-swelling event can be observed due to screening of charges by either proton association or by diffusion of counter-ions into the microgel network.<sup>11</sup>

The effect on the physicochemical properties, for example the swelling properties, can already be observed upon incorporation of small amounts of comonomers into the polymer networks. In **Figure 2.5**, a comparison of exemplary temperature-dependent DLS measurements and calculated de-swelling ratios  $\alpha$  is presented for four different copolymer microgels. The microgels were synthesized by precipitation polymerization of NIPAM and 5 mol% BIS. However, each microgel system is further differentiated by the incorporation of a specific comonomer. The addition of 2.5 mol% of 2-acrylamido-2-methylpropane sulfonic acid (AMPS) during the synthesis is visually represented in blue, while the addition of acrylic acid (AAc) in red. Similarly, the incorporation of 2-vinylpyridine (2-VP) is indicated in green and (3-acrylamidopropyl)-trimethylammoniumchlorid (APTAC) is depicted in orange. The monomers have to be further differentiated, as 2-VP (positive charge) and AAc (negative charge) contain weak ionic groups that are responsive to pH, while APTAC (positive charge) and

AMPS (negative charge) provide permanently charged groups. The comparison of the temperature-dependent de-swelling ratios shows that despite all microgels exhibiting a VPTT of about 32 °C, the swelling behavior is significantly influenced by the incorporated comonomers. The de-swelling is considerably shifted for microgels with permanently charged groups indicated by the plateau values for PNIPAM-co-AMPS microgels (blue) or slight increase in the de-swelling ratios for PNIPAM-co-APTAC (orange) microgels below 30 °C. In comparison, the microgels with comonomers that also introduce a pH-responsiveness show a more pronounced decrease of the de-swelling ratio leading up to the volume phase transition. PNIPAM-co-2-VP microgels (green) exhibit a change in the de-swelling ratio already starting at 20 °C. Initially, a minor slope can be observed, indicating a gradual transition. Subsequently, larger changes can be observed with increasing temperatures above 30 °C during the volume phase transition. For PNIPAM-co-AAc microgels (red), the two-step de-swelling can be observed even for low contents of incorporated AAc in the microgel network which is indicated by the pronounced decrease in the de-swelling ratio  $\alpha$  leading up to approximately 30 °C. At this point a plateau can be identified prior to the second de-swelling step starting at about 32 °C. The determined differences are a result of electrostatic interactions and changes in the solubility of the polymer chains containing the comonomers. In addition, the experiments show that the reported two-step de-swelling can be observed even for low contents of incorporated AAc (2.5 mol%). The inset in **Figure 2.5** presents the temperature-dependent DLS measurements where the hydrodynamic radius is plotted against the temperature. Compared to the sizes of the three other copolymer microgels (orange, blue and green) that show hydrodynamic radii of about 150 nm in the swollen state, PNIPAM-co-AAc microgels (red) exhibit a significantly increased hydrodynamic radius of about 400 nm. This observation gives an indication of possible differences in the formation mechanism of the microgels during the synthesis.

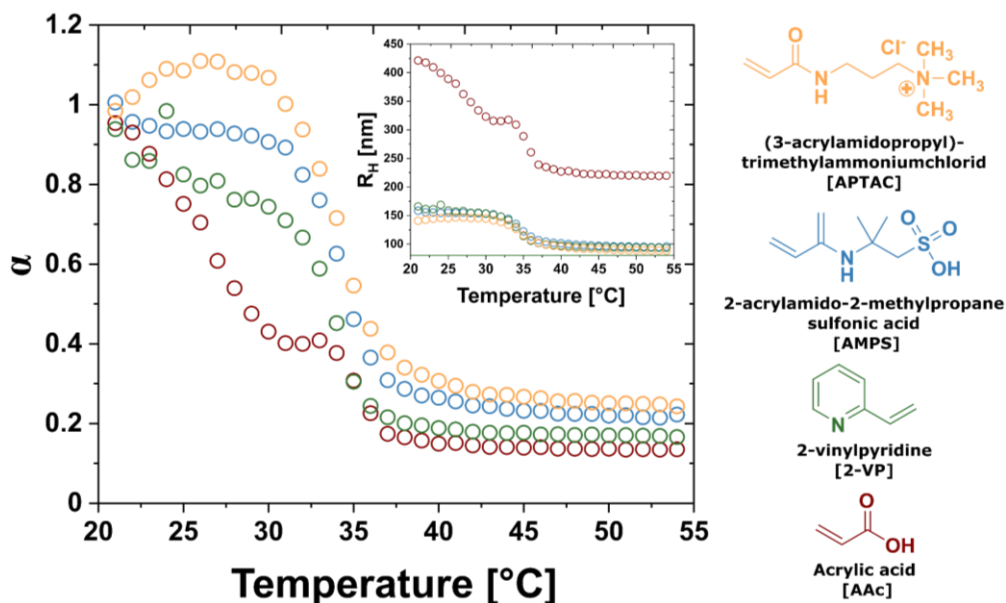


**Figure 2.5:** Calculated temperature-dependent de-swelling ratios  $\alpha$  for four PNIPAM-based microgels with different incorporated comonomers. The chemical structure of the four comonomers is presented in the corresponding color: (3-acrylamidopropyl)-trimethylammoniumchlorid (APTAC) in orange, 2-acrylamido-2-methylpropane sulfonic acid (AMPS) in blue, 2-vinylpyridine (2-VP) in green and acrylic acid (AA) in red. The inset shows the results of the respective temperature-dependent DLS measurements.

Beside a change in the swelling properties or VPTT, the introduction of functional groups via incorporation of multiple comonomers can provide entirely new properties to the microgel. For example, biological molecules like proteins or enzymes as well as inorganic, magnetic nanoparticles can be fully immobilized or captured and released.<sup>101, 102</sup> Additionally, special responsive stimuli can be introduced e.g., responsiveness to shear stress or the responsiveness to light by incorporation of azobenzenes<sup>29, 103</sup> or spiropyran derivatives<sup>104, 105</sup> into the polymer chains of the microgel.

Especially relevant for this work are comonomers containing functional groups that specifically recognize and complex ions. For example, the copolymerization and crosslinking of PNIPAM and 4-acrylamidobenz-18-crown-6 ether can allow for the tracing and removal of lead ions from the surrounding medium.<sup>106, 107</sup> Alternatively, comonomers containing  $\beta$ -diketone groups, known from other research fields like metallodrug design, can also be used to accumulate ions within the microgel network. Afterwards accumulated ions can be reduced to form metal nanostructures within the microgel networks and thereby introduce new possibilities to the hybrid systems. The application of this type of monomers will be discussed in more detail in **Chapter 2.2.3.**

## 2.2 Hybrid Microgels – The Combination of Microgels and Inorganic Nanoparticles

The interest in hybrid microgels increased significantly over the last years due to the possibility to combine magnetic, optical or catalytical properties of inorganic particles with the responsive and soft properties of microgels.<sup>108-110</sup> The properties of such hybrid systems depend not only on the composition but rather on the structure i.e. the number of inorganic particles, spatial distribution of the particle(s) and volume ratio between the microgel and the particle(s).

Over the past decades, three distinct routes to obtain hybrid microgel systems have been established.<sup>111</sup> Each synthesis route comes with specific advantages and disadvantages which will be evaluated in the following chapters.

### 2.2.1 Loading or Decoration by Diffusion

In terms of synthetic effort, the loading or decoration of microgels by diffusion of inorganic nanoparticles is the most accessible method to obtain hybrid microgel systems. Both, microgels and respective nanoparticles can be synthesized before to their combination and therefore allow for the highest versatility regarding the individual composition, size and morphology.

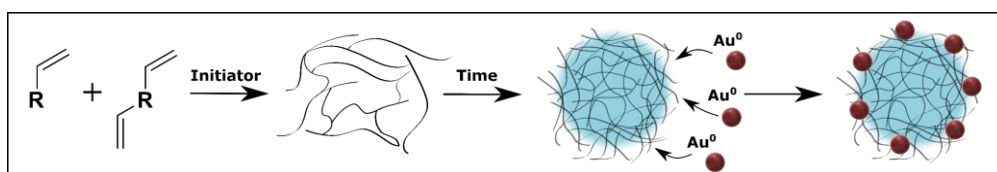


**Figure 2.6:** Schematic illustration of the decoration of a microgel with gold nanoparticles by diffusion onto a crosslinked polymer network. Microgels and nanoparticles are synthesized individually prior to the combination of both components.

**Figure 2.6** shows the principle of the decoration of microgels by diffusion and an exemplary resulting hybrid system. First, the microgel is synthesized by, for example, precipitation polymerization. Afterwards, the vigorous stirring or sonication of microgels in the presence of inorganic nanoparticles can lead to either the decoration of the outer periphery of the microgels or the diffusion of nanoparticles into the prior synthesized microgels. The structure of the resulting hybrid microgel particles strongly depend on various parameters including the size of the nanoparticles, the size and

charge of the microgels, and the mesh size of the microgels which is mostly influenced by the degree of crosslinking. Most of the experiments in literature show the accumulation of nanoparticles in the periphery of the microgels due to the low probability of nanoparticles diffuse into the networks as a consequence of the listed criteria. For the decoration of microgels, nanoparticles with different shapes like spheres or rods can be used.<sup>48, 112, 113</sup>

While easily realized, the fabrication of decorated (or loaded) hybrid microgels by diffusion comes with a large disadvantage. Compared to other methods presented in the following, there is no control over the number of particles that accumulate in the periphery or diffuse into the microgel. Another potential problem is leaking as nanoparticles in the periphery are either only entangled in the polymer chains that are not crosslinked or attracted by electrostatic interactions. Nanoparticles that diffused into the polymer network, can be entrapped within individual meshes of the network and are then retained only by steric hinderance.

The decoration of microgels is particular interesting as the change of the size of the microgel by an external stimulus has significant influence on the spatial distance between the nanoparticles. In particular, in phenomena where the distance between nanoparticles is important, such as the localized surface plasmon resonance of gold- or silver nanoparticles, it has been observed that the optical properties can be influenced by the swelling and de-swelling of decorated microgels. These changes in the microgel volume result in a rearrangement of the spatial position between the nanoparticles, ultimately affecting the optical response of the systems.<sup>112, 114, 115</sup>

## 2.2.2 Encapsulation of Nanoparticles

The encapsulation of nanoparticles can be achieved by the in situ formation of a polymer shell or scaffold around the particles. During a typical seeded precipitation polymerization, the monomers are soluble but the polymerized chains precipitate on the surface of the nanoparticle leading to the formation of the desired microgel shell.

Seeded precipitation polymerization of monomers and crosslinker moieties in presence of single inorganic nanoparticles was reported, for example, by Karg et. al in 2006.<sup>116</sup> The authors used a modified protocol for the precipitation polymerization of a PNIPAM-based microgel in the presence of silica nanoparticles and successfully realized the controlled encapsulation of one single nanoparticle in each microgel. In the following years, multiple groups developed altered and improved protocols to allow for the reproduceable encapsulation and modification of inorganic nanoparticles (gold, silver and silica) in different PNIPAM-based microgel systems.<sup>117, 118</sup> Furthermore, it was shown that the controlled encapsulation and potential in situ overgrowth of nanoparticles, for example gold nanoparticles synthesized via the well-known Turkevich protocol, makes them the preferred model systems for optical applications due to their low dispersity and controllable core size.<sup>119</sup>

A schematic representation of the encapsulation of a gold nanoparticle with an exemplary monomer and crosslinker is shown in **Figure 2.7**. In case of the encapsulation of gold nanoparticles, the nanoparticles are typically functionalized with butylamine prior to encapsulation.<sup>120, 121</sup> The functionalization increases the hydrophobicity of the surface of the gold nanoparticles further enhancing the attraction of precipitants to the individual surfaces. After the functionalization, the in situ polymerization can be performed analogously to a typical microgel synthesis.

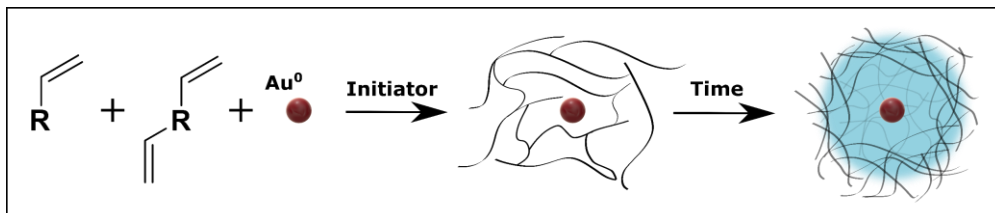


**Figure 2.7:** Schematic illustration of a seeded precipitation polymerization in the presence of a gold nanoparticle as seed.

In contrast to the loading or decoration of microgels by diffusion, the advantage of the encapsulation is the certainty that the synthesis results in the formation of microgels which contain a single nanoparticle within the microgel network.

### 2.2.3 Loading by In Situ Reduction

Loading by in situ reduction acts as the direct opposite to the approach by encapsulation of inorganic nanoparticles. For this approach, microgels can be designed, synthesized and modified prior to the formation of nanoparticles within the networks.

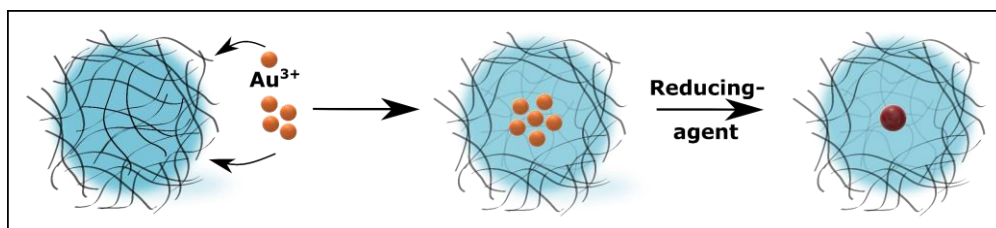


**Figure 2.8:** Schematic representation of the in situ formation of a gold nanoparticle within a microgel. Gold ions are introduced into the network by diffusion. Gathered gold ions can then be reduced by a strong reducing agent to form a spherical gold nanoparticle.

The diffusion of noble metal ions like gold and silver into microgels and the subsequent reduction within the networks using a strong reduction agent like sodium borohydride has been reported by several groups in the past.<sup>45, 46, 122-125</sup> The basic principle behind the method is schematically presented in **Figure 2.8**. Already in 2004, Kumacheva et al. presented the in situ synthesis of various nanoparticles in the presence of microgels. In their work, a PNIPAM-based copolymer was synthesized and carboxylic groups of incorporated acrylic acid (AAc) monomers were used to allow the electrostatic interaction with metal ions when in the deprotonated state. Thereby, the group showed the successful reduction of the metal ions and successive formation of multiple silver, cadmium selenide and iron oxide nanoparticles within the

microgels and in their periphery.<sup>126</sup> In other works, the reduction mostly results in microgels containing multiple nanoparticles with random spatial distribution, due to the uncontrollable diffusion and statistical distribution of metal ions in the microgels. Although hybrid microgel systems containing a random number and distribution of nanoparticles can be successfully used for catalysis experiments or similar applications, the control over the distribution and number of particles formed within the microgels remains an apparent challenge to make it an attractive alternative to the encapsulation approach.<sup>109, 127-129</sup>

Thies et al. first presented the successful formation and growth of single gold nanoparticles within complex copolymer microgels in 2018.<sup>130</sup> The poly-vinylcaprolactam-based (PVCL) copolymer microgels additionally contained acrylic acid monomers and acetoacetoxy ethyl methacrylate (AAEM) monomers which carry  $\beta$ -diketone groups. While carboxylic groups of the acrylic acid monomers increase the colloidal stability and the affinity of metal ions to the microgels,  $\beta$ -diketone groups are reported to specifically complex metal ions. The presence of  $\beta$ -diketone groups in the microgels allowed for the controlled formation of single gold nanoparticles close to the center of the microgel networks. The reason for the formation of only individual gold nanoparticles and the exact processes during the accumulation of ions and formation of nanoparticles still needs further investigation. Also, the group showed that an anisotropic overgrowth of the gold nanoparticles is possible which results in hybrid microgel systems that are challenging to obtain via the encapsulation approach.

Compared to the other techniques, the in situ formation of nanoparticles inside microgels could offer multiple advantages like an improved control over the chemical composition and architecture of the microgels and flexible but controlled loading of nanoparticles.

## 2.3 Characterization of Microgel Systems

Microgel systems can be characterized by a multitude of spectroscopic-, microscopic- and scattering techniques. In the following chapters, the essential techniques are outlined that were applied to characterize the various microgel systems in this thesis. This includes DLS and UV-Vis spectroscopy which allow to learn about the size and swelling properties of microgels in diluted dispersion. In addition, TEM is elaborated as a technique that can be used to visualize the microgels and provide information about the morphology especially in case of composite microgels.

### 2.3.1 Dynamic Light Scattering

DLS is one of the most prominent non-invasive techniques to measure the size distribution of small particles e.g., microgels in dispersions. The technique is based on the principle that particles in dispersion undergo random movement, known as Brownian motion. The particle motion and velocity are strongly dependent on the mass of the particles and the temperature of the surrounding medium. The velocity and both parameters can be correlated as follows:

$$v_m = \sqrt{\frac{2k_B T}{m}} \quad (2.9)$$

Here,  $v_m$  is the mean velocity,  $k_B$  is the Boltzmann constant,  $T$  corresponds to the temperature and  $m$  gives the mass of the individual particle.

As a result, particles with lower masses at a given density and thus smaller particles are moving at higher speeds while particles with a higher mass show an opposite behavior.

As for all other scattering techniques like static light scattering (SLS), SAXS or SANS, the most important quantity that is valid for all scattering experiments is the absolute value of the scattering vector  $\vec{q}$  which can be defined as:<sup>131</sup>

$$|\vec{q}| = \frac{4\pi n}{\lambda} \sin\left(\frac{\theta}{2}\right) \quad (2.10)$$

Here  $n$  is the refractive index of the dispersing medium,  $\lambda$  is the wavelength of the incident radiation and  $\theta$  gives the scattering angle between the incoming and scattered radiation. In **Figure 2.9 (a)**, a schematic illustration of a scattering process in a simplified DLS setup and the construction of an exemplary scattering vector  $\vec{q}$  is shown. In the illustration, the incident light with wave vector  $\vec{k}_{in}$  is scattered by a scattering center in the scattering volume at an angle of  $\theta$ . The direction of the scattered light is presented by wave vector  $\vec{k}_{out}$ . The absolute value of the scattering vector  $\vec{q}$  gives the difference between  $\vec{k}_{in}$  and  $\vec{k}_{out}$  and is a measure for the spatial resolution of a scattering event. Furthermore, the absolute value of the scattering vector  $\vec{q}$  has the dimension of reciprocal length.

For a typical DLS experiment, monochromatic, coherent light is focused on a probed volume resulting in the scattering of the light in all directions by interactions with the investigated particles.

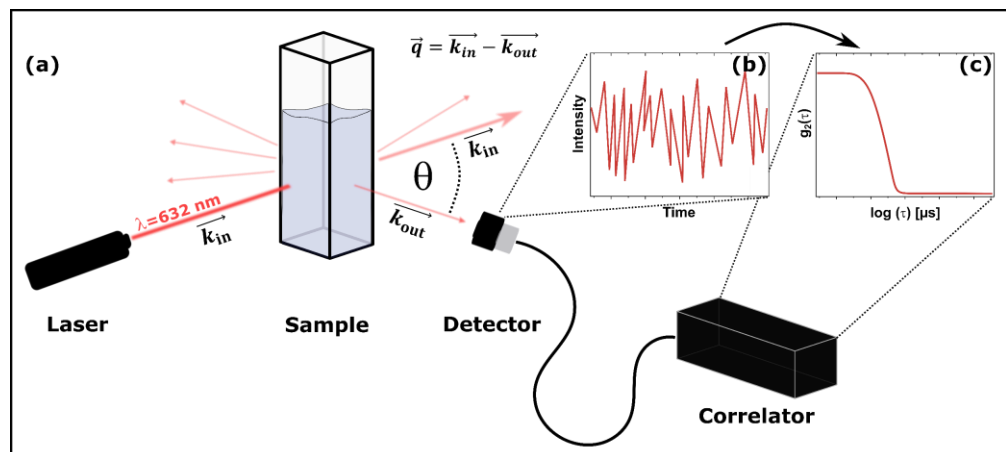


**Figure 2.9:** (a) Scheme of a setup for DLS experiments including the most crucial components: A monochromatic laser, the investigated sample, a detector and a correlator. The simplified illustration also shows the construction of the scattering vector  $\vec{q}$ . (b) Example of a typical observable change in scattering intensity as function of time due to diffusion of scattering objects in the scattering volume. (c) Theoretical mean auto correlation function  $g_2(\tau)$ .

Two different forms of scattering need to be considered: inelastic and elastic. Inelastic scattering occurs when energy is transferred between incident light and the scattering material. While an inelastic scattering event causes both, a change in the direction and the wavenumber of the scattered light, for elastic scattering, only a change in direction of the scattered light can be observed.

DLS experiments are considered as quasi-elastic scattering experiments as both types of scattered light are typically detected and processed. However, the changes

in energy involved in the scattering processes are usually very small compared to the energy of the incident light and therefore negligible.<sup>132</sup> Additionally, waves of scattered light can interfere dependent on the scattering direction and spatial position of the object that scatters the light. The time and spatial-dependent changes in constructive or destructive interference of the waves of scattered light are detected by a photomultiplier or an avalanche photodiode.

Due to the movement of particles, which results in a continuous change in the spatial position of particles and consequently a continuous change in the interference patterns of the scattered light, intensity fluctuations can be recorded as a function of time. A schematic illustration of exemplary intensity fluctuations as a function of time is presented in **Figure 2.9 (b)**.

The scattering intensities  $I(q, t)$  of scattered light can be analyzed using the normalized intensity-time autocorrelation function  $g_2(\tau)$ :<sup>126, 133, 134</sup>

$$g_2(\tau) = \frac{\langle I(t)I(t + \tau) \rangle}{\langle I(t) \rangle^2} \quad (2.11)$$

Here,  $I(t)$  is the scattering intensity at the time  $t$  and  $I(t + \tau)$  gives the scattering intensity after a certain correlation time  $\tau$ . The autocorrelation function describes the similarity of the signals at time  $t$  and after a certain time interval  $t + \tau$ .

While  $g_2(\tau)$  can be measured and calculated, the normalized electric field-time autocorrelation function  $g_1(\tau)$  is needed for the analysis of the obtained DLS data as  $g_1(\tau)$  is correlated to the relative motion of the particles to each other:<sup>131, 134</sup>

$$g_1(\tau) = \frac{\langle E(t)E(t + \tau) \rangle}{\langle E(t) \rangle^2} \quad (2.12)$$

Here,  $E(t)$  describes the scattered electric field at the time  $t$  and  $E(t + \tau)$  after the time interval  $\tau$ , respectively. As  $g_1(\tau)$  and the scattered electric fields are not directly accessible by measurements, the Siegert relation can be used which correlates  $g_1(\tau)$  and  $g_2(\tau)$ :<sup>131, 135</sup>

$$g_2(\tau) = 1 + \beta_{\text{Siegert}} |g_1(\tau)|^2 \quad (2.13)$$

The factor  $\beta_{\text{Siegert}}$  depends on the experimental geometry and the scattering properties of the particles. The decay of an exemplary intensity-time autocorrelation function  $g_2(\tau)$  is presented in **Figure 2.9 (c)**. For monodisperse, isotropic scattering objects the normalized electric field-time autocorrelation function can be simplified to an exponential function with a decay constant  $\Gamma$ :

$$g_1(\tau) = e^{-\Gamma\tau} \quad (2.14)$$

As for most, non-ideal samples, polydispersity of the systems causes a distribution in particle size and hence a distribution of decay constants. To take the normalized distribution of decay rates  $G(\Gamma)$  into consideration, **Equation 2.13** can be expanded as shown in **Equation 2.14**:

$$g_1(\tau) = \int_0^{\infty} G(\Gamma) e^{-\Gamma\tau} d\Gamma \quad (2.15)$$

The resulting data for the autocorrelation can be analyzed by different methods including the Cumulant method<sup>136</sup> or the CONTIN algorithm for non-monomodal distributions.<sup>137, 138</sup> For monomodal particle systems that show a Gaussian-like distribution around a mean value, the Cumulant method is often preferred before the use of advanced analytical procedures like the CONTIN method which requires complex numerical algorithms.

The Cumulant method involves a series expansion to the autocorrelation function (**Equation 2.15**) to reconstruct the function by its cumulants  $\mu$ :

$$g_1(\tau) = e^{-\bar{\Gamma}\tau} - \left( 1 + \frac{\mu_2}{2} \tau^2 - \frac{\mu_3}{3!} \tau^3 + \frac{\mu_4}{4!} \tau^4 \dots \right) \quad (2.16)$$

The function can also be rewritten as:

$$\ln(g_2(\tau) - 1) = \ln(\beta_{\text{Siegert}}) + 2 \left( -\bar{\Gamma}\tau + \frac{\mu_2}{2!} \tau^2 - \frac{\mu_3}{3!} \tau^3 + \frac{\mu_4}{4!} \tau^4 \dots \right) \quad (2.17)$$

Here,  $g_1(\tau)$  is replaced by  $g_2(\tau)$  through correlation of the Siegert relation (**Equation 2.13**) and the single exponential decay for a monodisperse system shown in **Equation 2.14** converted to a logarithmic mode:

$$g_2(\tau) = 1 + \beta_{\text{Siegert}} [e^{-\bar{\Gamma}\tau}]^2 \quad (2.18)$$

And further:

$$\ln(g_2(\tau) - 1) = \ln(\beta_{\text{Siegert}}) - 2\bar{\Gamma}\tau \quad (2.19)$$

The first cumulant  $\bar{\Gamma}$  in **Equation 2.16** and **Equation 2.17** indicates the mean value of decay constants and the second cumulant  $\mu_2$  describes variance of the relaxation rate distribution and can be used to quantify the dispersity of the system.

The Cumulant method as well as the CONTIN algorithm both allow for the extraction of the mean decay constant  $\bar{\Gamma}$  of the particles which is needed to calculate the diffusion coefficient  $D_T$  at a certain scattering vector  $q$ :

$$D_T = \frac{\bar{\Gamma}}{q^2} \quad (2.20)$$

Furthermore, the diffusion coefficient  $D_T$  which is the magnitude most DLS experiments are aiming for can be used to obtain the hydrodynamic radius  $R_H$  of the investigated particles. The correlation between  $D_T$  and  $R_H$  can be found in the Stokes-Einstein equation:

$$D_T = \frac{k_B T}{6\pi\eta R_H} \quad (2.21)$$

Here,  $k_B$  is the Boltzmann constant,  $T$  the temperature and  $\eta$  the viscosity of the surrounding medium.

In terms of characterization of microgels in dispersion, DLS is one of the most powerful techniques as it allows to follow the hydrodynamic size in dependence of the temperature. Information about the volume phase transition and the ratio between the size in the swollen and collapsed state usually act as characteristic quantities to compare different microgel systems. For simplification, microgels are assumed as perfect spheres when processing measured autocorrelation data.

### 2.3.2 Ultraviolet-visible Absorbance Spectroscopy

UV-Vis absorbance spectroscopy is a versatile and widely used analytical technique that can provide information about a variety of chemical and biochemical systems. During measurements, a sample is irradiated with light of varying wavelength in the UV and/or visible regions of the electromagnetic spectrum. Depending on the chemical and electronic structure, phenomena like absorption, reflection and scattering can occur.

In typical experiments, the investigated sample absorbs or scatter some parts of the incident light and the intensity of the transmitted light is measured relative to the incident light. The resulting spectrum provides information about the absorbance of the sample as a function of wavelength. The shapes and positions of signals of absorbance in the spectrums can reveal information about the structure and composition of investigated samples. For example, characteristic signals in the spectrum can be used to identify the presence of certain chemical functional groups, such as aromatic groups which absorb strongly in the UV region. The width of the signals can also provide information about the size and shape of the absorbing molecules or particles.<sup>139</sup>

The extinction which describes the combination of absorbance and scattering processes is related to the concentration of the species in the sample, as described by the Lambert-Beer's law:

$$E_{\lambda} = \log_{10} \left( \frac{I_0}{I} \right) = \varepsilon_{\lambda} \cdot c \cdot d \quad (2.22)$$

Here, the extinction  $E_{\lambda}$  describes the absorbance of the material for light with a certain wavelength  $\lambda$ .  $I_0$  and  $I$  show the intensity of the incident and transmitted light respectively. The concentration of the attenuating species is given by  $c$  and  $d$  is the optical path length through the sample volume.  $\varepsilon_{\lambda}$  relates to the molar attenuation coefficient of the attenuating species at a specific wavelength.

Alternatively, the attenuation of incident light based on interactions with the sample can be expressed with number density  $N$  (accessible for hybrid microgel systems through, for example, SAXS measurements) and the extinction cross section  $C_{\text{Ext.}}$ :

$$E_{\lambda} = \log_{10} \left( \frac{I_0}{I} \right) = \frac{C_{\text{Ext.}} N d}{2.303} \quad (2.23)$$

The extinction cross section  $C_{\text{Ext.}}$  which describes the probability of an absorption process and the molar attenuation coefficient  $\varepsilon_{\lambda}$  can be conversed by considering the Avogadro constant  $N_A$ :

$$C_{\text{Ext.}} = \frac{2.303}{N_A} \varepsilon_{\lambda} \quad (2.24)$$

A UV-Vis spectrophotometer consists of one or multiple light sources, a sample holder, monochromators or prisms and a detector and can be built in two distinct ways. Typically, a polychromatic light source is used in combination with scanning monochromators in front of the sample (scanning spectrophotometer). Thereby, only light of a single wavelength is directed on the sample volume at a time. As a result, the absorbance for light of one specific wavelength can be recorded but the scanning monochromators also allow to change the wavelength so the absorbance is typically measured as a function of the wavelength.

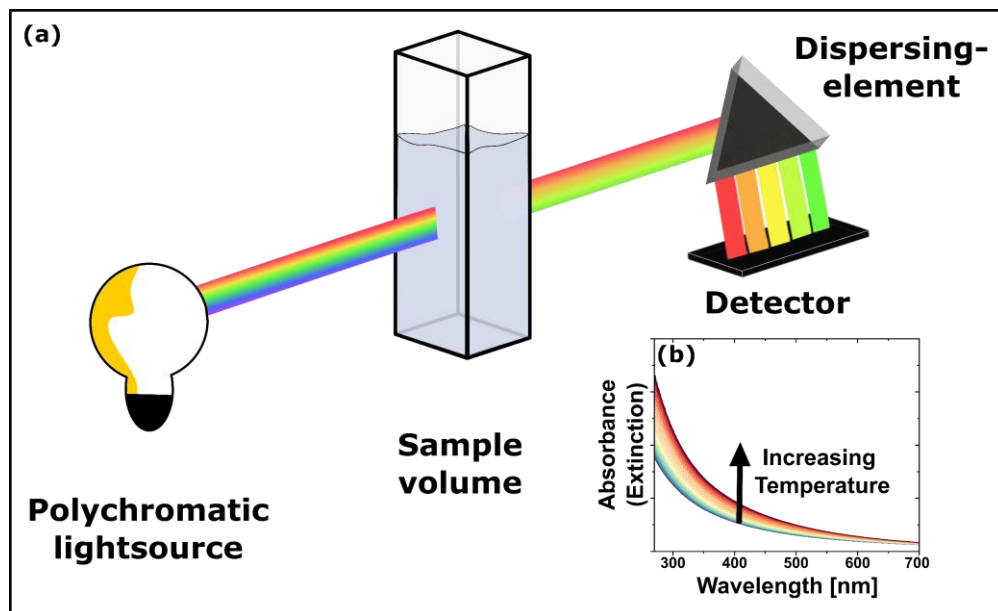


**Figure 2.10:** (a) Schematic illustration of a UV-Vis absorbance experiment with an array spectrophotometer. Polychromatic light is focused on a sample volume. The light that passes through the sample is separated by dispersing elements and the absorbance of the sample is detected as a function of the wavelength. The depiction shows an exemplary experiment where high-energy visible light with wavelengths below 400 nm (blue, violet) is absorbed by the sample. The illustration only shows the interaction with light of the visible spectrum but the same principles can be applied for light of the ultraviolet and infrared region. (b) Exemplary temperature-dependent UV-Vis absorbance measurements for a PNIPAM-based microgel. The increase in temperature is indicated by the change of the color from blue to red.

In this work, an array spectrophotometer was used to investigate all samples. A schematic representation of the setup of the UV-Vis spectrometer is shown in **Figure 2.10 (a)**. First, the polychromatic light is focused on the sample volume. The light that passes through the sample is separated into individual wavelengths by a dispersion element or reflection grid and detected as a function of the wavelength. In the schematic illustration, the sample absorbs light with higher energy (400 nm and below) and only light with wavelengths above 400 nm is transmitted. Compared to a scanning spectrophotometer, this setup allows for even quicker recording of spectra over the whole range of wavelengths.

In **Figure 2.10 (b)**, exemplary spectra for temperature-dependent UV-Vis spectroscopy measurements of a PNIPAM-based microgel are presented in the wavelength range from 280 to 700 nm. The colors of the spectra represent the increase in temperature from 15 °C (blue) to 55 °C (red) in steps of 1 °C. In opposite to the decrease in size observable in temperature-dependent DLS measurements, an increase in the absorbance can be detected with increasing temperature.

At first glance, microgels do not seem to be suitable for UV-Vis spectroscopy measurements as they do not provide a conjugated  $\pi$ -bond system or similar free-electron system that can absorb electromagnetic waves. Nonetheless, it has to be considered that the incident light  $I_0$  is not only reduced by the absorbance  $I_{\text{Abs.}}$  but also by scattering  $I_{\text{Scat.}}$ :

$$I_{\text{Trans.}} = I_0 - I_{\text{Abs.}} - I_{\text{Scat.}} \quad (2.25)$$

Thus, the absorbance by microgels is negligible and the observed difference between the transmitted intensity  $I_{\text{Trans.}}$  and the intensity of the incident light  $I_0$  is almost completely based on scattering. The extinction cross section is thereby directly related to the scattering cross section  $C_{\text{Ext.}} = C_{\text{Scat.}}$  and for non-absorbing samples the Lambert-Beer law in **Equation 2.23** can be adjusted to:

$$E_\lambda = \log_{10} \left( \frac{I_0}{I} \right) = \frac{C_{\text{Scat.}} N d}{2.303} \quad (2.26)$$

For simplification, in the following the term absorbance will still be used to describe the observed phenomena during UV-Vis measurements of microgels although they are mostly related to scattering of the microgels.

In principle, the Rayleigh-Debye-Gans (RDG) approximation would suggest that the light scattering intensity cross-section  $C_{\text{Scat.}}^{\text{RDG}}$  decreases with sixth power of the radius of the scattering object:<sup>140, 141</sup>

$$C_{\text{Scat.}}^{\text{RDG}} = \frac{24\pi^3 \left( \frac{4}{3} \pi R^3 \right)^2}{\lambda^4} \left( \frac{\left( \frac{n_{\text{microgel}}}{n_{\text{solvent}}} \right)^2 - 1}{\left( \frac{n_{\text{microgel}}}{n_{\text{solvent}}} \right)^2 + 2} \right)^2 \quad (2.27)$$

$R$  defines the radius of the microgel,  $\lambda$  is the wavelength of the incident light and  $n_x$  gives the refractive index of the microgel and the surrounding solvent.

The RDG theory is valid for particles with a low refractive index contrast relative to the solvent and dimensions that are smaller than the wavelength of visible light:<sup>141</sup>

$$\frac{4\pi R}{\lambda} \left| \frac{n_{\text{microgel}}}{n_{\text{solvent}}} - 1 \right| \ll 1 \quad (2.28)$$

For most microgels (like the microgels discussed in this work) the RDG is valid because the effective refractive index of the microgels in the swollen state at low temperatures is sufficiently low to fulfil the RDG criterion.<sup>68</sup> At higher temperatures, when the microgels are in the collapsed state, the difference in refractive index increases compared to the refractive index of water ( $n_{\text{H}_2\text{O}} = 1.333$ ) so that the RDG criterion is not necessarily fulfilled. In this case, Mie theory for a homogeneous sphere is a better model to describe the data.

For temperature-dependent absorbance measurements of microgels, it would be reasonable to assume that, due to the high dependency on the radius, the scattering intensity and thus the absorbance of the microgels would decrease with increasing temperature as the microgels collapse. However, it can be observed that the absorbance increases during the temperature induced microgel collapse which can be attributed to the transition from fuzzy spheres to hard sphere-like scatterers. In the swollen state, the outer, fuzzy parts of the microgel make up for a large part of the particle volume but do not significantly contribute to the detected scattering. The scattering is dominated by the inner, rather homogeneous core region with a constant refractive index. During the volume phase transition, the polymer chains of the fuzzy shell collapse onto the higher crosslinked core while water is released from the microgel network. As a result, the polymer volume fraction of the microgel region rises resulting in an increase of the scattering.<sup>73</sup> The polymer volume of a microgel can be approximated by **Equation 2.29**, as long as the microgels are considered as homogeneous spheres:

$$\phi = \frac{V_{\text{polymer}}}{V_{\text{microgel}}} = \frac{V_{\text{polymer}}}{\frac{4}{3}\pi R^3} \quad (2.29)$$

Thus, in regard to the RDG theory, the increase in size and the refractive index contrast of the higher crosslinked core region outweighs the decrease in the effective size of the microgel during the volume phase transition.

### 2.3.3 Transmission Electron Microscopy

Transmission electron microscopy (TEM) is a type of microscopy that uses electrons instead of light to examine the structure of materials. The method is based on the interaction of a focused beam of accelerated electrons that pass through the investigated specimen. In 1931, Ernst Ruska was the first to develop and operate a TEM and thereby overcome the resolution limit set by the wavelength of visible light.<sup>142-144</sup> Image resolution quantifies the shortest distance between two points on a specimen that can still be distinguished as two separate entities by a detector, camera or observer. Mathematically, the resolution in a perfect optical system can be described by Abbe's equation:

$$d = \frac{0.61 \lambda}{n \sin \alpha} \quad (2.30)$$

Herein,  $\lambda$  is the wavelength of the radiation,  $n$  is the refractive index of the viewing medium, and  $\alpha$  the semi-angle of collection of the magnifying lens. Most of the time ' $n \sin \alpha$ ' (often referred to as numerical aperture) can be approximated by 1 so that the resolution is equal to about half of the wavelength of the radiation source. Therefore, the best resolution that can be achieved by "classical" visible light microscopy is approximately 250 nm when assuming a radiation light source with violet light (the lower end of the visible light spectrum) with a wavelength of 400 nm. In electron microscopy however, the theoretically achievable resolution is limited by the wavelength of electrons.

The wavelength of an electron can be derived by de Broglie's equation:

$$\lambda = \frac{h}{p} \quad (2.31)$$

with Planck's constant  $h$  and momentum  $p$ .

Louis de Broglie was the first to show that not only light shows wave-particle duality but every other matter particle also has wave and particle characteristics and that the wavelength decreases inversely proportional with increasing momentum.

As the momentum is dependent on the mass at rest  $m_0$  and the velocity  $v$ :

$$p = m_0 v = \sqrt{2m_0 e U_A} \quad (2.32)$$

a connection can be made between the wavelength and the acceleration voltage of electrons  $U_A$  with  $e$  as the unit charge:

$$\lambda = \frac{h}{\sqrt{2m_0 e U_A}} \quad (2.33)$$

For acceleration voltages above 50 kV, relativistic effects have to be considered which adjust **Equation 2.33** by taking light velocity  $c$  into account:

$$\lambda = \frac{h}{\sqrt{e U_A \left( 2m_0 + \frac{e U_A}{c^2} \right)}} \quad (2.34)$$

Assuming an acceleration voltage of 80 kV (which was used for most of the imaging in this work), the electrons possess a wavelength of 4.2 pm which results in a theoretical resolution on the order of a few picometers. There is still a discrepancy between theoretical limits and the resolution limit that can be realized in real applications. For the moment, the electromagnetic lenses of an electron microscope act as the restrictive part to achieve these theoretical values. Due to lens aberration the maximum achievable resolution, as of now, is about 0.1 nm.<sup>144-146</sup>

**Figure 2.11** presents the essential components of a TEM in **(a)** and the corresponding position of the respective components in the JEOL JEM 2100Plus transmission electron microscope which was used during this work in **(b)**. The individual components will be discussed in more detail in the following paragraphs. In general, a TEM consists of five major components:

1. The electron gun
2. The condenser lens
3. The objective lens including the specimen stage
4. The projector lens
5. The fluorescent screen or detectors like charged-coupled device (CCD) or complementary metal oxide semiconductor (CMOS) cameras, scanning transmission electron microscopy (STEM) detectors, energy-dispersive X-ray spectroscopy (EDX) or electron energy loss spectroscopy (EELS) detector

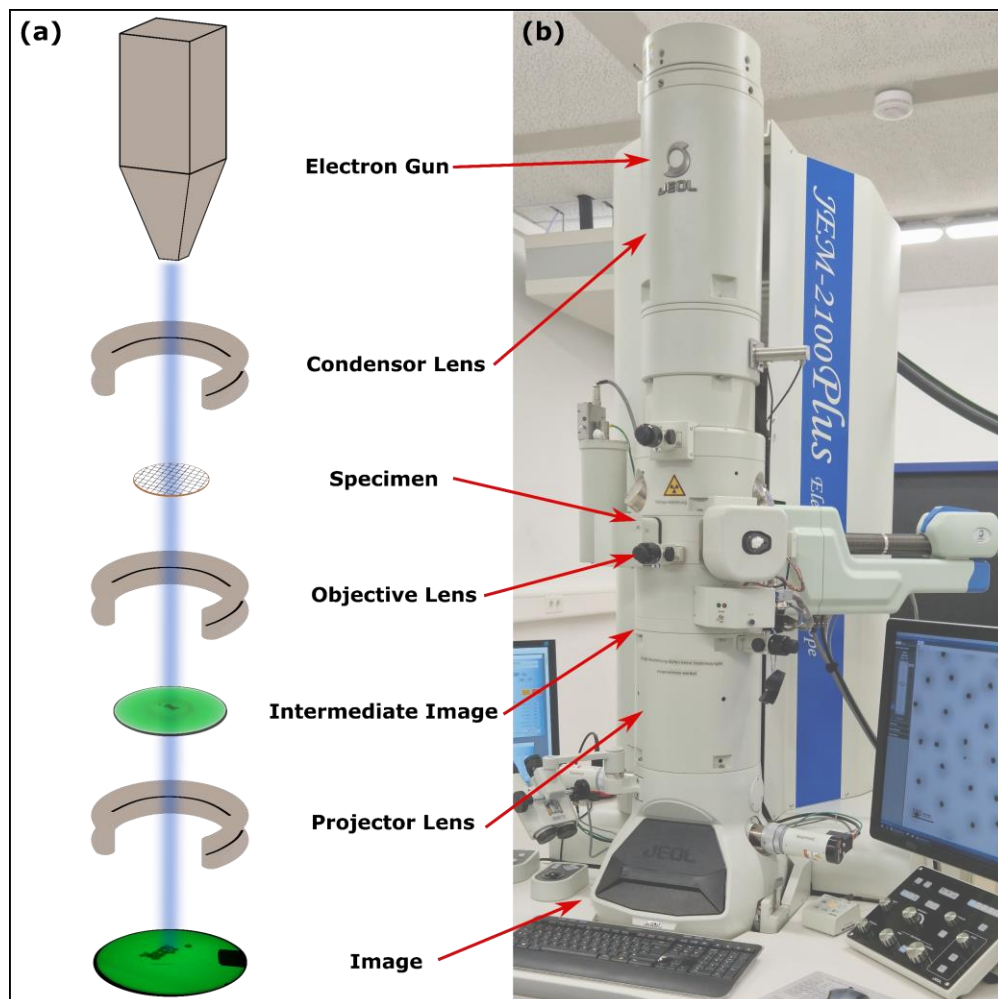


**Figure 2.11:** (a) Schematic representation of the essential components of a transmission electron microscope (TEM). (b) Digital photograph of the JEOL JEM 2100Plus transmission electron microscope which was used within the scope of this work. Red arrows show the position of the individual components in the microscope.

### *Electron Guns*

The electron gun is a key component of a transmission electron microscope. It produces a beam of electrons that is used to illuminate the specimen and form an image.

It can be differentiated between two types of electron guns used in TEMs: Thermionic-emission guns and field emission guns (FEG emitter). Both types of electron guns come with their own advantages and disadvantages which will be discussed in the following:

A **thermionic electron gun** is based on a triode system. A simplified presentation of a thermionic electron gun is shown in **Figure 2.12 (a)**. The triode system consists of a cathode, a Wehnelt electrode and an anode. The cathode (a twisted tungsten wire or in modern TEMs (and the TEM operated in this work) a LaB<sub>6</sub> crystal) is heated up to over 2000 °C. By heating up the “V”-shaped wire or crystal respectively, electrons acquire enough energy to overcome the work function and are emitted into the vacuum. The emitted electrons travel towards the anode under influence of the acceleration voltage applied between the cathode and the anode. Typically, the acceleration voltage is between 80 and 300 kV. The Wehnelt electrode which is placed between the cathode and the anode, acts as a control grid and also serves as an electromagnetic lens. By adding negative voltage to the Wehnelt electrode, the emission of the electrons is suppressed for most areas of the cathode. Only the emitter tip is placed in a relative position to the cathode so that electrons can be emitted and directed towards the anode. Therefore, the applied bias of the Wehnelt electrode not only controls the emission current but also the width of the electron beam which is further connected to the achievable resolution. A thermionic electron gun comes with the advantage of being comparably inexpensive due to not requiring an ultra-high vacuum. At the same time thermionic electron guns have a lower lifetime, higher energy spread and generally a lower achievable resolution than field emission guns.

**Field emission guns (FEGs)** are often preferred over thermionic guns, due to their superior performance in terms of brightness, stability and energy resolution but also come at much higher costs. FEG emitters rely on the field emission phenomenon. By applying a strong electric field to the cathode using an extraction anode, the potential barrier is strongly reduced (Schottky effect). The lower thermal energy required to overcome the barrier for electrons to leave the cathode tip is reflected by a lower energy range of the emitted electrons. Typically, in a so-called Schottky field emitter, the cathode is made from a very fine tungsten tip. The basic principle is very similar to a thermionic emission gun. In **Figure 2.12 (b)**, the simplified structure of a field emission gun is presented. The tungsten tip is heated by means of a heating current and an extraction voltage (extractor) is applied to release the electrons out of the tip. The electrons are then further accelerated and focused into condenser lens by applying a high voltage between the cathode and anode. Recently, “cold” field emission guns gained more importance as they can further improve the achievable

resolution of an electron microscope. A “cold” FEG makes use of the tunneling effect which does not heat the cathode at all during emission. The lower temperature that is needed to release electrons from the cathode tip further reduces the energy range of the emitted electrons.

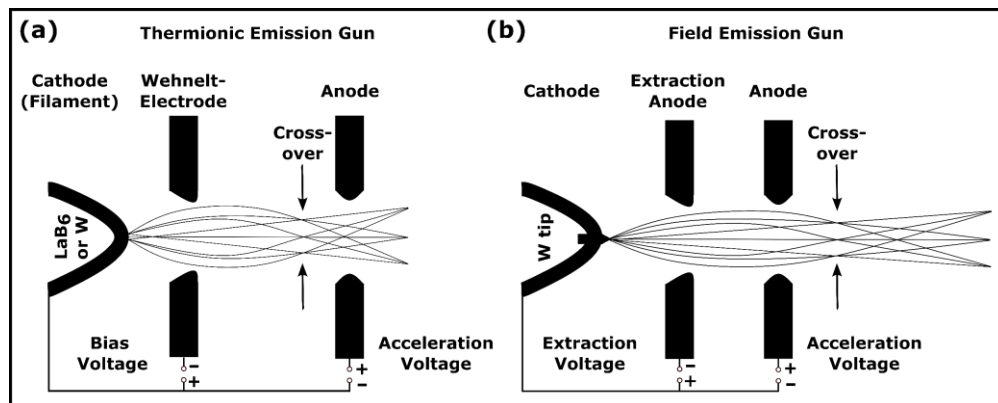


**Figure 2.12:** Basic structure of electron guns used in electron microscopy. **(a)** Thermionic emission gun **(b)** Field emission gun (FEG).

### *Lenses and Lens Aberrations*

Electromagnetic lenses are essential components of a transmission electron microscope and function as a direct equivalent to glass lenses in light microscopes. In both cases, the lenses keep the beam of light or electrons on the optical axis, respectively. Electromagnetic lenses use a combination of rotationally symmetric magnetic fields to focus the beam of electrons onto the specimen and to form an image of the transmitted or scattered electrons. By applying a magnetic field, electrons that pass through the lens are forced on a spiral path around the optical axis. **Figure 2.13 (a)** presents the functionality of an electromagnetic lens and **Figure 2.13 (b)** shows a digital photograph of a condenser lens. In contrast to a light microscope, the electromagnetic lens can be controlled by adjusting the magnetic fields. Hereby, it is possible to change properties of the final image like the depth of field, allowing to observe different features without altering the specimen.

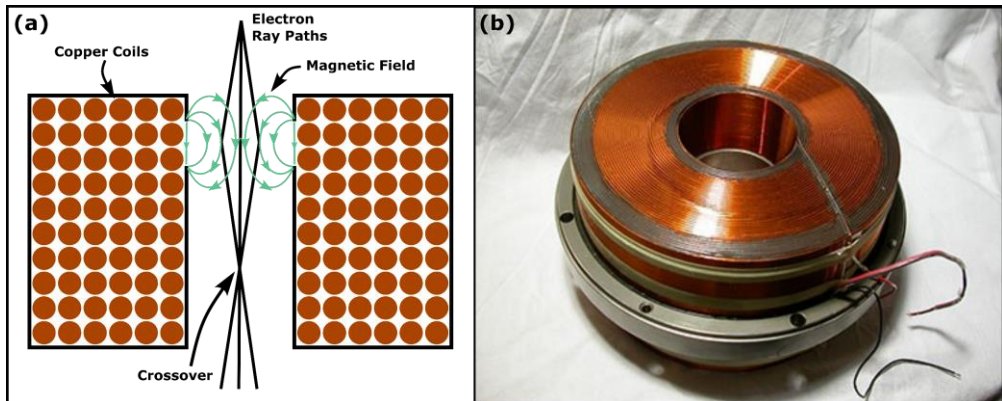


**Figure 2.13:** (a) Schematic diagram of an electromagnetic lens found in electron microscopes. (b) Digital photograph of an electromagnetic lens. The Figure is adapted from D. Williams and C. Carters detailed textbook about transmission electron microscopy.<sup>144</sup>

Typically, the lens system of a TEM is complex and consists of a multitude of different lenses and apertures. Nonetheless, two main types of electromagnetic lenses can be identified:

**The condenser lens** is the first lens that the electron beam passes after it is emitted from the electron source. The condenser lens focuses the electrons after the gun crossover into a narrow, parallel beam that can be directed onto the specimen.

**The objective lens** is located below the specimen and is used to focus the electrons that have passed through the specimen (or have been scattered) onto the detector to form an image. Moreover, the objective lens serves to (initially) magnify the image of the specimen. In addition to the condenser and objective lenses, other electromagnetic lenses are used in the TEM to adjust the electron beam's properties and improve the image quality. For example, intermediate lenses can be used to correct aberrations of the electron beam caused by the lenses, as well as any distortions caused by the specimen. Additionally, energy filters can be used to remove electrons of certain energies from the beam, improving the contrast and resolution of the image.

Due to the rotational symmetry of the magnetic fields in the lenses, it is impossible to eliminate field inhomogeneities resulting in occurrence of lens aberrations. Although there are plenty of possible aberrations, only three main aberrations which have significant influence on the imaging via TEM, are discussed in the following.<sup>147</sup>

**Chromatic Aberration** is caused by the slight distributions of wavelengths of the electrons released by the electron gun and resulting differences in energies. The

electromagnetic lenses affect the motion of electrons based on the Lorentz force which is dependent on the magnetic field and the velocity of the electrons. As the wavelength of the electrons is connected to its momentum and velocity, small differences in the wavelengths can cause electrons to be refracted differently by the electromagnetic lens. The schematic representation of chromatic aberration is presented in **Figure 2.14 (a)**. In the scheme, different colored lines represent the path of electrons with different wavelengths. The electromagnetic lenses are shown as lenses known from optical microscopy to simplify the representation. Due to the slight distribution in wavelengths resulting in different energies, electrons are not focused in the same spot on the optical axis. As a consequence, this results in a blurred image of the investigated specimen. The energy spread of the electrons and the resulting amount of chromatic aberration is strongly dependent on the type of electron source as well as the stability of the acceleration voltage and lens currents. Nowadays, there are correctors that can almost completely eliminate the effects of chromatic aberration.

**Spherical Aberration** occurs due to inhomogeneities of the magnetic field of the electromagnetic lenses. The inhomogeneities of the magnetic field get larger with higher distances from the optical axis resulting in a stronger refraction of the electrons which are further away from the optical axis compared to electrons that pass the lens closer to the optical axis. **Figure 2.14 (b)** shows the schematic refraction of electron rays by an optical lens. The same processes can be adapted to electromagnetic lenses. The scheme shows that electrons that are further away from the optical axes are diffracted stronger towards the optical axis than electrons next to the optical axis leading to different focus points. The smallest beam diameter that is directly connected to the resolution and quality of the image can be achieved at the circle of least confusion. The degree of spherical aberration is strongly dependent on the cross-section of the lens determined by the size of the lens aperture. Spherical aberration can be corrected completely in modern microscopes by installation of specific spherical aberration correctors that combine multipoles and rotational symmetry lenses.

**Axial Astigmatism** can be observed for most electromagnetic lenses due to imperfections of parts and materials of the lenses themselves. If, for example, the coil material shows inhomogeneities or imprecise processing, the perfect rotational symmetry is not achieved. As a result, asymmetry of the focusing field leads to

different focus points for the sagittal or meridional planes. In **Figure 2.14 (c)**, the differences for the focus points E and F affected by asymmetry of the focusing field are presented for the sagittal plane ABF and the meridional plane CDE. Axial astigmatism can be easily compensated by introduction of an adjustable quadrupole field that can reduce the distortions resulting from the lenses.

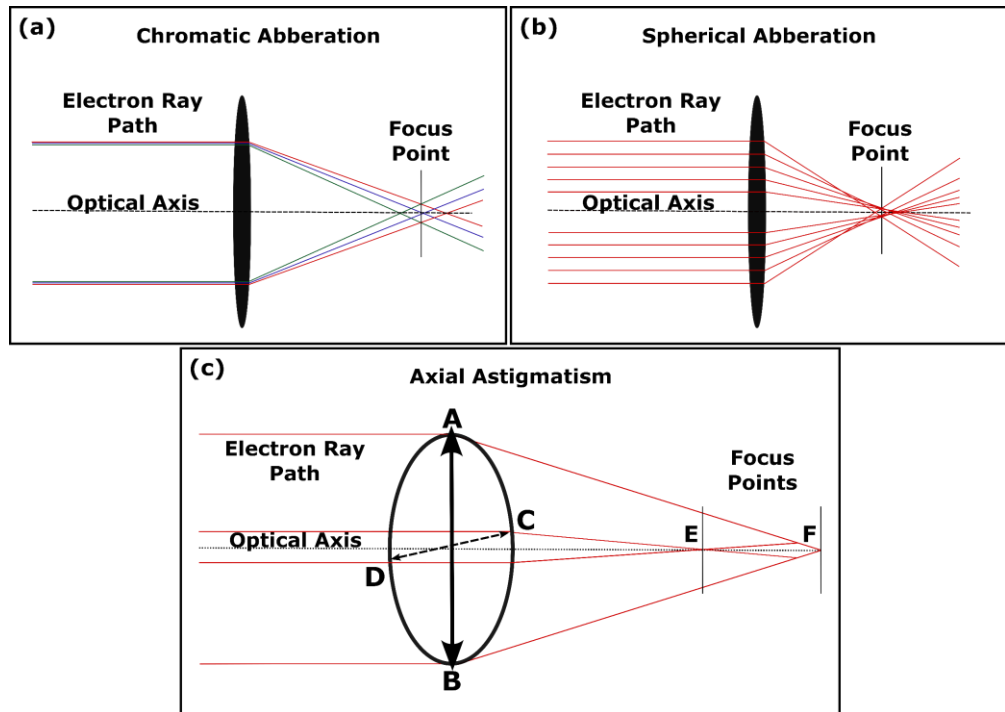


**Figure 2.14:** Schematic illustration of the three most prominent lens aberrations that can occur during TEM imaging. (a) Chromatic aberration (b) Spherical aberration (c) Axial astigmatism.

### *Electron-Sample Interactions and Contrast in Electron Microscopy*

Beside the resolution of the instrument, good image contrast is also required to obtain information about the sample. During imaging, the contrast is reflected by different greyscale levels in the camera image. The contrast of a TEM image arises from the scattering of electrons of the incident beam by the specimen. Therefore, parts of the specimens, where electrons are scattered and cannot be collected by the electromagnetic lenses, appear dark while electrons that pass through the sample undirected or slightly scattered appear bright on the detector.

Electrons can interact in three distinct ways when passing through a thin specimen. The possible interactions are shown in **Figure 2.15** and described in more detail in the following.

Electrons can be transmitted through the specimen without any interaction occurring inside the specimen which are referred to as **unscattered electrons** (**Figure 2.15 (a)**).

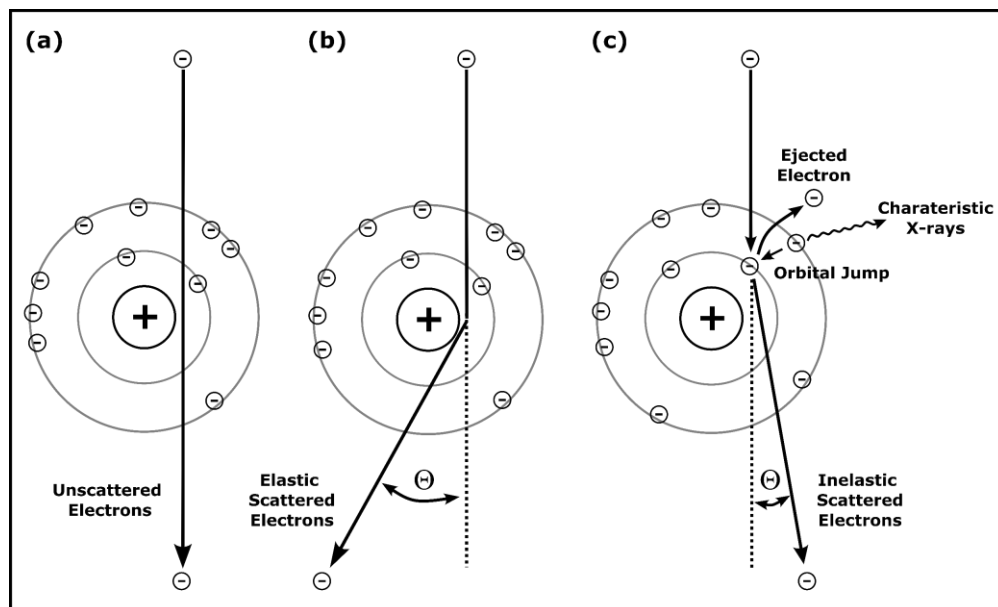


**Figure 2.15:** Schematic representation of possible scattering events of incident electrons by atoms of the investigated specimen. **(a)** Unscattered electrons that experience no interactions with the specimen. **(b)** Elastic scattering of electrons by the nucleus of the atom. **(c)** Inelastic scattering and the exemplary emission of a characteristic X-ray due to energy transfer.

Most electrons experience **elastic scattering** when interacting with the electrons of the sample. The term 'elastic' refers to the conservation of kinetic energy and total momentum during the scattering process. During elastic scattering, the incident electrons interact with the sample causing them to change direction but without any transfer of energy or excitation. As a result, the scattered electrons retain the same energy as the incident electrons. For the classical mechanics model of elastic scattering, electrons are mainly scattered by the nucleus. The principle is shown in **Figure 2.15 (b)**. As the nucleus is multiple times heavier than the incident electrons the position is almost not affected during the scattering event. The positive charged nucleus will attract the negative electrons which are then redirected by Coulomb forces.

Rutherford's differential cross-section is commonly given to describe the probability that an electron is elastically scattered from  $d\sigma_{\text{el.}}$  into a solid angle segment  $d\Omega$  with the angle  $\theta$ :<sup>148</sup>

$$\frac{d\sigma_{\text{el.}}}{d\Omega} = \left( \frac{e^2}{4E_0\pi\epsilon_0} \right)^2 Z^2 \frac{1}{\sin^4\left(\frac{\theta}{2}\right)} \quad (2.35)$$

Here,  $Z$  describes the atomic number of the nucleus and  $E_0$  the kinetic energy of the electron.  $\epsilon_0$  gives the permittivity. **Equation 2.35** shows that the scattering angle increases with a higher atomic number of the nucleus with a dependence of  $Z^2$  while at the same time increases with decreasing kinetic energy of the incident electron. Furthermore, the thickness of the investigated specimen plays an important role for the contrast of the image as the probability of electrons being scattered is greatly increased with every layer of atoms the electrons have to pass (mass-thickness contrast). Directly connected to mass-thickness contrast is the diffraction contrast which is especially relevant for crystalline specimen. In crystalline specimen scattered electrons are not continuously distributed with scattering angles but discontinuously distributed as diffracted waves. Diffraction contrast results from changing diffraction conditions at different areas of the specimen. Additionally, phase contrast which is produced by changes in the phases of scattered electromagnetic waves gets dominant with increasing magnification. More detailed information about diffraction contrast and phase contrast can be found in the textbook of David. B Williams and C. Barry Carter.<sup>144</sup>

Electrons passing the sample can also experience **inelastic scattering** where the kinetic energy of the incident electrons is not conserved during the scattering process. Inelastic scattering processes are particularly interesting as they are not only relevant for the imaging process but also can be useful to gain additional information about the sample when using characterization methods like EDX or EELS. When an incident electron interacts with a specimen atom, energy can be transferred from the incident electron to another electron. Depending on the amount of energy transferred, different events can occur. **Figure 2.15 (c)** shows one of the possibilities which is the release of characteristic X-rays. If the energy of the incident electron is high enough to transfer energy to an electron of the specimen at an inner shell, the electron of the specimen can either move to a position at a higher energy level (outer shell) or get emitted into the vacuum. In both cases the vacant position closer to the nucleus will be filled by an

electron from a higher energy level. The difference of energy is released by the emission of an X-ray quantum which is characteristic for each individual atom and can therefore be used for chemical composition analysis with EDX. Furthermore, the orbital jump of an electron from a higher energetic level to a lower energetic level can result in the release of an Auger electron which can be detected as part of Auger electron spectroscopy. The loss of energy due to the energy transfer to another electron can also be measured via EELS.

### *Sample Preparation and Investigation of Microgel Systems with Transmission Electron Microscopy*

Beside the operation of the instrument, the proper preparation of the investigated sample is crucial for the successful imaging in TEM. TEM is typically used for investigations of specimen in research fields such as material science and biology where the vastly different properties of the samples require distinct preparation methods.

Samples in material science often consist of one or multiple inorganic materials which may be in the form of fibers, powders, in thin films or in bulk. The challenge to prepare these samples is the thinning of the specimen so that the electron beam can penetrate the sample without destroying the structure or material. Depending on the type and initial geometry of the sample, different processing techniques like electropolishing, ion milling, microtomy or simple grinding or crushing can be applied to process the materials.

The main difference between specimen in material science and biology is the water content of biological samples which bring their own set of challenges for preparation as liquid dynamics need to be suppressed for proper investigation. As TEM operates in an ultra-high vacuum, potential effects towards the samples need to be considered. For example, all common liquids will evaporate immediately, materials can degas and loose particles can detach from the surface of the specimen resulting in the alteration or destruction of the morphology and shape of the investigated sample. To still allow for the investigation of sensitive and intact samples in TEM, there are a multitude of different strategies to “protect” the specimen from the harsh conditions during the imaging. The common method to examine biological ultra structures is the chemical fixation and subsequent embedment in a resin.<sup>149, 150</sup> Typically, the procedure involves several steps with different fixations agents that crosslink possible cellular structures

into a matrix and therefore preserve the internal structure during preparation and during the imaging. Afterwards, the water in the structure is usually changed carefully to different solvents (dehydration) and finally infiltrated by resin which can be cured under UV light. This method allows to receive a precise impression of the ultrastructure which is no longer affected by conditions in TEM. The cured resin blocks can be sectioned extremely thin by using cutting tools like a microtome and afterwards contrasted by different staining techniques like negative and positive staining before imaging.

Negative staining is a method that is commonly used for investigation of samples that show a low electron contrast like protein complexes, viruses, micelles or macromolecules due to the fact that they mostly consist of light atoms like carbon, hydrogen and oxygen.<sup>149, 151, 152</sup> To enhance the contrast of the specimen and allow for the imaging of shape or morphology, not the sample itself but the surrounding background can be modified. Normally, the carrier material of a TEM grid consists of a thin film of amorphous carbon or polymer blend which also does not provide significant contrast during the imaging. In negative staining, the sample is adsorbed onto the surface of the grid and afterwards embedded in a film of electron dense stain compound which usually are heavy metal salts, such as uranyl acetate, osmium tetroxide or ammonium molybdate. The heavy metal ions produce a high relative contrast compared to the investigated sample. Compared to positive staining, where the actual specimen is stained, the investigated sample should be unaltered while the contrast of the background is strongly increased.<sup>150</sup>

Although microgels are mostly composed of light atoms like carbon, hydrogen, oxygen and nitrogen, the contrast is usually considerably more distinct compared to singular polymer chains or biological molecules like proteins. Therefore, they do not require extensive preparation prior to the imaging. Microgel samples can be prepared by drop casting and drying of microgel dispersion on the grid. The reason for the difference in contrast is the high density of polymer chains in the spherical microgel based on crosslinking of polymer chains. Additionally, when microgels are investigated in TEM in dried state, the microgels lose most of the content of water leading to further accumulation of polymer chains. In dried state and also dependent on the degree of crosslinking, microgels can be imaged as spheres without noticeable topographical features. In the literature, negative staining is rarely used for imaging of microgels, due to sufficient contrast of the microgels without further modification. Experiments

showed that negative staining improves the visibility of the periphery and the transition of the microgels and the background.<sup>10</sup> However, the technique does not allow to gain additional information about the morphology or topography when investigating microgels with a degree of crosslinking above 5 mol%.<sup>153</sup> Electron microscopy methods are particularly interesting for hybrid microgel systems consisting of inorganic nanoparticles and a microgel scaffold as they provide established measurement techniques that allow for the visualization of the combined systems on a nanometer scale. Nanoparticles made of metals like gold or silver as well as nanoparticles based on silicon dioxide show a strong contrast compared to the microgels due to the high (electron) density and the comparably heavy core of the atoms resulting in pronounced scattering of the electron beam. Thereby, the exact position, number and shape of the nanoparticles within the microgels can be determined. Additionally, nanoparticles in the periphery but also within the microgels can be used as fiducial markers during experiments like TEM tomography.<sup>154</sup> In contrast to most biological samples based on light atoms, another advantage of the investigation of microgels with EM is the lower sensitivity towards radiation damage from the electron beam.

### 3. Synopsis

The term microgel was first introduced by William Baker following his initial synthesis of crosslinked polybutadiene latex particles in 1949.<sup>155</sup> Since then, the synthesis and consequently also the characterization of such macromolecular objects have received growing attention from research and industry. Despite the significant interest, the internal structure and composition on a nanoscale remain challenging to examine and are still not well-understood. To fully comprehend the interplay of monomers during the phase transition, interactions with nanoparticles or ions, that diffuse into the microgels, the understanding of the spatial distribution of crosslinker molecules and other comonomers plays an important role.

This thesis focuses on the characterization of structure-property relations of multifunctional PNIPAM-based copolymer microgels depending on the composition and synthesis route. The two works presented in **Chapter 4** and **Chapter 5** involve characterization methods like DLS, SAXS, UV-Vis spectroscopy and electron microscopy.

In the systematic study presented in **Chapter 4**, a new synthesis route to provide access to hybrid microgels based on PNIPAM was established. Previously, most attempts to introduce single nanoparticles into microgel networks were performed by controlled seeded precipitation polymerization in the presence of nanoparticles as seed particles. In this work, the introduction of specific functionalities through the choice of different comonomers allowed for the in situ formation of monodisperse, single gold nanoparticles in the microgels. **Figure 3.1** shows the basic principle of the synthesis process supported by corresponding exemplary TEM images.

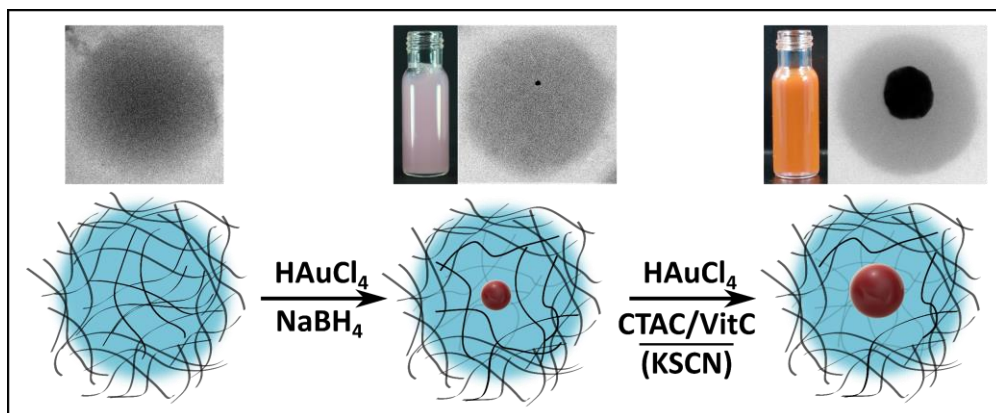


**Figure 3.1:** Schematic overview of the contents of **Chapter 4**. The sketch presents the principle of in situ formation of single gold nanoparticles in complex PNIPAM-based microgels and the growth of the nanoparticles by multiple times. The result of each synthesis step is highlighted by TEM images and also digital photographs of the dispersions of the hybrid microgel dispersion.

The in situ formation of gold nanoparticles within the microgels was realized by using complex PNIPAM-based copolymer microgels which contain  $\beta$ -diketone functional groups. The functional groups are introduced by incorporation of acetoacetoxy ethyl methacrylate (AAEM) monomers into the crosslinked polymer network. The  $\beta$ -diketone groups are reported to complex and reduce metal ions and therefore allow for the selective accumulation and controlled reduction of metal ions within the microgel.<sup>156-158</sup> In combination with the introduction of negative charge by incorporating acryl acid (AAc) monomers, the successful in situ formation of single gold nanoparticles inside of the microgels could be observed. To investigate the influence of the different comonomers during the in situ synthesis, systematic investigations were performed with microgels of increasing complexity i.e. more complex compositions. It was found that the combination of the complexing  $\beta$ -diketone groups and charge introduced by AAc are essential for the controlled formation of single gold nanoparticles. On the contrary, less complex compositions lead to the uncontrolled formation of multiple or not any nanoparticles within the microgels. It was also shown that the ratio between the microgels and the used gold ions has an influence on the amount of gold nanoparticles formed and thus the controllability of the reaction. Finally, a surfactant-free as well as a surfactant-supported one-step overgrowth protocol was applied which allowed for the increase in size by multiple times while maintaining the spherical shape. An exemplary TEM image of the hybrid microgel after the surfactant-supported overgrowth is also presented in **Figure 3.1**. Both, the hybrid microgels after the initial in situ formation and after the growth process are supplemented with digital photographs of the

concentrated aqueous microgel dispersions. A change in color of the dispersion from pink to orange is observed due to the increase in size of the gold nanoparticles in the microgels.

The introduction of an accessible, reproducible protocol for the controlled in situ formation of gold nanoparticles within PNIPAM-based microgels was a successful step towards the conception of new pathways to receive hybrid microgel systems with defined sizes and single inorganic cores. However, specific processes, like the interplay of the different monomers as well as the distribution of the monomers in the microgel network remain not fully understood. More detailed investigations and new or improved measurement techniques are required to gain deeper insights into structural inhomogeneities and distribution of components in such complex microgel networks.

A first step towards this objective was accomplished in the second study of this work where the significance of a novel analytical methodology was evaluated through screening of the swelling behavior of a large number of different microgels. Typically, DLS measurements are used for microgel characterization as the method provides fast and easy access to the size and dispersity of the particles, in dependence of the temperature. In this thesis, a combination of temperature-dependent DLS and temperature-dependent UV-Vis absorbance measurements was used to characterize and compare three categories of microgel systems in regard to their swelling behavior. UV-Vis absorbance spectroscopy has the advantage of being comparable to DLS in terms of accessibility, cost-efficiency and fast measurement times. The combination of both techniques shows the potential to provide deeper insights into structural inhomogeneities and possible differences between the global volume phase transition and local structural changes.

The idea for the correlation of data from DLS and UV-Vis absorbance spectroscopy was first presented by Ponomareva et al. who used this novel approach to characterize the swelling behavior of PNIPAM-based core-shell microgels with gold cores and different crosslinker degrees. The authors showed that for the investigated samples, a linear dependency can be found for the relative change in hydrodynamic radius and the relative change in absorbance, dependent on the temperature. The linear dependency underlines that temperature-dependent UV-Vis and DLS

measurements can potentially be used interchangeably for characterization of microgels.<sup>73</sup>

One main goal of this thesis was to verify whether such a linear dependency is valid for microgel systems with different complexities and compositions. The concept of this work is schematically illustrated in **Figure 3.2**. 30 microgel systems including hybrid core-shell microgels with silica cores synthesized by seeded precipitation polymerization and microgels without inorganic cores synthesized by regular precipitation polymerization have been investigated. The “classical” coreless PNIPAM microgels were further diversified by variation of the crosslinker content and initiator. In addition, copolymer microgels were synthesized by addition of comonomers during the polymerization to make the particles more complex in regard to their composition. The results are presented in **Chapter 5**.

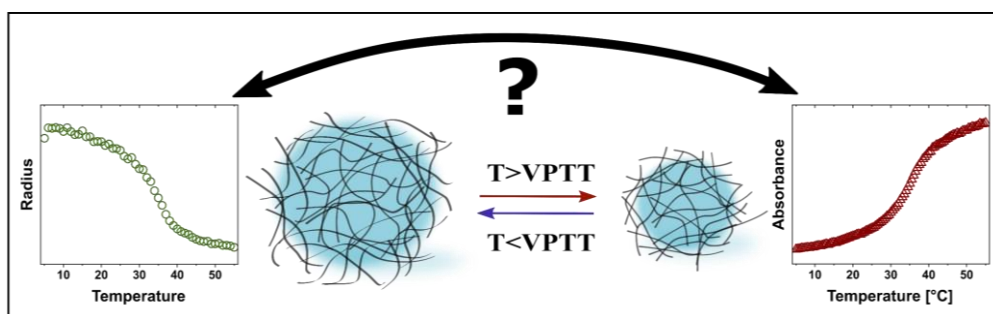


**Figure 3.2:** Schematic overview of the contents of **Chapter 5**. One main emphasis of this work was the correlation of data from temperature-dependent DLS (green curve) and temperature-dependent UV-Vis absorbance measurements (red curve) for microgels that show a temperature-dependent swelling behavior to obtain new insights into the networks structure.

The systematic investigation revealed that core-shell microgels with silica cores and “classical” PNIPAM microgels, without the addition of comonomers, mostly follow the linear correlation that was already found by Ponomareva et al. for PNIPAM core-shell microgels with gold cores.<sup>73</sup> The relative change in the hydrodynamic radius can therefore be directly correlated to the relative change in absorbance of the microgel dispersion. For copolymer microgels, deviations from the linear correlation behavior were observed. These deviations are likely a result of heterogeneities in the microgel networks which impact the local and global microgel collapse. In addition, the prediction of the temperature evolution of the hydrodynamic radius, based only on simple absorbance measurements, was validated to be possible. This is the case for microgel systems that show a linear correlation between absolute changes in the

normalized absorbance and absolute changes in the normalized hydrodynamic radius.



## 3.1 Contributions to Joint Publications

The following parts of this thesis have been published previously. The contributions of all involved authors are listed below.

### **Chapter 4: PNIPAM-based copolymer microgels as nanoreactors for the in situ synthesis of gold nanoparticles**

Marius Otten, Diana Hildebrandt, Saskia Mölders, Marco Hildebrandt, Andrij Pich and Matthias Karg

Manuscript in preparation for submission

M.K and I designed the study. I synthesized the copolymer microgels and conducted all in situ reduction and overgrowth experiments presented in this work. D.H. and S.M. realized ideas for experiments and tried out multiple reaction conditions and parameters for the synthesis of the copolymer microgels as well as the formation and overgrowth process of the gold nanoparticles as part of their bachelor theses. M.H. performed and analyzed the SAXS measurements. Moreover, I measured and evaluated all DLS data and performed TEM imaging of all samples. I designed and prepared all figures and wrote the first version of the manuscript. All authors contributed with helpful discussion and proofread the manuscript.

### **Chapter 5: Following the volume phase transition of thermoresponsive microgels by dynamic light scattering and turbidity: Correlations depend on microgel homogeneity**

Marius Otten, Marco Hildebrandt, Ben Pfeffing, Victoria Voigt, Thomas Hellweg and Matthias Karg

Manuscript in preparation for submission

M.K and I designed the study. V.V., B.P. and I synthesized the “classical” PNIPAM microgels and copolymer microgels and performed the characterization via DLS, UV-Vis absorbance spectroscopy and electrophoretic mobility measurements. M.H. provided most of the core-shell particles and contributed with helpful discussion,

especially regarding the interpretation of data and the prediction of hydrodynamic radii of the microgel systems using the data from the UV-Vis absorbance measurements. I processed and evaluated the data from DLS and UV-Vis absorbance measurements for all microgel systems. Furthermore, I designed and prepared all figures and wrote the first version of the manuscript. All authors contributed with helpful discussion and

# 4. PNIPAM-based copolymer microgels as nanoreactors for the in situ synthesis of gold nanoparticles

*Marius Otten,<sup>1</sup> Diana Hildebrandt,<sup>1</sup> Saskia Mölders,<sup>1</sup> Marco Hildebrandt,<sup>1</sup>*

*Andrij Pich,<sup>2,3</sup> and Matthias Karg<sup>1,\*</sup>*

<sup>1</sup>Institut für Physikalische Chemie I: Kolloide und Nanooptik, Heinrich-Heine-Universität Düsseldorf, Universitätsstr. 1, 40225 Düsseldorf, Germany

<sup>2</sup>DWI-Leibnitz-Institute for Interactive Materials e.V., 52056 Aachen, Germany

<sup>3</sup>Functional and Interactive Polymers, Institute for Technical and Macromolecular Chemistry, RWTH Aachen University, 52056 Aachen, Germany

## **4.1 Abstract**

Core-shell microgels and nanoparticle-loaded microgels attract great attention in research fields such as catalysis, optics and biomedicine due to their optical properties and possibilities of externally switching and manipulation. A common strategy to introduce nanoparticles into microgels is the encapsulation by seeded precipitation polymerization of monomers and crosslinker molecules in presence of the nanoparticles. Encapsulation provides a consistent and well understood method that allows for the preparation of core-shell colloids with a wide variety of inorganic cores and microgel shells with different morphologies and compositions. Recent investigations revealed that also in situ formation of nanoparticles inside of the microgels present a controlled way to obtain small, single metal nanoparticles within complex crosslinked polymer networks that can act as starting point for further processing and post-modifications.

In this work we systematically investigate the influence of various comonomers in PNIPAM-based microgels with respect to the formation of gold nanoparticles in the microgels by an in situ approach. With increasing complexity of the microgels by gradually adding different comonomers during the synthesis, we present new findings on the influence of the individual monomers. With our results we confirm, that the formation of single, monodisperse particles is possible in PNIPAM-based microgels, but a complex system with two comonomers is needed to achieve the controlled formation. Without the addition of comonomers AAEM and AAc to the system, the formation is either not possible or strongly hampered. Additional experiments with different ratios between the added gold ions and microgels suggested the existence of specific sites in the microgel that are favored by free diffusing gold ions and also have an impact on the size of the formed gold nanoparticles. Two different ways to overgrow the nanoparticles revealed that the overgrowth mechanism known for systems synthesized by encapsulations is neither affected by functional groups that are present in the microgel nor the formation mechanism of the particles via in situ synthesis.

## 4.2 Introduction

Crosslinking of polymer chains during polymerization can lead to the formation of micro- or nano-meter sized gel-like networks that are known as micro- and nanogels. These soft, deformable objects can react to external stimuli like changes in pH, temperature or ionic strength, which enable the microgels to either swell or de-swell in the surrounding solvent resulting in a change of the effective size.<sup>1, 64, 159</sup> These characteristics make them attractive systems for different applications like the usage as carrier for (bio)molecules in medical applications<sup>160-162</sup> or as responsive coatings.<sup>39, 40</sup> The combination of microgels and nanoparticles e.g. made from gold, silver or silicon dioxide, allow for the development of beneficial or completely new synergy-effect of both types of materials. Generally, a distinction can be made between common classes of hybrid microgels.

Beside microgels homogeneously or partially loaded with multiple nanoparticles<sup>163, 164</sup> and microgels covered with nanoparticles,<sup>49, 50, 165, 166</sup> especially core-shell microgels with single nanoparticles as cores experienced an ever-increasing interest in research fields like sensing,<sup>167-169</sup> photonics<sup>118, 170</sup> and catalysis<sup>46, 171</sup>. The existence of only a single, monodisperse metal nanoparticle within the microgel can enhance the morphology- and size- dependent electronic and optical properties like often desired surface plasmon resonance which is a fundamental principle for several colour-based biosensor applications and sensors.<sup>172, 173</sup> The phenomenon is based on the interaction between free electrons in metals and incident light of visible wavelengths. Upon irradiation, the free electrons show coherent oscillations, so called plasmons, at a defined frequency depending on the morphology, size and spacing of the metal nanoparticles.<sup>174, 175</sup> A surrounding semi-transparent microgel shell can be varied in terms of size and composition and thereby allow to define the effective interparticle distance of the nanoparticles. Further, the microgel shell can increase the colloidal stability of the nanoparticles in dispersion.<sup>172</sup>

In literature, three different pathways are known to obtain hybrid materials of microgel networks and noble metal nanoparticles. The controlled encapsulation by polymerization of monomers and crosslinker moieties in presence of single inorganic nanoparticles has been already reported by Karg et. al in 2006.<sup>116</sup> The group introduced a method to encapsulate silica nanoparticles with a hydrophobic surface

into PNIPAM microgel networks by radical polymerization. Based on that idea, in the following years the procedure has been further refined by Contreras-Cáceres et al. to enable the reproduceable encapsulation and growth of gold nanoparticles in a variety of PNIPAM-based microgel systems.<sup>47</sup> The encapsulation of inorganic nanoparticles by microgel shells offers a well understood and consistent technique that shows high flexibility in regard to the composition, size and shape of the inorganic core as well as the microgel shell.

Further, hybrid microgel systems can also be obtained by diffusion of metal nanoparticles into prior synthesized microgels or their periphery. While technically an easy and accessible method, the synthesis via diffusion comes with comparably large disadvantages as there is no precise control over the number of particles diffusing into the microgel network and the possible occurrence of leaking of the particles over time based on the absence of covalent or strong non-covalent interactions between the nanoparticles and the microgels.<sup>113, 176</sup>

As the third method and in direct opposite to the encapsulation, in situ synthesis of nanoparticles within microgels allows for the precise adjustment of the desired microgel shell before the subsequent preparation of the hybrid system. Although, many groups showed that is possible to form various metal nanoparticles in the periphery and inside of microgel networks by harsh reduction conditions, controlling the size, number and position of the nanoparticles remain a prevalent challenge.<sup>125, 163, 177-181</sup>

To address these problems, Thies et al. first presented the successful formation and growth of single gold nanoparticles within complex PVCL-based microgels in 2018.<sup>130</sup> By incorporation of the negatively charged monomer acrylic acid (AAc) and acetoacetoxy ethyl methacrylate (AAEM) which contains  $\beta$ -diketone groups that are reported to be able to complex surrounding metal ions,<sup>172, 182</sup> they presented a novel strategy to perform a in situ synthesis of single gold metal nanoparticles in microgels. To our knowledge this system is unique until this day and outlines the potential for the in situ as attractive pathway for the fabrication of hybrid microgels. Hereby, the synthesis of microgels prior to the in situ synthesis could provide several advantages like an improved control over the chemical composition and architecture of the microgel shell and flexible but controlled loading of nanoparticles.

In this work we present new findings regarding the course of the mechanism and influences on the in situ formation and growth of single gold nanoparticles in complex copolymer-microgels. To get a deeper understanding on influences and dependencies on the in situ formation process, we systematically synthesized PNIPAM-based microgels with different comonomer compositions and compared the properties and capabilities towards the formation of gold nanoparticles within the microgels via the in situ mechanism. We report that the successful formation of single gold nanoparticles in PNIPAM-based microgels with pronounced swelling capacities is possible but strongly dependent on a cleverly chosen composition of the microgel system. Additional experiments revealed the strong dependency on the ratio between used microgels and gold ions during the in situ synthesis that lead to an increase in size and number of the formed nanoparticles. We could localize the formation of the nanoparticles inside of the microgels and also show the one-step growth of the gold nanoparticles by more than eight-times using surfactant-free and surfactant-supported overgrowth approaches. Our findings are supported by TEM imaging, SAXS measurements, temperature-dependent DLS measurements and the determination of the surface charge via electrophoretic mobility measurements.

## 4.3 Experimental Section

### 4.3.1 Materials

Tetrachloroauric(III) acid trihydrate ( $\text{HAuCl}_4 \cdot 3\text{H}_2\text{O}$ , Sigma Aldrich, 99.995 %), acetoacetoxy ethyl methacrylate (AAEM, Sigma Aldrich, 95 %), acrylic acid (AAC, Sigma Aldrich, 99 %), 3,9-Divinyl-2,4,8,10-tetraoxaspiro[5.5]undecane (VOU, Sigma Aldrich, 98 %), 2,2'-Azobis[N-(2-carboxyethyl)-2-methylpropionamide] n-Hydrate (ACMA, FUJIFILM Wako Pur Chemical Corporation, 95 %), sodium dodecyl sulfate (SDS, Sigma-Aldrich, p.a.), sodium borohydride ( $\text{NaBH}_4$ , Merck, 99 %), potassium thiocyanate (KSCN, Fisher Scientific, 98 %), cetyltrimethylammonium chloride (CTAC, Sigma Aldrich, 25 wt% in  $\text{H}_2\text{O}$ ), L(+)-ascorbic acid (Roth, 99 %) and phosphate buffer solution (PBS buffer, pH7, Pan React AppliChem) were used as received. *N*-isopropylacrylamide (NIPAM; TCI, 98 %) was recrystallized from cyclohexane. Water used for all syntheses and

measurements was purified with a MilliQ system (Millipore). The final resistivity of the water was 18 M $\Omega$  cm.

### **4.3.2 Synthesis**

**Synthesis of microgels.** Microgels were prepared by precipitation polymerization. We present an overview of the chemical structures of all monomers, the crosslinker and the initiator that were used for the synthesis of the PNIPAM-based copolymer microgels in **Scheme S4.1** in the **Supporting Information**. All batches were synthesized in a total volume of 50 ml using 100 ml three-necked flasks equipped with a reflux condenser, dropping funnel and gas inlet. NIPAM (507 mg, 4.48 mmol), stabilizer SDS (6.6 mg, 0.023 mmol), crosslinker VOU (26.7 mg, 0.125 mmol, 2.8 mol%) and comonomer AAEM (112.6 mg, 0.5259 mmol, 11.7 mol%) were dissolved in 40 ml of water under stirring and heating to 70 °C. The solutions were purged with nitrogen for at least 30 min. During that time the zwitterionic initiator ACMA (23.3 mg, 0.0563 mmol) was dissolved in 5 ml water. After heating, the initiator solution was added. Depending on the synthesis, solutions of 40.35 mg (0.56 mmol, 12.5 mol%), 8.07 mg (0.112 mmol, 2.5 mol%) or 1.61 mg (0.224 mmol, 0.5 mol%) acrylic acid were prepared in water. Ten minutes after the start of the reaction, which is indicated by slight turbidity of the reaction mixture, the respective solution of acrylic acid in water was added dropwise using a dropping funnel. After 4 h, the dispersion was cooled to room temperature and purified by extensive dialysis against water for one week. After dialysis we freeze-dried all microgel samples.

For additional experiments, we synthesized microgels with different composition of comonomers. Apart from the changed components the reaction was performed analogue to the protocol described before. We summarize the masses and abbreviations for all microgels in **Table 4.1**.

**Table 4.1:** Summary of the synthesis details for all prepared copolymer microgels.

Microgel	m(PNIPAM) [mg] (mmol)	m(AAEM) [mg] (mmol)	m(AAc) [mg] (mmol)	m(VOU) [mg] (mmol)	m(SDS) [mg] (mmol)	m(ACMA) [mg] (mmol)
$\mu$ gel- PNIPAM	507 (4.48)	-	-	26.7 (0.125)	6.6 (0.023)	23.3 (0.0563)
$\mu$ gel- AAC <sub>12.5%</sub>	507 (4.48)	-	40.35 (0.56)	26.7 (0.125)	6.6 (0.023)	23.3 (0.0563)
$\mu$ gel-AAEM	507 (4.48)	112.6 (0.526)	-	26.7 (0.125)	6.6 (0.023)	23.3 (0.0563)
$\mu$ gel- AAEM- AAC <sub>2.5%</sub>	507 (4.48)	112.6 (0.526)	8.07 (0.112)	26.7 (0.125)	6.6 (0.023)	23.3 (0.0563)
$\mu$ gel- AAEM- AAC <sub>12.5%</sub>	507 (4.48)	112.6 (0.526)	40.35 (0.56)	26.7 (0.125)	6.6 (0.023)	23.3 (0.0563)
$\mu$ gel- AAEM- AAC <sub>0.5%</sub>	507 (4.48)	112.6 (0.526)	1.61 (0.0224)	26.7 (0.125)	6.6 (0.023)	23.3 (0.0563)

**In situ growth of gold nanoparticles.** For in situ synthesis, 562  $\mu$ l of microgel solution with a concentration of 1 wt% were transferred into a 4 ml screw top vial. 10  $\mu$ l of tetrachloroauric(III) acid trihydrate ( $\text{HAuCl}_4 \cdot 3\text{H}_2\text{O}$ ) solution (0.01 M) were added. For simplicity, we will only use  $\text{HAuCl}_4$  in the following. After stirring for 60 minutes at room temperature, the reduction of gold was initiated by the addition of 1.5 ml of a cold  $\text{NaBH}_4$  solution (0.02 M). The dispersion was then allowed to stir for additional 90 minutes. The course of the reaction could be followed visually due to the spontaneous change in colour. Right after the addition of  $\text{NaBH}_4$  the dispersion turned from yellow to pink to a light grey. Eventually, after a short amount of time the dispersion turned back to a pinkish colour due to agglomeration of excess gold that forms black aggregates or clusters which rapidly precipitate at the bottom of the vial or gather in the foam at the top of the dispersion that is formed during the reduction process.

We performed additional experiments where we adjusted the amount of  $\text{HAuCl}_4$  solution used for the in situ synthesis. Beside the added amount of  $\text{HAuCl}_4$ , the

experiments were performed analogue to the process described before. Depending on the volume of  $\text{HAuCl}_4$  used for the in situ synthesis, the colour of the dispersion shortly after the reduction varied from light pinkish to deep grey, which is an indication for the number of gold particles and gold aggregates that formed in- and outside of the microgels.

Purification of the hybrid microgels was performed in a two-step process due to the high amount of elemental gold formed outside of the microgels caused by the use of the strong reducing agent sodium borohydride. First excess gold that formed during the synthesis was removed by short cycles of centrifugation. Hybrid microgels were centrifuged five times for 45 s at 5600 rcf. After each cycle a black sediment could be identified at the bottom of the tube which can be attributed to excess gold. The dispersion of hybrid microgels was separated and the process repeated. After the separation of the excess gold species, the microgels were centrifuged five times for 20 minutes at 5600 rcf. Microgels after the in situ synthesis can be redispersed after centrifugation but long durations or high centrifugal forces lead to irreversible aggregation. After centrifugation the hybrid microgels were dialyzed against water for one week and finally freeze-dried.

**One-step overgrowth of the gold cores.** For the surfactant-supported growth of the gold nanoparticles a modified version based on a protocol by Honold et al. was used.<sup>183</sup> The protocol is based on a surfactant-assisted seeded-growth used to overgrow gold nanoparticles. First, a feed solution was prepared by adding 112  $\mu\text{l}$   $\text{HAuCl}_4$  (0.130 M) and 184  $\mu\text{l}$  cetyltrimethylammonium chloride (CTAC) (0.78 M) to 29 ml of water. Next, 200  $\mu\text{l}$  of the hybrid microgel dispersion (2 wt%) were combined with 200  $\mu\text{l}$  CTAC (0.1 M) to create a precursor stock solution. Under heavy stirring, 200  $\mu\text{l}$  of the precursor stock solution, 25.4  $\mu\text{l}$  CTAC (0.78 M) and 388  $\mu\text{l}$  of an ascorbic acid solution (0.049 M) were successively added to 7.975 ml of water in a 100 ml glass vial. The prepared seed solution was combined with the feed solution and stirred for twenty minutes at room temperature. Within the first minutes of the reaction, a shift in colour of the dispersion from light pink to orange-brown could be observed. The obtained microgels with overgrown gold nanoparticles were centrifuged five times for 10 min at 5600 rcf and freeze-dried afterwards.

For additional experiments we used a surfactant-free one-step approach for the growth of gold nanoparticles. First, 15  $\mu\text{l}$  of 1M KSCN solution were added into a 4 ml

screw top vial. Upon addition of 50  $\mu$ l of 0.05 M H<sub>2</sub>AuCl<sub>4</sub> under heavy stirring, the formation of an orange solid was observed. Next, 1.6 ml of phosphate-buffer (pH 7) were transferred to the reaction solution leading to a spontaneous discoloration. Finally, 1 mL of the hybrid microgel dispersion (1 wt%) was added to the solution and stirred for 24 h at room temperature. During the progress of the reaction a slow shift of the colour from initially light pink to a deep red was observed.

After the growth process the purification of the obtained microgels was realized by sequential steps of repeated centrifugations. Initially, large gold particles and aggregates that formed outside of the microgels were removed by short centrifugation cycles. The dispersion was centrifuged five times at 5600 rcf for 15 s each. After each cycle, the black sediment was removed prior to the next cycle of centrifugation. At these short times of centrifugation, the larger fraction of the hybrid microgels remained stable in dispersion in the supernatant. In the next step, hybrid microgels with increased size of gold nanoparticles were separated from small amount of unreacted hybrid microgels. The hybrid microgels were centrifuged five times for 50 s at 5600 rcf. After each step, the supernatant was removed and hybrid the residue containing the hybrid microgels was redispersed in water. Finally, the hybrid microgels were dialyzed against water for one week and freeze dried afterwards.

### **4.3.3 Methods**

Experimental details for all characterization techniques can be found in the **Supporting Information** in **Chapter 4.6**.

## 4.4 Results and Discussion

We started with the determination of the essential components of a microgel network to provide an environment for a controlled in situ formation of a gold nanoparticles. To achieve a pronounced temperature-responsive behaviour, we decided to choose NIPAM as main monomer for all synthesized microgels. At the same time, we retained VOU as crosslinker and ACMA as zwitterionic initiator which have been previously reported in microgel systems for the controlled in situ synthesis of nanoparticles.<sup>130</sup> We first synthesized two microgels without the addition of the comonomer AAEM to prove the necessity of the  $\beta$ -diketone groups for the coordination of gold ions and the resulting formation of nanoparticles upon reduction.

Consequently, microgel  $\mu$ gel-PNIPAM consists only of PNIPAM crosslinked with VOU while  $\mu$ gel-AAc<sub>12.5%</sub> is based on the same monomers but with the addition of negatively charged comonomer acrylic acid. For both microgel syntheses, ACMA was used as initiator for the polymerization. As expected, we could not observe a formation of nanoparticles in both microgel systems applying our in situ synthesis protocol. Temperature-dependent DLS measurements for both microgels and TEM images after in situ synthesis and purification are provided in **Figure S4.1 and S4.2 in the Supporting Information**. The observations for the experiments indicate the importance and necessity of the metal-ion complexing AAEM monomer within the microgels for the in situ synthesis approach that is used in this work.

Next, we incorporated the  $\beta$ -diketone group containing monomer AAEM into the PNIPAM-based microgels and examined the influence on the in situ synthesis.

### 4.4.1 $\mu$ gel-AAEM

Obtained P(NIPAM-co-AAEM) microgels ( $\mu$ gel-AAEM) exhibit a hydrodynamic diameter  $D_H$  of  $358 \pm 11$  nm at 20 °C in the swollen state. We can observe aggregation of the microgel particles which starts at 34 °C close to the corresponding, well-known VPTT of crosslinked PNIPAM chains in water.<sup>1, 69, 91, 184</sup> Prior to the aggregation, the particles show a hydrodynamic diameter  $D_H$  of  $268 \pm 2$  nm in the collapsed state

at 33 °C. Due to the hydrophobic character of incorporated AAEM the VPTT is shifted to a temperature of 23 °C (**Figure S4.3**).

The observed aggregation-behaviour of the microgels can be explained by weak colloidal stability as a result of the ratio between hydrophobic AAEM monomers and NIPAM monomers as well as the absence of functional groups that ensure stability for example by electrostatic repulsion. This is further validated by electrophoretic mobility measurements that revealed a zeta potential of -2 mV which indicate the absence of charges within the microgel. Despite the weak colloidal-stability we performed in situ experiments with the *μgel*-AAEM particles which are carried out at room temperature below the VPTT.

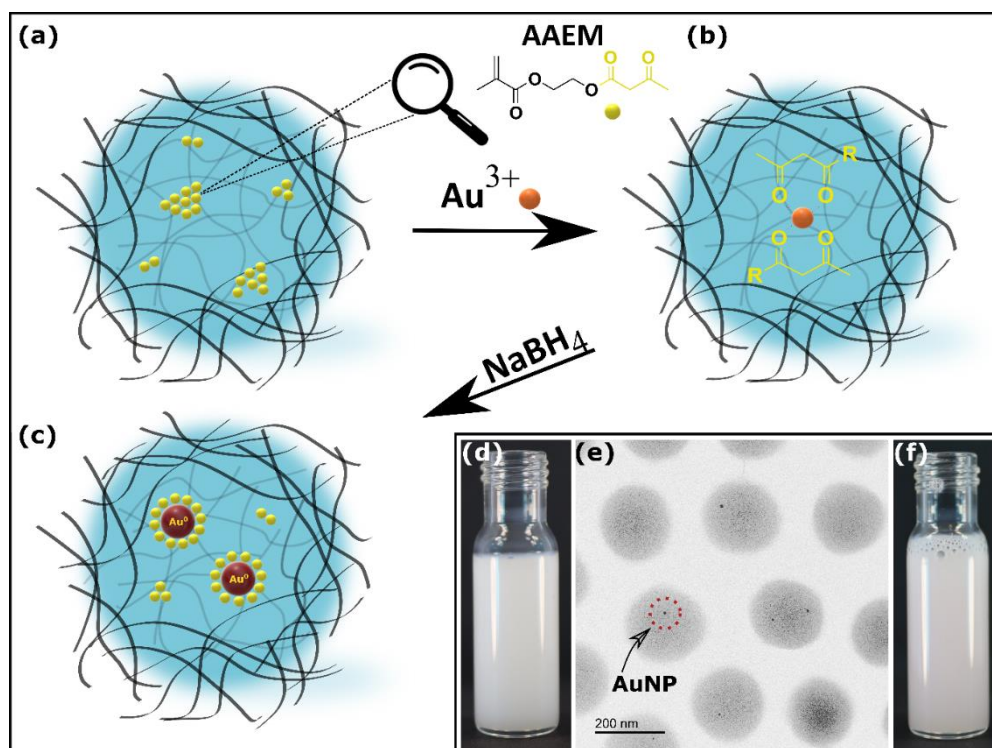


**Figure 4.1:** (a) - (c) Schematic illustration of the proposed reaction mechanism for the in situ formation of gold nanoparticles in AAEM containing microgels. (d) Digital photograph of the initial microgel dispersion prior to the in situ synthesis. (e) Exemplary TEM image of *μgel*-AAEM after in situ synthesis. We marked one formed gold particle (AuNP) with a red circle for clarification. (f) Digital photograph of the corresponding microgel dispersion after in situ synthesis and purification.

Our findings for the in situ synthesis of *μgel*-AAEM are presented in **Figure 4.1**. We first want to introduce a possible reaction mechanism for the in situ process in (a) - (c). We suggest that the incorporation of AAEM, more precisely the  $\beta$ -diketone groups, into the microgels allow for the coordination of gold-ions diffusing into the microgels

(**Figure 4.1 (a)** and **(b)**). The coordinated gold-ions can subsequently be reduced by only a strong reduction agent like sodium borohydride leading to the formation of gold nanoparticles (**Figure 4.1 (c)**). Further, **(d)** shows a digital photograph of the microgel before the in situ synthesis. A typical milky white colour can be identified which is expected for microgel and latex dispersions.<sup>111</sup> The TEM image in **(e)** shows purified microgels with gold nanoparticles in some of the microgels after the in situ synthesis.

For *μgel-AAEM*, we performed the in situ synthesis with three different amounts of HAuCl<sub>4</sub> to investigate the dependency of the gold ion concentration and consequently the ratio between microgels and added gold ions. In the TEM image presented in **(e)**, we used 50 μl (0.01M) of HAuCl<sub>4</sub> for the in situ synthesis. The image shows purified microgels that partially contain gold nanoparticles. With 50 μl of HAuCl<sub>4</sub> used for the synthesis, we can report an inconsistent, uncontrolled formation of gold nanoparticles. More precisely, we found the formation of single particles only within about one third of the particles, while we observed the formation of two or more particles in about 10 % of the microgels. The remaining microgels do not show presence of nanoparticles at all. By using lower amounts of HAuCl<sub>4</sub> during the synthesis, the amount of empty microgels is increasing. Still, we occasionally found the formation of multiple gold nanoparticles within few microgels. Higher amounts of HAuCl<sub>4</sub> led to a decreased amount of unloaded microgels but we observed the formation of multiple gold nanoparticles up to 10 per microgel in certain instances. We present exemplary TEM images for all three amounts of HAuCl<sub>4</sub> in **Figure S4.4**. For all three amounts of HAuCl<sub>4</sub> the size  $D_{\text{TEM}}$  of the formed nanoparticles was determined in a range between  $8 \pm 2$  nm for the lowest to  $7 \pm 2$  nm for the highest amount. As a result, the size of the formed gold nanoparticles is seemingly not affected by the used amount of HAuCl<sub>4</sub> for *μgel-AAEM*.

The inconsistent and uncontrolled formation of the particles is also reflected by the change in colour of the microgel dispersion after the in situ formation and purification. The microgel dispersion presented in the digital photograph in **(f)** shows a slight change from initially white to barely perceptible pink. The weak colouring suggests that the majority of the microgels do not contain gold nanoparticles.

Independent of the ratio of gold ions to microgels and various reaction conditions, we could not realize a in situ synthesis where every microgel only contains a single gold nanoparticle. This observation might be connected to inhomogeneities in the internal

architecture within and between the microgels caused by the different reactivities of the monomers. We assume that the formation of gold nanoparticles can only occur in AAEM rich domains that presumably favor and cause the accumulation of gold ions in these regions of the microgels.

Surprisingly, we found that after the in situ synthesis with  $\mu\text{gel-AAEM}$ , priorly unstable microgels exhibit colloidal stability and can be heated above the VPTT without aggregation although they only show a slightly more negative zetapotential of -9 mV at 20 °C (**Figure S4.5**). We suppose that the recovered colloidal stability is caused by a structural change of the functional groups. A strong reduction agent like sodium borohydride could likely reduce  $\beta$ -diketone functionalities and thus enhance the hydrophilicity leading to an increase in the colloidal stability.

In a next step, we added acrylic acid as a second comonomer during the synthesis of the microgel.

#### 4.4.2 $\mu\text{gel-AAEM-AAc}$

With the addition of 2.5 mol% AAc during the synthesis, we obtained microgels with a hydrodynamic diameter  $D_H$  of  $309 \pm 2$  nm at 20 °C. Compared to  $\mu\text{gel-AAEM}$ , the new obtained microgels  $\mu\text{gel-AAEM-AAc}_{2.5\%}$ , show colloidal stability at higher temperatures due to the electrostatic repulsion of the negatively charged carboxylic acid groups. We validated this assumption by determination of the electrophoretic mobility and found a zetapotential of -39 mV at 20 °C. Using temperature-dependent DLS measurements shown in **Figure 4.2 (a)**, we could determine the VPTT of the microgels at 27.7 °C. Compared to  $\mu\text{gel-AAEM}$  the shift of the VPTT to lower temperatures is less pronounced due to the additional incorporation of the hydrophilic acrylic acid. Compared to the lower volume swelling capacity of 1.2 of PVCL microgels known from the literature,<sup>130</sup>  $\mu\text{gel-AAEM-AAc}_{2.5\%}$  show a volume swelling ratio  $\beta$  of 3.1. The volume swelling ratio  $\beta$  describes the quotient of the volume of the microgel in the swollen state divided by the volume in the collapsed state and thereby quantifies the possible increase in volume during the swelling of the microgel (**Equation S4.1**).

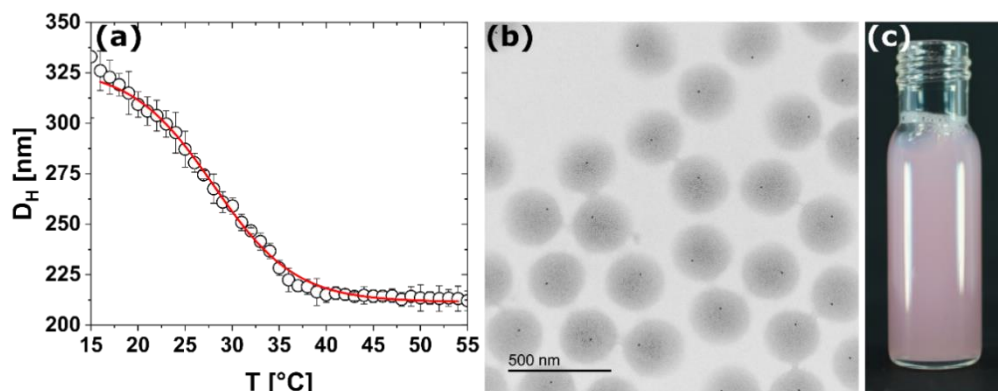


**Figure 4.2:** (a) Temperature-dependent measurement of the hydrodynamic diameter by of  $\mu\text{gel-AAEM-AAc}_{2.5\%}$  by dynamic light scattering. The solid red line corresponds to a Boltzmann fit-function which was applied to determine the VPTT of the microgel. (b) Exemplary TEM image after the in situ synthesis and purification of  $\mu\text{gel-AAEM-AAc}_{2.5\%}$  where a single gold nanoparticle can be identified in every microgel. (c) Digital photograph of the corresponding hybrid microgel dispersion.

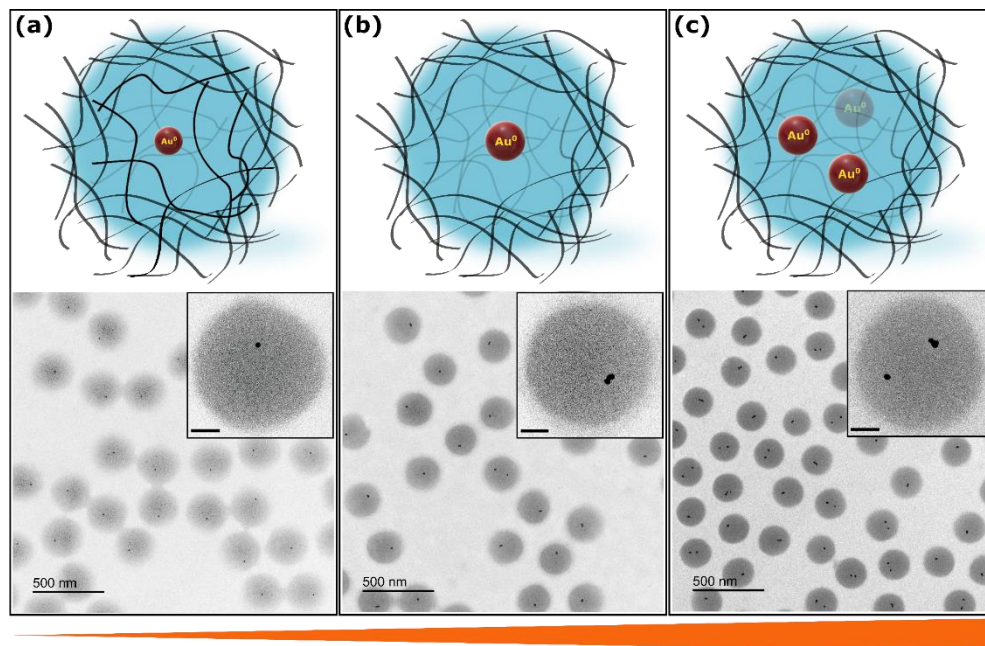
In **Figure 4.2 (b)** we show a TEM image of the microgels after the successful in situ synthesis and a digital photograph of the corresponding pink dispersion of the microgel particles after purification in **Figure 4.2 (c)**. The presented TEM image verifies the successful formation of small, single gold particles with a size  $D_{\text{TEM}}$  of  $10 \pm 1$  nm in each individual microgel. Our findings lead to the assumption that the incorporation of acrylic acid into the microgels network is mandatory for the course of the consistent and controlled in situ synthesis. Compared to the in situ synthesis for  $\mu\text{gel-AAEM}$ , we want to highlight that for  $\mu\text{gel-AAEM-AAc}_{2.5\%}$  a significant lower amount of  $\text{HAuCl}_4$  is needed for the uniform formation of single nanoparticles in the microgels which we cannot explain by our experiments.

Similar to our findings for  $\mu\text{gel-AAEM}$ , we observed a change in the physicochemical properties of the microgels with incorporated nanoparticles. After the in situ synthesis the VPTT of the hybrid microgels is shifted towards higher temperatures by almost  $9^\circ\text{C}$  to  $36.2^\circ\text{C}$  and an increase in size by almost 80 nm to  $389 \pm 13$  nm at  $20^\circ\text{C}$  can be observed for  $\mu\text{gel-AAEM-AAc}_{2.5\%}$ . The observations are in good agreement with our assumption of a reduction of functional groups by the strong reducing agent sodium borohydride leading to the higher hydrophilicity of the microgels.

We synthesized two microgels with AAC contents of 12.5 mol% and 0.5 mol% added during the synthesis of the microgels to further investigate the influence of the charged comonomers on the in situ synthesis. For microgels with 12.5 mol% AAC we could not find a noticeable difference for the properties of the hybrid microgels and gold nanoparticles before and after the in situ synthesis. Despite the increase of AAC by

five times compared to  $\mu\text{gel-AAEM-AAc}_{2.5\%}$ , microgel  $\mu\text{gel-AAEM-AAc}_{12.5\%}$  shows a nearly identical hydrodynamic diameter of  $D_H$  of  $308 \pm 12$  nm at  $20$  °C and a VPTT of  $25.2$  °C. The size after the in situ synthesis is increased to  $392 \pm 22$  nm with a VPTT of  $36.5$  °C (**Figure S4.6**). Also, the size  $D_{\text{TEM}}$  of the gold nanoparticles was determined as  $9 \pm 1$  nm which matches the sizes we found for  $\mu\text{gel-AAEM-AAc}_{2.5\%}$ . In case of microgels with 0.5 mol% AAc content, TEM images after the in situ synthesis resemble our results for the experiments for  $\mu\text{gel-AAEM}$  without the addition of AAc and only shows the formation of particles in few microgels (**Figure S4.7**). From our observations, we conclude that a certain amount of charged functional groups is needed to allow a controllable and uniform in situ synthesis that appears to be influenced by the introduced charged carboxylic acid groups but higher amounts of charged groups do not further alter the results.

We wanted validate the proposed mechanism in regard to complexation of gold ions and the location of the formation of the gold nanoparticles. Therefore, we performed an experiment where we centrifuged the microgel dispersion ten times after the initial addition of  $\text{HAuCl}_4$  and successive stirring for 60 minutes. After each cycle of centrifugation, we removed the supernatant and redispersed the microgels in water. By repeating the process ten times, we ensured that freely diffusing gold ions are completely removed from the supernatant and thus only ions that are complexed by the  $\beta$ -diketone groups remain inside of the microgels. After the cycles of the centrifugation the gold ions were reduced by addition of strong reduction agent sodium borohydride. In **Figure S4.8** in the **Supporting Information**, we present exemplary TEM images that show the resulting microgels after reduction. The images confirm that formation of the gold nanoparticles occurs within the microgels and show the existence of microgels with a single gold nanoparticle. Thereby, we could disprove the possibility of small nanoparticles diffusing into the microgels after the formation on the outside. To further strengthen this point, we present the results for an experiment where sodium borohydride was added only 60 seconds after the addition of  $\text{HAuCl}_4$  to the microgels. The recorded TEM images reveal that only few microgels contain formed gold nanoparticles (**Figure S4.9**). The short time frame before reduction seems to be insufficient to saturate the  $\beta$ -diketone groups with free diffusing gold ions. Still, the high amount of free gold ions outside of the microgels did not lead to a subsequent loading of the microgels after the reduction.



#### Amount of HAuCl<sub>4</sub>

**Figure 4.3:** Schematic illustration and corresponding TEM images for in situ experiments with  $\mu$ gel-AAEM-AAc<sub>2.5%</sub> for different amounts of HAuCl<sub>4</sub>. The applied amount is increasing in ascending order from left to right which is indicated by the orange bar below the images. The amount used are (a) 10  $\mu$ l, (b) 50  $\mu$ l and (c) 100  $\mu$ l of a 0.01M HAuCl<sub>4</sub> while using 562  $\mu$ l of a 1 wt% microgel dispersion. The insets show TEM images of single particles at higher magnifications. The scale bars in the insets represents a magnitude of 50 nm.

Similar to our experiments for  $\mu$ gel-AAEM we compare the results after the in situ synthesis and purification of three different applied amounts of substance of HAuCl<sub>4</sub> in **Figure 4.3** to get a deeper understanding of the influence of the ratio between added gold ions and microgels. In (a) - (c) we present schematics and the corresponding TEM images of in situ syntheses performed with  $\mu$ gel-AAEM-AAc using amounts of 10, 50 and 100  $\mu$ l (0.01M) of HAuCl<sub>4</sub> in ascending order. Results for the synthesis presented in (a) are almost identical to the results we presented in **Figure 4.2 (b)** which emphasizes on the reproducibility of the synthesis. In contrast to our observations in (a), in (b), five times the amount of HAuCl<sub>4</sub> led to a growth in size of the nanoparticles by about 40 % to  $14 \pm 4$  nm. TEM imaging reveals that the increase in size is partially caused by the formation of two nanoparticles that appear to be similar in size and are located very close to each other and thus appear to grow together during the in situ process. We cannot confirm whether the increase in size is completely based on the assembly of two single particles for all particles or can also be caused by successive growth of initial, single gold particles. Occasionally, we can observe the formation of an isolated second nanoparticle which is the case in less

than 5 % of the microgels. In **(c)**, doubling of the amount did not further increase the size of the gold nanoparticles ( $D_{\text{TEM}}$  of  $13 \pm 4$  nm) but caused the increased formation of second nanoparticles in some cases and also third nanoparticles in very few microgels. Further increase of amount of  $\text{HAuCl}_4$  only causes the formation of additional nanoparticles within the microgels.

Our observations for  $\mu\text{gel-AAEM-AAc}$  differ from the results that we found for  $\mu\text{gel-AAEM}$ . The increase in size of the nanoparticles with increased amount of added  $\text{HAuCl}_4$  as well as the formation of multiple nanoparticles in direct proximity indicate a difference in the internal architecture i.e., distribution of AAEM monomer in the microgels. We want to highlight that the introduction of comonomers into a polymer-based system is known for being challenging and our experiments underline that every comonomer adds a new layer of complexity to the system either regard to the properties of the microgel or subsequent functionalization and reactions. Detailed investigations on the internal structure are needed in the future to understand and control these complex copolymer microgel systems.

### 4.4.3 One-Step Gold Overgrowth

Next, we want to present results for the one-step growth of the gold nanoparticles within the microgels using a surfactant-supported approach. By the addition of the cationic surfactant CTAC, the overgrowth process of gold nanoparticles is reported to provide controlled reaction conditions which results in the growth of uniform sizes and shapes and only a low number of gold particles formed outside of the microgels.<sup>183</sup>

We can confirm that no gold particles outside of the microgels are formed during the surfactant-supported overgrowth and therefore centrifugation is sufficient for purification. Although we expected that electrostatic interactions between negative charged acrylic acid moieties and partly positively charged CTAC molecules could potentially have an influence on the process, we report the successful spherical growth of the gold nanoparticles by the surfactant-supported protocol and show our findings in **Figure 4.4**.

In **(a)**, we present the UV-Vis absorbance spectra for the hybrid microgels before and after the overgrowth process. For the hybrid microgels after the initial in situ synthesis we can observe a decrease in the absorbance with increasing wavelengths and no distinct extreme values because of the dominant scattering contribution of the microgel compared to the small gold nanoparticles. In contrast, hybrid microgels after the surfactant-supported overgrowth show a local maximum at 560 nm which can be attributed to the pronounced LSPR of the gold nanoparticles. The narrow latitude of the signal is based on the comparably uniform distribution of the particles size and shape and covers wavelengths from 500 to 650 nm.

The optical characterization is validated by TEM imaging in **(b)** and the visual impression of the microgel dispersion in **(c)**. For the mostly spherical shaped particles within the microgels, we determined an average size  $D_{\text{TEM}}$  of  $76 \pm 9$  nm which corresponds to a growth by about eight times. Compared to the light pinkish solution for the microgels that hold smaller gold nanoparticles, the digital photograph shows the characteristic shift to a darker orange-brownish colour for the hybrid microgels after the overgrowth process and purification.

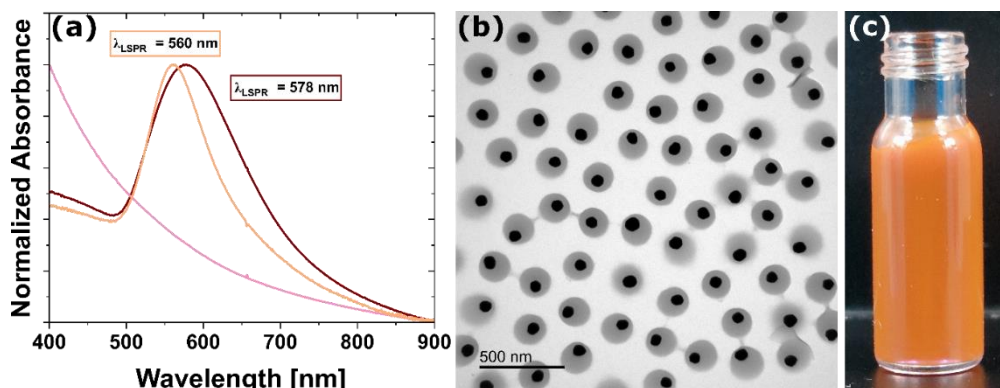


**Figure 4.4:** Summary for our findings for the surfactant-supported gold nanoparticle overgrowth. (a) Absorbances for the hybrid microgels before and after the overgrowth process. According to the colour of the hybrid microgel dispersions, the spectrum in pink corresponds to the microgels after the initial in situ synthesis, the spectrum in orange refers to the microgels after surfactant-supported one-step overgrowth and the spectrum in dark-red represents the microgels after the surfactant-supported one-step overgrowth. (b) Exemplary TEM images after the surfactant-supported overgrowth of the gold nanoparticles in *μgel-AAEM-AAc<sub>2.5%</sub>*. (c) Digital photograph of the corresponding microgel dispersion.

Further we wanted to address, if the overgrowth process is affected by the underlying overgrowth mechanism or by the composition of the microgels and influences by the surrounding functional groups. Therefore, we iterated the overgrowth of our particles with a surfactant-free approach.

Compared to the surfactant-supported approach, overgrown particles show a higher number of irregular shapes. In the **Supporting Information** we present exemplary TEM images that show that we could not achieve an evenly growth of all nanoparticles to obtain uniform particles in size and shape (**Figure S4.10**). We determined an increase in size  $D_{\text{TEM}}$  from  $10 \pm 1$  nm to  $83 \pm 13$  nm which equals a growth by almost nine times. Due to the uncontrolled nature of the surfactant-free reaction, we can not only observe the growth of spherical particles with partially misshaped morphologies but also rods and triangles independent on different tested reaction conditions. The larger average size but lower uniformity of the particles is expressed by a change to a dark red color of the dispersion compared to the pinkish color of the initial, small gold nanoparticles and the orange-brownish color of the smaller, more uniform gold nanoparticles for the surfactant-supported overgrowth. The visual difference and difference in size are accompanied by a shift of the LSPR signal in the corresponding UV-Vis absorbance spectrum in **Figure 4 (a)**. The shift to higher wavelength to 578 nm and a broader signal that covers wavelength from approximately 500 to 700 nm are in good agreement with the observed lower uniformity of the particles shape and size and an overall smaller size of the gold nanoparticles.

We can confirm that growth of gold nanoparticles formed by a in situ mechanism is independent on the composition of the microgel and possible for both, the one-step surfactant-supported and surfactant-free approach. Experiments show that the surfactant-supported approach leading to a more uniform growth of spherical particles but a more pronounced growth in size can be achieved by the surfactant-free growth. The uncontrolled nature of the surfactant-free growth mechanism could possibly be enhanced by careful adjustment of the reaction conditions.

Determined characteristics including sizes of the microgels and formed gold nanoparticles, VPTTs and the corresponding surface charges are summarized for all microgels and hybrid microgel systems in **Table S4.1** and **Table S4.2**, respectively.

#### 4.4.4 Characterization via small-angle X-ray scattering (SAXS)

Along with the determination of the size and morphology of the gold nanoparticles within the microgels using TEM, we further want to verify the results by the means of SAXS measurements of the hybrids microgels. **Figure 4.5 (a)** and **(b)** show the change in the scattering profiles prior and after the in situ synthesis for *μgel-AAEM* and *μgel-AAEM-AAc<sub>2.5%</sub>* respectively. In **(a)**, the SAXS scattering profile in black represents *μgel-AAEM* prior the formation of gold nanoparticles while the blue profile shows the scattering profile after the in situ synthesis with 50 μl of HAuCl<sub>4</sub>. For the microgel system without nanoparticles we found the expected scattering behaviour for the investigated *q*-regime without visible form factor minima. We applied a porod function (orange) with a slope of  $q^{-4}$  to roughly describe the data of the microgel. For the data recorded from the hybrid microgels after the in situ synthesis we applied a hard sphere model to describe the scattering contribution of formed gold nanoparticles and added a porod function to consider the contribution of the microgel in the lower *q*-regime below 0.02 nm<sup>-1</sup> (red). The red dashed line shows the fit solely for a hard sphere. We can confirm that the combination of both functions sufficiently describes the scattering data over the whole investigated *q*-range. A noticeable difference between both scattering profiles can be found in the *q*-range of 0.2 nm<sup>-1</sup> < *q* < 0.8 nm<sup>-1</sup> where the system with formed gold nanoparticles shows a slight increased scattering intensity which is properly described by the fit for a hard sphere. The increase in scattering intensity is attributed to the formation of the gold

nanoparticles but only slightly pronounced due to the small size and the formation in only about 40 % of the microgel particles. Based on the hard sphere fit we obtained an average particle diameter of  $9 \pm 3$  nm which is slightly higher than the diameter of  $8 \pm 2$  nm determined by TEM. The difference in size is most likely attributed to the better statistics provided by SAXS measurements of the dispersion but confirms the dimensions of the gold nanoparticles within the microgels. Additional information about the parameters applied to fit all scattering profiles can be found in **Table S4.3 - S4.6** in the **Supporting Information**.

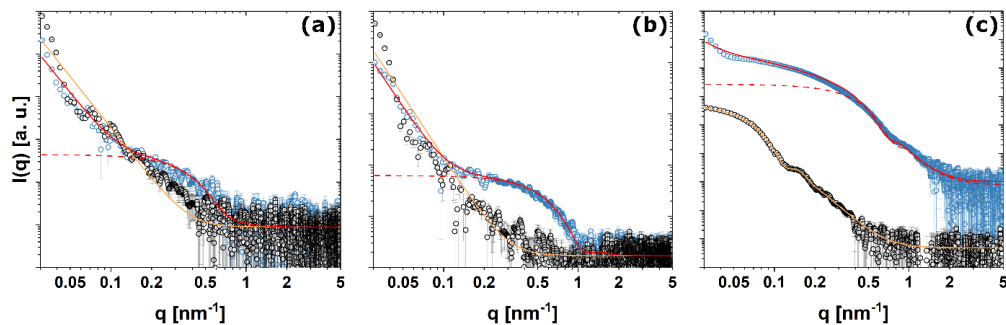


**Figure 4.5:** Radially averaged SAXS profiles for different investigated microgels before and after the formation of gold nanoparticles via in situ synthesis and overgrowth procedure. **(a)** Scattering profiles before (black) and after (blue) in situ synthesis of  $\mu\text{gel-AAEM}$  with  $50 \mu\text{l HAuCl}_4$ . **(b)** Comparison of scattering profiles prior (black) and after the formation of gold nanoparticles (blue) for  $\mu\text{gel-AAEM-AAC}_{2.5\%}$  with  $10 \mu\text{l}$  of  $\text{HAuCl}_4$ . **(c)** Scattering profiles for  $\mu\text{gel-AAEM-AAC}_{2.5\%}$  after surfactant-supported overgrowth of the gold nanoparticles (black) and  $\mu\text{gel-AAEM}$  after in situ synthesis with  $100 \mu\text{l}$  of  $\text{HAuCl}_4$  (blue). Solid red and orange lines and dashed red lines correspond to different fit functions and models to describe the scattering profiles of the microgels and hybrid systems. The right y-axis in each diagram gives the intensity. We adjusted the intensity values for all scattering profiles for better comparability and visibility.

Similar observations can be found for the scattering profiles in **(b)** where we present the results for  $\mu\text{gel-AAEM-AAC}_{2.5\%}$ . Again, the black scattering profile shows the data for the microgel without gold nanoparticles and the scattering profile in blue relates to the microgel system after the in situ synthesis with  $10 \mu\text{l}$  of  $\text{HAuCl}_4$  respectively. According to both systems investigated in **(a)**, we used a porod function to describe the data of the microgel (orange) which is again combined with the hard sphere model for the microgel system after the in situ synthesis (red). Compared to the behaviour for  $\mu\text{gel-AAEM}$  after in situ synthesis in **(a)**, we can now observe a noticeable increase in scattering intensity in the  $q$ -range of  $0.2 \text{ nm}^{-1} < q < 1.0 \text{ nm}^{-1}$  whereas the microgels before in situ synthesis show no noticeable difference in their scattering profile. The strong increase in intensity is based on the uniform formation of one gold nanoparticle in every microgel resulting in a higher number of gold nanoparticles in the probed volume. While no form factor minima can be observed due to the small size and number of the gold nanoparticles the hard sphere model describes the scattering

profile in a sufficient way. Fitting procedure of the scattering profile after the in situ synthesis resulted in an average particle diameter of  $7 \pm 1$  nm which again is close to the diameter received by analysis of TEM images ( $10 \pm 1$  nm). The comparably large difference for both methods is once again likely based on the smaller amounts of particles recorded and analysed during TEM studies.

Finally, in **(c)** we compare the recorded scattering profiles for *μgel-AAEM-AAc<sub>2.5%</sub>* after surfactant-supported overgrowth of the gold nanoparticles presented in black and *μgel-AAEM* after in situ synthesis with a higher amount of 100 μl HAuCl<sub>4</sub> shown in blue. As previously described, the in situ synthesis with higher amounts of HAuCl<sub>4</sub> led to the uncontrolled formation of multiple gold nanoparticles within the microgels while the surfactant-supported overgrowth allowed for the growth of the gold nanoparticles in size by about eight times. Compared to the investigation on microgel systems with smaller gold nanoparticles in **(a)** and **(b)** an overall higher relative intensity is observable which is based on the correlation of the scattering intensity and the radius of the scattering object to the power of six. The higher scattering intensity results in visible form factor oscillations in the  $q$ -range of  $0.1 \text{ nm}^{-1} < q < 0.4 \text{ nm}^{-1}$ . Based on the distinct form factor oscillations we were able to perfectly describe the overgrown gold nanoparticles with a model for a hard sphere (orange). The resulting diameter determined by the fit function  $70 \pm 12$  nm is in good agreement with the diameter obtained by TEM investigation ( $76 \pm 9$  nm) and deviates only within the error values. For *μgel-AAEM* after the in situ synthesis with 100 μl HAuCl<sub>4</sub> we used a combination of porod function and fractal model (red). While the porod function again covers the contribution of the microgel, the fractal model allows to describe the contribution of multiple singular gold nanoparticles according to the hard sphere model (dashed red) but also an additional portion of dimers and trimers in spatial proximity formed by aggregation of nanoparticles. Using the fractal model, we were able to successfully describe the scattering profile caused by the presence of gold aggregates with different sizes. The received diameter of  $12 \pm 3$  nm noticeably differs from the diameter obtained by TEM evaluation which was determined to be  $7 \pm 2$  nm. This observation is again based on the strong deviation of nanoparticles sizes which could not fully be covered by TEM analysis. The fractal model also provided the correlation length which characterizes the average size of an aggregate of gold nanoparticles within the microgels in the dispersion. Based on a correlation length of 12.4 nm we report that the majority of the gold nanoparticles

formed during the in situ synthesis with higher amounts H<sub>2</sub>AuCl<sub>4</sub> in *μgel-AAEM* are aggregates of two gold nanoparticles.

## 4.5 Conclusion

In this work, we presented the successful in situ formation and growth of gold nanoparticles in PNIPAM-based microgels. We relied on a systematic approach where we synthesized different microgels with increasing complexity by adding additional functional groups for each microgel system and thus got a better understanding of the individual effects of each component on the in situ formation process.

By incorporation of AAEM monomer into the PNIPAM-based microgel networks we initially showed an uncontrolled way to form gold nanoparticles inside of the microgels. The introduction of AAEM groups and therefore β-diketone moieties allow for the complexation of free gold ions and are necessary for the successful formation of nanoparticles in case of our applied reaction pathway. At the same time the addition of AAEM functionalities leads to a decrease in colloidal stability of the microgels due to the hydrophobic character of the functional groups.

Introduction of charge in form of AAc to the system restored the colloidal stability of the microgels because of the electrostatic repulsion of negatively charged carboxylic acid groups. The increase in colloidal stability is further accompanied by a generally improved environment for the in situ formation. Within the negatively charged P(NIPAM-co-AAEM-co-AAc) microgels we were able to achieve the formation of single, monodisperse gold nanoparticles.

For in situ experiments with different amounts of chloroauric acid, we found that the size and number of the formed gold particles can be varied within certain limits. The experiments indicated the existence of AAEM rich domains or sites forming during the microgel synthesis that are favoured for the initial accumulation and complexation of gold ions and influence the reachable size of the formed nanoparticles. The spatial position and dimensions of these AAEM rich sites within the microgels are most likely dependent on the other reaction components and conditions.

With our experiment we also showed that not only individual monomers have a major influence on the results of the in situ formation and growth, but that especially the (spatial) composition and interactions between different components in respect to charge and hydrophilicity are crucial for the understanding of the underlying mechanism. This is further highlighted by the fact that rather complex systems are needed for a controlled in situ synthesis that are challenging to characterize.

Finally, investigations on the spherical growth of the nanoparticles within the PNIPAM-based microgels suggested not only that a one-step growth of the particles by almost nine times can be achieved but that the growth process is not affected by the initial formation mechanism nor the surrounding functional groups.

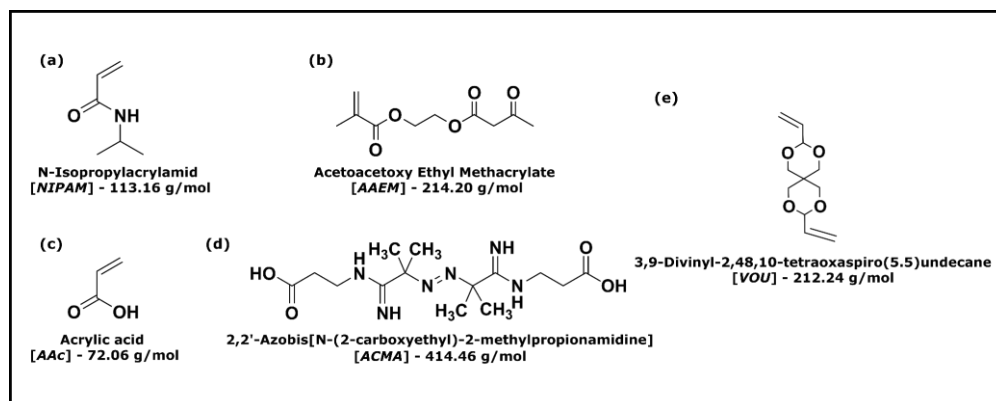
Future experiments should focus on a better understanding of the chemical structure of the microgels and the mechanism of the in situ formation – especially looking at the role of charge introduced by AAc and the change that the microgel system undergoes upon the reduction of the gold ions.

#### *Acknowledgments*

The authors acknowledge the DFG and the State of NRW for funding the cryo-TEM (INST 208/749-1 FUGG). M.K. acknowledges the Deutsche Forschungsgemeinschaft (DFG) for funding through the Emmy Noether programme (DFG, grant no. KA3880/1-1). The authors also would like to thank Déborah Feller (HHU Düsseldorf) for assistance with the surfactant-supported overgrowth protocol. This work benefited from the use of the SasView application, originally developed under NSF award DMR-0520547. SasView contains code developed with funding from the European Union's Horizon 2020 research and innovation programme under the SINE2020 project, grant agreement No 654000.

## 4.6 Supporting Information

### MATERIALS



**Scheme S4.1:** Chemical structure of monomers NIPAM (a), AAEM (b) and AAc (c) used for the synthesis of the PNIPAM-based copolymer microgels in this work. The zwitterionic initiator ACMA and the crosslinker VOUs are shown in (d) and (e), respectively.

### METHODS

**Transmission electron microscopy (TEM).** TEM was performed on a JEOL JEM-2100Plus operating in bright-field mode at 80 kV acceleration voltage. Samples were prepared by drop-casting 7  $\mu$ L of dilute microgel dispersions on carbon-coated copper grids (200 mesh, Science Services). The diameter of the microgels were obtained using the image analysis software ImageJ.

**Ultraviolet-visible (UV-Vis) absorbance spectroscopy.** UV-Vis absorbance spectra were recorded using a Specord® S600 (Analytic Jena AG) spectrophotometer. Dilute, aqueous microgel dispersions (0.02 wt%) were measured in PMMA cuvettes with a light path of  $d = 1$  cm. For every measurement a reference spectrum (water) was recorded and subtracted. Measurements were performed in the wavelength range of 182 to 1019 nm. All measurements were performed at 20 °C.

**Electrophoretic light scattering (ELS).** Electrophoretic mobilities were determined using a Zetasizer Nano ZS (Malvern Panalytical). Aqueous microgel dispersions were diluted to 0.02 wt% and measured in folded capillary cells (DTS 1070, Malvern Panalytical). For all samples, we performed measurements at 20 °C and 50 °C with equilibration times of 600 seconds. Each measurement was repeated three times.

**Temperature-dependent dynamic light scattering (DLS).** Hydrodynamic diameter,  $D_H$  were determined by DLS using a Zetasizer Nano S (Malvern Panalytical). The device detects scattered light at a scattering angle of 173 °. We performed singular measurements at 20 and 50 °C and also measurements in a temperature range of 15 and 55 °C in steps of 1 °C with a thermal stability of  $\pm 0.1$  °C. Samples equilibrated for 10 minutes at each temperature before the respective measurement. We performed three measurements with an acquisition time of 60 s for each temperature. All samples were diluted to a concentration of 0.02 wt% and were measured in triplicate in semimicro PMMA cuvettes. Presented error bars are the product of the intensity weighted mean hydrodynamic diameter (z-average) and the polydispersity index which is given by the cumulant analysis performed by the Malvern measurement software. The polydispersity index is an indication of the overall distribution of the determined size, assuming a single mean.

**Small-angle X-ray scattering (SAXS).** SAXS measurements were performed on a Xeuss 2.0 (XENOCs) equipped with an X-ray source that provides a beam with an energy of 8.048 keV. The sample-to-detector distances were set to 0.55 m and 2.495 m and measurements were performed with acquisition times of 900 s and 1800 s, respectively. Scattering patterns were recorded with a Pilatus3R 300 K detector providing an area of  $83.8 \times 106.5$  mm<sup>2</sup> and a pixel size of  $172 \times 172$   $\mu$ m<sup>2</sup>. In this case the setup provides a  $q$ -range of  $0.03 \text{ nm}^{-1} < q < 5 \text{ nm}^{-1}$ . Scattering profiles for both sample-to-detector distances were merged in the  $q$ -range between  $0.1 \text{ nm}^{-1}$  and  $0.25 \text{ nm}^{-1}$ . Dilute samples were measured in 1 mm round capillaries (WJM Glas) at a temperature of 20 °C. The measured signal was background-corrected for the scattering of water and finally radially averaged with the Foxtrot software provided by Xenocs.<sup>185</sup> Fitting of the scattering profiles was conducted with the SasView software.<sup>186</sup>

## RESULTS AND DISCUSSION

### *μgel*-PNIPAM & *μgel*-AAc<sub>12.5%</sub>

**Figure S4.1 (a)** and **S4.2 (a)** present results from temperature-dependent measurements of the hydrodynamic diameter by DLS for *μgel*-PNIPAM and *μgel*-AAc<sub>12.5%</sub>. The volume swelling ratio  $\beta$  was determined to be 2.9 and 2.2 for the microgels, respectively. The following **Equation S4.1** describes the calculation of  $\beta$ :<sup>97</sup>,

187

$$\beta = \frac{(R_H(20^\circ\text{C}))^3}{(R_H(50^\circ\text{C}))^3} \quad (\text{S4.1})$$

*μgel*-AAc with incorporated carboxylic acid groups possess a lower volume swelling capacity compared to *μgel*-PNIPAM. Due to electrostatic repulsion the possibility of the polymer chains to converge during the collapse above the VPTT is noticeably reduced and consequently leading to the difference in the swelling capacity. The temperature-dependent measurements of the size for *μgel*-PNIPAM in **Figure S4.1 (a)** show the low polydispersity of the microgels only containing PNIPAM without comonomers. The presented error bars are the product of the intensity weighted mean hydrodynamic diameter (z-average) and the polydispersity index which is given by the cumulant analysis and thus allow to get an impression of the polydispersity in plots of the hydrodynamic diameter in dependence of the temperature for all discussed microgels. The *μgel*-PNIPAM microgels were found to be neutral in charge with a value of 1 mV determined by electrophoretic mobility measurements. **Figure S4.1 (b)** and **Figure S4.2 (b)** show exemplary TEM images after the in situ synthesis of gold nanoparticles in presence of the microgels without purification. In the TEM image in **Figure S4.1 (b)** we can observe a large number of gold nanoparticles outside of the microgels that form aggregates of uncontrolled shape and size. We cannot report the formation of nanoparticles inside of the microgels.

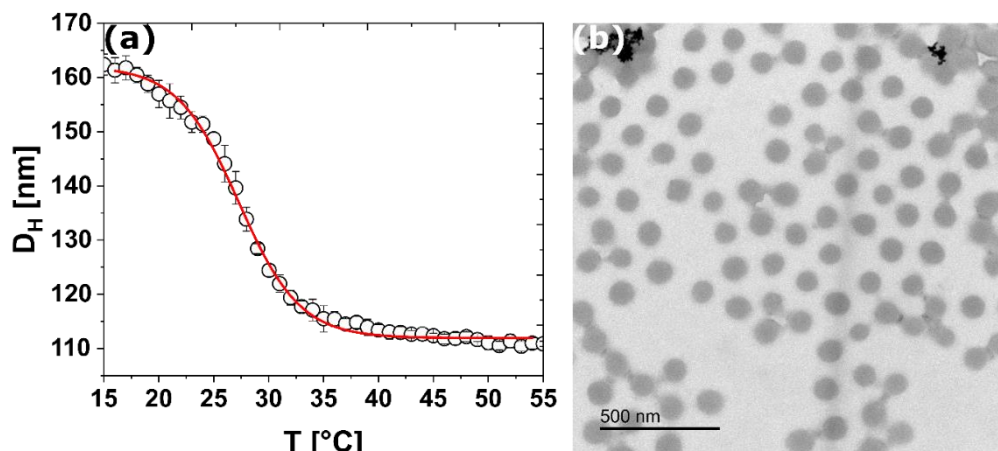


**Figure S4.1:** (a) Hydrodynamic diameter of  $\mu\text{gel-PNIPAM}$  in dependence of temperature as determined by DLS. The solid red line corresponds to a Boltzmann fit which was applied to determine the VPTT of the microgel at 27.2 °C. (b) Exemplary TEM image after the *in situ* synthesis prior to purification. Large gold aggregates can be identified outside of the microgels while the formation of singular gold nanoparticles within the microgels cannot be observed.

For the temperature-dependent measurements of size for  $\mu\text{gel-AAc}_{12.5\%}$  presented in **Figure S4.2 (a)**, large error-bars indicate a high polydispersity of the microgel system. Measurements of the electrophoretic mobility of the microgels reveal a zeta potential of -38 mV and thus confirm the incorporation of acrylic acid monomer into the polymer chains. Analogue to **Figure S4.1 (b)**, TEM images in **Figure S4.2 (b)** underline that microgels that only contain PNIPAM and AAc are not suitable for the *in situ* synthesis protocol and successful formation of gold nanoparticles within the microgels, respectively. Again, only large aggregates of formed gold particles can be observed outside of the microgel particles while the formation of singular gold nanoparticles within the microgels cannot be observed.

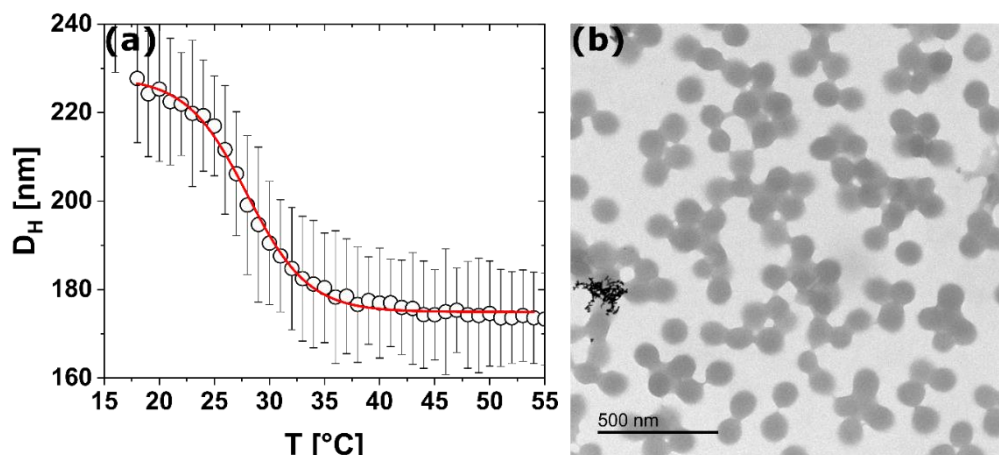


**Figure S4.2:** (a) Hydrodynamic diameter of  $\mu\text{gel-AAc}$  in dependence of temperature as determined by DLS. The solid red line corresponds to a Boltzmann fit which was applied to determine the VPTT of the microgel at 27.9 °C. (b) Exemplary TEM image after the *in situ* synthesis without purification. Large gold aggregates can be identified outside of the microgels while the formation of singular gold nanoparticles within the microgels cannot be observed.

#### $\mu\text{gel-AAEM}$

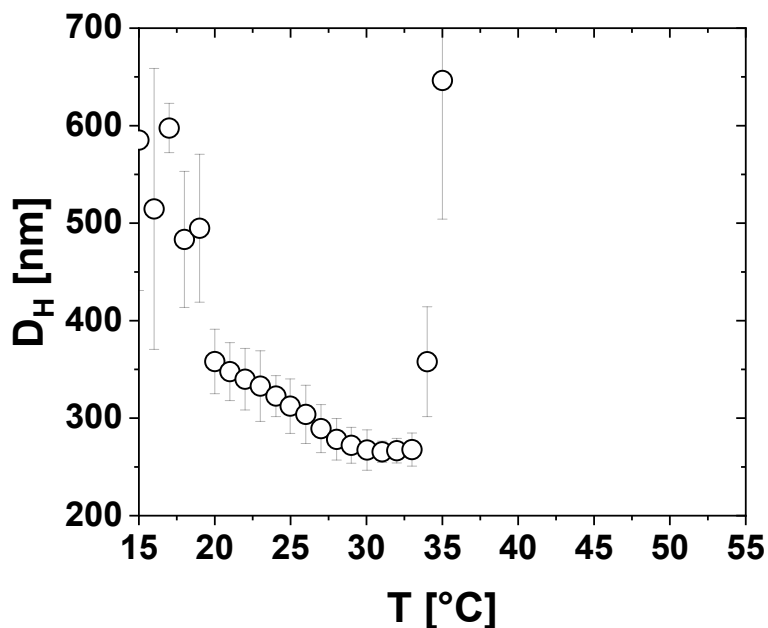
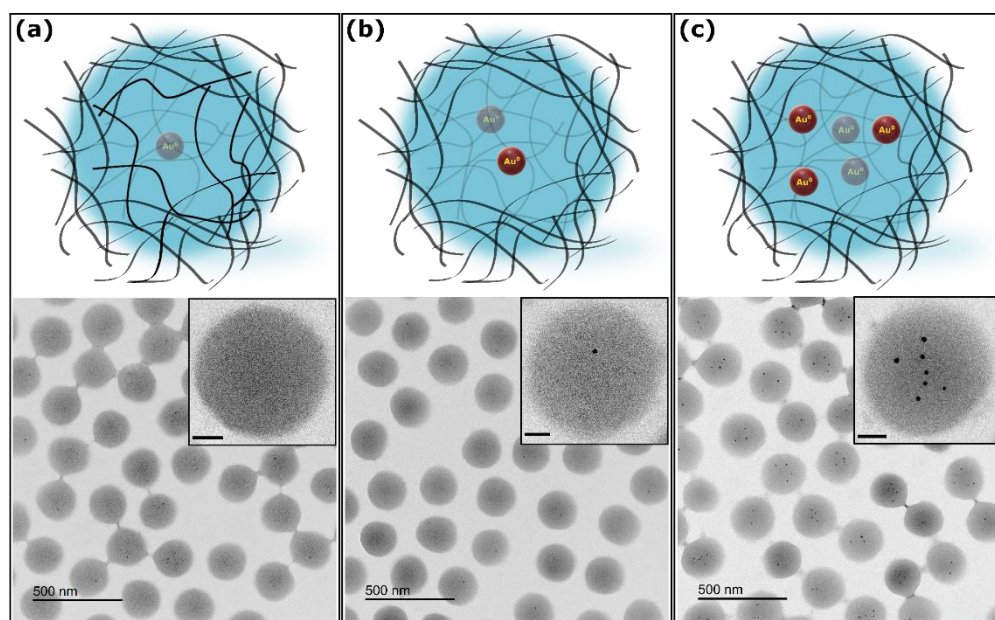


**Figure S4.3:** Hydrodynamic diameter of  $\mu\text{gel-AAEM}$  in dependence of temperature as determined by DLS.

In **Figure S4.3** the temperature-dependent change of the hydrodynamic diameter is presented for  $\mu\text{gel-AAEM}$ . The low colloidal stability of the microgel system is reflected by the abrupt increase in the hydrodynamic diameter above 33 °C. The aggregation

of the microgels is reversible upon cooling of the dispersion. Below 20 °C, the determined hydrodynamic diameter and also the polydispersity which is reflected by the error bars increase significantly. The determined volume swelling ratio  $\beta$  is 2.4 using the hydrodynamic diameter of  $358 \pm 11$  nm in the swollen state at 20 °C and  $268 \pm 3$  nm in the collapsed state at 33 °C prior to aggregation of the microgels.

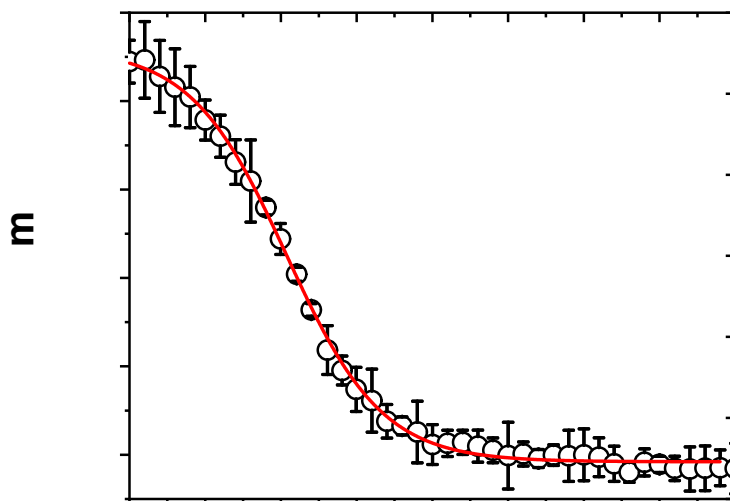


#### Amount of HAuCl<sub>4</sub>

**Figure S4.4:** Schematic illustration and corresponding TEM images for in situ growth experiments with  $\mu$ gel-AAEM using different amounts of HAuCl<sub>4</sub> increasing from left to right. The amount used are (a) 50  $\mu$ l, (b) 100  $\mu$ l and (c) 200  $\mu$ l of a 0.01M HAuCl<sub>4</sub> while consistently using 562  $\mu$ l of a 1 wt% microgel dispersion. The insets show TEM images of single microgels at higher magnifications. The scale bars in the insets correspond to 50 nm.

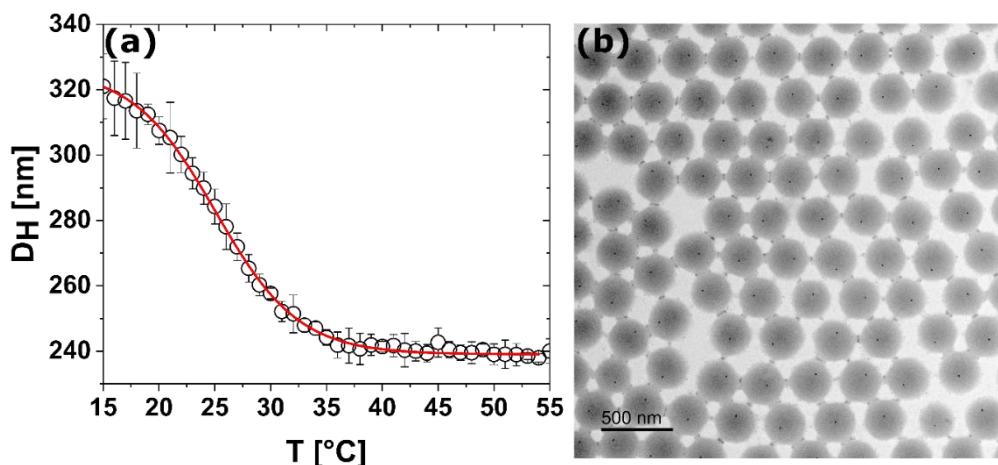
Similar to the experiments presented in **Figure 4.3** in the main manuscript, we performed in situ experiments with different amounts of HAuCl<sub>4</sub> of the same concentration with  $\mu$ gel-AAEM. Three characteristics can be identified comparing the three TEM images in **Figure S4.4**. First, a higher amount of gold ions is needed to cause initial formation of gold nanoparticle compared to in situ experiments with  $\mu$ gel-AAEM-AAc. Further, it was not possible to achieve a formation of a single nanoparticle in every microgel. Low amounts of HAuCl<sub>4</sub> will not lead to the formation of nanoparticles in only a negligible small portion of the microgels as shown in (a). With an increased amount of HAuCl<sub>4</sub> in (b), the number of microgels that contain one or multiple gold nanoparticles can be increased. Still, a high number of empty microgels can be found until the amount of HAuCl<sub>4</sub> is high enough so that multiple nanoparticles

are obtained in every (imaged) microgel shown in (c). Interestingly, the size of the formed gold nanoparticles is nearly independent of the amount of  $\text{HAuCl}_4$  used for the in situ synthesis, ranging from  $7 \pm 2$  nm to  $8 \pm 2$  nm.



**Figure S4.5:** Hydrodynamic diameter of  $\mu\text{gel-AAEM}$  in dependence of temperature as determined by DLS. The measurements were performed after the in situ synthesis with  $100 \mu\text{l}$   $\text{HAuCl}_4$  and purification. The solid red line corresponds to a Boltzmann fit which was applied to determine the VPTT of the microgel at  $25.6^\circ\text{C}$ .

In **Figure S4.3** we showed that  $\mu\text{gel-AAEM}$  aggregates upon exceeding a temperature of  $33^\circ\text{C}$ . The temperature-dependent determination of the hydrodynamic diameter via DLS presented in **Figure S4.5** highlights the increase in colloidal stability of  $\mu\text{gel-AAEM}$  after the in situ synthesis at high temperatures. The swelling profile corresponds to the microgel particles imaged by TEM shown in **Figure S4.4 (c)**. After the reduction of gold ions and possible reduction of functional groups, the obtained microgels exhibit a hydrodynamic diameter of  $296 \pm 5$  nm at  $20^\circ\text{C}$  in the swollen state. A hydrodynamic diameter of  $218 \pm 1$  nm at  $50^\circ\text{C}$  in the collapsed state leads to a calculated volume swelling ratio  $\beta$  of 2.5. Compared to the swelling profile prior to the in situ synthesis presented in **Figure S4.3**, the hydrodynamic diameter of the microgel after the in situ synthesis is decreased by about 60 nm in the swollen state at  $20^\circ\text{C}$  and about 40 nm at  $33^\circ\text{C}$ , respectively. Moreover, small error bars suggest a lower polydispersity compared to microgels prior to the in situ synthesis.

$\mu$ gel-AAEM-AAc

**Figure S4.6:** (a) Hydrodynamic diameter of  $\mu$ gel-AAEM-AAc<sub>12.5%</sub> in dependence of temperature as determined by DLS. The solid red line corresponds to a Boltzmann fit-function which was applied to determine the VPTT of the microgel at 25.1 °C. (b) Exemplary TEM image after the in situ synthesis and purification of  $\mu$ gel-AAEM-AAc<sub>12.5%</sub> where a single gold nanoparticle can be identified in every microgel.

To investigate the possible influence of higher contents of AAEM incorporated into the microgel network, we synthesized microgels with incorporated AAEM and 12.5 mol% of acrylic acid ( $\mu$ gel-AAEM-AAc<sub>12.5%</sub>). The synthesized microgels exhibit a volume swelling capacity  $\beta$  of 2.1. The corresponding swelling profile is presented in **Figure S4.6 (a)** where the microgel shows a hydrodynamic diameter of  $308 \pm 12$  nm in the swollen state at 20 °C and  $240 \pm 4$  nm in the collapsed state at 50 °C. Compared to  $\beta$  of 3.1 that was calculated for  $\mu$ gel-AAEM-AAc<sub>2.5%</sub> in the main manuscript, the lower volume swelling capacity is most likely based on the higher number of incorporated carboxylic acid groups (Determined zeta potential of -40 mV). Apart from the lower volume swelling capacity,  $\mu$ gel-AAEM-AAc<sub>12.5%</sub> shows almost identical properties to  $\mu$ gel-AAEM-AAc<sub>2.5%</sub> in respect to the effective size in the swollen state. Furthermore, TEM imaging presented in **Figure S4.6 (b)** reveal the formation of gold nanoparticles with a size  $D_{TEM}$  of  $9 \pm 1$  nm in every microgel. The determined size of the gold nanoparticles is in agreement with the results for the in situ synthesis with  $\mu$ gel-AAEM-AAc<sub>2.5%</sub> which are described in the main manuscript and gold nanoparticles with a size  $D_{TEM}$  of  $8 \pm 1$  nm were found. Thereby, we conclude that the outcome of the in situ synthesis is not affected by higher contents of AAEM for our investigated systems.

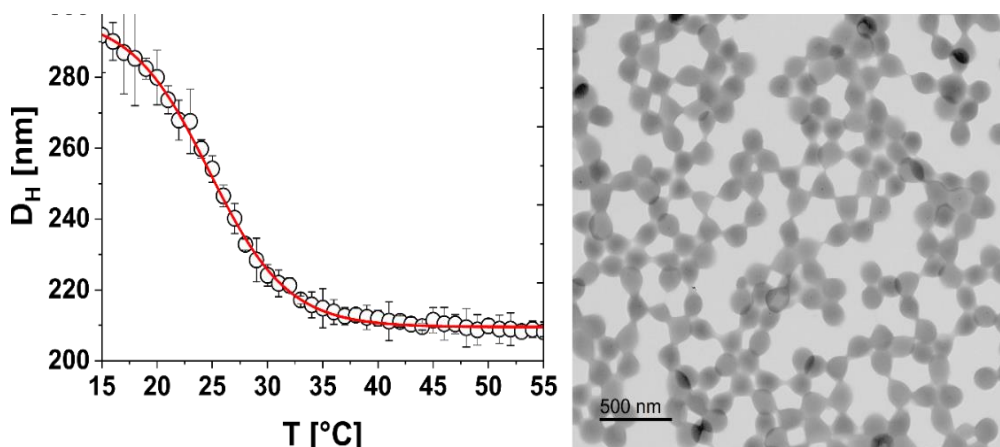


**Figure S4.7:** (a) Hydrodynamic diameter of  $\mu\text{gel-AAEM-AAc}_{0.5\%}$  in dependence of temperature as determined by DLS. The solid red line corresponds to a Boltzmann fit-function which was applied to determine the VPTT of the microgel at 24.7 °C. (b) Exemplary TEM image after the in situ synthesis and purification of  $\mu\text{gel-AAEM-AAc}_{0.5\%}$  where single gold nanoparticles can only be identified in few microgels.

Analogue to the experiments with higher contents of AAc presented in **Figure S4.6**, we verified if the in situ synthesis is effected when AAc contents lower than 2.5 mol% are incorporated into the microgels. The swelling profile for the microgel with 0.5 mol% of incorporated AAc ( $\mu\text{gel-AAEM-AAc}_{0.5\%}$ ) presented in **Figure S4.7 (a)** shows a swelling behaviour similar to  $\mu\text{gel-AAEM-AAc}_{2.5\%}$  and  $\mu\text{gel-AAEM-AAc}_{12.5\%}$  with a hydrodynamic diameter of  $280 \pm 8$  nm at 20 °C in the swollen state and  $210 \pm 8$  nm at 50 °C in the collapsed state. As a result, the swelling capacity  $\beta$  can be determined as 2.4. Surprisingly, measurements of the electrophoretic mobility (-33 mV) reveal that despite the small amount of AAc incorporated into the polymer network, the charge of the microgels is in the same order of magnitude as the microgels systems with larger amount of AAc incorporated. In **Figure S4.7 (b)**, we present an exemplary TEM image after the in situ synthesis. The formation of nanoparticles in less than 10% of the microgels can be observed. Therefore, we conclude that that the incorporated content of 0.5 mol% of AAc is insufficient for the successful in situ synthesis in every microgel and certain content of AAc in the microgels is necessary to allow for the controlled formation of the gold nanoparticles. The formation of gold nanoparticles in a few isolated microgels is likely based on the statistical incorporation of AAc monomer during the microgel synthesis. The findings are in good agreement with our findings for the in situ synthesis with  $\mu\text{gel-AAEM}$  where the microgels were synthesized without the addition of AAc. For both microgel systems, an uncontrolled, uneven outcome of the in situ synthesis can be observed whereby the amount of formed gold

nanoparticles could be adjusted for  $\mu\text{gel-AAEM}$  by using higher amounts of  $\text{HAuCl}_4$  (**Figure S4.4**).

In **Figure S4.8** we present TEM images for modified in situ synthesis experiment with  $\mu\text{gel-AAEM-AAc}_{2.5\%}$ . We observe the successful formation of single gold nanoparticles with a low polydispersity ( $D_{\text{TEM}} = 10 \pm 1 \text{ nm}$ ) inside each microgels and a neglectable number of nanoparticles outside of the microgels. In contrast to the synthesis described for  $\mu\text{gel-AAEM-AAc}_{2.5\%}$  in the main manuscript, microgels were centrifuged ten times after addition and stirring with  $\text{HAuCl}_4$  for one hour. After each step of centrifugation, the supernatant was removed and replaced to ensure the complete removal of  $\text{HAuCl}_4$  outside of the microgels. Despite adjustments to the synthesis protocol, the formed nanoparticles do not show a difference to the synthesis described in the main manuscript where the gold nanoparticles also exhibit a diameter  $D_{\text{TEM}}$  of  $10 \pm 1 \text{ nm}$ . Due to removal of the supernatant we cannot observe the formation of gold nanoparticles outside of the microgels. The experiment allows to localize the position of the reduction of gold ions within the microgels.

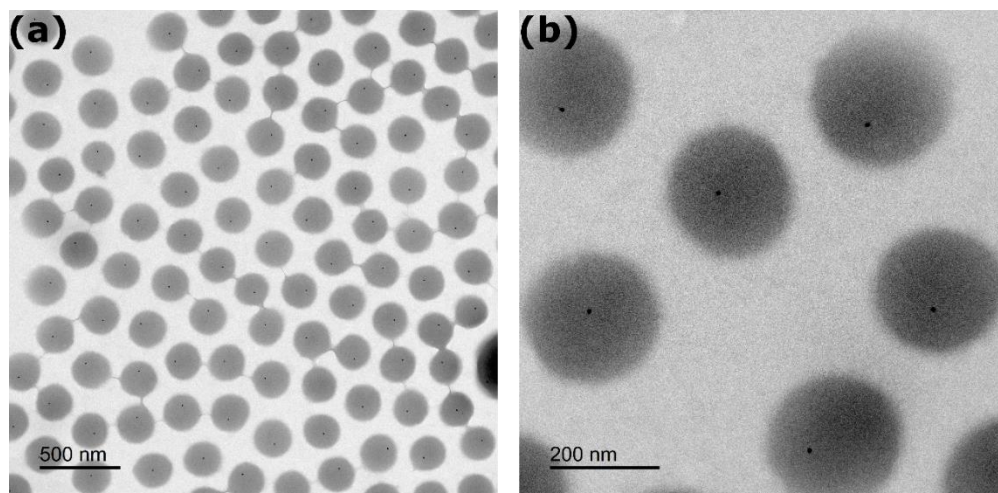


**Figure S4.8:** Exemplary TEM images after the modified in situ synthesis of gold nanoparticles in presence of  $\mu\text{gel-AAEM-AAc}_{2.5\%}$  at 20k magnification (**a**) and 50k magnification (**b**) prior to purification.

Further, we validated the time-scale on which the diffusion of gold inside the microgels and complexation take place. We performed a modified in situ synthesis experiment with  $\mu\text{gel-AAEM-AAc}_{2.5\%}$  where we initiated the reduction of gold ions already 60 seconds after the addition of  $\text{HAuCl}_4$  to the microgels. The corresponding TEM images in **Figure S4.9** reveal that the diffusion of a sufficient number of gold ions inside the

microgels is on a time-scale which takes longer than 60 seconds. Only about one third of the microgels contain a formed gold nanoparticle while the remaining microgels remain empty. The size and shape of formed nanoparticles do not differ from the regular synthesis with  $\mu\text{gel-AAEM-AAc}_{2.5\%}$  and  $\mu\text{gel-AAEM-AAc}_{12.5\%}$  and show a determined size  $D_{\text{TEM}}$  of  $9 \pm 1$  nm.

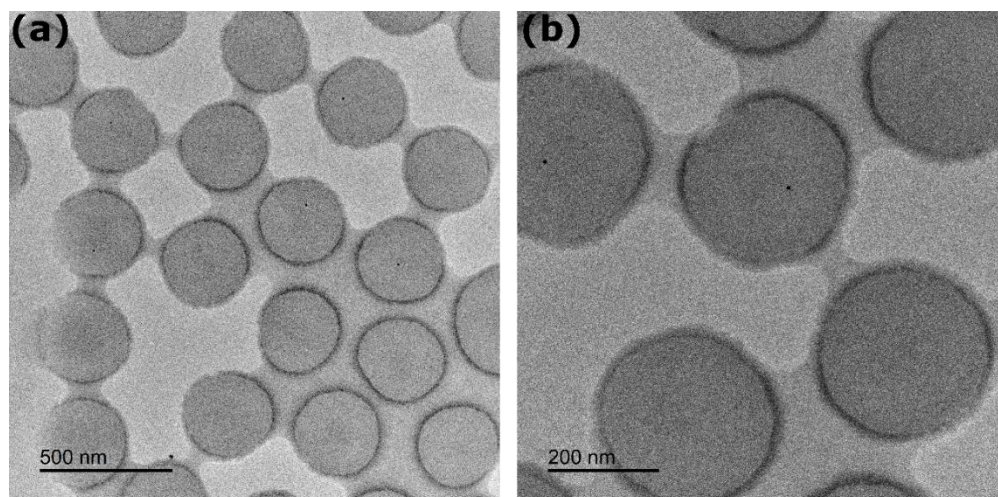


**Figure S4.9:** Exemplary TEM images after the modified in situ synthesis with and purification of  $\mu\text{gel-AAEM-AAc}_{2.5\%}$  at 20k magnification (a) and 50k magnification (b).

### One-Step Gold Overgrowth

**Figure S4.10** provides additional results for the surfactant-free overgrowth approach described in the main manuscript. In (a) we present a schematic representation of the proposed reaction mechanism for the one-step overgrowth of gold nanoparticles without addition of a surfactant. In the presented approach, gold (III) ions are first reduced by the weak reduction agent potassium thiocyanate to a state of gold (I) ions. The pre-reduced gold ions are then further reduced to elemental gold on the surface of the existing gold nanoparticles over a duration of multiple hours causing the noticeably growth in size. The exemplary TEM image in (b) shows that we could achieve a growth of all nanoparticles. Based on the TEM image we determined an increase in size  $D_{\text{TEM}}$  from  $10 \pm 1$  nm to  $83 \pm 13$  nm, in other words we could increase the average diameter of the cores by almost a factor of nine. At the same time, we can observe that the surfactant-free synthesis route favors the growth of non-uniform particles in size and shape. The uncontrolled nature of reaction is reflected by the color of the corresponding microgel dispersion shown in (c). Compared to the orange-brownish color of the dispersion of the surfactant-supported approach shown in the

main manuscript, the dispersion of the surfactant-free approach shows a dark red color. The corresponding UV-Vis absorbance spectrum shown in the main manuscript (**Figure 4.4 (a)**) exhibits a red shift of 18 nm compared to the spectrum for the surfactant-supported approach and a broader full width at half maximum, both caused by an overall larger size of grown gold nanoparticles and a higher number of particles that show a non-spherical morphology.<sup>81, 83, 188-5</sup>

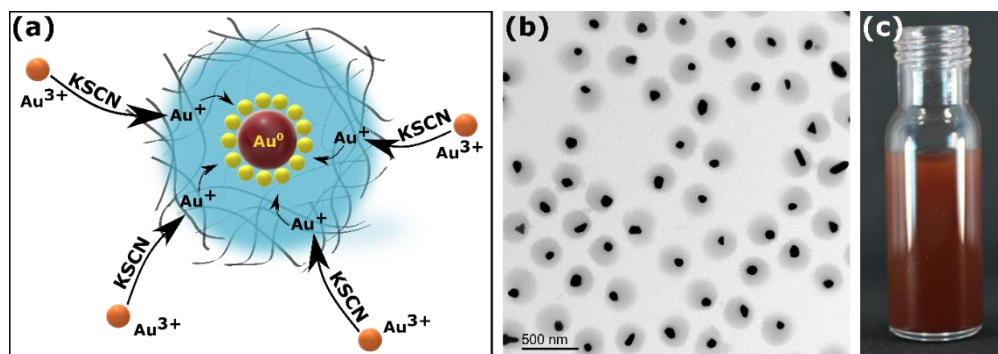


**Figure S4.10:** Summary for our findings for the surfactant-free gold nanoparticle overgrowth. **(a)** Schematic illustration of the postulated reaction mechanism for the overgrowth process. **(b)** Exemplary TEM image after the surfactant-free overgrowth of the gold nanoparticles in  $\mu\text{gel-AAEM-AAc}_{2.5\%}$  and a digital photograph of the corresponding microgel dispersion in **(c)**.

We summarized properties of all microgel systems prior to in situ syntheses (**Table S4.1**) and after in situ syntheses experiments (**Table S4.2**) including hydrodynamic diameter at 20 and 50 °C and VPTT determined by DLS, volume swelling ratios  $\beta$ , zeta potential and electrophoretic mobility measurements at 20 and 50 °C. In **Table S4.2**, we additionally present  $D_{\text{TEM}}$  of the gold nanoparticles formed during the in situ syntheses.

#### *Characterization via small-angle X-ray scattering (SAXS)*

Finally, in **Table S4.3 - S4.6** we present an overview of the fitting parameters that were applied to describe the scattering patterns that were recorded for selected microgel systems prior to the in situ syntheses, after the formation of gold nanoparticles and after the overgrowth of the gold nanoparticles.

**Table S4.1 :** Summary of determined  $D_H$  above and below the VPTT, VPTTs, volume de-swelling ratios  $\beta$ , zeta potential and electrophoretic mobility at 20 °C and 50 °C of all microgels discussed in this work.

Microgel	$D_H$ @ 20 °C [nm]	$D_H$ @ 50 °C [nm]	$\beta$	VPTT [°C]	Zetapotential @ 20 °C [mV]	Zetapotential @ 50 °C [mV]	Electrophoretic Mobility @ 20 °C [ $\mu\text{m}\cdot\text{cm}/\text{V}\cdot\text{s}$ ]	Electrophoretic Mobility @ 50 °C [ $\mu\text{m}\cdot\text{cm}/\text{V}\cdot\text{s}$ ]
$\mu\text{gel-PNIPAM}$	158 ± 1	111 ± 1	2.9	27.2	1 ± 1	-5 ± 1	0.1 ± 0.0	-0.1 ± 0.0
	228 ± 8	175 ± 7	2.2	27.9	-38 ± 1	-34 ± 1	-2.7 ± 0.0	-3.9 ± 0.1
$\mu\text{gel-AAEM-AAc}_{12.5\%}$	358 ± 11	aggreg.	-	23	-2 ± 1	-2 ± 1	-0.2 ± 0.0	-0.2 ± 0.0
	309 ± 2	213 ± 4	3.1	27.7	-39 ± 1	-30 ± 1	-2.8 ± 0.1	-3.3 ± 0.0
$\mu\text{gel-AAEM-AAc}_{12.5\%}$	308 ± 12	240 ± 4	2.1	25.2	-40 ± 1	-35 ± 1	-2.9 ± 0.1	-3.9 ± 0.0
	280 ± 8	210 ± 2	2.4	24.7	-33 ± 1	-24 ± 1	-2.3 ± 0.1	-2.8 ± 0.1

**Table S4.2:** Summary of determined  $D_H$  above and below the VPTT, VPTTs,  $D_{EM}$  of formed gold nanoparticles, zeta potential and electrophoretic mobility at 20 °C and 50 °C of all composite microgels discussed in this work.

Composite Microgel	$D_H$ @ 20 °C [nm]	$D_H$ @ 50 °C [nm]	VPTT [°C]	$D_{EM}$ (Au-Nanoparticle) [nm]	Zetapotential @ 20 °C [mV]	Zetapotential @ 50 °C [mV]	Electrophoretic Mobility @ 20 °C [ $\mu\text{m}\cdot\text{cm}/\text{V}\cdot\text{s}$ ]	Electrophoretic Mobility @ 50 °C [ $\mu\text{m}\cdot\text{cm}/\text{V}\cdot\text{s}$ ]
<i>μgel-AAEM In Situ 10 μl</i>	291 ± 2	235 ± 4	-	7 ± 2	-	-	-	-
<i>μgel-AAEM In Situ 50 μl</i>	346 ± 3	250 ± 8	-	8 ± 2	-	-	-	-
<i>μgel-AAEM In Situ 100 μl</i>	296 ± 5	218 ± 2	25.6	8 ± 2	-9 ± 1	0 ± 1	-0.6 ± 0.0	-0.1 ± 0.0
<i>μgel-AAEM-AAc<sub>2.5%</sub> - In Situ 10 μl</i>	390 ± 13	293 ± 3	36.2	10 ± 1	-30 ± 1	-28 ± 1	-2.1 ± 0.0	-3.1 ± 0.0
<i>μgel-AAEM-AAc<sub>2.5%</sub> - In Situ 50 μl</i>	333 ± 12	246 ± 8	-	14 ± 4	-	-	-	-
<i>μgel-AAEM-AAc<sub>2.5%</sub> - In Situ 100 μl</i>	312 ± 1	238 ± 8	-	14 ± 4	-	-	-	-
<i>μgel-AAEM-AAc<sub>2.5%</sub> - surfactant-free Overgrowth</i>	357 ± 12	210 ± 4	-	83 ± 13	-	-	-	-
<i>μgel-AAEM-AAc<sub>2.5%</sub> - surfactant-supported Overgrowth</i>	325 ± 7	278 ± 8	-	76 ± 9	-	-	-	-
<i>μgel-AAEM-AAc<sub>12.5%</sub> - In Situ 10 μl</i>	392 ± 22	346 ± 2	36.5	9 ± 1	-	-	-	-

**Table S4.3:** Fit parameters applied to describe the scattering profiles of microgels prior to in situ synthesis.

Composite Microgel	Model	Scale	BG [a.u.]	Porod Law Slope
<i>μ</i> gel-AAEM	Porod	$1.9 \cdot 10^{-10} \pm 1.5 \cdot 10^{-12}$	$8.8 \cdot 10^{-5} \pm 3.0 \cdot 10^{-6}$	4
	<i>μ</i> gel-AAc <sub>2.5%</sub>	$1.4 \cdot 10^{-10} \pm 1.6 \cdot 10^{-12}$	$1.6 \cdot 10^{-4} \pm 280 \cdot 10^{-6}$	4

**Table S4.4:** Fit parameters applied to describe the scattering profiles of microgels after the formation of gold nanoparticles via in situ synthesis using a combination of a porod function and a hard sphere model. For comparison we also included the diameter of the gold nanoparticles determined by TEM imaging.

Composite Microgel	Model	Scale	BG [a.u.]	D <sup>TEM</sup> (Au-Nanoparticle) [nm]	D <sup>SAXS</sup> (Au-Nanoparticle) [nm]	σ	SLD [ $10^{-6} \text{Å}^{-3}$ ]	SLD (Solvent) [ $10^{-6} \text{Å}^{-3}$ ]	Scale (Porod)
<i>μ</i> gel-AAEM In Situ 50 $\mu$ l	Hard Sphere + Porod	$1.1 \cdot 10^{-9} \pm 4.3 \cdot 10^{-11}$	$5.0 \cdot 10^{-5}$	$7.7 \pm 1.8$	$9.0 \pm 2.7$	0.30	124.7	9.5	$9.4 \cdot 10^{-11} \pm 12 \cdot 10^{-12}$
	Hard Sphere + Porod	$1.6 \cdot 10^{-8}$	$1.4 \cdot 10^{-4}$	$9.7 \pm 1.1$	$7.4 \pm 0.9$	0.12	124.7	9.5	$7.2 \cdot 10^{-11} \pm 1.3 \cdot 10^{-12}$

**Table S4.5:** Fit parameters applied to describe the scattering profiles of microgels after the formation of gold nanoparticles via in situ synthesis and overgrowth of the nanoparticles with a surfactant-supported approach using a hard sphere model. For comparison we also included the diameter of the gold nanoparticles determined by TEM imaging.

Composite Microgel	Model	Scale	BG [a.u.]	$D_{TEM}$ (Au-Nanoparticle) [nm]	$D_{SAXS}$ (Au-Nanoparticle) [nm]	$\sigma$	$\sigma$	SLD [ $10^{-6} \text{ \AA}^{-2}$ ]	SLD (Solvent) [ $10^{-6} \text{ \AA}^{-2}$ ]
<i>μ</i> gel-AAEM-AAc <sub>2.9%</sub> -surfactant-supported Overgrowth	Hard Sphere	$1.6 \cdot 10^{-8}$	$4.8 \cdot 10^5$	$76.4 \pm 9.1$	$70.0 \pm 11.9$	0.17	0.17	124.7	9.5

**Table S4.6** Fit parameters applied to describe the scattering profiles of microgels after the formation of gold nanoparticles via in situ synthesis with a high amount of HAuCl<sub>4</sub> using a combination of a porod function and a fractal model. For comparison we also included the diameter of the gold nanoparticles determined by TEM imaging.

Composite Microgel	Model	BG [a.u.]	Scale	$D_{TEM}$ (Au-Nanoparticle) [nm]	$D_{SAXS}$ (Au-Nanoparticle) [nm]	$\sigma$	SLD [ $10^{-6} \text{ \AA}^{-2}$ ]	SLD (Solvent) [ $10^{-6} \text{ \AA}^{-2}$ ]	Fractal dimension	Correlation Length [nm]
<i>μ</i> gel-AAEM In Situ 100 $\mu$ l	Fractal + Porod	$1.2 \cdot 10^{-4}$	$2.1 \cdot 10^{-7} \pm 1.3 \cdot 10^{-10}$	$7.1 \pm 1.8$	$12.2 \pm 2.5$	0.2	124.7	9.5	2.2	12.4

# **5. Following the volume phase transition of thermoresponsive microgels by dynamic light scattering and turbidity: Correlations depend on microgel homogeneity**

*Marius Otten,<sup>1</sup> Marco Hildebrandt,<sup>1</sup> Ben Pfeffing,<sup>1</sup> Victoria Voigt,<sup>1</sup> Thomas Hellweg<sup>2</sup>  
and Matthias Karg<sup>1,\*</sup>*

<sup>1</sup>Institut für Physikalische Chemie I: Kolloide und Nanooptik, Heinrich-Heine-Universität Düsseldorf, Universitätsstr. 1, 40225 Düsseldorf, Germany

<sup>2</sup>Institut für Physikalische und Biophysikalische Chemie, Universität Bielefeld, Universitätsstr. 25, 33615 Bielefeld, Germany

## **5.1 Abstract**

Thermoresponsive microgels undergo a temperature-induced volume phase transition that is typically scrutinized by dynamic light scattering focusing on the global changes in size via the diffusion coefficient. The resulting changes in structure on a local scale are typically addressed by much more complex and costly measurements using small-angle neutron scattering and/or X-ray scattering. In this work we study the volume phase transition of poly-*N*-isopropylacrylamide-based microgels by a combination of temperature-dependent dynamic light scattering and simple, fast and much more efficient absorbance measurements. Absorbances at fixed wavelength are used as direct measure for the dispersion turbidity. We link the obtained absolute changes in hydrodynamic radius to the absolute changes in turbidity. By doing so we compare “classical” PNIPAM microgels from precipitation polymerization, charged copolymer microgels from precipitation copolymerization as well as core-shell microgels from seeded precipitation polymerization. In total we systematically study and compare 30 different microgels. The direct comparison of data from dynamic light scattering and absorbance spectroscopy provides insights into structural homogeneity and deviation from the established fuzzy sphere morphology. We also demonstrate how turbidity data can be used to recalculate swelling curves.

## 5.2 Introduction

Microgels are three-dimensional, crosslinked polymer networks that exhibit unique properties between singular polymer chains and macroscopic gels. On the one hand, the character of the soft particles commonly in the nano- or micron sized regime provide colloidal stability and allow swelling in a good solvent while being not completely dissolvable and retaining a spherical shape. On the other hand, the properties of the individual polymer chains and monomers can be introduced to the microgel networks and therefore unfold a new playing-field with a vast number of possibilities including the tunability of external stimuli like temperature or pH responsiveness.<sup>1, 30, 159, 189, 190</sup> A common example for microgels with a temperature-dependent swelling behavior are polymer networks based on *N*-isopropylacrylamide (NIPAM).<sup>100, 191</sup> If incorporated into a microgel network, the microgel can undergo a phase transition at a certain temperature that causes a de-swelling of the microgel network. The temperature which is at about 32 °C for microgels based on NIPAM is known as volume phase transition temperature (VPTT).<sup>192</sup> The introduction of charges or other moieties with a pronounced hydrophobicity or hydrophilicity by incorporation of comonomers into the microgel network can then further alter the VPTT and the overall swelling behavior.<sup>11, 59, 193</sup> While copolymer microgel systems are interesting for a multitude of potential applications,<sup>160, 162</sup> many aspects about the distribution of the components within the microgel and the influence on the inner structure are still unknown. The characterization of microgels in terms of size and morphology can be realized by imaging techniques like electron<sup>-84, 180, 194-196</sup> or atomic force microscopy<sup>94, 99, 197-200</sup>. Recently, also super-resolution optical microscopy was used to image internal microgel structures with a spatial resolution of about 28 nm.<sup>77</sup> While a powerful tool, the downside of imaging techniques is that only a small fraction of a synthesized system can be analyzed at a time, resulting in an overall bad statistic and methods like e.g. dSTORM were only sparsely used up to now. The problem can be bypassed by using spectroscopy techniques. Dynamic light scattering (DLS) also known as photon correlation spectroscopy (PCS) is a well-established method to characterize the size of microgel systems in dispersion.<sup>65, 94, 99, 201</sup> The technique uses the time correlation of the fluctuation of scattered light intensity stemming from the random movement of the particles in the dispersion.<sup>202, 203</sup> Further a mathematical processing

of the recorded data is needed to calculate the size of the scattering particles of the system.<sup>204, 205</sup>

Another method for characterization is spectrophotometry which was already used in 1986 when Pelton and Chibante synthesized PNIPAM-based microgels for the first time.<sup>64</sup> By measuring the absorbance in dependence of the temperature (or in this case scattering cross-section as the measurements almost resemble the setup of a static light scattering experiment without the angle dependency), Pelton and Chibante found that absorbance increases with increasing temperature, especially around the VPTT of the microgel. From a scattering theory perspective this observation is counter-intuitive as the scattering of a spherical scattering object depends on the 6<sup>th</sup> power of the size.<sup>206</sup> The observable increase in the absorbance is justified by the network character of the microgels. Tadgell et al. recently found that the observed behavior is connected to the distinct change of the refractive index environment during the collapse of the microgel.<sup>207</sup> Thereby, the converge of chains within the microgel and the reduction of water in the microgel is potentially leading to an increase in absorbance. Almost 40 years ago, Pelton and Chibante thus were able to follow the relative swelling behavior of microgels in a similar way to temperature-dependent DLS measurements. Surprisingly, as UV-Vis absorbance measurements are a common method for characterization of linear temperature-responsive polymers,<sup>208</sup> the question arises why the use is rare for the characterization of microgels and if the method could possibly provide new insights into the properties of the systems.

Recently Ponomareva et al. showed a linear dependency when the normalized data of temperature-dependent absorbance measurements is plotted against normalized data of temperature-dependent dynamic light scattering measurements for core-shell microgels with a gold core.<sup>73</sup> The resulting linear dependency for systems with different core to shell ratios and crosslinker degrees of the PNIPAM shell clarify that the relative swelling behavior can be followed by dynamic light scattering or absorbance measurements almost interchangeable.

In this work we present new findings on the correlation between the data of absorbance and light scattering measurements for microgel systems. To get a deeper understanding, we synthesized 30 different microgel divided in three groups of microgels systems.

The analysis of our data revealed a different behavior for SiO<sub>2</sub>-core-shell microgels and PNIPAM microgels compared to copolymer microgels where we incorporated different comonomers into the microgel during the synthesis. While we found an almost perfect agreement of the relative swelling behavior detected by DLS and absorbance measurements for the former microgels independent of the degree of crosslinking or charge, we revealed a strong deviation of the relative swelling behavior between both techniques for all investigated copolymer microgels possibly based on differences in the internal structures and inhomogeneous distribution of comonomers within the microgel particles.

Additionally, we revealed that temperature dependent absorbance measurements can potentially be used to predict and validate results of dynamic light scattering measurements as they can be performed with a high output and also do not require any form of mathematical operation to process the data. The quality of the calculated data is drastically influenced by the agreement of the relative swelling behavior observed by DLS and absorbance measurements. Our findings are supported by temperature-dependent light scattering, temperature-dependent UV-Vis absorbance measurements and the determination of charge that is present in the microgel and on the surface of the particles via electrophoretic mobility measurements.

## 5.3 Experimental Section

### 5.3.1 Materials

Acrylic acid (AAc, Sigma Aldrich, 99 %), 2-Acrylamido-2-methyl-1-propanesulfonic acid (AMPS, Sigma Aldrich, 99%), (3-Acrylamidopropyl) trimethylammonium chloride (APTAC, 75 wt% in water, Sigma Aldrich), 2-vinylpyridine (2-VP, Sigma-Aldrich, 97%), potassium peroxydisulfate (KPS, Sigma Aldrich, ≥99%), 2,2'-Azobis(2-methylpropionamide) dihydrochloride (V50, Acros Organics, 98%), *N,N'*-methylenebisacrylamide (BIS, Sigma Aldrich, 99%), Tetraethyl orthosilicate (TEOS, Sigma Aldrich, 98%), cyclohexane (Fischer Scientific, analy. reag. grade), L-Arginine (PanReacAppliChem, ≥99%), 3-(Trimethoxysilyl) propyl methacrylate (MPS, Sigma Aldrich, 98%), sodium dodecyl sulfate (SDS, Sigma Aldrich, p.a.), sodium hydroxide

(NaOH, Fischer Scientific,  $\geq 99.9\%$ ), rhodamine b isothiocyanate (RITC, Sigma Aldrich, mixed isomers), ammonium hydroxide ( $\text{NH}_{3(\text{aq.})}$ , Sigma Aldrich, 30-33%) and ethanol (EtOH, Chemsolute,  $\geq 99.9\%$ ) were used as received. *N*-isopropylacrylamide (NIPAM; TCI, 98 %) was purified by recrystallization from cyclohexane. Water used for all syntheses and measurements was purified with a MilliQ system (Millipore). The final resistivity of the water was 18 M $\Omega$  cm.

### 5.3.2 Synthesis

#### *PNIPAM Microgels*

Microgels were prepared by free-radical precipitation polymerization. All batches were synthesized in a total volume of 100 ml using 250 ml three-necked flasks equipped with a reflux condenser and gas inlet. NIPAM (507 mg, 4.48 mmol) and the respective amount of crosslinker BIS were dissolved in 95 ml of water under stirring and heating to 70 °C. The solutions were purged with nitrogen for at least 30 min. During that time 25 mg (0.092 mmol) of the initiator was dissolved in 5 ml of water. We used KPS and V50 as initiators to obtain slightly anionic and cationic microgels, respectively. Additionally, we performed polymerizations with only 1 mg of KPS (0.003 mmol) to yield almost neutral microgels.

Each of the three microgel systems was synthesized with three different amounts of crosslinker of 0.99 mol%, 5.44 mol% and 16.31 mol% leading to a total of nine different batches of PNIPAM microgels. Each reaction was stirred for 4 h before the dispersions were allowed to cool to room temperature. Purification was performed by dialysis for 1 week. The dialysis bag had a molecular weight cut-off (MWCO) of 10000-20000 Da and the water was changed every 24 h. After dialysis we freeze-dried all microgel samples.

An overview of the PNIPAM microgels and all relevant masses and volumes is presented in **Table 5.1**. The description of the microgel batches is consisting of the different initiator and amount of initiator used for the initiation of the polymerization and the molar weight of the incorporated crosslinker BIS.

**Table 5.1:** Overview of synthesis parameters for PNIPAM microgels. The crosslinker content given in mol% refers to the amount of NIPAM monomer used and corresponds to the nominal value.

Microgel system	Crosslinker [mol%]	m(BIS) [mg] ( $\mu$ mol)	m(initiator) [mg] ( $\mu$ mol)	m(NIPAM) [mg] (mmol)
<i>KPS</i> <sub>25mg</sub> - 1.0	1.0	7 (5)	25 (92) - KPS	507 (4.48)
<i>KPS</i> <sub>25mg</sub> - 5.4	5.4	38 (244)	25 (92) - KPS	507 (4.48)
<i>KPS</i> <sub>25mg</sub> - 16.3	16.3	113 (732)	25 (92) - KPS	507 (4.48)
<i>KPS</i> <sub>1mg</sub> - 1.0	1.0	7 (5)	1 (3) - KPS	507 (4.48)
<i>KPS</i> <sub>1mg</sub> - 5.4	5.4	38 (244)	1 (3) - KPS	507 (4.48)
<i>KPS</i> <sub>1mg</sub> - 16.3	16.3	113 (732)	1 (3) - KPS	507 (4.48)
<i>V50</i> <sub>25mg</sub> - 1.0	1.0	7 (5)	25 (92) - V50	507 (4.48)
<i>V50</i> <sub>25mg</sub> - 5.4	5.4	38 (244)	25 (92) - V50	507 (4.48)
<i>V50</i> <sub>25mg</sub> - 16.3	16.3	113 (732)	25 (92) - V50	507 (4.48)

### Copolymer Microgels

Copolymer microgels have been synthesized mostly analogue to the synthesis protocol described for the PNIPAM microgels. In a 250 ml three-neck flask 251 mg (2.22 mmol) NIPAM and BIS were dissolved in 95 mL of water under stirring. Again, each of the following microgels was synthesized with three different amounts of crosslinker 0.99 mol%, 5.44 mol% and 16.31 mol% which equal 6.9 mg (0.0045 mmol), 37.6 mg (0.2439 mmol) and 112.8 mg (0.7317 mmol). After heating to 70 °C, the solution was purged with nitrogen for 30 min. Meanwhile, 2.5 mol% of the respective comonomer was dissolved in 13 mL of water. We used four different comonomers for our experiments: AAc, AMPS, 2-VP and APTAC. Combined with three different amounts of crosslinker results in a total of twelve copolymer microgels. The AMPS solution was neutralised by adding 1 equivalent of 1 M sodium hydroxide solution prior to further processing.

The polymerization was then initiated by either adding 2 mg of KPS or V50 diluted in water. For the negatively charged comonomers AAc and AMPS we used KPS while the reactions with the positively charged comonomers 2-VP and APTAC were initiated with V50. 10 min after the start of the polymerization which is indicated by an observable turbidity of the dispersion, the dissolved comonomer was added dropwise using a dropping funnel. The reaction was cooled down to room temperature after a reaction time of 4 h. The microgels were purified by dialysis against water for 1 week.

A molecular weight-cut off of 10000-20000 Da was used whereby the water was changed every 24 h. After dialysis also in the case of the copolymer microgels we freeze-dried all samples.

An overview of the PNIPAM microgels and all relevant masses and volumes is presented in **Table 5.2**. As all copolymer microgels are also based on the same amount of NIPAM as main monomer we simplified the description of the microgel systems by only indicating the incorporated comonomer with the respective molar weight used. The information of the incorporated comonomer in the name is followed by the crosslinker degree of the microgel network.

**Table 5.2:** Overview of synthesis parameters for copolymer microgels. The crosslinker content given in mol% refers to the amount of NIPAM monomer used and corresponds to the nominal value.

Microgel system	Crosslinker [mol%]	m(BIS) [mg] ( $\mu$ mol)	Comonomer [mol%]	m(NIPAM) [mg] (mmol)	m(initiator) [mg] ( $\mu$ mol)
AAC <sub>2.5mol%</sub> - 1.0	1.0	7 (5)	2.5 - AAC	251 (2.22)	2 (6)
AAC <sub>2.5mol%</sub> - 5.4	5.4	38 (244)	2.5 - AAC	251 (2.22)	2 (6)
AAC <sub>2.5mol%</sub> - 16.3	16.3	113 (732)	2.5 - AAC	251 (2.22)	2 (6)
AMPS <sub>2.5mol%</sub> - 1.0	1.0	7 (5)	2.5 - AMPS	251 (2.22)	2 (6)
AMPS <sub>2.5mol%</sub> - 5.4	5.4	38 (244)	2.5 - AMPS	251 (2.22)	2 (6)
AMPS <sub>2.5mol%</sub> - 16.3	16.3	113 (732)	2.5 - AMPS	251 (2.22)	2 (6)
APTAC <sub>2.5mol%</sub> - 1.0	1.0	7 (5)	2.5 - APTAC	251 (2.22)	2 (6)
APTAC <sub>2.5mol%</sub> - 5.4	5.4	38 (244)	2.5 - APTAC	251 (2.22)	2 (6)
APTAC <sub>2.5mol%</sub> - 16.3	16.3	113 (732)	2.5 - APTAC	251 (2.22)	2 (6)
2-VP <sub>2.5mol%</sub> - 1.0	1.0	7 (5)	2.5 - 2-VP	251 (2.22)	2 (6)
2-VP <sub>2.5mol%</sub> - 5.4	5.4	38 (244)	2.5 - 2-VP	251 (2.22)	2 (6)
2-VP <sub>2.5mol%</sub> - 16.3	16.3	113 (732)	2.5 - 2-VP	251 (2.22)	2 (6)

### *Core-Shell Microgels*

The inorganic silica cores in the core-shell microgels investigated in this work have been synthesized by two different routes to allow the formation of silica cores with different sizes.

The synthesis of the first type of silica cores is based on the amino acid L-arginine and adapted by Hartlen et al.<sup>209</sup> In a 100 mL three-neck flask 81.9 mg (0.47 mmol) were solved in 78 mL water under constant stirring at 60 °C. After 30 min of equilibration, the solution was overlaid with 4.05 mL cyclohexane follow by another 30 min of equilibration. To avoid mixing of the aqueous and organic phase, the stirring speed was significantly lowered and the flask was only heated up to the lower end of the phase boundary. After equilibration 4.95 mL (22.2 mM) TEOS were added and the reaction carried out for 72 h. During that time a turbidity of the aqueous phase could be observed due to scattering of the formed silica particles.

To enable the covalent binding of PNIPAM polymer chains to the silica particles to form core-shell particles, the surface of the silica particles was functionalized with MPS without prior purification. Therefore, the aqueous phase which contains the silica particles was removed and again overlaid with 9 mL of cyclohexane. After heating to 60 °C and equilibration under slow stirring for 30 min, 90 mL of MPS (372.7 nM) were added to the organic phase. The functionalization was finished after 24 h under permanent stirring at 60 °C. Afterwards the aqueous phase was separated. The functionalized silica particles were used without further purification after freeze-drying. The resulting silica cores exhibit a radius of  $18 \pm 2$  nm.

The second type of silica cores is based on the Stöber method.<sup>210</sup> Before the Stöber synthesis, the xanthene dye RITC was functionalised with APS to label the silica particles. APS was added dropwise to an RITC solution (10 mM) in ethanol and afterwards stirred in the dark for 2 h. The amount of APS corresponds to a 10-fold excess to ensure the covalent binding of all dye molecules. Afterwards the functionalised dye solution was diluted with ethanol by five times. The traceable fluorescence of the silica particles is not relevant for the experiments of this work and is therefore not further discussed.

For the synthesis of the silica particles, 10 mL of ammonium hydroxide solution (30-33 %) were added to 125 mL of EtOH and heated to 50°C in a 250 mL three-neck

flask equipped with a reflux condenser. After equilibration for 20 min, a mixture of 5 mL TEOS (0.02 mM) and 20 mL EtOH was heated to 50°C and rapidly added to the solution. As soon as the solution showed a slight turbidity, 2 mL of the diluted functionalized RITC solution was added dropwise. The solution was allowed to stir overnight and afterwards cooled to room temperature. The purification of the silica particles was realized by centrifugation at 2599 rcf for 90min and redispersed in ethanol. This process was repeated three times.

For further processing, the surface of the silica particles was functionalized with MPS. In a first step, the pH of the particle dispersion was adjusted to 9-10 by the addition of ammonium hydroxide solution (30-33 %). Then 62  $\mu$ L (260.9 nM) MPS were added to achieve a calculated surface density of 1 MPS molecule per 40  $\text{\AA}^2$  on the surface of the silica particles. The dispersion was stirred for 24 h and a solution of SDS in EtOH is added during cooling. The amount of SDS was adjusted to obtain a final concentration of 0.2 mM to stabilize the silica particles. The particles were again purified three times by centrifugation at rotation speeds of 2599 rcf for 90 min and each time redispersed in ethanol. The resulting silica cores exhibit a radius of  $53 \pm 3$  nm.

The encapsulation of the silica particles of both synthesis routes was performed by free-radical seeded precipitation polymerisation based on the same protocol. As the masses and volumes used for the encapsulation vary dependent on the batch of core-shell particles, an overview of all masses and volumes is presented in **Table 5.3**. The table is divided into two methods for the synthesis of the silica cores. For the overview of the different core-shell systems we choose a description including properties and molar masses for a better distinction. **C** (Core) and the subscript represent the determined radius of the silica core while **S** (Shell) and the subscript indicate the hydrodynamic radius of the overall core-shell microgel. The following number ranging from 2.5 to 15 shows the molar percentage of incorporated crosslinker BIS. For two of the microgel systems, AMPS was incorporated into the microgel shell as commoner which is shown including the molar percentage.

For the synthesis of the microgel shell, NIPAM, BIS and SDS were dissolved in water in a three-neck flask equipped with a reflux condenser and gas inlet. The mixture was heated to 70 °C and purged with nitrogen for 30 min. After equilibration, the respective volume or mass of MPS functionalized silica particle dispersion is added. The

dispersion was allowed to stir for another 30 min before the initiator KPS dissolved in water was added to start the polymerization. The reaction was carried out for 6 h and then the reaction mixture was cooled to room temperature. Purification was performed by centrifugation at 2599 rcf for 180 min and repeated three times. After dialysis we again freeze-dried all microgel samples.

5. Following the volume phase transition of thermoresponsive microgels by dynamic light scattering and turbidity: Correlations depend on microgel homogeneity

**Table 5.3:** Overview of synthesis parameters for core-shell microgels. The crosslinker content given in mol% refers to the amount of NIPAM monomer used and corresponds to the nominal value.

Microgel system	m(NIPAM) [mg] (mmol)	m/V (SiO <sub>2</sub> ) [mg/μL]	m(KPS) [mg] (μmol)	m(BIS) [mg] (mmol)	m(SDS) [mg] (μmol)	V(H <sub>2</sub> O) [mL]
C <sub>18</sub> S <sub>65</sub> -15 <sup>a</sup>	1500 (13.3)	100 mg	15 (18)	306 (2.0)	-	1500
C <sub>18</sub> S <sub>100</sub> -15	3050 (27.0)	136 mg	40 (140)	623 (4.0)	-	600
C <sub>18</sub> S <sub>155</sub> -15	4000 (35.4)	122 mg	100 (350)	817.4 (5.3)	-	600
C <sub>18</sub> S <sub>155</sub> -15-co-AMPS <sub>1mol%</sub>	4000 (35.4)	135 mg	100 (350)	817.4 (5.3)	-	600
C <sub>18</sub> S <sub>163</sub> -15-co-AMPS <sub>2.5mol%</sub>	4000 (35.4)	132 mg	100 (350)	817.4 (5.3)	-	600
C <sub>53</sub> S <sub>154</sub> -2.5 <sup>b</sup>	113 (1.0)	438 μl (0.125 μM)	2 (7)	4 (0.03)	1.4 (5.0)	20
C <sub>53</sub> S <sub>152</sub> -5	113 (1.0)	438 μl (0.125 μM)	2 (7)	8 (0.05)	1.4 (5.0)	20
C <sub>53</sub> S <sub>158</sub> -10	113 (1.0)	480 μl (0.125 μM)	2 (7)	15 (0.1)	1.4 (5.0)	20
C <sub>53</sub> S <sub>152</sub> -15	113 (1.0)	333 μl (0.125 μM)	2 (7)	23 (0.15)	1.4 (5.0)	20

<sup>a</sup>Cores labelled as C<sub>18</sub> were synthesized by the protocol of Hartlen et al.<sup>209</sup> <sup>b</sup>Cores labelled as C<sub>53</sub> were synthesized by the protocol of Stöber et al.<sup>210</sup>

### 5.3.3 Methods

Experimental details for all characterization techniques can be found in the **Supporting Information in Chapter 5.7**.

## 5.4 Results

We synthesized 30 different types of microgels which can be assigned to three general categories: 1) Microgels solely based on NIPAM and BIS (“classical” microgels), 2) PNIPAM-based copolymer microgels, and 3) core-shell microgels with silica nanoparticle cores and PNIPAM shells. For simplicity, these microgels will be referred to as “PNIPAM microgels”, “copolymer microgels” and “core-shell microgels” in the following. All of the different microgels were analyzed by temperature-dependent DLS and UV/vis absorbance spectroscopy. Motivated by the previous work of Ponomareva et al.<sup>73</sup>, we aimed to correlate the absolute changes in absorbance at a fixed wavelength, i.e. the turbidity, to the absolute change in hydrodynamic radius. To do so, data were recorded in a temperature range from 5 to 55 °C in steps of 1 °C.

### 5.4.1 PNIPAM microgels

We synthesized a total of nine PNIPAM microgels that differ in crosslinker content and amount and type of the used ionic radical initiator (KPS and V50). More details of the synthesis conditions can be found in **Table 5.1**. The measured electrophoretic mobilities summarized in **Figure S5.1 and S5.2** in the **Supporting Information** reveal a positive charge for the microgels synthesized with V50 and negative charges for the batches synthesized with KPS. Reducing the amount of KPS to 1 mg led to microgels with lower charges as expected. The results obtained from measurements at 50 °C revealed increased electrophoretic mobilities, roughly by a factor of two larger than at 20 °C for each microgel system.

**Figure 5.1** summarizes the results from DLS and absorbance measurements for the PNIPAM microgels synthesized with 5 mol% BIS and 25 mg of KPS as a representative system.

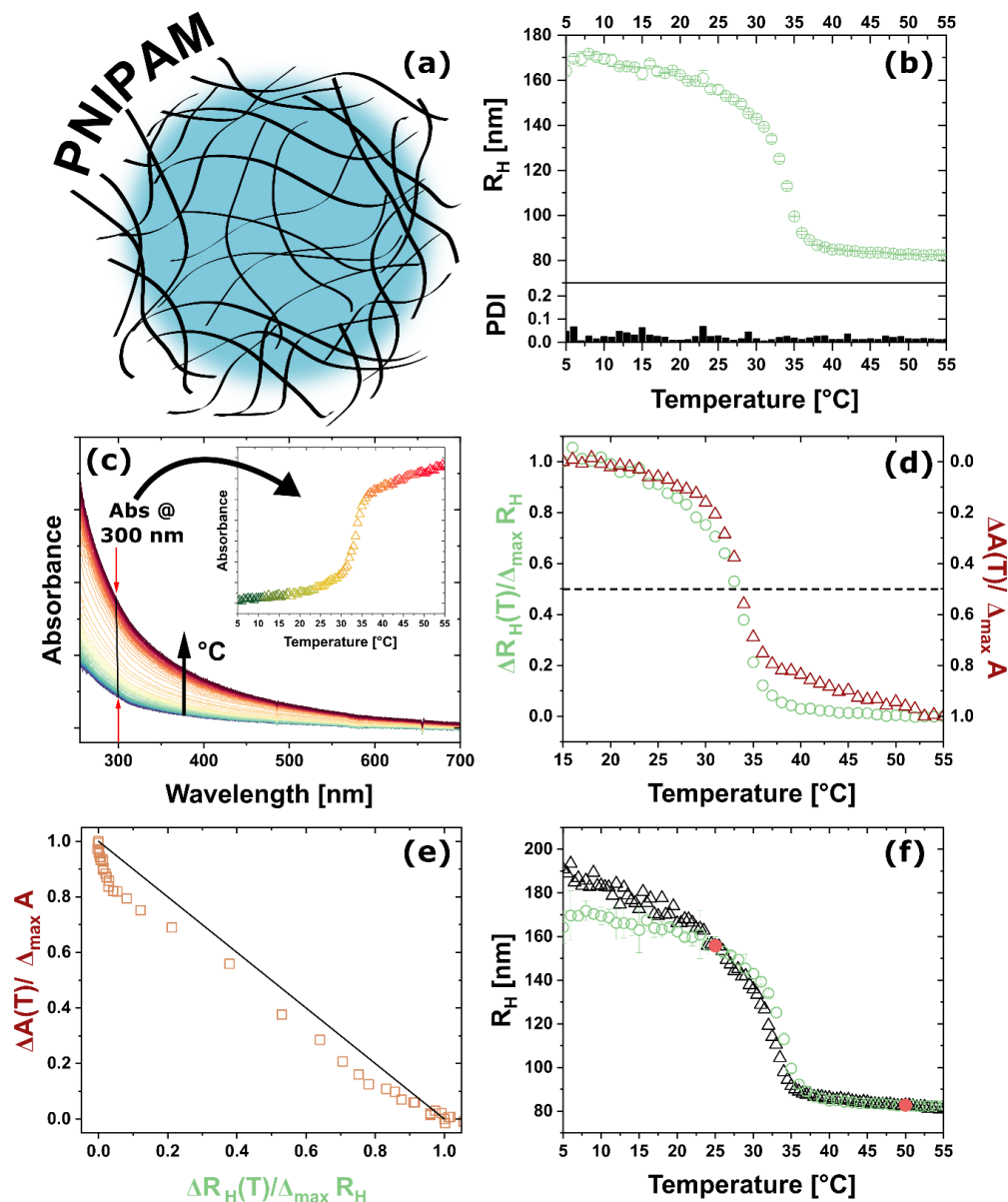


**Figure 5.1:** Overview of the characterization and processing of the measurement data for a PNIPAM microgel (5 mol% BIS, 25 mg KPS). **(a)** Schematical representation of the microgel swollen in water. **(b)** Hydrodynamic radii and polydispersity indices (PDI) from temperature-dependent DLS measurements. **(c)** Spectra from temperature-dependent UV-Vis absorbance measurements. The inset in **(c)** shows the plot of the absorbances measured at 300 nm against temperature. **(d)** Plot of the normalized data from **(b)** in green and **(c)** in red against temperature. **(e)** Plot of the normalized change in absorbance against the normalized change in hydrodynamic radii. The black line has a slope of -1 and corresponds to the dependence given in **Equation 5.3**. **(f)** Comparison of the DLS data (green) and the calculated hydrodynamic radii by use of the absorbance data (black). Red dots represent the reference points from DLS at 25 and 50 °C which are needed for the calculation.

**Figure 5.1 (a)** shows a schematic illustration of the PNIPAM microgel with the crosslinked polymer chains (black lines) and the high-water content schematically illustrated by the blue sphere. The swelling curve obtained from DLS shown in **Figure 1 (b)** reveals the typical VPT behavior of PNIPAM microgels with a VPTT of approximately 32 °C. The hydrodynamic radius decreases continuously starting from approximately 170 nm at 5-10 °C until reaching a plateau with values of approximately 82 nm for temperatures of 40 °C and higher. We want to highlight the differences between the collapsed and swollen state, where we observe a small but significant and almost linear decrease in radius between temperatures of 5 and 25 °C. In contrast, the radius remains almost constant for temperatures of 40 °C and higher (collapsed regime). The reported PDIs obtained from second order cumulant analysis are small ( $< 0.1$ ) and are slightly larger in the swollen than in the collapsed state. Similarly, the standard deviation in radius obtained from three individual measurements per temperature is slightly larger in the swollen state (error bars in green). Although these differences between swollen and collapsed state are small, they point to the better defined structure in the collapsed state where the microgels behave more closely to rigid and homogeneous spheres<sup>211</sup> and the less defined/more complex structure in the swollen state with a fuzzy sphere morphology<sup>69</sup> and dangling chains in the outer periphery.<sup>212</sup>

**Figure 5.1 (c)** shows absorbance spectra recorded in the same temperature range as the DLS data. All spectra reveal a continuous, power-law like decrease in absorbance with increasing wavelength that is related to light scattering from the (non-absorbing) microgels.<sup>73, 207</sup> With increasing temperature starting at 5 °C (blue), the scattering increases and the slope of the absorbance spectra changes. The change in scattering can be nicely quantified by plotting absorbances recorded at 300 nm as a function of temperature (inset of **Figure 5.1 (c)**). The data reveal a continuous increase in absorbance with increasing temperature. In other words, as the microgels shrink the turbidity of the dispersion increases. This, at a first glance counterintuitive observation, is related to the increasing polymer volume fraction and consequently increasing effective refractive index as well as to the transition from a fuzzy sphere morphology to collapsed spheres with a rather homogeneous polymer density and thus refractive index.<sup>73</sup> Similar to the DLS data we observe a sigmoidal-shaped transition with an inflection point at approximately 32 °C. In order to permit an easier

comparison of the DLS and turbidity data, we normalized both datasets according to **Equation 5.1 and 5.2**.

$$\frac{A(T) - A_{\text{swollen}}}{A_{\text{collapsed}} - A_{\text{swollen}}} = \frac{\Delta A(T)}{\Delta_{\text{max}}A} \quad (5.1)$$

$$\frac{R_H(T) - R_{H,\text{collapsed}}}{R_{H,\text{collapsed}} - R_{H,\text{swollen}}} = \frac{\Delta R_H(T)}{\Delta_{\text{max}}R_H} \quad (5.2)$$

For the swollen state we used absorbances ( $A_{\text{swollen}}$ ) and radii ( $R_{H,\text{swollen}}$ ) determined at 15 °C. The collapsed state values ( $A_{\text{collapsed}}$  and  $R_{H,\text{collapsed}}$ ) correspond to 50 °C. The values  $A(T)$  and  $R_H(T)$  correspond to the respective values of absorbance/radius at any given temperature  $T$  in between 15 °C and 50 °C. The resulting data is plotted in **Figure 5.1 (d)**. Please note that we inverted the y-axis for the reduced absorbance data to allow a direct comparison between both datasets. Both curves have a sigmoidal shape and overlap except for some slight deviation at temperatures right below the VPTT and some larger deviations just above the VPTT. Importantly, both curves reveal inflection points at very similar temperatures. In other words, the datasets from both measurements reveal nearly the same VPTT. By plotting the reduced absorbances (**Equation 5.1**) as a function of the reduced radii (**Equation 5.2**) we observe a linear relationship with a slope close to -1 in **Figure 5.1 (e)**. This is similar to the findings for gold-PNIPAM core-shell microgels reported in our earlier work.<sup>73</sup> However, for the PNIPAM microgels in this work, the data (orange symbols) lie below the solid black line that corresponds to:<sup>213</sup>

$$\frac{\Delta A(T)}{\Delta_{\text{max}}A} = 1 - \frac{\Delta R_H(T)}{\Delta_{\text{max}}R_H} \quad (5.3)$$

What we believe to be the origin of this deviation will be discussed later when we directly compare the findings for the different microgel systems. We now want to test whether the absorbance data can be used to calculate theoretical swelling curves, i.e., the temperature evolution of the hydrodynamic radii ( $R_{H,\text{calc}}(T)$ ). Therefore, we rewrite **Equation 5.3** to obtain:

$$\left[ \Delta_{\text{max}}R_H \cdot \left( 1 - \frac{\Delta A(T)}{\Delta_{\text{max}}A} \right) \right] + R_{H,\text{collapsed}} = R_{H,\text{calc}}(T) \quad (5.4)$$

The calculation of  $R_{H,calc}(T)$  requires two known reference points, i.e., the radii in the swollen and collapsed state that define  $\Delta_{max}R_H$ . We used different reference points including the previously used values corresponding to temperatures of 15 °C and 55 °C (see **Supporting Information, Figure S5.12**). Reasonably good agreement between calculated and measured radii was found when using 25 °C and 50 °C as the reference temperatures as shown in **Figure 5.1 (f)**. Here the green symbols correspond to the swelling curve measured by DLS and the black symbols correspond to the values of  $R_{H,calc}(T)$  calculated using radii measured at 25 and 50 °C indicated by the red circles. The calculated and the measured data match closely in the collapsed state for temperatures of approximately 37 °C and higher. In between the chosen reference temperatures, the calculated radii still match closely to the measured ones although the curve is shifted to slightly higher temperatures that also shifts the obtainable VPTT to a slightly higher value. Below 25 °C, i.e., in the swollen state, measured and calculated data deviate stronger with an increasing deviation for decreasing temperature. Similar data and calculations for all PNIPAM microgels can be found in **Figure S5.3 - S5.11** in the **Supporting Information** and relevant radii and VPT temperatures are summarized in **Table S5.1**.

We will now present the results obtained for copolymer microgels.

## 5.4.2 Copolymer Microgels

We synthesized a total of twelve PNIPAM-based microgels with different amounts of crosslinker and different comonomers. We chose four different comonomers: AAc, AMPS, APTAC and 2-VP. More details of the synthesis conditions can be found in **Table 5.2**. Negative charges are introduced by AAc and AMPS while APTAC and 2-VP provide positive charges. Measurements of the electrophoretic mobility that validate the incorporation of the comonomers into the microgel networks are presented in **Figure S5.13 and S5.14**.

As an example, for the analysis of the copolymer microgels we present the data of a PNIPAM-based microgel with 2.5 mol% of incorporated 2-VP monomer and a nominal crosslinker content of 15 mol% in **Figure 5.2** in a similar fashion as previously presented for the PNIPAM microgels (**Figure 5.1**). **Figure 5.2 (b)** compares the

reduced hydrodynamic radii with the reduced absorbances in dependence of temperature. While the reduced absorbances show the typical sigmoidal shape, the reduced radii profile is significantly shifted towards lower temperatures and also shows a more complex evolution. The transition temperatures that we determined from the first derivatives that are also shown in the graph reveals a difference of approximately 5 °C (transition at 32 °C from DLS and at 37 °C from absorbance). The differences in the evolution of both profiles becomes even clearer when plotting the reduced absorbances as a function of the reduced radii in **Figure 5.2 (c)**. Here the dashed area highlights the difference from the ideal linear behavior (solid black line).

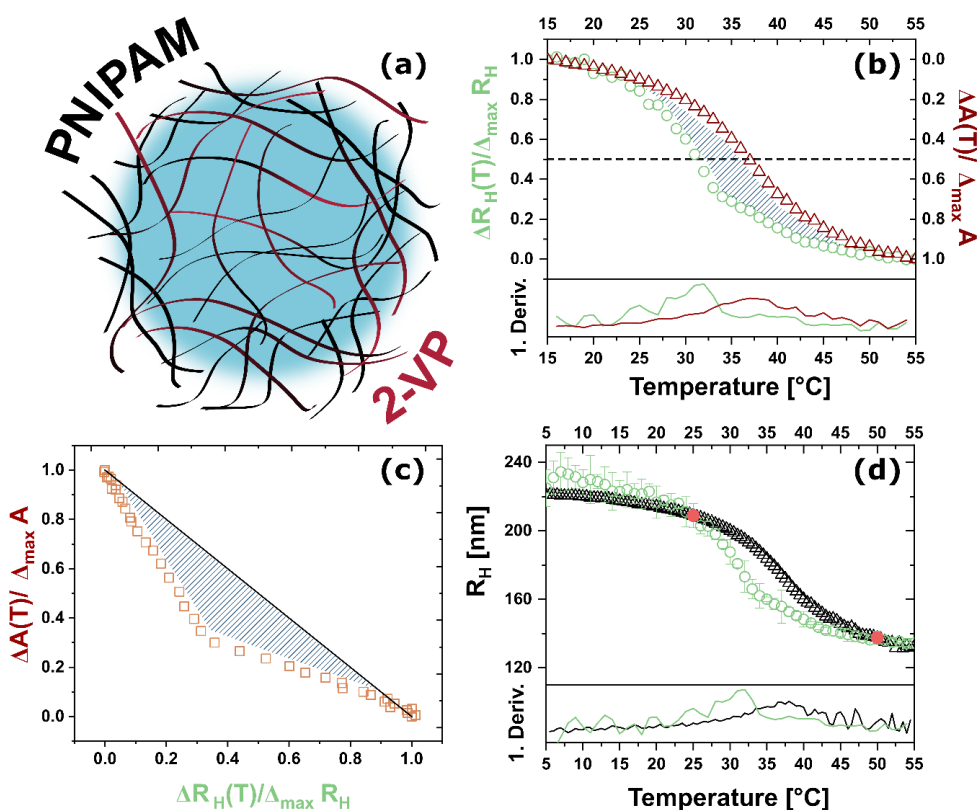


**Figure 5.2:** Overview of the processed data for a copolymer microgel based on PNIPAM, 2.5 mol% 2-VP added during the polymerization and crosslinked with 15 mol% BIS. The polymerization was initiated with 2 mg of KPS. **(a)** Schematic representation of the microgel swollen in water with 2-VP polymer chains implied in red. **(b)** Plot of the normalized hydrodynamic radii obtained from temperature-dependent DLS measurements (green) and temperature-dependent absorbance measurements (red) against temperature. Also shown are the first derivatives in the respective color. **(c)** Plot of the normalized absorbance against the normalized hydrodynamic radii. The black line indicates a slope of -1. **(d)** Comparison of the DLS initial data (green) and the calculated hydrodynamic radii by use of the absorbance data (black). Red dots represent the reference points from DLS at 25 °C and 50 °C which are needed for the calculation. Additionally presented is the first derivative of both functions in the respective color.

Due to the deviation also the measured and, based on the absorbance data, calculated hydrodynamic radii ( $R_{H,calc}(T)$ ) shown in **Figure 5.2 (d)** significantly deviate. Agreement between measured and calculated radii is only observed in the collapsed state, i.e., for temperatures of approximately 45 °C and higher. Thus, in the presented case, a reliable prediction of hydrodynamic radii on the basis of absorbance data is not possible for the copolymer microgel.

The complete data for all twelve copolymer microgels can be found in the **Supporting Information in Figure S5.15 - S5.26**. A summary including relevant radii and VPT temperatures can be found in **Table S5.2**.

We will now present the results for the core-shell microgels.

### 5.4.3 Core-shell microgels

In total we synthesized nine different core-shell microgels that contain silica cores and PNIPAM-based shells. The investigated systems include five microgel systems with a mean core radius of  $18 \pm 2$  nm, 15 mol% BIS and varying shell sizes leading to total hydrodynamic radii ranging from 65 nm to 163 nm. In addition, two of these systems contain 2.5 mol% of AMPS (nominal amount in the synthesis). The remaining four microgel systems contain cores with a mean radius of  $53 \pm 3$  nm and increasing crosslinker contents from 2.5 to 15 mol%. A summary of the synthesis conditions can be found in **Table 5.3**. Additional details on all investigated core-shell microgels can be found in **Figure S5.27 - S5.35** and **Table S5.3**.

In **Figure 5.3** we exemplary present the results for the core-shell microgels with a core radius of  $18 \pm 2$  nm, 2.5 mol% of AMPS and 15 mol% BIS.

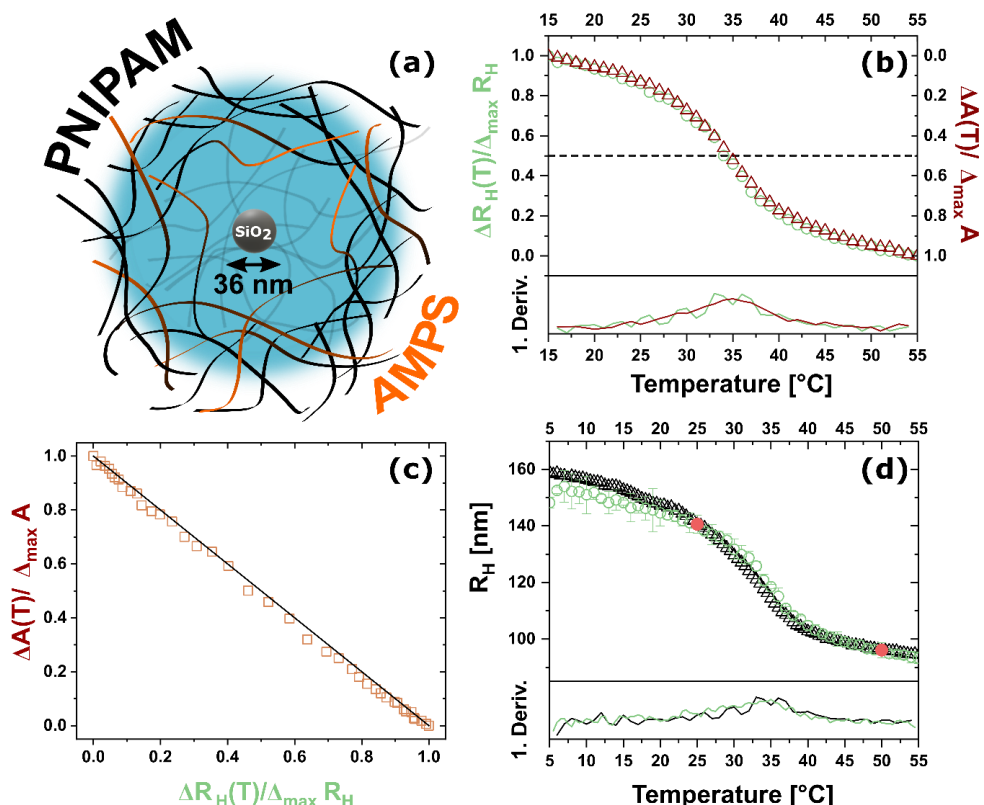


**Figure 5.3:** Overview of the processed data for an SiO<sub>2</sub>-core-shell microgel. The microgel shell is based on PNIPAM, 2.5 mol% AMPS added during the encapsulation and crosslinked with 15 mol% BIS. The polymerization was initiated with 100 mg of KPS. **(a)** Schematical representation of the microgel swollen in water with AMPS polymer chains implied in orange and the silica core in the center of the microgel in grey. **(b)** Plot of the normalized hydrodynamic radii obtained from temperature-dependent DLS measurements (green) and temperature-dependent absorbance measurements (red) against the temperature. Also shown are the first derivatives in the respective color. **(c)** Plot of the normalized absorbance against the normalized hydrodynamic radii. The black line indicates a slope of -1. **(d)** Comparison of the DLS initial data (green) and the calculated hydrodynamic radii by use of the absorbance data (black). Red dots represent the reference points from DLS at 25 °C and 50 °C which are needed for the calculation. Additionally presented is the first derivative of both functions in the respective color.

The schematic illustration of the microgel in **Figure 5.3 (a)** shows the silica core in the center of the microgel. **Figure 5.3 (b)** shows almost perfect overlap of the reduced hydrodynamic radii and reduced absorbance profiles. Both profiles show a sigmoidal shape with matching points of inflection, i.e., VPTTs. The derivatives that are also plotted in the graph reveal a VPTT of 35 °C. Furthermore, in **Figure 5.3 (c)** we see the perfect correlation between reduced hydrodynamic radii and reduced absorbances following the ideal linear behavior with a slope of -1. The agreement of the relative swelling behavior and the resulting linear behavior can eventually be used to calculate the hydrodynamic radii based on the absorbance values with almost perfect agreement in the temperature range between 25 °C and 50 °C in

(Figure 5.3 (d)). Only small deviations between calculated and measured hydrodynamic radii can be found at temperatures below 25 °C, which are nearly within the experimental errors.

In the following we will discuss the observations and trends for all 30 investigated microgel systems.

## 5.5 Discussion

Figure 5.4 summarizes the findings of all 30 microgel systems by plotting the reduced absorbances as a function of the reduced hydrodynamic radii for the three classes of microgels.

The three different types of symbols in each plot correspond to the different crosslinker contents: 1.0 mol% (circle), 5.4 mol% (square) and 16.3 mol% (triangle). Different colors represent different microgel systems (e.g., initiators, comonomers and core-shell ratio). We will only discuss the overall trends that are observable and not go into further detail with each individual sample so that the different symbols and colors only allow to differentiate between the large number of samples in each plot.

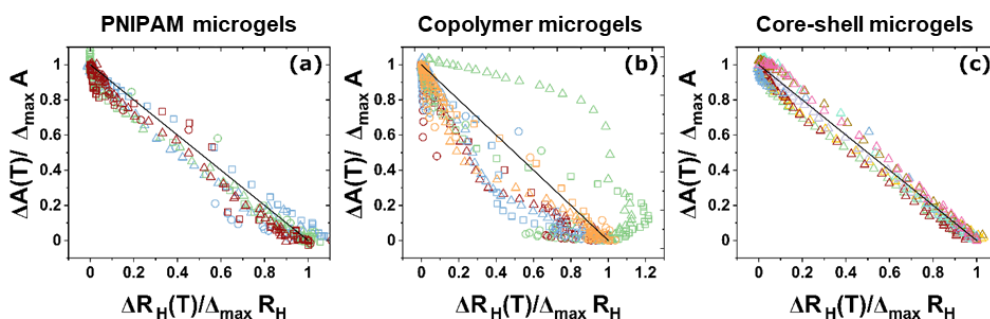


Figure 5.4: Direct comparison of all 30 microgels by plotting the reduced absorbances as a function of the reduced hydrodynamic radii. (a) PNIPAM microgels, (b) copolymer microgels, and (c) core-shell microgels. The solid black lines in each plot correspond to the linear behavior. Different symbols correspond to different amounts of crosslinker: 1.0 mol% (circles), 5.4 mol% (squares) and 16.3 mol% (triangles). Different colors represent different microgel systems e.g., comonomers and core to shell ratios but are only shown to distinguish different microgel systems in the plots.

Comparing the summarized data for the three types of microgel systems we can observe that all nine investigated PNIPAM microgels in Figure 5.4 (a) and all nine core-shell microgels in Figure 5.4 (c) show a linear correlation between the reduced absorbances and reduced hydrodynamic radii. The data scatter around the solid black

line that corresponds to the ideal linear behavior with a slope of -1 (see **Equation 5.3**). Overall, the core-shell microgels better follow the hypothetical linear behavior. The data of the PNIPAM microgels (**a**) scatter slightly more around the auxiliary line. Here, the deviations are strongest for samples with a low crosslinker degree (circles). Interestingly none of the copolymer microgels reveals such a linear correlation (**Figure 5.4 (c)**). For some samples, the data lie completely above and for some samples completely below the auxiliary line. Only in a few cases the data scatter around the solid black line. Obviously, the correlation between changes in hydrodynamic size and accompanied changes in turbidity depends strongly on the microgel composition and morphology. We want to highlight that all investigated microgels are strictly copolymers with a complex internal architecture. The PNIPAM microgels in (**a**) are copolymers of the main monomer NIPAM and the crosslinker BIS. Due to the different polymerization rates, these microgels show a pronounced fuzzy sphere morphology with an inner, higher crosslinked core region and an outer lower density shell that has a gradient in crosslinking.<sup>69</sup> This fuzzy sphere morphology is most pronounced in the swollen state and was found for microgels with medium (5.5 mol%) and low (1.4 mol%) crosslinker contents. Ponomareva et al. have recently shown that this fuzzy sphere morphology is also observed for core-shell microgels with relatively small gold nanoparticle cores.<sup>73</sup> It is worth to note that in this work, the gold cores were small enough that it can be assumed that these do not affect the swelling properties of the microgels. Microgels with different sizes and crosslinker contents spanning a broad range (5 – 25 mol%) were all described with the fuzzy sphere model in the swollen state. In this work two important findings were discussed: 1) The linear correlation between absolute changes in normalized absorbance and hydrodynamic radius that led to a master curve behavior for all studied microgels. 2) The increase in turbidity with increasing degree of microgel shrinking was attributed to the transition from fuzzy spheres with low/none scattering outer shells in the swollen state to more homogeneous spheres of higher effective refractive index in the collapsed state. The latter explanation was later confirmed by Tadgell et al. using recursive T-matrix Mie simulations.<sup>207</sup> It is worth to note that the gold cores in these works were too small to significantly scatter light. Thus, both measurements, DLS (at 632.8 nm) and turbidity (different wavelengths probed) were not affected by the presence of the cores.

The fuzzy sphere morphology of PNIPAM microgel shells was also found for silica-PNIPAM core-shell microgels with silica cores of significant size.<sup>214</sup> Due to the surface functionalization of the silica cores with covalently bound methacrylate groups prior to the seeded precipitation polymerization, these core-shell microgels are expected to have covalent bonds between the PNIPAM network shells and the silica cores. Our findings for the PNIPAM microgels and the variety of investigated core-shell microgels in **Figure 5.4 (a)** and **(c)** suggest that all of these microgels possess the typical fuzzy sphere like morphology with a transition to more homogeneous spheres with increasing degree of shrinking. The direct comparison also suggests that the core-shell microgels in **(c)** have slightly better-defined morphologies as these follows closer the expected ideal linear trend. In particular, when looking at the data for PNIPAM microgels in **(a)** we see that there is also a small influence of the crosslinker content. Microgels with higher crosslinker contents follow the ideal linear behavior better. This suggests that the fuzzy sphere morphology is less defined for lower crosslinker contents, which we attribute to the larger mesh sizes. We believe that the internal structure of the lower crosslinker microgels is more inhomogeneous as compared to higher crosslinked microgels.

We believe that the differences observed are related to differences of the internal structure, in particular the network homogeneity, and potentially also the polydispersity in size of the microgels. The extreme case is obviously presented by the studied copolymer microgels in **(b)** that contain charged comonomers in addition to NIPAM and BIS. We believe that these most likely contain local domains that differ in composition and therefore, show a more complex collapse mechanism than the classical fuzzy sphere microgels. For the PNIPAM microgels and also most of the studied core-shell microgels, the temperature-induced collapse is expected to start in the outer periphery where the PNIPAM chains possess the largest molecular weight. This is followed by collapse and rearrangements in the inner microgel region<sup>213</sup> that contains shorter PNIPAM chains. We want to highlight that a combination of small- and wide-angle X-ray scattering has also revealed a more complex collapse mechanism for uncrosslinked PNIPAM chains.<sup>215</sup> A correlation peak in the scattering profiles at high  $q$  that emerges during the collapse was attributed to the formation of microglobules. Results from an *in situ* high speed atomic force microscopy study indicate that such heterogeneities are also present in microgels. However, in that work, the presence of decanano-sized domains in the microgels was attributed to the

synthesis protocol.<sup>216</sup> In any case, those domains would be too small to affect the absorbance profiles that we use in this work to probe the turbidity changes of the microgels during collapse. Here, the effective refractive index and its radial profile are relevant rather than differences on the nanometer-scale. Now, in case of the copolymer microgels in **(b)** the collapse of the chain segments inside the microgels does not only depend on the chain length but also on the composition. It is known from literature that the introduction of charged comonomers like acrylic acid strongly affects the volume phase transition behavior of PNIPAM-based microgels.<sup>11</sup> Furthermore, due to the differences in polymerization rates, such copolymer microgels are expected to show an even more complex internal structure. A recent study by Wiehemeier et al. showed that the global collapse of copolymer microgels as typically followed by DLS is rather unrelated to the local collapse within the microgels.<sup>217</sup> DLS might even show no collapse at all despite of the presence of a local microphase separation which can be revealed by molecular level probes.

To summarize we believe that whether or not thermoresponsive microgels show a linear correlation between absolute changes in normalized turbidity and absolute changes in normalized hydrodynamic radius is related to the fuzzy sphere morphology, the homogeneity of the fuzzy spheres and also the overall size polydispersity of the microgels. For “ideal” fuzzy spheres we expect that the degree of reduction in hydrodynamic radius is directly proportional to the changes in turbidity. Core-shell microgels fulfill this direct correlation the best indicating that their microgel structure shows the smallest degree of local heterogeneities. Their microgel shell match nicely to the fuzzy sphere model. Surprisingly, this is the case over a broad range of crosslinker contents and also when additional comonomers are used. Similarly, this is the case for “classical” microgels although the precipitation polymerization leads to somewhat more pronounced local heterogeneities.<sup>216</sup> In contrast, the collapse behavior of “classical” PNIPAM microgels show a more pronounced dependence of the crosslinker content, indicating that with increasing crosslinking the microgels match better to the fuzzy sphere model. The introduction of different comonomers however, completely alters the global volume phase transitions behavior. We claim that there is a significant difference in local microgel structure based on the synthesis protocol: classical precipitation polymerization, precipitation polymerization in presence of additional comonomers, and seeded precipitation polymerization.

## 5.6 Conclusion

We systematically studied 30 different types of microgels focusing on temperature-dependent absorbance as well as dynamic light scattering measurements. In particular we compared the temperature trends of the hydrodynamic radii and absorbances at fixed wavelength that are a direct measure of the dispersion turbidity. The thermoresponsive microgels under investigation are all PNIPAM-based and comprise “classical” PNIPAM microgels that were synthesized by free radical precipitation polymerization of NIPAM in presence of the crosslinker *N,N*-methylenebisacrylamide. Furthermore, we studied copolymer microgels that were synthesized by precipitation polymerization in presence of different charged comonomers. Lastly, we studied core-shell microgels that were synthesized by seeded precipitation polymerization and that differ vastly in composition and morphology.

Except for the charged copolymer microgels, we found a linear correlation between absolute changes in normalized absorbance and absolute changes in normalized hydrodynamic radius. When plotting both quantities against each other revealed data collapsed on a master curve (slope of -1). In other words, changes in hydrodynamic radius translate directly to changes in absorbance when data are normalized to the maximum changes between the swollen and collapsed state. This correlation is slightly better fulfilled for the core-shell microgels than for the “classical” PNIPAM microgels, in particular for low crosslinker contents. The charged copolymer microgels show a completely uncorrelated behavior. Here, the prediction/recalculation of the swelling curve, i.e., the temperature evolution of the hydrodynamic radius, based on simple and fast absorbance measurements is not possible. We attribute the deviations from the linear correlation between absorbances and hydrodynamic size to heterogeneities that impact the global and local microgel collapse and also to the overall polydispersity of the microgels. While DLS only follows the volume phase transition globally via changes of the diffusion coefficient that are then used to compute the hydrodynamic size, the turbidity changes during the phase transition depend on changes of the total microgel volume, changes of the internal polymer and thus refractive index profile, as well as the local and global refractive index contrast with respect to the aqueous environment. The strongest support for these differences and the role of structural homogeneity was identified through the pronounced

difference between the volume phase transition temperature determined from DLS and that obtained from the absorbance measurements in case of the charged copolymer microgels. Contrary, where we found the best agreement between the phase transition temperatures, that is the case for core-shell microgels and some of the “classical” PNIPAM microgels, we could calculate theoretical swelling curves based on the temperature-dependent absorbances using only two reference points for the hydrodynamic radius. We believe that such a correlation will be very helpful for future studies, for example on large microgels and core-shell microgels<sup>218</sup> where the influence of gravitation might already hamper DLS measurements. In addition, absorbance measurements are fast, simple, do not require any data treatment other than proper background correction and can be performed in parallel using temperature-controlled sample changers. In our case we could measure seven samples in parallel using affordable standard spectrometer setups. Surprisingly the value of such simple measurements and the extraction of turbidity profiles for the study of the volume phase transition of microgels has mostly been overlooked in the past.

Our results suggest that the combination of DLS and absorbance measurements allow to gain deeper insights into structural homogeneity and potential differences between the global volume phase transition and local structural changes. The systematic comparison between the different microgels point to strong differences in internal structure and composition depending on the polymerization technique. According to this, single batch precipitation copolymerization using charged comonomers leads to the most heterogeneous microgels that deviate the most from the established fuzzy sphere picture. Contrary, seeded precipitation polymerization in the presence of methacrylate-surface-functionalized silica nanoparticles leads to core-shell microgels where the shells fit best to the fuzzy sphere model.

Future studies should focus on a better understanding of the inner structure and composition of the complex microgels accompanied by temperature-dependent form factor analysis. Ideally temperature-jump experiments that allow following time-dependent changes in turbidity<sup>213</sup> are combined with *in situ* temperature-jump experiments using synchrotron small-angle X-ray scattering.

### *Acknowledgments*

M.K. acknowledges the Deutsche Forschungsgemeinschaft (DFG) for funding through grant no. KA3880/6-1. The authors thank Yichu Zhou, Duong Pham Thuy and Julia Fink for synthesis and supply of the core-shell microgels. M.K. would like to acknowledge Frank Scheffold (University of Fribourg, Switzerland) for fruitful discussions at the Kavli Institute for Theoretical Physics (KITP), Santa Barbara (USA) during the “Nanoparticle Assemblies: A New Form of Matter with Classical Structure and Quantum Function” program. This research was supported in part by the National Science Foundation under Grant No. NSF PHY-1748958.

## 5.7 Supporting Information

### METHODS

#### **Temperature-dependent Ultraviolet-visible (UV-Vis) absorbance spectroscopy.**

Absorbance spectra were recorded using a Specord® S600 (Analytic Jena AG) spectrophotometer. The spectrometer is equipped with an 8-fold cuvette holder and a peltier cooler unit which allowed for a temperature control with an accuracy of  $\pm 0.1$  °C and a possible temperature range reaching from -5 to +105 °C at 25°C ambient temperature. The particles in dispersion were measured in PMMA cuvettes with a light path of  $d = 1$  cm. For every measurement a reference spectrum in water was recorded and subtracted. Another position in the 8-fold holder was used for a cuvette sensing probe in water to allow for accurate control of the temperature in all cuvettes. Measurements were performed in the wavelength range of 182 to 1019 nm at temperatures between 5 and 55 °C in steps of 1°C whereby the samples equilibrated for 10 minutes at each temperature before the respective measurement. Measured particle dispersions were diluted in water to a concentration of 0.02 wt%.

**Temperature-dependent dynamic light scattering (DLS).** DLS experiments were performed using a Zetasizer Nano S (Malvern Panalytical) to determine Hydrodynamic radii  $R_H$  of the microgel systems. The device detects scattered light at a scattering angle of 173°. We measurements in a temperature range of 15 and 55 °C in steps of  $1\pm 0.1$  °C. Samples equilibrated for 10 minutes at each temperature before the respective measurement and we performed three measurements with an acquisition time of 60 s for each temperature. All samples were diluted to a concentration of 0.02 wt% and were measured in semimicro PMMA cuvettes. Particle sizes were calculated by means of the three measurements. Presented error bars are given by the standard deviation of the measurements of the hydrodynamic diameter. The polydispersity index is an indication of the overall distribution of the determined size, assuming a single mean and is calculated by the cumulant analysis performed by the Malvern Panalytical measurement software.

**Electrophoretic light scattering (ELS).** Electrophoretic mobility of the particle systems was determined using a Zetasizer Nano ZS (Malvern Panalytical). Samples were diluted to 0.02 wt% and measured in Folded Capillary Cells (DTS 1070, Malvern Panalytical). For all samples, we performed measurements at 20 °C and 50 °C with equilibration times of 600 seconds. Each measurement was repeated three times.

## RESULTS AND DISCUSSION

### *PNIPAM Microgels*

In **Figure S5.1 and S5.2** we present the results for the measurements of the electrophoretic mobility for all nine investigated PNIPAM microgels at 20 °C and 50 °C respectively. The colored bars represent the three different amounts of crosslinker that were used for the different syntheses of the PNIPAM microgels. With our measurements we validate the synthesis of negatively charged microgels by using a larger amount of the initiator KPS (25 mg), positively charged microgels by using the initiator V50 and low charged (neutral) microgels by using the least amount of KPS (1mg) to initiate the polymerization. The measurements for polymerizations initiated with KPS show a negative electrophoretic mobility whereby microgels initiated with 25 mg KPS show higher values reaching from -2 to -4 depending on the temperature. In contrast, V50 initiated microgels show a positive electrophoretic mobility between 0.75 and 1.75 at 20 °C and between 3 and 3.75 at 50 °C.

Two trends for the measurements could be identified. Overall, the electrophoretic mobility increases for all PNIPAM microgels at temperatures of 50 °C above the VPTT compared to the measurements at 20 °C below the VPTT. The observation can be explained with collapse of the microgel so that the polymer chains converge on a smaller volume which leads to an increase of the charge density. The collapse also causes the microgel to show a more hard-sphere-like character that also has an influence on the measurement.

For the measurements at 20 °C a trend can observe where microgels with a higher crosslinker degree of 5.44 mol% (yellow) and 16.31 mol% (blue) show a noticeable higher electrophoretic mobility compared to the measurements of the PNIPAM microgels with a low crosslinker degree of 0.99 mol% (red). This trend cannot be found

at 50 °C. Again, the observation is based on the collapsed state of the microgel particles at high temperatures but also the degree of crosslinker. With a higher degree of crosslinking, the microgel network is more rigid and the character of a fuzzy sphere with a large amount of polymer chains with higher mobility is decreased. Therefore, a higher degree of crosslinking is increasing the density of charge and thus the electrophoretic mobility. At higher temperatures the degree of crosslinker has less influence on the electrophoretic mobility as the microgel is present in a collapsed state.

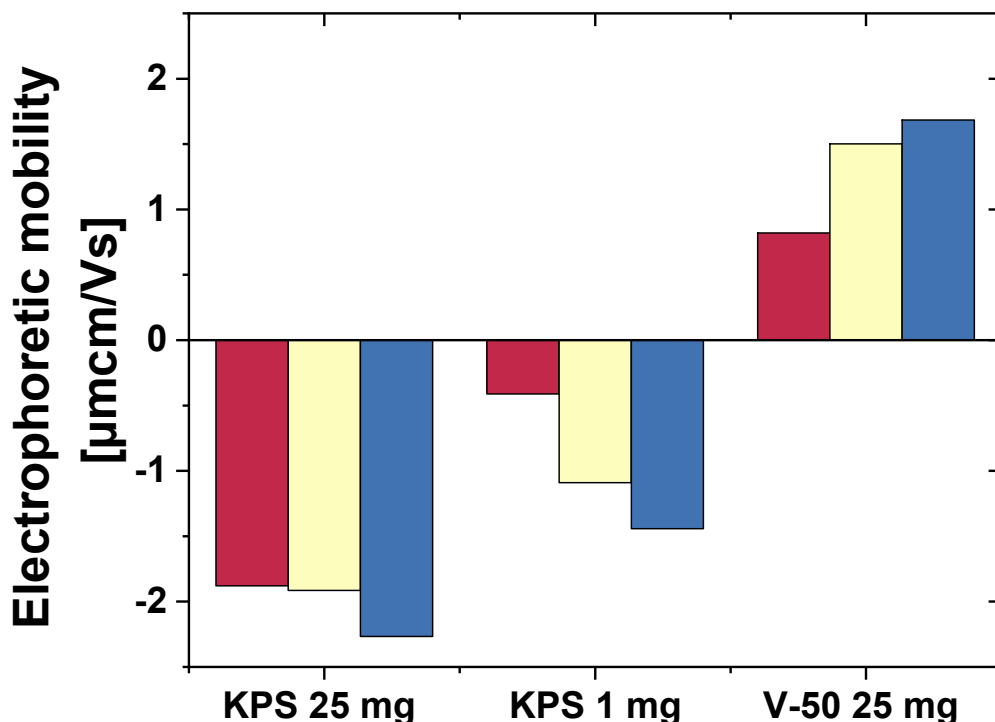


**Figure S5.1:** Overview of the electrophoretic mobility measurements at 20 °C for all PNIPAM microgels synthesized in this work. The color of the bars represents the respective crosslinking degree of the PNIPAM microgel. Microgels with 0.99 mol% BIS (red), 5.44 mol% (yellow) and 16.31 mol% (blue) have been investigated.

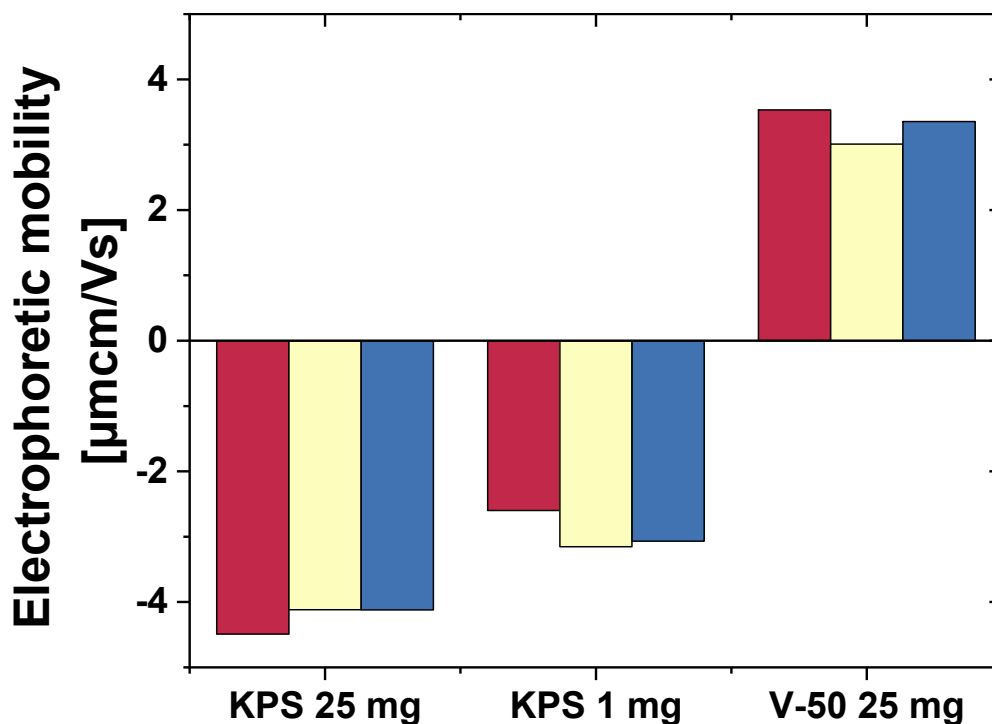


**Figure S5.2:** Overview of the electrophoretic mobility measurements at 50 °C for all PNIPAM microgels synthesized in this work. The color of the bars represents the respective crosslinking degree of the PNIPAM microgel. Microgels with 0.99 mol% BIS (red), 5.44 mol% (yellow) and 16.31 mol% (blue) have been investigated.

As part of the **Supporting Information**, we present measured and processed data for all 30 microgel systems in this work. (PNIPAM microgels in **Figure S5.3 - S5.11**, copolymer microgels in **Figure S5.15 - S5.26**, SiO<sub>2</sub>-core-shell microgels in **Figure S5.27 - S5.36**) The presentation of data is the same for all systems and also very similar to the presentation of data in the main manuscript. In the following, we will discuss one exemplary microgel system to further clarify all contents and features that can be found in the figures for all 30 systems. Additionally, we summarized properties of the microgel systems including VPTT determined by DLS and absorbance measurements, hydrodynamic radii at 25 and 50 °C and important components of the systems in **Table S5.1** (PNIPAM microgels), **Table S5.2** (copolymer microgels) and **Table S5.3** (Core-shell microgels with SiO<sub>2</sub> cores).

In **Figure S5.3** the data for a PNIPAM microgel with a crosslinker content of 0.99 mol% BIS is presented. The polymerization during the microgel synthesis was initiated with 1 mg (0.08 mol%) KPS. In **(a)** the hydrodynamic radii are plotted against the temperature. The microgel systems shows the expected temperature-dependent

swelling behavior with a VPTT at 32 °C. The transition in size is very distinct around the VPTT which is based on the loose crosslinking of the polymer network. Also due to the low degree of crosslinking, we can observe the overall large absolute change in size from a hydrodynamic radius of around 400 nm at 5 °C to 150 nm at 55 °C. The error bars for each determined hydrodynamic radius are given by the mean of the standard deviation for the three measurements performed at the respective temperature. We also present the polydispersity index calculated at each temperature below the swelling curve which is given by the cumulant analysis performed by the Malvern Panalytical measuring software. We found that microgels with a low amount of crosslinker tend to have a higher polydispersity and larger error bars at temperatures below the VPTT which is based on the more diffusive character of the particles at these temperatures.

The recorded absorbance values are plotted against the wavelength in **(b)**. The colored lines represent the measurements in dependence of the temperature from 5 to 55 °C in steps of 1 °C. The color gradient from blue to red hereby represent the increasing temperature from cold (blue) to hot (red). In agreement with the sharp transition observed for the DLS measurements in **(a)**, we observe a high density of functions at high and low temperatures but only scattered function at temperatures around the VPTT (yellow). This is further validated by the inset where the absorbance values at 300 nm are plotted against the respective temperature. We can observe a temperature-dependent behavior which appears similar to the swelling behavior of the DLS data. A detailed discussion of the relation can be found in the main manuscript.

**Figure S3 (c) and (d)** show the plot of the normalized data from DLS (green) and absorbance (red) measurements against the respective temperature. For a simplified comparison we inverted the y-axis for the absorbance (red) in **(d)**. Thereby, both functions show the same temperature-dependent behavior. The plots are supported by the first derivative below the functions whereby the maximum of the first derivative equate to the VPTT of the respective measurement technique. It can be observed that the normalized DLS and absorbance data are in good agreement for low temperatures at 5 °C and high temperatures at 55 °C and exactly at the VPTT at 32.5 °C. In contrast, we found deviations at temperatures shortly before and after the VPTT.

In a next step the normalized absorbance data is plotted against the normalized hydrodynamic radii in **(e)**. The solid black auxiliary line possesses a slope of -1.

The plot is a measure for the match of the swelling behavior for both measurement techniques. We observe distinct deviations from the auxiliary line for some data points which is in good agreement with our observations in **(d)**.

Finally, the plot in **(f)** compares the initially measured DLS data (green) with calculated hydrodynamic radii by the use of data from the absorbance measurements (red). The two red points at 25 and 50 °C represent two reference points that are also needed for the calculation. Also presented are the first derivatives of the functions in the respective color which allow for the determination of the VPTT. As the match of the data from DLS and absorbance measurements clarified by the plot in **(e)** play an important role for the result of the calculation of the hydrodynamic radii, we can observe that the deviations in **(e)** also lead to deviations between the calculated and initial data for the hydrodynamic radii especially shortly below and above the VPTT but also for very low temperatures between 5 and 20 °C. Despite the deviations the trend of the swelling behavior and the overall size range can be successfully modeled using the absorbance data.

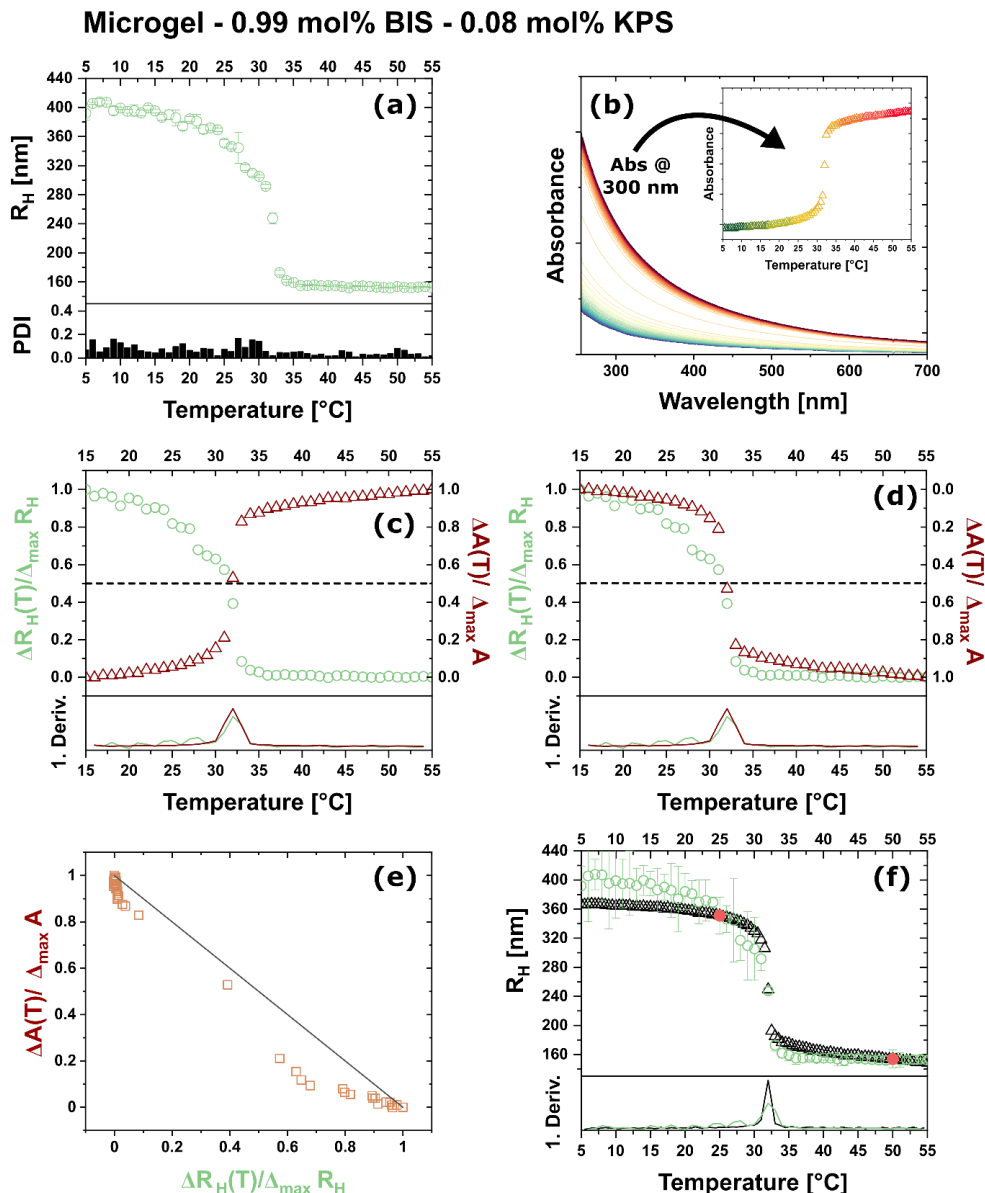


**Figure S5.3:** Overview of the characterization and processing of the measurement data for an microgel based on PNIPAM which is crosslinked with 0.99 mol% BIS. The polymerization was initiated with 1 mg (0.08 mol%) of KPS. Temperature-dependent DLS measurements including the poly dispersity indices (PDI) and temperature dependent UV-Vis absorbance measurements are presented in (a) and (b) respectively. The inset in (b) shows the plot of the absorbance values at 300 nm against the respective temperature. (c) Plot of the normalized data from (a) in green and (b) in red against the temperature. (d) Alternative representation of the plot in (c). The y-axis that shows the normalized absorbance data is inverted to simplify the comparison of the normalized data. Both plots (c) and (d) include the first derivatives of the functions in the respective color. (e) Plot of the normalized absorbance against the normalized hydrodynamic radii. The black line indicates a slope of -1. (f) Comparison of the DLS data (green) and the calculated hydrodynamic radii by use of the absorbance data (black). Red dots represent the reference points from DLS at 25 and 50 °C which are needed for the calculation. Additionally presented is the first derivative of both functions in the respective color.

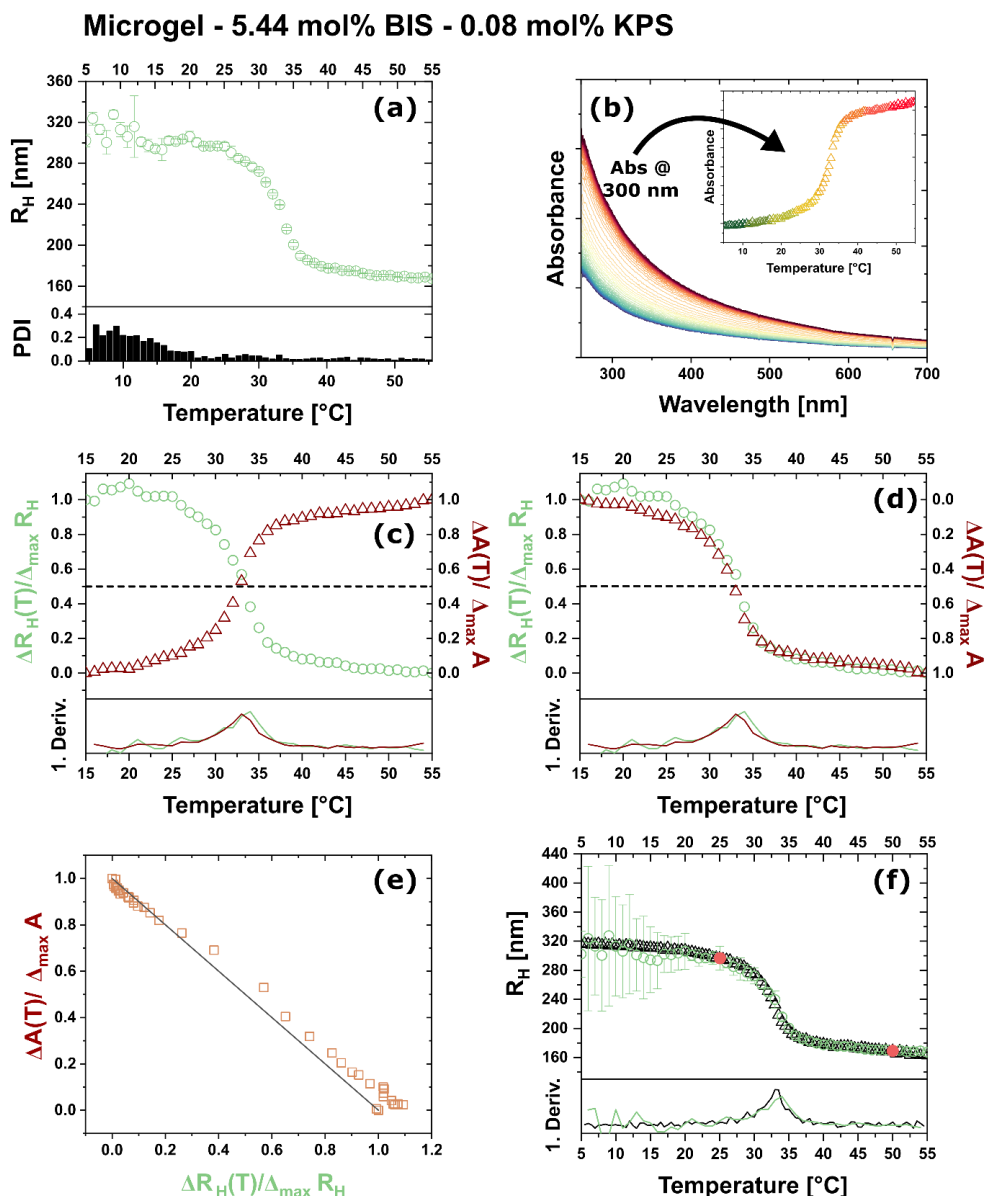


**Figure S5.4:** Overview of the characterization and processing of the measurement data for a microgel based on PNIPAM which is crosslinked with 5.44 mol% BIS. The polymerization was initiated with 1 mg (0.08 mol%) of KPS. Temperature-dependent DLS measurements including the poly dispersity indices (PDI) and temperature dependent UV-Vis absorbance measurements are presented in (a) and (b) respectively. The inset in (b) shows the plot of the absorbance values at 300 nm against the respective temperature. (c) Plot of the normalized data from (a) in green and (b) in red against the temperature. (d) Alternative representation of the plot in (c). The y-axis that shows the normalized absorbance data is inverted to simplify the comparison of the normalized data. Both plots (c) and (d) include the first derivatives of the functions in the respective color. (e) Plot of the normalized absorbance against the normalized hydrodynamic radii. The black line indicates a slope of -1. (f) Comparison of the DLS data (green) and the calculated hydrodynamic radii by use of the absorbance data (black). Red dots represent the reference points from DLS at 25 and 50 °C which are needed for the calculation. Additionally presented is the first derivative of both functions in the respective color.

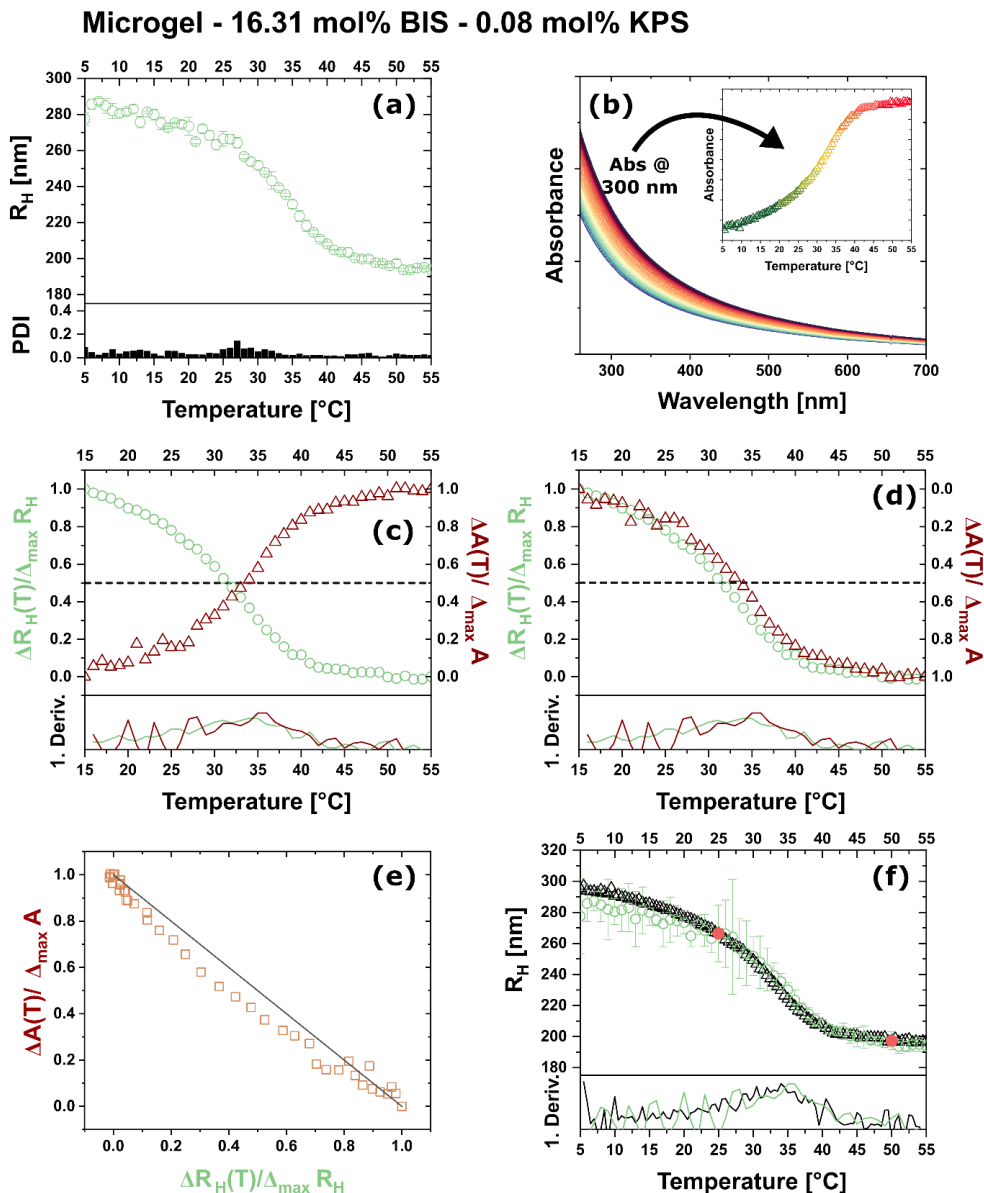


**Figure S5.5:** Overview of the characterization and processing of the measurement data for an microgel based on PNIPAM which is crosslinked with 16.31 mol% BIS. The polymerization was initiated with 1 mg (0.08 mol%) of KPS. Temperature-dependent DLS measurements including the poly dispersity indices (PDI) and temperature dependent UV-Vis absorbance measurements are presented in (a) and (b) respectively. The inset in (b) shows the plot of the absorbance values at 300 nm against the respective temperature. (c) Plot of the normalized data from (a) in green and (b) in red against the temperature. (d) Alternative representation of the plot in (c). The y-axis that shows the normalized absorbance data is inverted to simplify the comparison of the normalized data. Both plots (c) and (d) include the first derivatives of the functions in the respective color. (e) Plot of the normalized absorbance against the normalized hydrodynamic radii. The black line indicates a slope of -1. (f) Comparison of the DLS data (green) and the calculated hydrodynamic radii by use of the absorbance data (black). Red dots represent the reference points from DLS at 25 and 50 °C which are needed for the calculation. Additionally presented is the first derivative of both functions in the respective color.

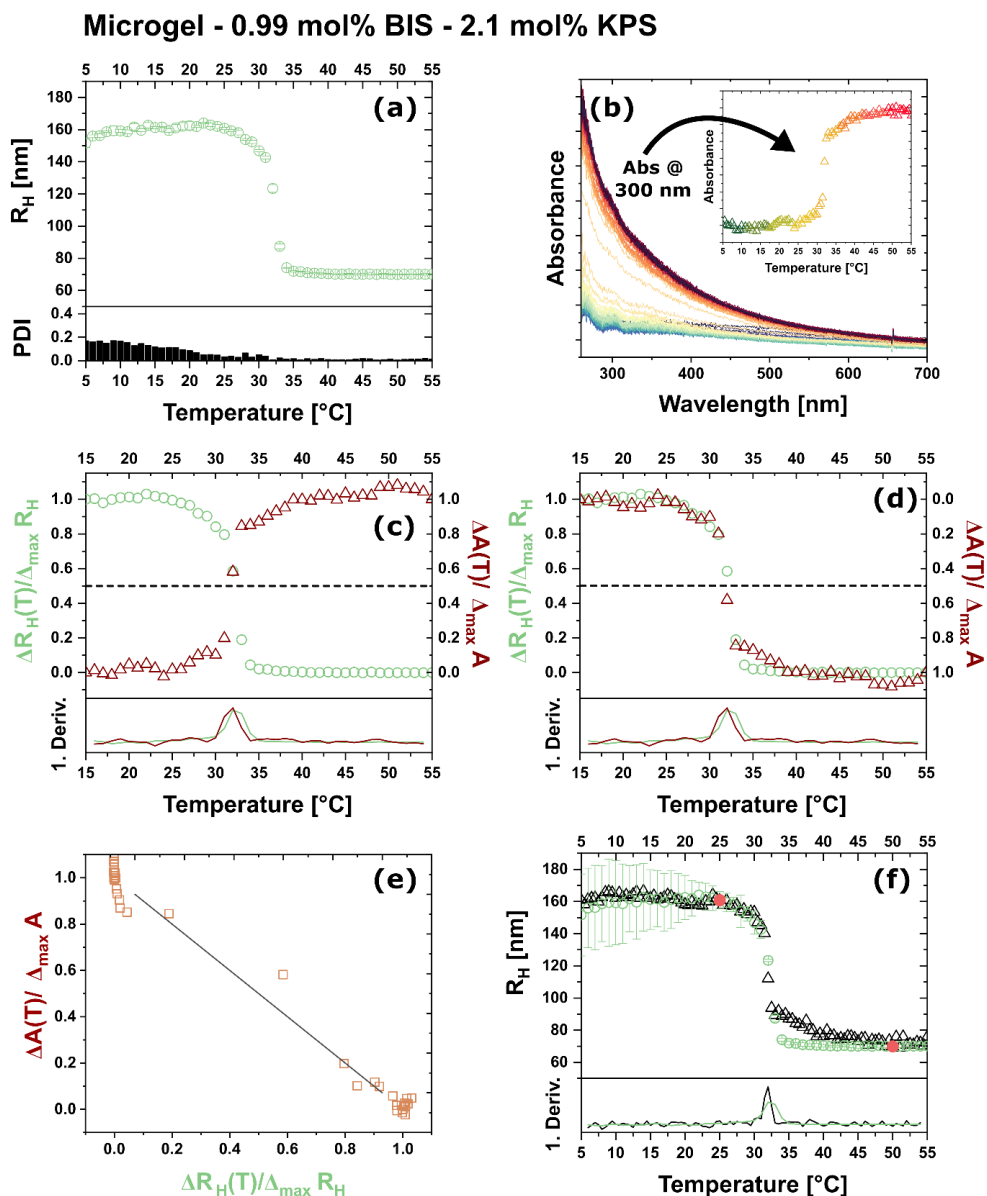


**Figure S5.6:** Overview of the characterization and processing of the measurement data for a microgel based on PNIPAM which is crosslinked with 0.99 mol% BIS. The polymerization was initiated with 25 mg (2.1 mol%) of KPS. Temperature-dependent DLS measurements including the poly dispersity indices (PDI) and temperature dependent UV-Vis absorbance measurements are presented in (a) and (b) respectively. The inset in (b) shows the plot of the absorbance values at 300 nm against the respective temperature. (c) Plot of the normalized data from (a) in green and (b) in red against the temperature. (d) Alternative representation of the plot in (c). The y-axis that shows the normalized absorbance data is inverted to simplify the comparison of the normalized data. Both plots (c) and (d) include the first derivatives of the functions in the respective color. (e) Plot of the normalized absorbance against the normalized hydrodynamic radii. The black line indicates a slope of -1. (f) Comparison of the DLS data (green) and the calculated hydrodynamic radii by use of the absorbance data (black). Red dots represent the reference points from DLS at 25 and 50 °C which are needed for the calculation. Additionally presented is the first derivative of both functions in the respective color.

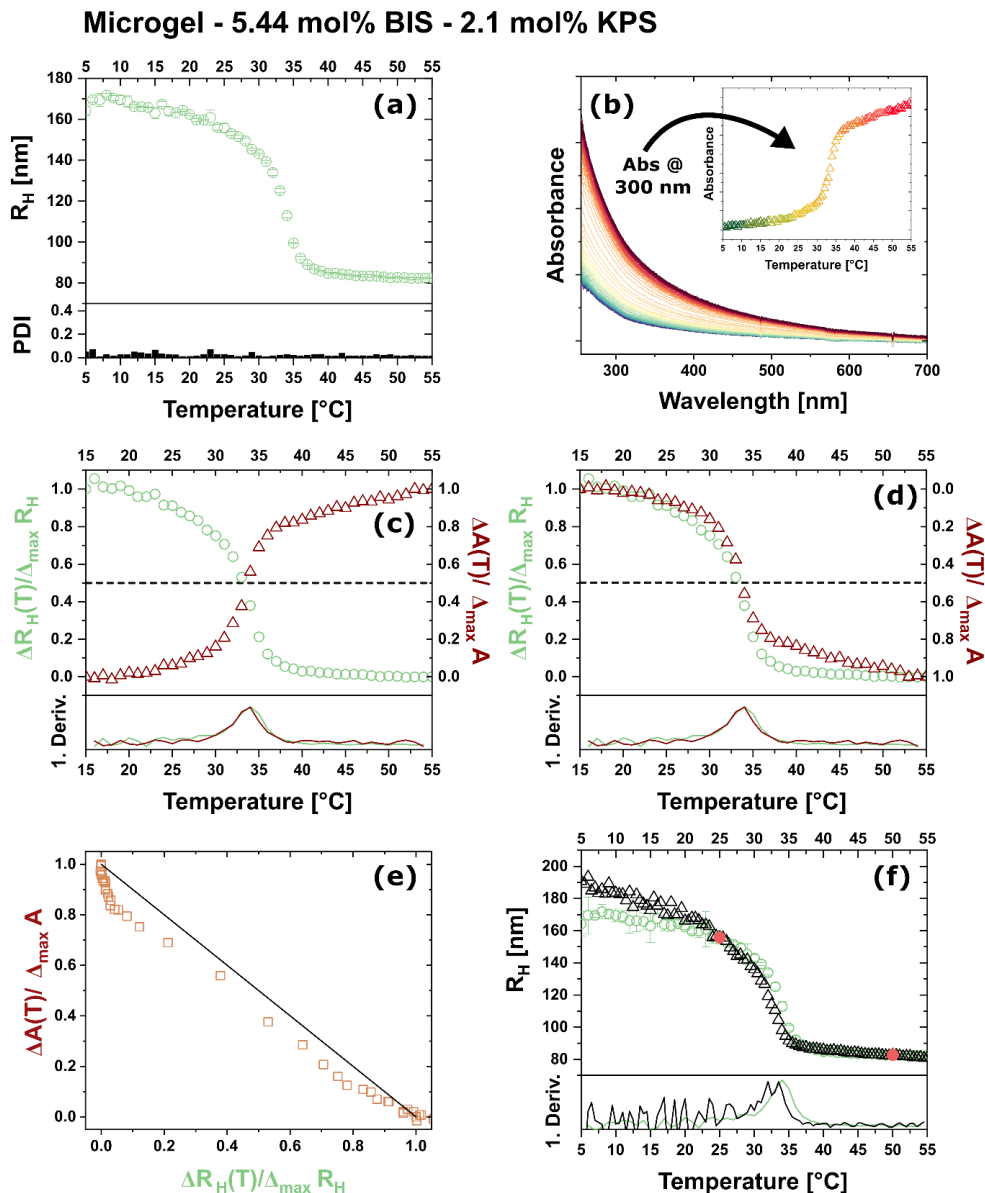


**Figure S5.7:** Overview of the characterization and processing of the measurement data for an microgel based on PNIPAM which is crosslinked with 5.44 mol% BIS. The polymerization was initiated with 25 mg (2.1 mol%) of KPS. Temperature-dependent DLS measurements including the poly dispersity indices (PDI) and temperature dependent UV-Vis absorbance measurements are presented in (a) and (b) respectively. The inset in (b) shows the plot of the absorbance values at 300 nm against the respective temperature. (c) Plot of the normalized data from (a) in green and (b) in red against the temperature. (d) Alternative representation of the plot in (c). The y-axis that shows the normalized absorbance data is inverted to simplify the comparison of the normalized data. Both plots (c) and (d) include the first derivatives of the functions in the respective color. (e) Plot of the normalized absorbance against the normalized hydrodynamic radii. The black line indicates a slope of -1. (f) Comparison of the DLS data (green) and the calculated hydrodynamic radii by use of the absorbance data (black). Red dots represent the reference points from DLS at 25 °C and 50 °C which are needed for the calculation. Additionally presented is the first derivative of both functions in the respective color.

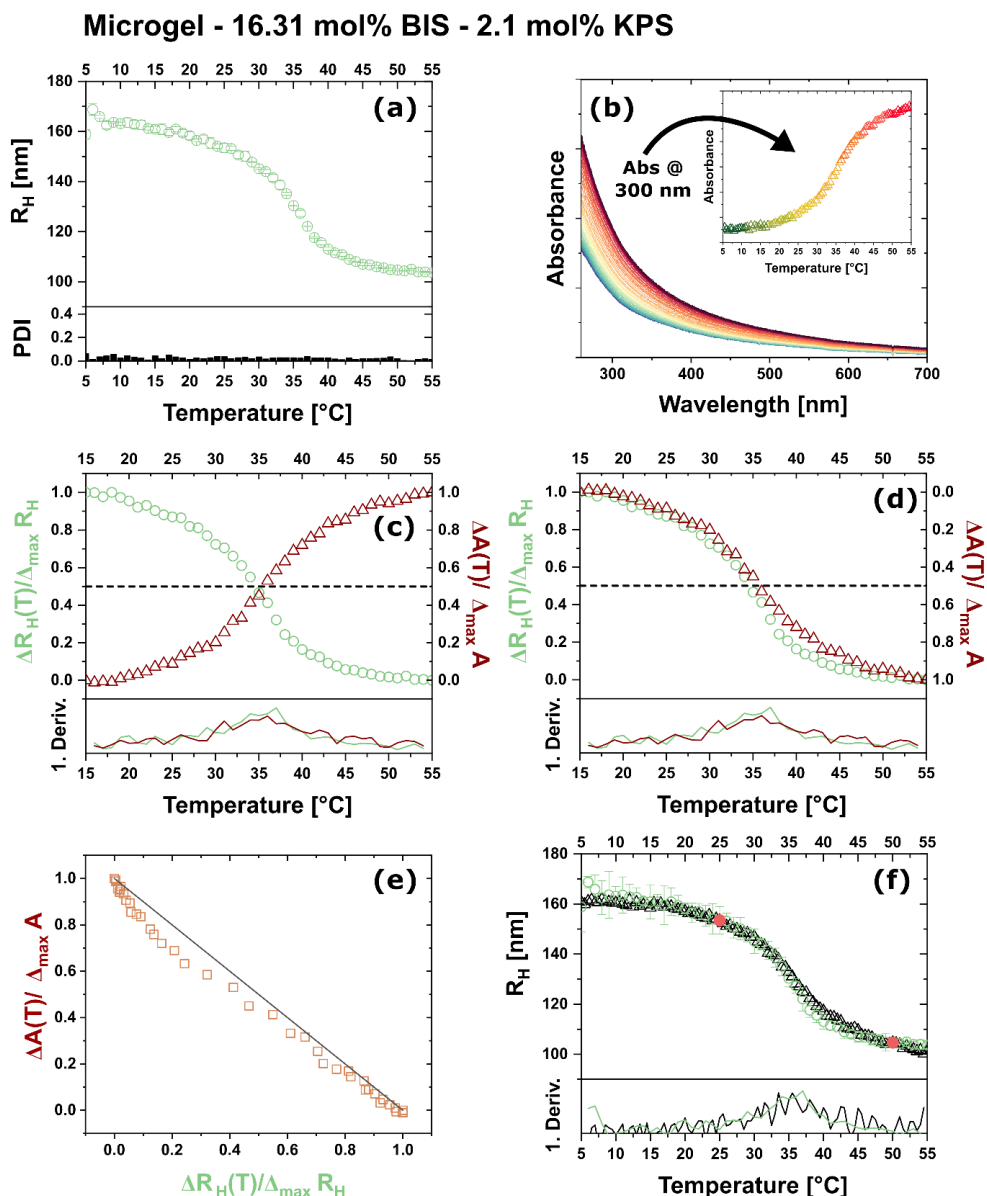


**Figure S5.8:** Overview of the characterization and processing of the measurement data for a microgel based on PNIPAM which is crosslinked with 16.31 mol% BIS. The polymerization was initiated with 25 mg (2.1 mol%) of KPS. Temperature-dependent DLS measurements including the polydispersity indices (PDI) and temperature dependent UV-Vis absorbance measurements are presented in (a) and (b) respectively. The inset in (b) shows the plot of the absorbance values at 300 nm against the respective temperature. (c) Plot of the normalized data from (a) in green and (b) in red against the temperature. (d) Alternative representation of the plot in (c). The y-axis that shows the normalized absorbance data is inverted to simplify the comparison of the normalized data. Both plots (c) and (d) include the first derivatives of the functions in the respective color. (e) Plot of the normalized absorbance against the normalized hydrodynamic radii. The black line indicates a slope of -1. (f) Comparison of the DLS data (green) and the calculated hydrodynamic radii by use of the absorbance data (black). Red dots represent the reference points from DLS at 25 and 50 °C which are needed for the calculation. Additionally presented is the first derivative of both functions in the respective color.

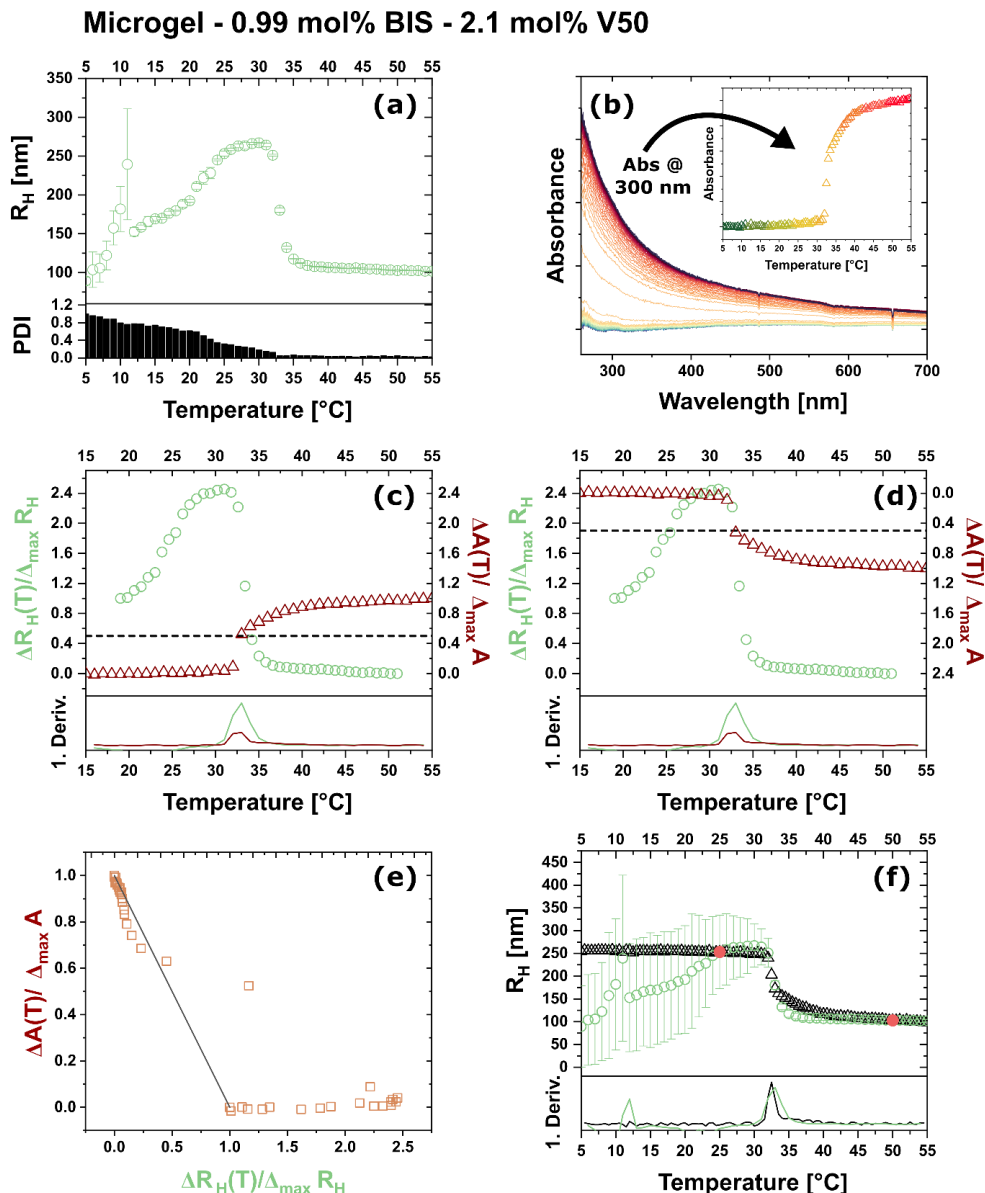


**Figure S5.9:** Overview of the characterization and processing of the measurement data for an microgel based on PNIPAM which is crosslinked with 0.99 mol% BIS. The polymerization was initiated with 25 mg (2.1 mol%) of V50. Temperature-dependent DLS measurements including the poly dispersity indices (PDI) and temperature dependent UV-Vis absorbance measurements are presented in (a) and (b) respectively. The inset in (b) shows the plot of the absorbance values at 300 nm against the temperature. (c) Plot of the normalized data from (a) in green and (b) in red against the temperature. (d) Alternative representation of the plot in (c). The y-axis that shows the normalized absorbance data is inverted to simplify the comparison of the normalized data. Both plots (c) and (d) include the first derivatives of the functions in the respective color. (e) Plot of the normalized absorbance against the normalized hydrodynamic radii. The black line indicates a slope of -1. (f) Comparison of the DLS data (green) and the calculated hydrodynamic radii by use of the absorbance data (black). Red dots represent the reference points from DLS at 25 and 50 °C which are needed for the calculation. Additionally presented is the first derivative of both functions in the respective color.

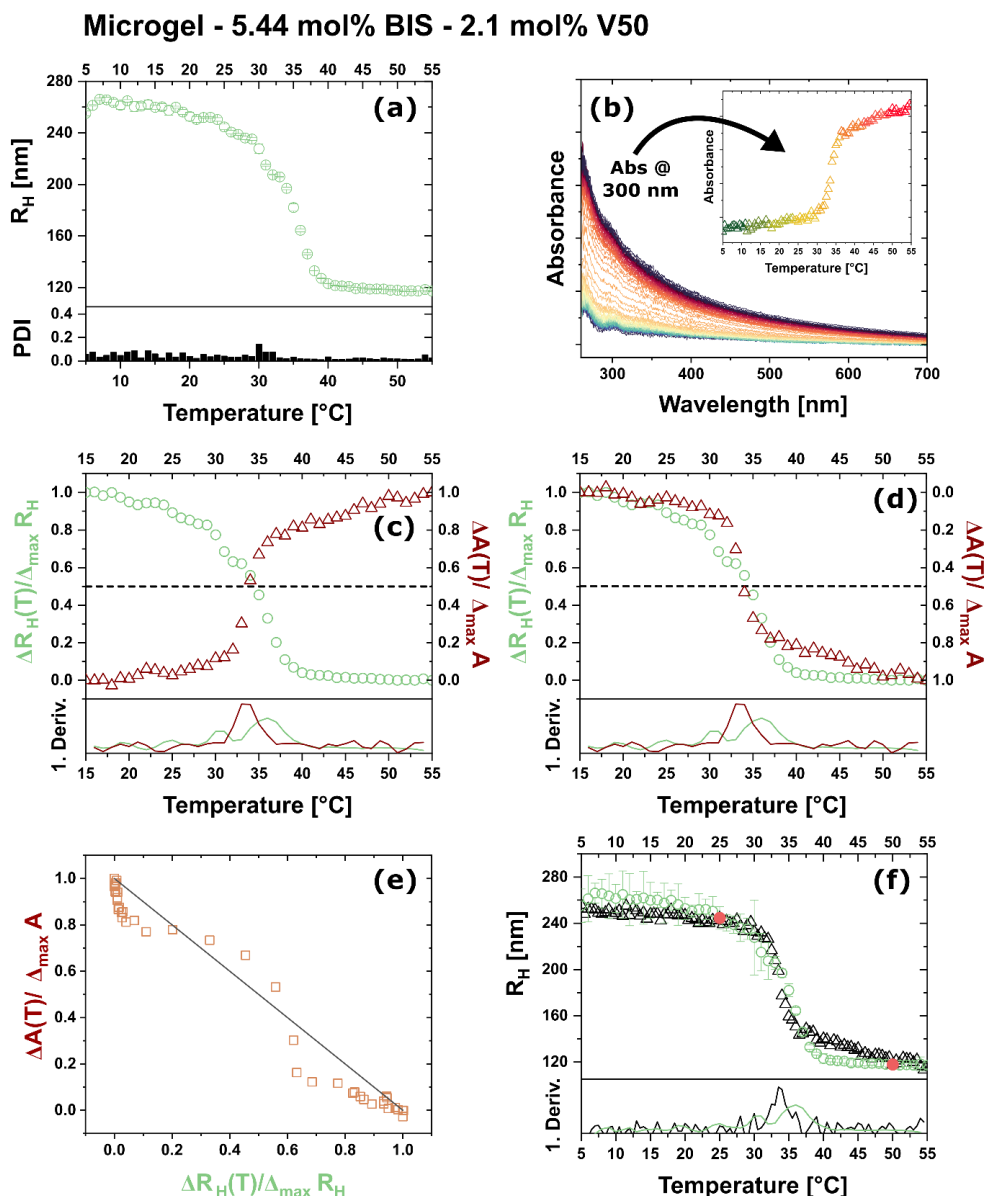


**Figure S5.10:** Overview of the characterization and processing of the measurement data for a microgel based on PNIPAM which is crosslinked with 5.44 mol% BIS. The polymerization was initiated with 25 mg (2.1 mol%) of V50. Temperature-dependent DLS measurements including the poly dispersity indices (PDI) and temperature dependent UV-Vis absorbance measurements are presented in (a) and (b) respectively. The inset in (b) shows the plot of the absorbance values at 300 nm against the respective temperature. (c) Plot of the normalized data from (a) in green and (b) in red against the temperature. (d) Alternative representation of the plot in (c). The y-axis that shows the normalized absorbance data is inverted to simplify the comparison of the normalized data. Both plots (c) and (d) include the first derivatives of the functions in the respective color. (e) Plot of the normalized absorbance against the normalized hydrodynamic radii. The black line indicates a slope of -1. (f) Comparison of the DLS data (green) and the calculated hydrodynamic radii by use of the absorbance data (black). Red dots represent the reference points from DLS at 25 and 50 °C which are needed for the calculation. Additionally presented is the first derivative of both functions in the respective color.

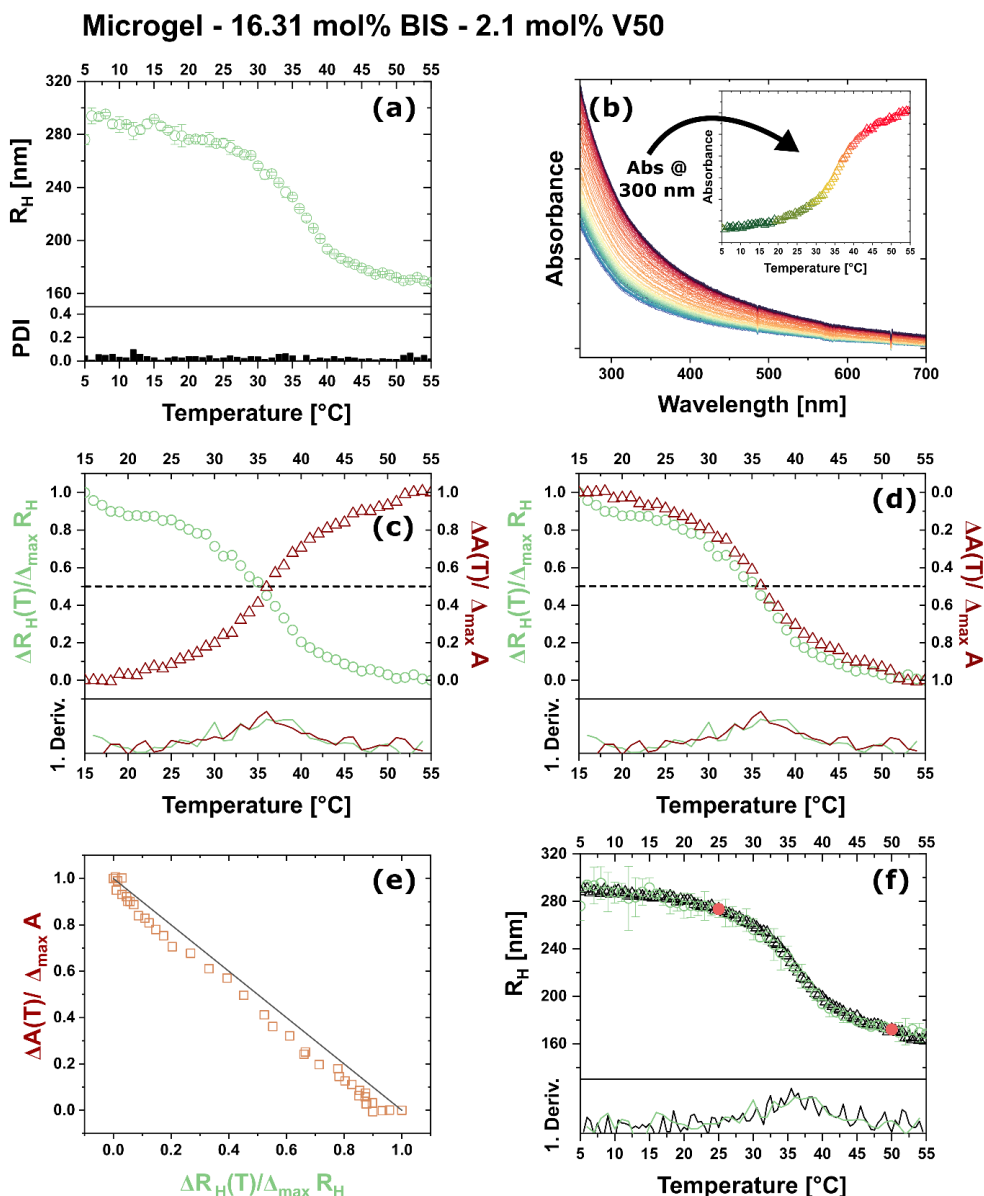


**Figure S5.11:** Overview of the characterization and processing of the measurement data for an microgel based on PNIPAM which is crosslinked with 16.31 mol% BIS. The polymerization was initiated with 25 mg (2.1 mol%) of V50. Temperature-dependent DLS measurements including the poly dispersity indices (PDI) and temperature dependent UV-Vis absorbance measurements are presented in (a) and (b) respectively. The inset in (b) shows the plot of the absorbance values at 300 nm against the respective temperature. (c) Plot of the normalized data from (a) in green and (b) in red against the temperature. (d) Alternative representation of the plot in (c). The y-axis that shows the normalized absorbance data is inverted to simplify the comparison of the normalized data. Both plots (c) and (d) include the first derivatives of the functions in the respective color. (e) Plot of the normalized absorbance against the normalized hydrodynamic radii. The black line indicates a slope of -1. (f) Comparison of the DLS data (green) and the calculated hydrodynamic radii by use of the absorbance data (black). Red dots represent the reference points from DLS at 25 °C and 50 °C which are needed for the calculation. Additionally presented is the first derivative of both functions in the respective color.

5. Following the volume phase transition of thermoresponsive microgels by dynamic light scattering and turbidity: Correlations depend on microgel homogeneity

**Table S5.1:** Determined hydrodynamic radii below the VPTT at 25 °C and above the VPTT at 50 °C, VPTT by DLS and absorbance measurements and important components of the investigated PNIPAM microgels.

Microgel system	Crosslinker [mol%]	m(Initiator) [mg] (μmol)	R <sub>H</sub> @25 °C [nm]	R <sub>H</sub> @50 °C [nm]	VPTT DLS [°C]	VPTT Abs. [°C]
KPS <sub>25mg</sub> - 0.99	0.99	25.0 (92.0) - KPS	161 ± 5	70 ± 0	32.5	32.0
KPS <sub>25mg</sub> - 5.44	5.44	25.0 (92.0) - KPS	155 ± 2	83 ± 0	34.0	34.0
KPS <sub>25mg</sub> - 16.31	16.31	25.0 (92.0) - KPS	153 ± 5	105 ± 2	36.0	36.0
KPS <sub>1mg</sub> - 0.99	0.99	1.0 (3.0) - KPS	351 ± 25	154 ± 13	32.0	32.0
KPS <sub>1mg</sub> - 5.44	5.44	1.0 (3.0) - KPS	297 ± 17	169 ± 1	34.0	33.0
KPS <sub>1mg</sub> - 16.31	16.31	1.0 (3.0) - KPS	266 ± 18	197 ± 6	34.0	35.0
V50 <sub>25mg</sub> - 0.99	0.99	25.0 (92.0) - V50	253 ± 80	103 ± 4	33.0	33.0
V50 <sub>25mg</sub> - 5.44	5.44	25.0 (92.0) - V50	245 ± 10	118 ± 2	36.0	33.5
V50 <sub>25mg</sub> - 16.31	16.31	25.0 (92.0) - V50	274 ± 7	172 ± 2	37.0	36.0

In **Figure S5.12** we present results for the calculations to find suitable reference points for the calculations of the hydrodynamic radii by using absorbance data. The plot shows the sum of difference between initial measured DLS data and calculated hydrodynamic radii for different reference points used for the calculations. The calculations were performed for the three microgel systems discussed in the main manuscript. We found that for the calculations, reference points that cover a large or small temperature range lead to large difference in the final calculated values. We observed the best agreement for all three types of microgels (PNIPAM microgels in **(a)**, copolymer microgels in **(b)** and SiO<sub>2</sub>-core-shell microgels in **(c)**) for reference point which are selected 5-15 °C below and 5-15 °C above the VPTT. Therefore, we found the lowest divergences for reference points at 20 and 50, 25 and 45 as well as 25 and 50 (red bar). We finally decided to choose the reference points at 25 and 50 °C as we found the lowest deviations between DLS and calculated data on average.

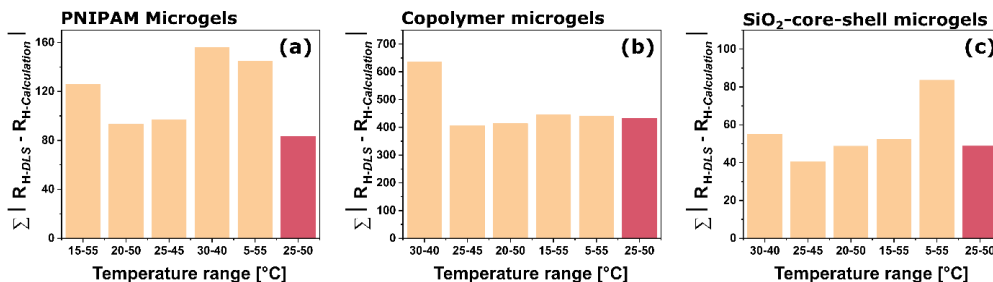


**Figure S5.12:** Overview of the results for using different reference points for the calculation of the hydrodynamic radii with the data from absorbance measurements. The sum of derivations between the initial DLS data and the calculated data is represented by the different bar for (a) PNIPAM microgels (b) copolymer microgels and (c) SiO<sub>2</sub>-core-shell microgels.

### Copolymer Microgel

In **Figure S5.13** and **S5.14** we present the results for the measurements of the electrophoretic mobility for all twelve investigated copolymer microgels at 20 °C and 50 °C respectively. The colored bars represent the three different amounts of crosslinker that were used for the different syntheses of the copolymer microgels. With our measurements we validate the incorporation of the comonomers into the microgel and the resulting charge of the network. The measurements show a negative electrophoretic mobility for copolymer microgels with incorporated AAc and AMPS with values between -1.25 and -2.5 at temperatures of 20 °C and -3.5 and -4 at 50 °C. As opposed to this, APTAC and 2-VP copolymer microgels show positive values between 0.5 and 2 at 20 °C and 3.5 and 4 at 50 °C. Similar to our findings for the NIPAM microgels (**Figure S5.1** and **S5.2**), we found an overall higher electrophoretic mobility at 50 °C above the VPTT compared to measurements at 20 °C. Also, the electrophoretic mobility increases with increasing crosslinker degrees (especially comparing very soft microgels with a crosslinker degree of 0.99 mol% BIS (red) and very high crosslinker degree of 16.31 mol% (blue)) at temperatures below the VPTT.

As for the NIPAM microgels we can explain the observations for the copolymer microgels with increasing rigidity of the microgel network by an increasing amount of incorporated crosslinker monomer and the collapse of microgel causing in the existence of the microgel network in an overall smaller volume. The result is an increasing charge density and therefore a higher detectable electrophoretic mobility.

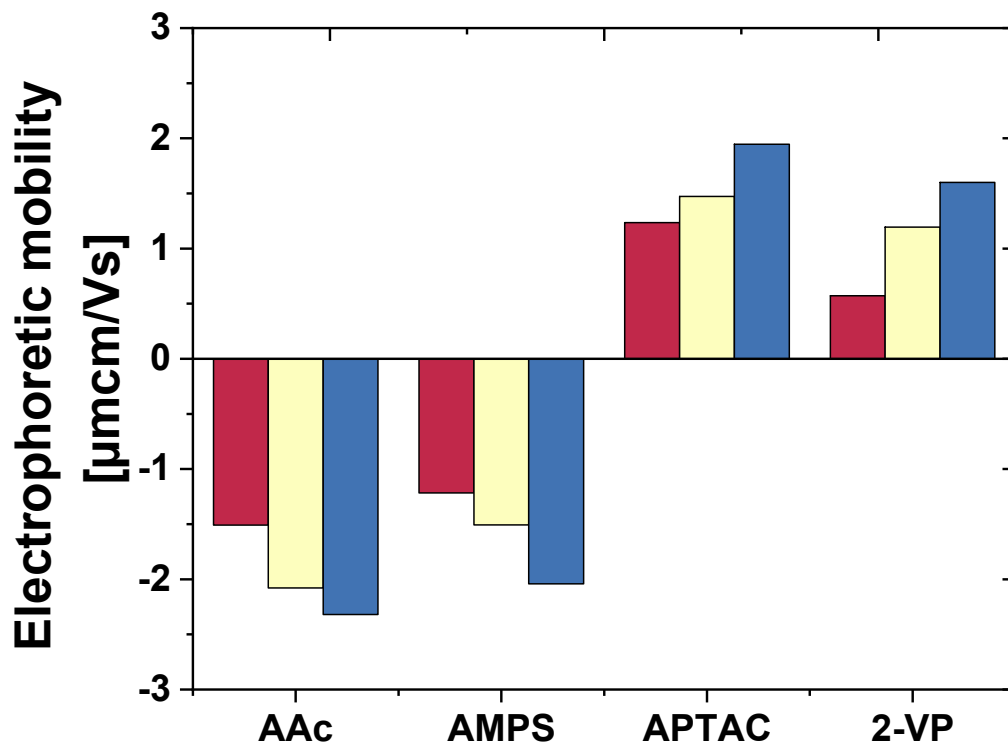


**Figure S5.13:** Overview of the electrophoretic mobility measurements at 20 °C for all copolymer microgels synthesized in this work. The color of the bars represents the respective crosslinking degree of the copolymer microgel. Microgels with 0.99 mol% BIS (red), 5.44 mol% (yellow) and 16.31 mol% (blue) have been investigated.

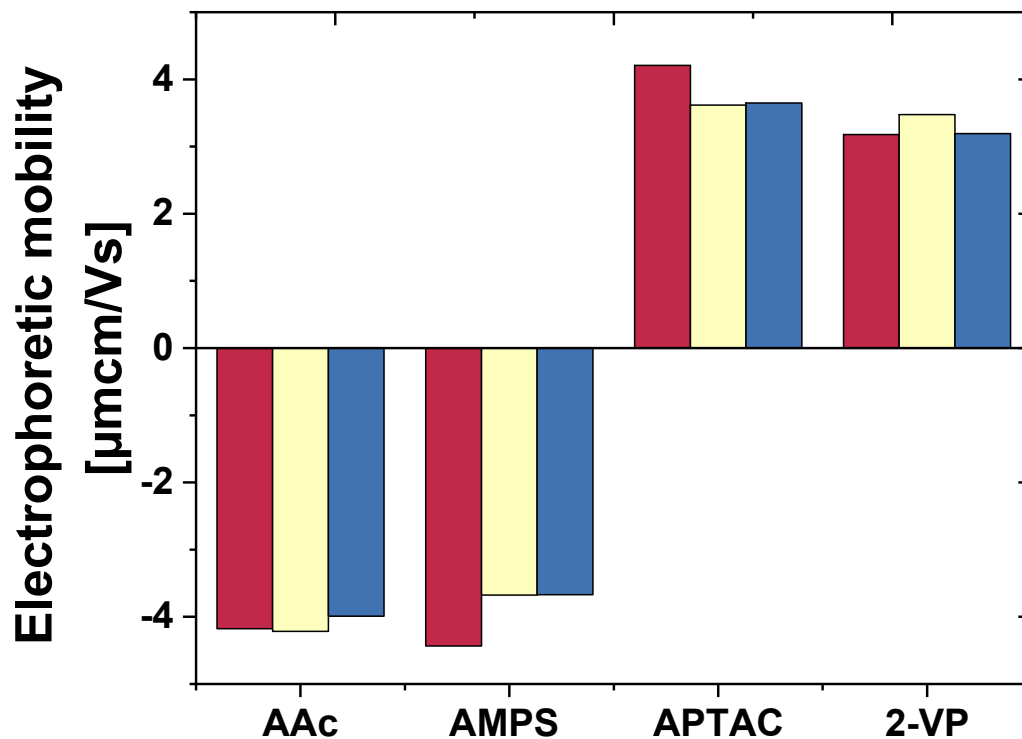


**Figure S5.14:** Overview of the electrophoretic mobility measurements at 50 °C for all copolymer microgels synthesized in this work. The color of the bars represents the respective crosslinking degree of the copolymer microgel. Microgels with 0.99 mol% BIS (red), 5.44 mol% (yellow) and 16.31 mol% (blue) have been investigated.

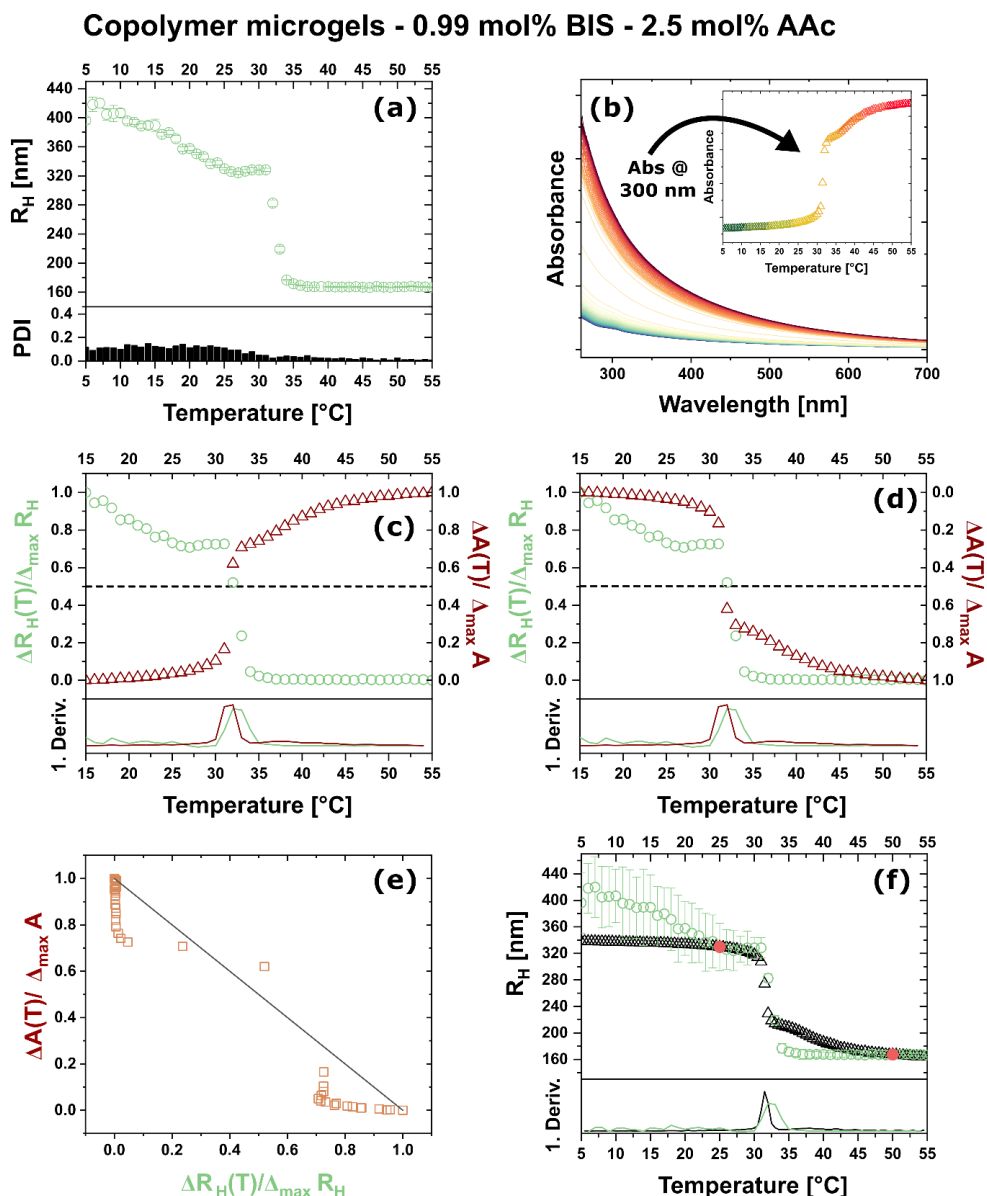


**Figure S5.15:** Overview of the characterization and processing of the measurement data for a copolymer microgel with a crosslinking degree of 0.99 mol% BIS. During the synthesis 2.5 mol% AAc were added to the reaction. The polymerization was initiated with 2 mg of KPS. Temperature-dependent DLS measurements including the poly dispersity indices (PDI) and temperature dependent UV-Vis absorbance measurements are presented in (a) and (b) respectively. The inset in (b) shows the plot of the absorbance values at 300 nm against the respective temperature. (c) Plot of the normalized data from (a) in green and (b) in red against the temperature. (d) Alternative representation of the plot in (c). The y-axis that shows the normalized absorbance data is inverted to simplify the comparison of the normalized data. Both plots (c) and (d) include the first derivatives of the functions in the respective color. (e) Plot of the normalized absorbance against the normalized hydrodynamic radii. The black line indicates a slope of -1. (f) Comparison of the DLS data (green) and the calculated hydrodynamic radii by use of the absorbance data (black). Red dots represent the reference points from DLS at 25 and 50 °C which are needed for the calculation. Additionally presented is the first derivative of both functions in the respective color.

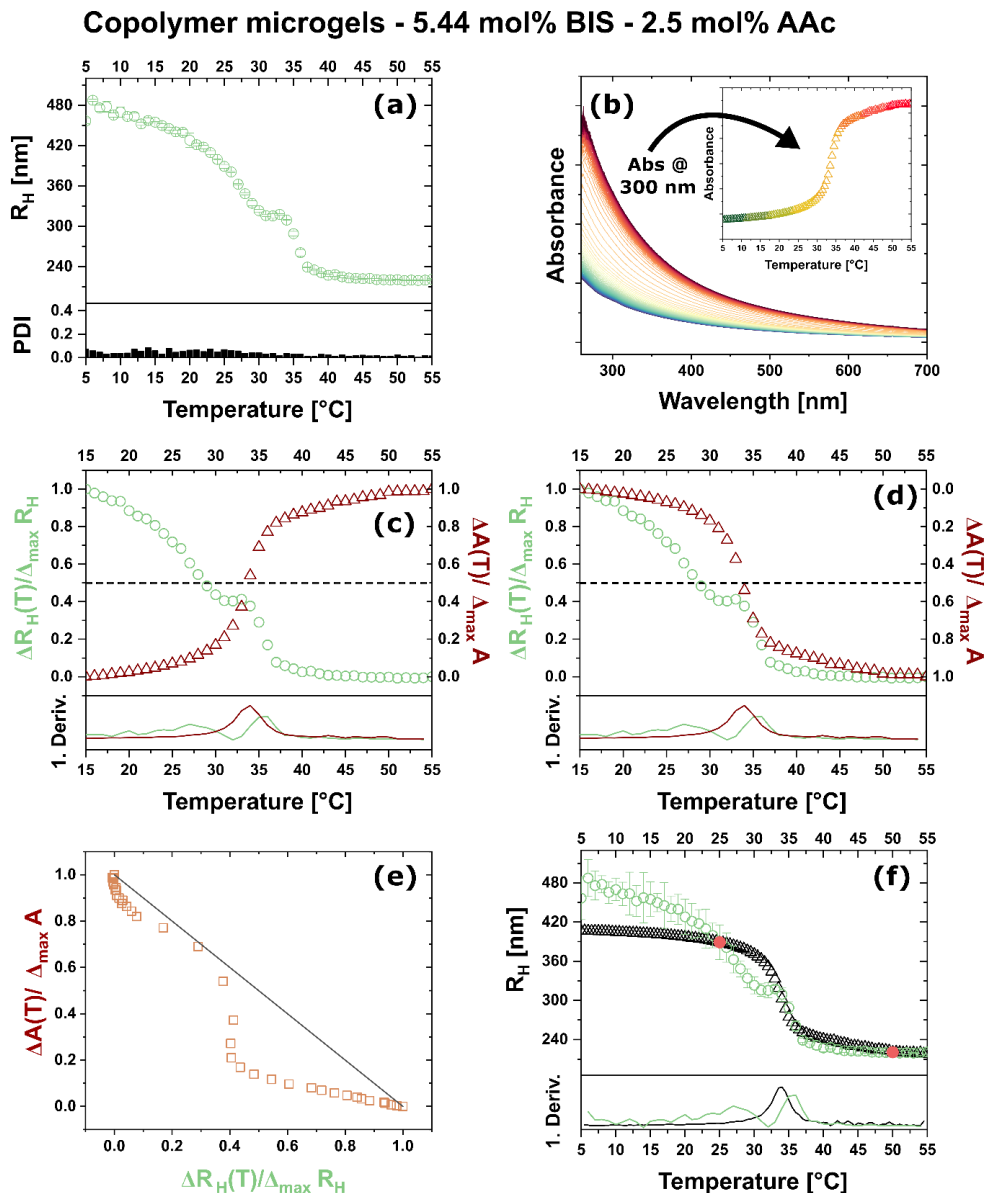


**Figure S5.16:** Overview of the characterization and processing of the measurement data for a copolymer microgel with a crosslinking degree of 5.44 mol% BIS. During the synthesis 2.5 mol% AAc were added to the reaction. The polymerization was initiated with 2 mg of KPS. Temperature-dependent DLS measurements including the poly dispersity indices (PDI) and temperature dependent UV-Vis absorbance measurements are presented in (a) and (b) respectively. The inset in (b) shows the plot of the absorbance values at 300 nm against the respective temperature. (c) Plot of the normalized data from (a) in green and (b) in red against the temperature. (d) Alternative representation of the plot in (c). The y-axis that shows the normalized absorbance data is inverted to simplify the comparison of the normalized data. Both plots (c) and (d) include the first derivatives of the functions in the respective color. (e) Plot of the normalized absorbance against the normalized hydrodynamic radii. The black line indicates a slope of -1. (f) Comparison of the DLS data (green) and the calculated hydrodynamic radii by use of the absorbance data (black). Red dots represent the reference points from DLS at 25 and 50 °C which are needed for the calculation. Additionally presented is the first derivative of both functions in the respective color.

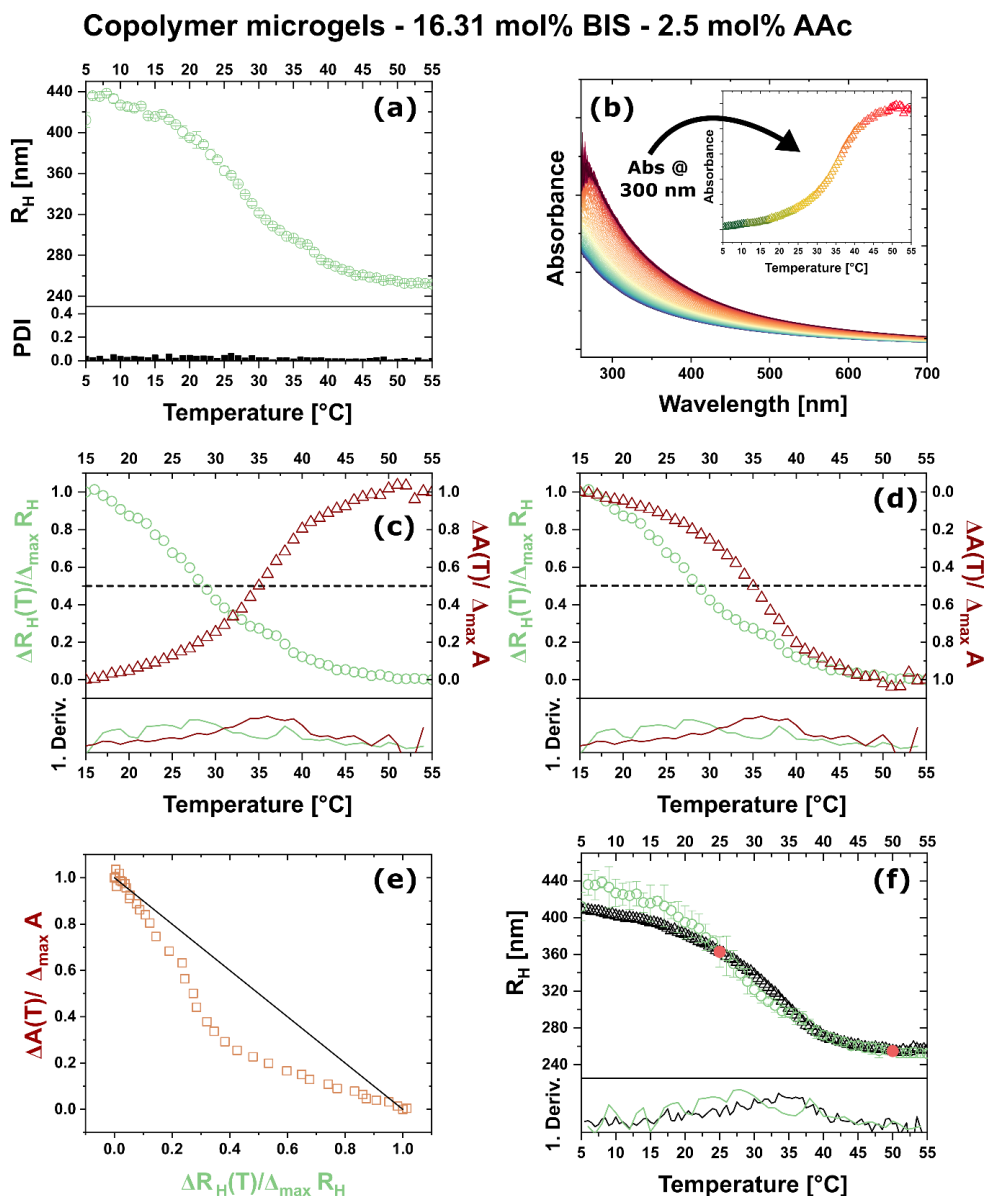


**Figure S5.17:** Overview of the characterization and processing of the measurement data for a copolymer microgel with a crosslinking degree of 16.31 mol% BIS. During the synthesis 2.5 mol% AAc were added to the reaction. The polymerization was initiated with 2 mg of KPS. Temperature-dependent DLS measurements including the poly dispersity indices (PDI) and temperature dependent UV-Vis absorbance measurements are presented in (a) and (b) respectively. The inset in (b) shows the plot of absorbance values at 300 nm against the respective temperature. (c) Plot of the normalized data from (a) in green and (b) in red against the temperature. (d) Alternative representation of the plot in (c). The y-axis that shows the normalized absorbance data is inverted to simplify the comparison of the normalized data. Both plots (c) and (d) include the first derivatives of the functions in the respective color. (e) Plot of the normalized absorbance against the normalized hydrodynamic radii. The black line indicates a slope of -1. (f) Comparison of the DLS data (green) and the calculated hydrodynamic radii by use of the absorbance data (black). Red dots represent the reference points from DLS at 25 and 50 °C which are needed for the calculation. Additionally presented is the first derivative of both functions in the respective color.

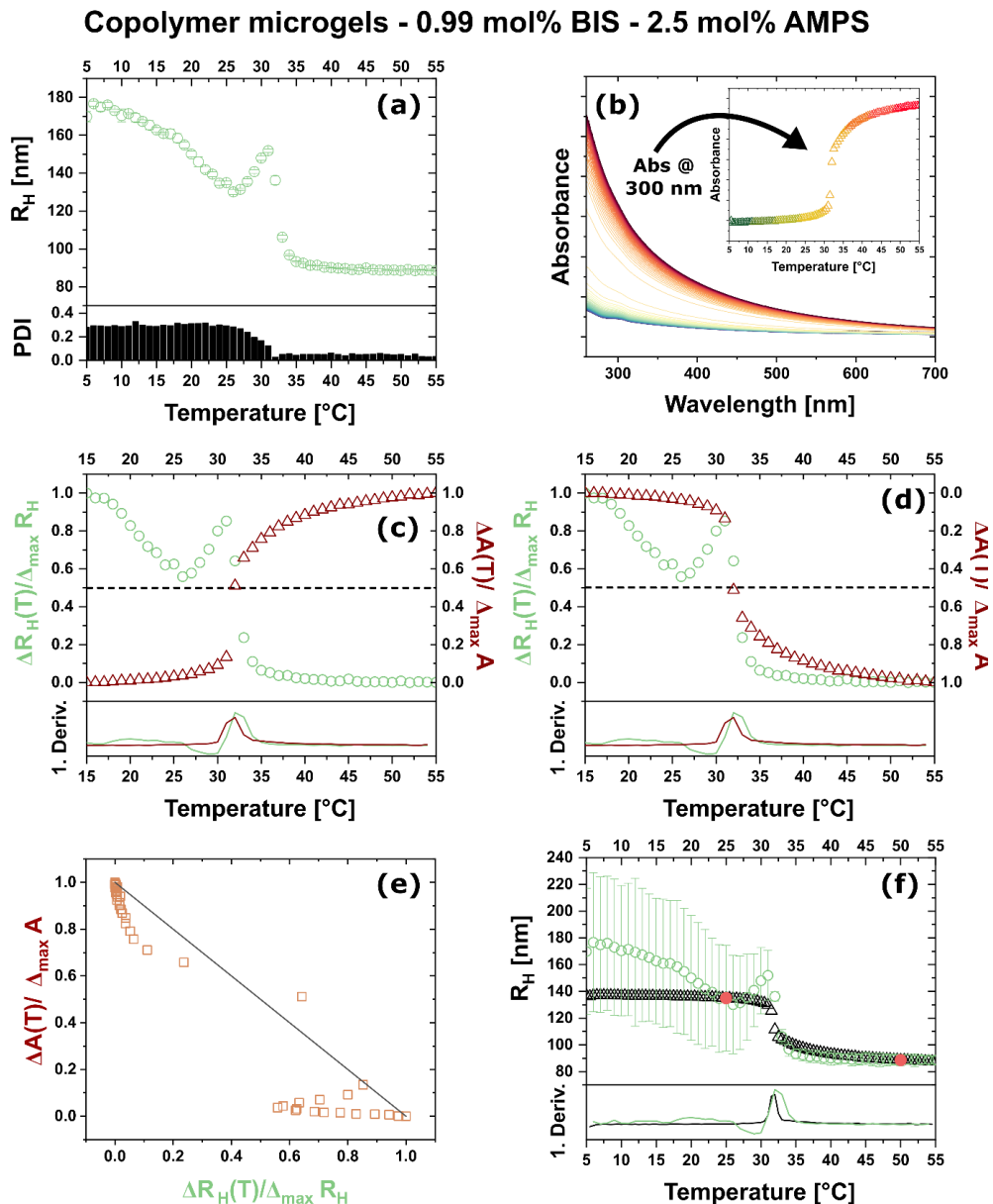


**Figure S5.18:** Overview of the characterization and processing of the measurement data for a copolymer microgel with a crosslinking degree of 0.99 mol% BIS. During the synthesis 2.5 mol% AMPS were added to the reaction. The polymerization was initiated with 2 mg of KPS. Temperature-dependent DLS measurements including the poly dispersity indices (PDI) and temperature dependent UV-Vis absorbance measurements are presented in (a) and (b) respectively. The inset in (b) shows the plot of the absorbance values at 300 nm against the respective temperature. (c) Plot of the normalized data from (a) in green and (b) in red against the temperature. (d) Alternative representation of the plot in (c). The y-axis that shows the normalized absorbance data is inverted to simplify the comparison of the normalized data. Both plots (c) and (d) include the first derivatives of the functions in the respective color. (e) Plot of the normalized absorbance against the normalized hydrodynamic radii. The black line indicates a slope of -1. (f) Comparison of the DLS data (green) and the calculated hydrodynamic radii by use of the absorbance data (black). Red dots represent the reference points from DLS at 25 and 50 °C which are needed for the calculation. Additionally presented is the first derivative of both functions in the respective color.

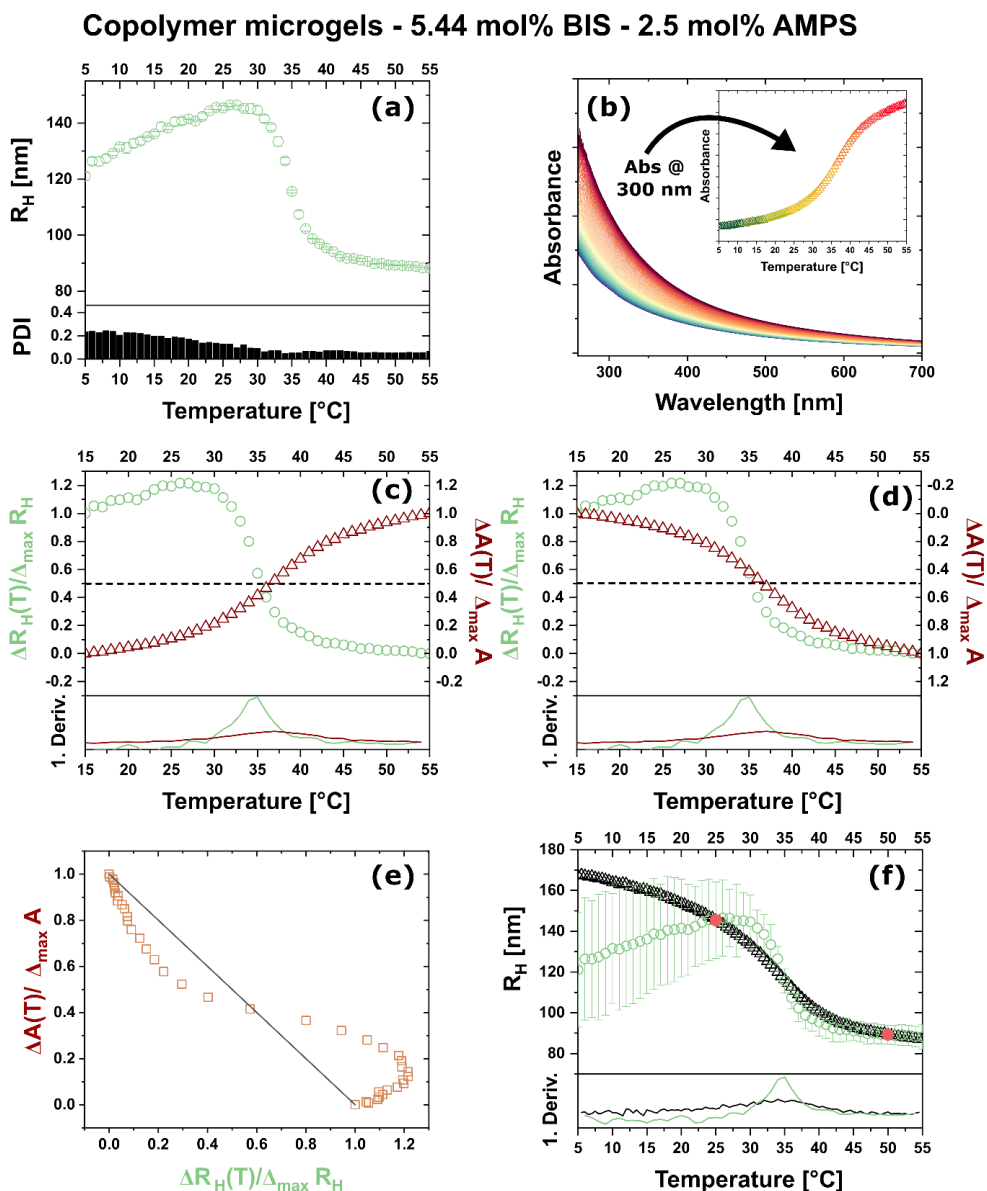


**Figure S5.19:** Overview of the characterization and processing of the measurement data for a copolymer microgel with a crosslinking degree of 5.44 mol% BIS. During the synthesis 2.5 mol% AMPS were added to the reaction. The polymerization was initiated with 2 mg of KPS. Temperature-dependent DLS measurements including the poly dispersity indices (PDI) and temperature dependent UV-Vis absorbance measurements are presented in (a) and (b) respectively. The inset in (b) shows the plot of the absorbance values at 300 nm against the respective temperature. (c) Plot of the normalized data from (a) in green and (b) in red against the temperature. (d) Alternative representation of the plot in (c). The y-axis that shows the normalized absorbance data is inverted to simplify the comparison of the normalized data. Both plots (c) and (d) include the first derivatives of the functions in the respective color. (e) Plot of the normalized absorbance against the normalized hydrodynamic radii. The black line indicates a slope of -1. (f) Comparison of the DLS data (green) and the calculated hydrodynamic radii by use of the absorbance data (black). Red dots represent the reference points from DLS at 25 and 50 °C which are needed for the calculation. Additionally presented is the first derivative of both functions in the respective color.

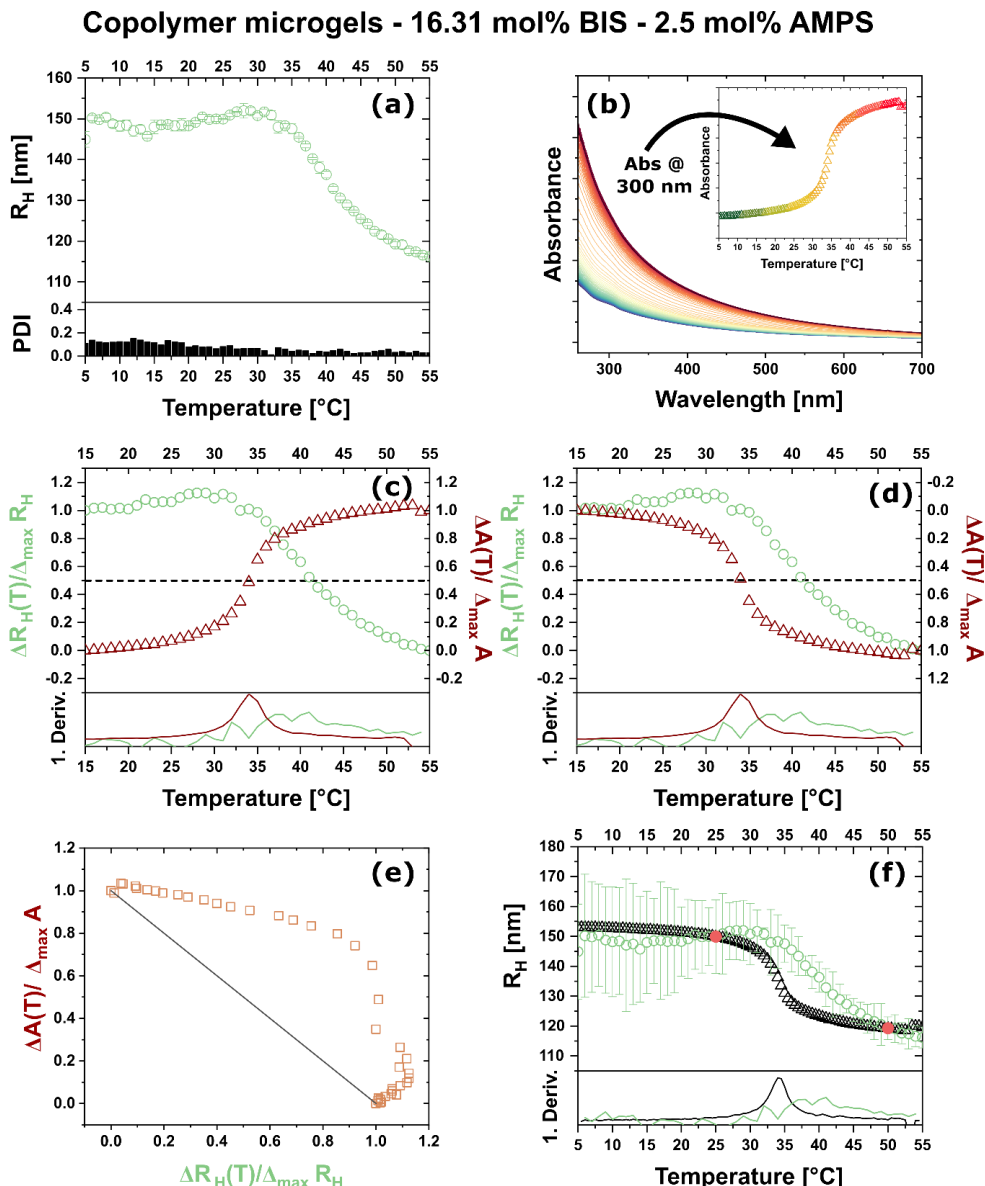


**Figure S5.20:** Overview of the characterization and processing of the measurement data for a copolymer microgel with a crosslinking degree of 16.31 mol% BIS. During the synthesis 2.5 mol% AMPS were added to the reaction. The polymerization was initiated with 2 mg of KPS. Temperature-dependent DLS measurements including the polydispersity indices (PDI) and temperature dependent UV-Vis absorbance measurements are presented in (a) and (b) respectively. The inset in (b) shows the plot of the absorbance values at 300 nm against the respective temperature. (c) Plot of the normalized data from (a) in green and (b) in red against the temperature. (d) Alternative representation of the plot in (c). The y-axis that shows the normalized absorbance data is inverted to simplify the comparison of the normalized data. Both plots (c) and (d) include the first derivatives of the functions in the respective color. (e) Plot of the normalized absorbance against the normalized hydrodynamic radii. The black line indicates a slope of -1. (f) Comparison of the DLS data (green) and the calculated hydrodynamic radii by use of the absorbance data (black). Red dots represent the reference points from DLS at 25 and 50 °C which are needed for the calculation. Additionally presented is the first derivative of both functions in the respective color.

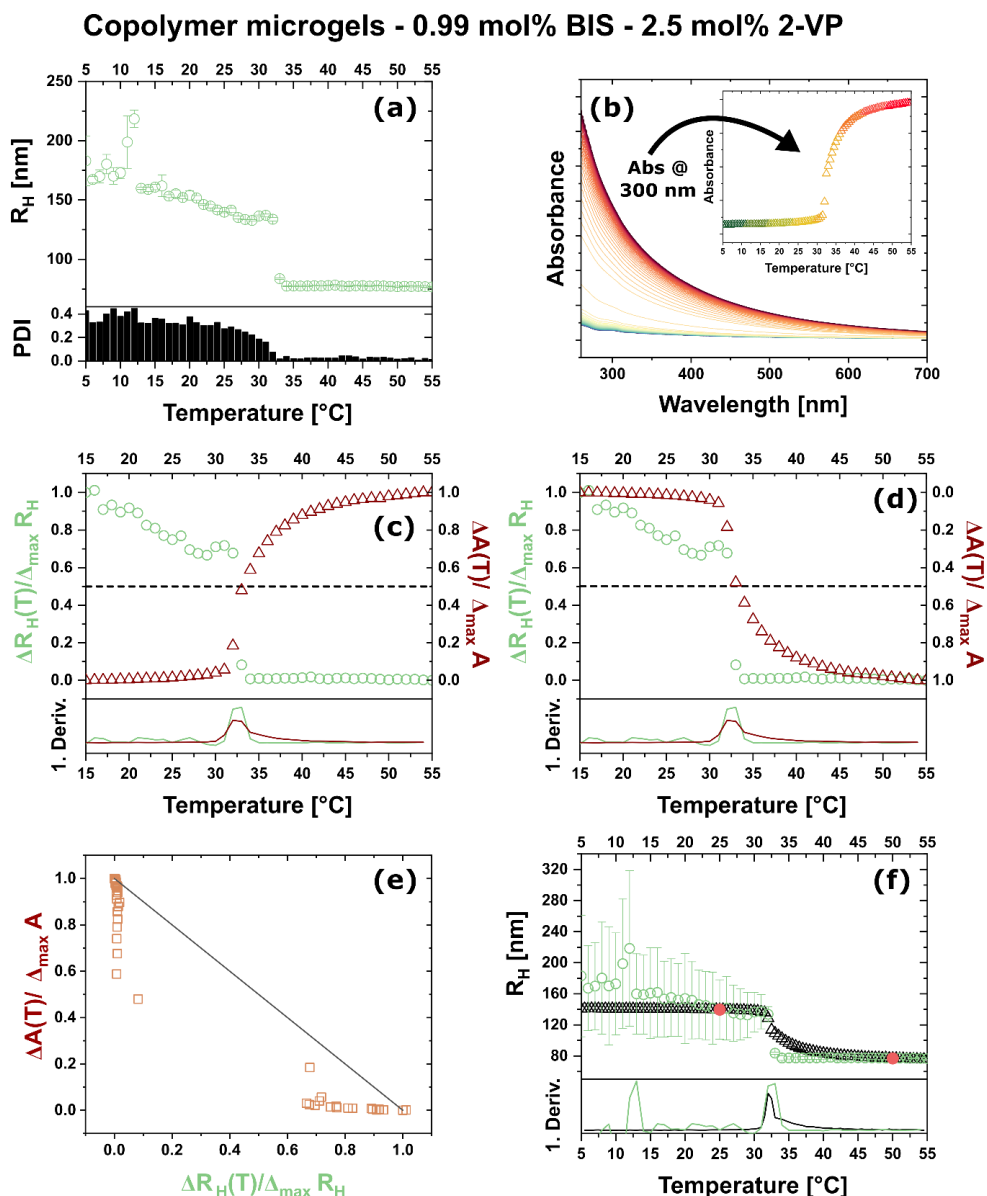


**Figure S5.21:** Overview of the characterization and processing of the measurement data for a copolymer microgel with a crosslinking degree of 0.99 mol% BIS. During the synthesis 2.5 mol% 2-VP were added to the reaction. The polymerization was initiated with 2 mg of KPS. Temperature-dependent DLS measurements including the poly dispersity indices (PDI) and temperature dependent UV-Vis absorbance measurements are presented in (a) and (b) respectively. The inset in (b) shows the plot of absorbance values at 300 nm against the respective temperature. (c) Plot of the normalized data from (a) in green and (b) in red against the temperature. (d) Alternative representation of the plot in (c). The y-axis that shows the normalized absorbance data is inverted to simplify the comparison of the normalized data. Both plots (c) and (d) include the first derivatives of the functions in the respective color. (e) Plot of the normalized absorbance against the normalized hydrodynamic radii. The black line indicates a slope of -1. (f) Comparison of the DLS data (green) and the calculated hydrodynamic radii by use of the absorbance data (black). Red dots represent the reference points from DLS at 25 and 50 °C which are needed for the calculation. Additionally presented is the first derivative of both functions in the respective color.

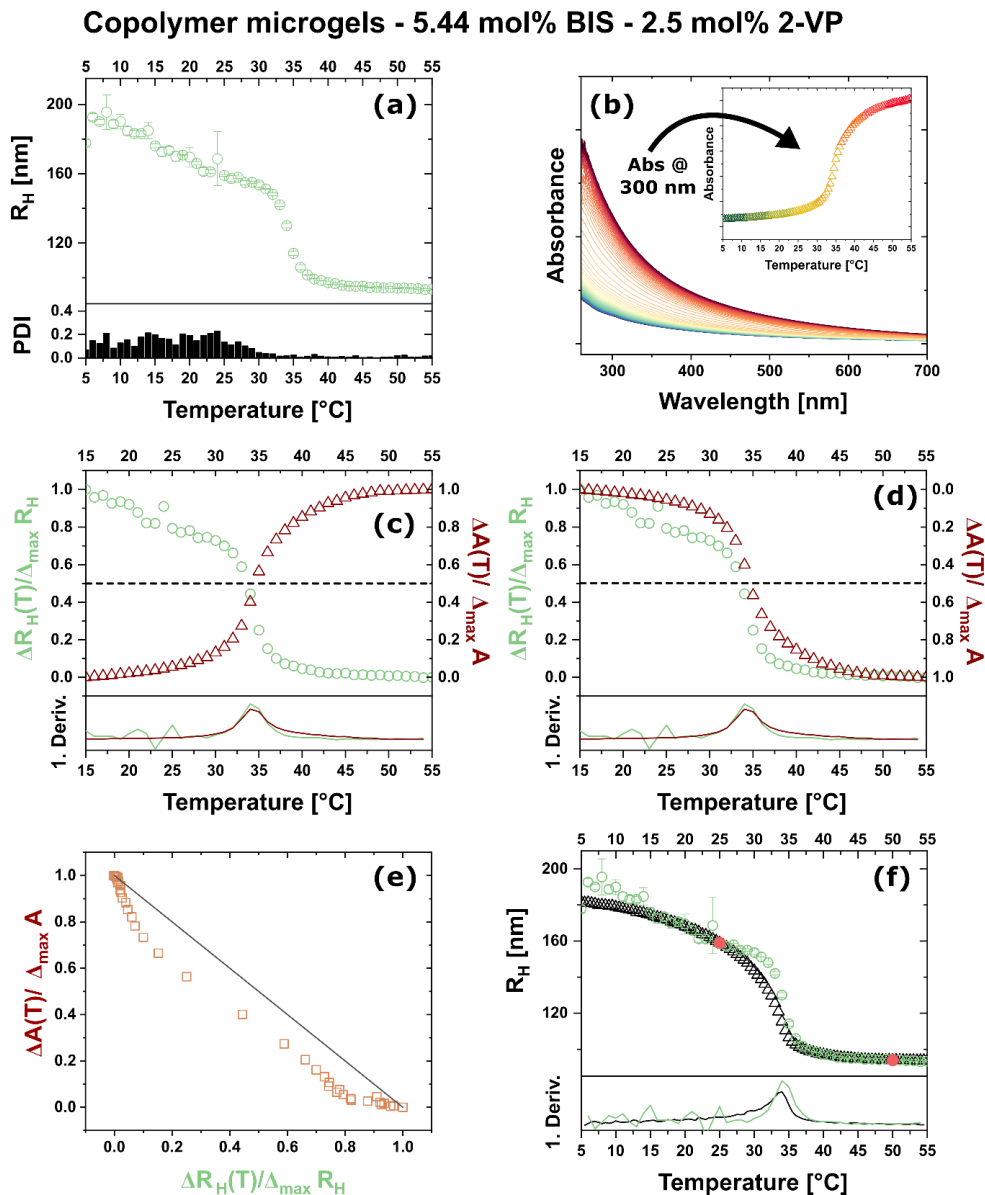


**Figure S5.22:** Overview of the characterization and processing of the measurement data for a copolymer microgel with a crosslinking degree of 5.44 mol% BIS. During the synthesis 2.5 mol% 2-VP were added to the reaction. The polymerization was initiated with 2 mg of KPS. Temperature-dependent DLS measurements including the poly dispersity indices (PDI) and temperature dependent UV-Vis absorbance measurements are presented in (a) and (b) respectively. The inset in (b) shows the plot of the absorbance values at 300 nm against the respective temperature. (c) Plot of the normalized data from (a) in green and (b) in red against the temperature. (d) Alternative representation of the plot in (c). The y-axis that shows the normalized absorbance data is inverted to simplify the comparison of the normalized data. Both plots (c) and (d) include the first derivatives of the functions in the respective color. (e) Plot of the normalized absorbance against the normalized hydrodynamic radii. The black line indicates a slope of -1. (f) Comparison of the DLS data (green) and the calculated hydrodynamic radii by use of the absorbance data (black). Red dots represent the reference points from DLS at 25 and 50 °C which are needed for the calculation. Additionally presented is the first derivative of both functions in the respective color.

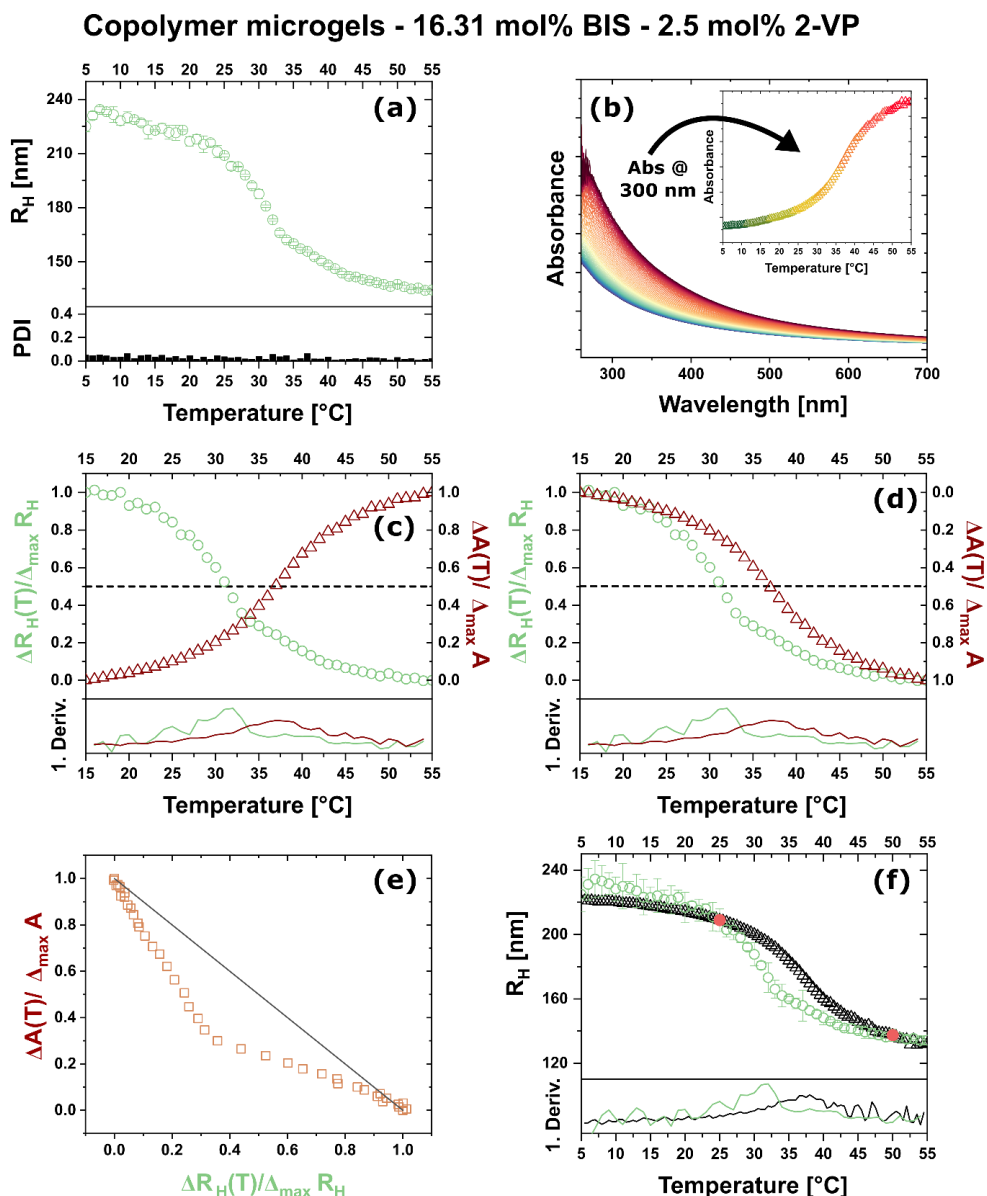


**Figure S5.23:** Overview of the characterization and processing of the measurement data for a copolymer microgel with a crosslinking degree of 16.31 mol% BIS. During the synthesis 2.5 mol% 2-VP were added to the reaction. The polymerization was initiated with 2 mg of KPS. Temperature-dependent DLS measurements including the poly dispersity indices (PDI) and temperature dependent UV-Vis absorbance measurements are presented in (a) and (b) respectively. The inset in (b) shows the absorbance values at 300 nm against the respective temperature. (c) Plot of the normalized data from (a) in green and (b) in red against the temperature. (d) Alternative representation of the plot in (c). The y-axis that shows the normalized absorbance data is inverted to simplify the comparison of the normalized data. Both plots (c) and (d) include the first derivatives of the functions in the respective color. (e) Plot of the normalized absorbance against the normalized hydrodynamic radii. The black line indicates a slope of -1. (f) Comparison of the DLS data (green) and the calculated hydrodynamic radii by use of the absorbance data (black). Red dots represent the reference points from DLS at 25 and 50 °C which are needed for the calculation. Additionally presented is the first derivative of both functions in the respective color.

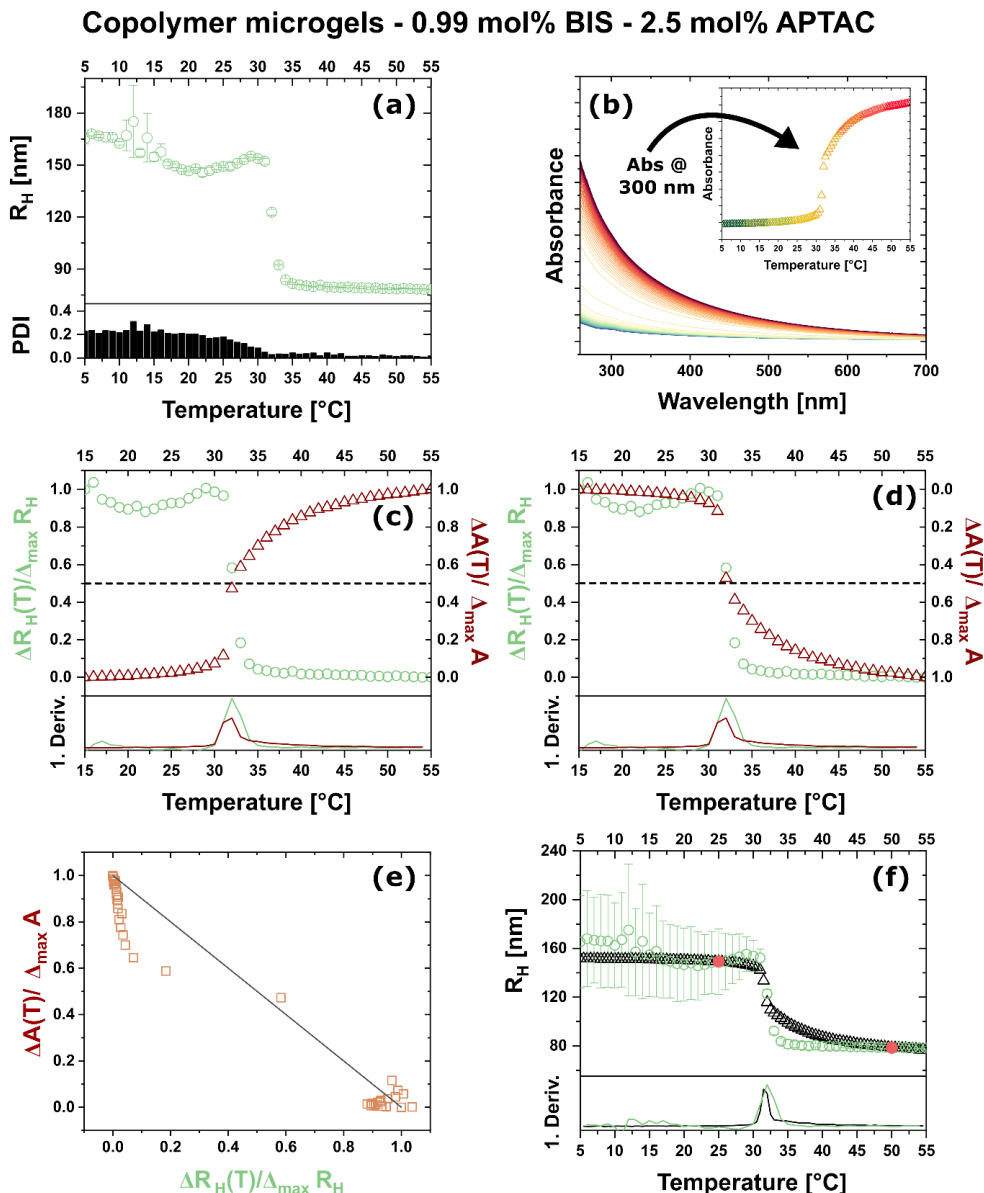


**Figure S5.24:** Overview of the characterization and processing of the measurement data for a copolymer microgel with a crosslinking degree of 0.99 mol% BIS. During the synthesis 2.5 mol% APTAC were added to the reaction. The polymerization was initiated with 2 mg of KPS. Temperature-dependent DLS measurements including the poly dispersity indices (PDI) and temperature dependent UV-Vis absorbance measurements are presented in (a) and (b) respectively. The inset in (b) shows the plot of the absorbance values at 300 nm against the respective temperature. (c) Plot of the normalized data from (a) in green and (b) in red against the temperature. (d) Alternative representation of the plot in (c). The y-axis that shows the normalized absorbance data is inverted to simplify the comparison of the normalized data. Both plots (c) and (d) include the first derivatives of the functions in the respective color. (e) Plot of the normalized absorbance against the normalized hydrodynamic radii. The black line indicates a slope of -1. (f) Comparison of the DLS data (green) and the calculated hydrodynamic radii by use of the absorbance data (black). Red dots represent the reference points from DLS at 25 and 50 °C which are needed for the calculation. Additionally presented is the first derivative of both functions in the respective color.

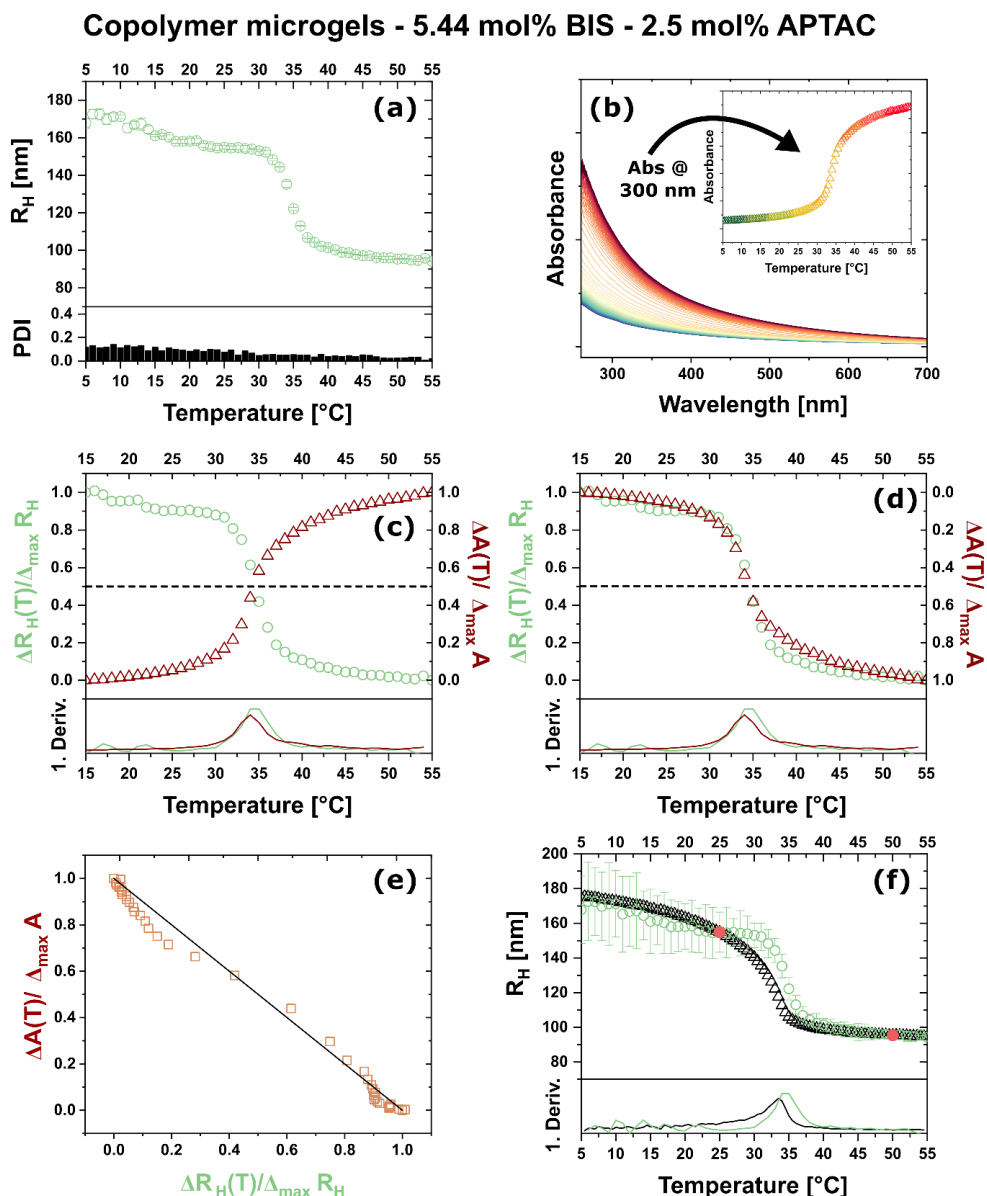


**Figure S5.25:** Overview of the characterization and processing of the measurement data for a copolymer microgel with a crosslinking degree of 5.44 mol% BIS. During the synthesis 2.5 mol% APTAC were added to the reaction. The polymerization was initiated with 2 mg of KPS. Temperature-dependent DLS measurements including the poly dispersity indices (PDI) and temperature dependent UV-Vis absorbance measurements are presented in (a) and (b) respectively. The inset in (b) shows the plot of the absorbance values at 300 nm against the respective temperature. (c) Plot of the normalized data from (a) in green and (b) in red against the temperature. (d) Alternative representation of the plot in (c). The y-axis that shows the normalized absorbance data is inverted to simplify the comparison of the normalized data. Both plots (c) and (d) include the first derivatives of the functions in the respective color. (e) Plot of the normalized absorbance against the normalized hydrodynamic radii. The black line indicates a slope of -1. (f) Comparison of the DLS data (green) and the calculated hydrodynamic radii by use of the absorbance data (black). Red dots represent the reference points from DLS at 25 and 50 °C which are needed for the calculation. Additionally presented is the first derivative of both functions in the respective color.

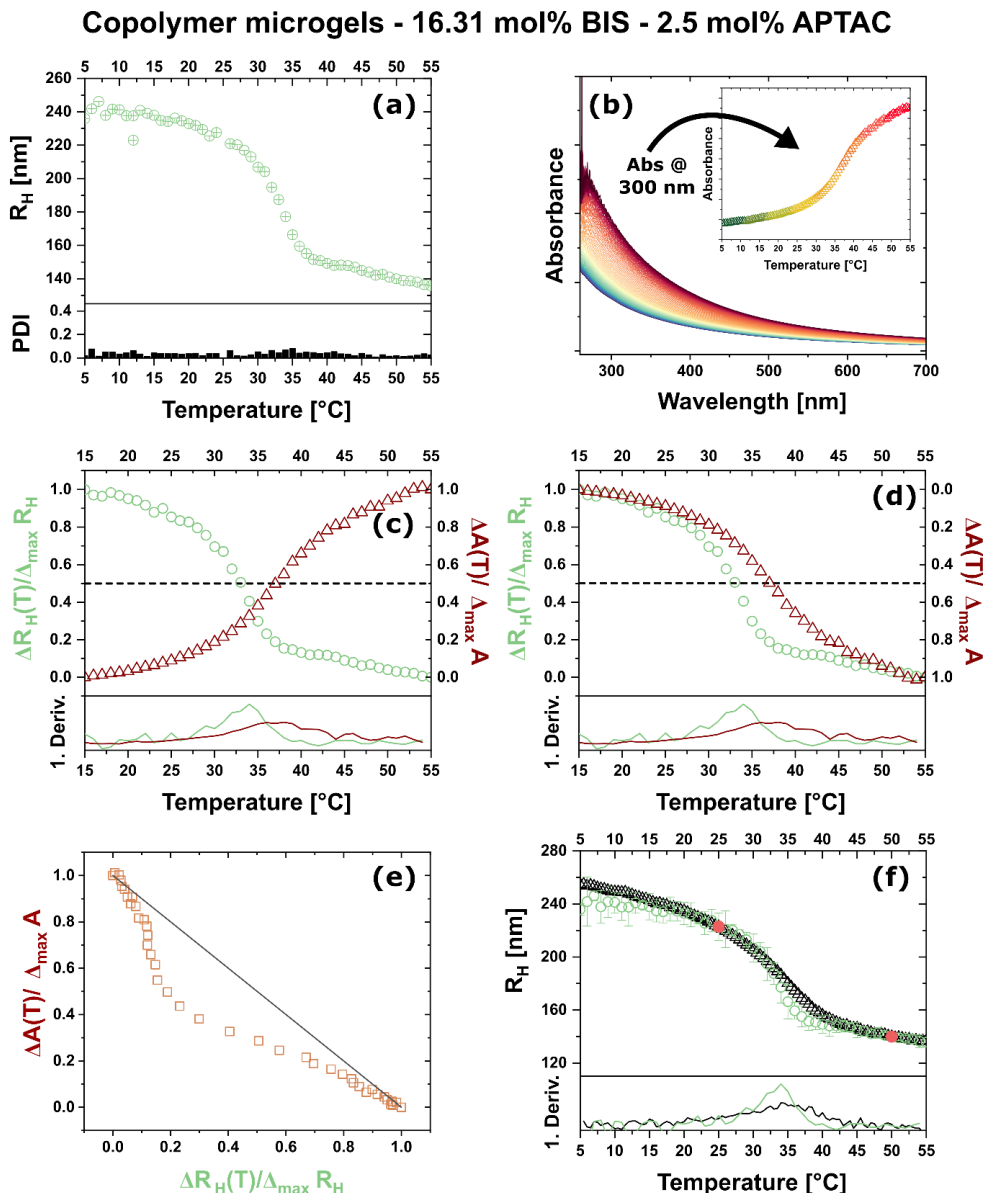


**Figure S5.26:** Overview of the characterization and processing of the measurement data for a copolymer microgel with a crosslinking degree of 16.31 mol% BIS. During the synthesis 2.5 mol% APTAC were added to the reaction. The polymerization was initiated with 2 mg of KPS. Temperature-dependent DLS measurements including the poly dispersity indices (PDI) and temperature dependent UV-Vis absorbance measurements are presented in (a) and (b) respectively. The inset in (b) shows the plot of absorbance values at 300 nm against the respective temperature. (c) Plot of the normalized data from (a) in green and (b) in red against the temperature. (d) Alternative representation of the plot in (c). The y-axis that shows the normalized absorbance data is inverted to simplify the comparison of the normalized data. Both plots (c) and (d) include the first derivatives of the functions in the respective color. (e) Plot of the normalized absorbance against the normalized hydrodynamic radii. The black line indicates a slope of -1. (f) Comparison of the DLS data (green) and the calculated hydrodynamic radii by use of the absorbance data (black). Red dots represent the reference points from DLS at 25 and 50 °C which are needed for the calculation. Additionally presented is the first derivative of both functions in the respective color.

5. Following the volume phase transition of thermoresponsive microgels by dynamic light scattering and turbidity: Correlations depend on microgel homogeneity

**Table S5.2:** Determined hydrodynamic radii below the VPTT at 25 °C and above the VPTT at 50 °C, VPTT by DLS and absorbance measurements and important components of the investigated copolymer microgels.

Microgel	Crosslinker [mol%]	Comonomer [mol%]	R <sub>H</sub> @ 25 °C [nm]	R <sub>H</sub> @ 50 °C [nm]	VPTT DLS [°C]	VPTT Abs. [°C]
AAC <sub>2.5mol%</sub> - 0.99	0.99	2.5 - AAc	330 ± 36	167 ± 3	32.5	31.5
AAC <sub>2.5mol%</sub> - 5.44	5.44	2.5 - AAc	389 ± 27	221 ± 6	35.5	34.0
AAC <sub>2.5mol%</sub> - 16.31	16.31	2.5 - AAc	363 ± 16	255 ± 3	28.0	36.5
AMPS <sub>2.5mol%</sub> - 0.99	0.99	2.5 - AMPS	135 ± 39	89 ± 4	33.0	32.0
AMPS <sub>2.5mol%</sub> - 5.44	5.44	2.5 - AMPS	145 ± 19	89 ± 5	34.5	37.0
AMPS <sub>2.5mol%</sub> - 16.31	16.31	2.5 - AMPS	150 ± 12	120 ± 4	39.0	34.0
APTAC <sub>2.5mol%</sub> - 0.99	0.99	2.5 - APTAC	149 ± 27	79 ± 2	32.0	31.5
APTAC <sub>2.5mol%</sub> - 5.44	5.44	2.5 - APTAC	155 ± 12	95 ± 2	33.5	34.0
APTAC <sub>2.5mol%</sub> - 16.31	16.31	2.5 - APTAC	223 ± 10	140 ± 3	34.0	37.0
2-VP <sub>2.5mol%</sub> - 0.99	0.99	2.5 - 2-VP	140 ± 38	77 ± 1	32.5	32.5
2-VP <sub>2.5mol%</sub> - 5.44	5.44	2.5 - 2-VP	159 ± 21	94 ± 2	34.0	34.0
2-VP <sub>2.5mol%</sub> - 16.31	16.31	2.5 - 2-VP	209 ± 7	138 ± 4	32.0	37.0

Core-Shell Microgels with SiO<sub>2</sub> cores

SiO<sub>2</sub>-core-shell microgel - 15 mol% BIS - r<sub>core</sub>: 18 nm

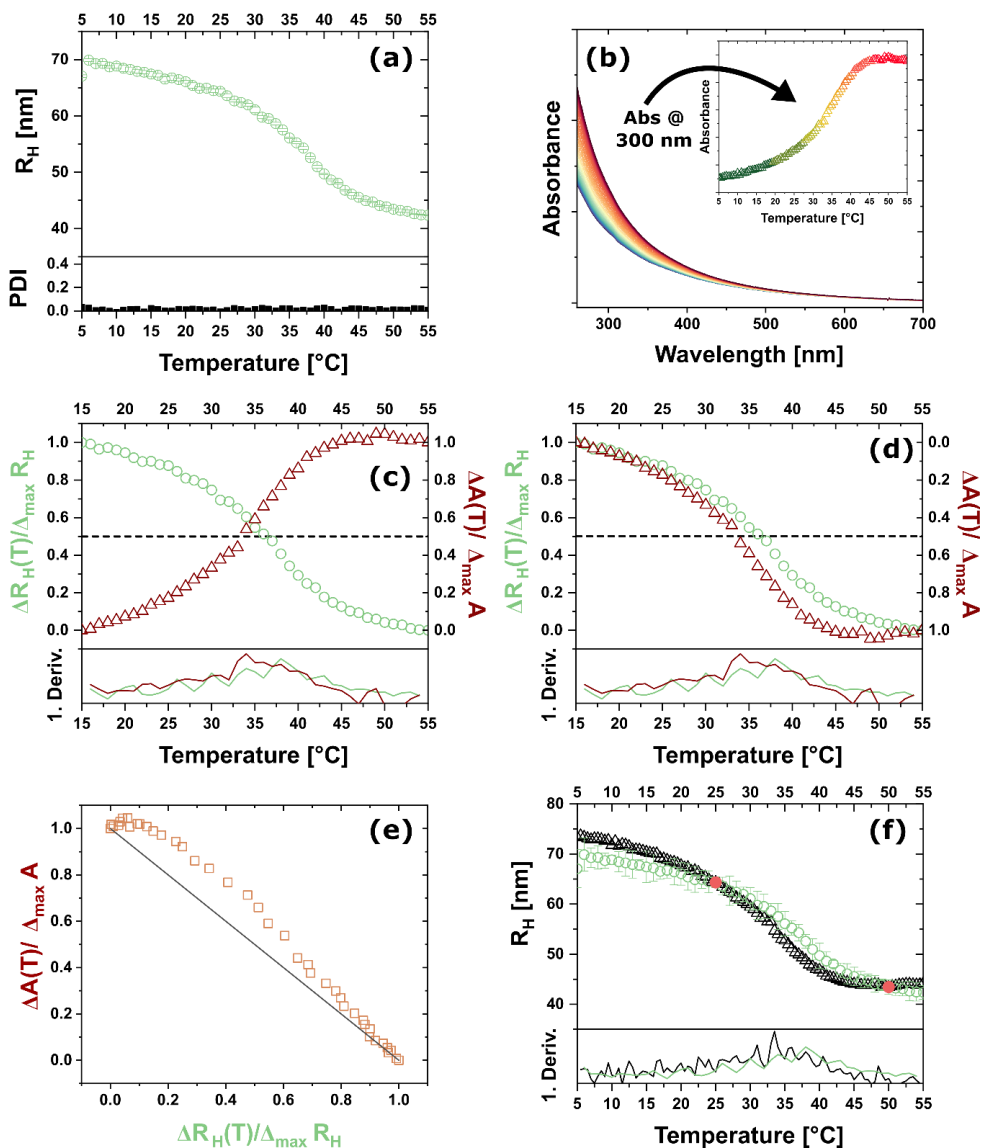


**Figure S5.27:** Overview of the characterization and processing of the measurement data for a core-shell microgel with a SiO<sub>2</sub> core. The microgel shell is crosslinked with 15 mol% BIS and the encapsulated silica core has a radius of 18 ± 2 nm. Temperature-dependent DLS measurements including the polydispersity indices (PDI) and temperature dependent UV-Vis absorbance measurements are presented in (a) and (b) respectively. The inset in (b) shows the plot of the absorbance values at 300 nm against the respective temperature. (c) Plot of the normalized data from (a) in green and (b) in red against the temperature. (d) Alternative representation of the plot in (c). The y-axis that shows the normalized absorbance data is inverted to simplify the comparison of the normalized data. Both plots (c) and (d) include the first derivatives of the functions in the respective color. (e) Plot of the normalized absorbance against the normalized hydrodynamic radii. The black line indicates a slope of -1. (f) Comparison of the DLS data (green) and the calculated hydrodynamic radii by use of the absorbance data (black). Red dots represent the reference points from DLS at 25 and 50 °C which are needed for the calculation. Additionally presented is the first derivative of both functions in the respective color.

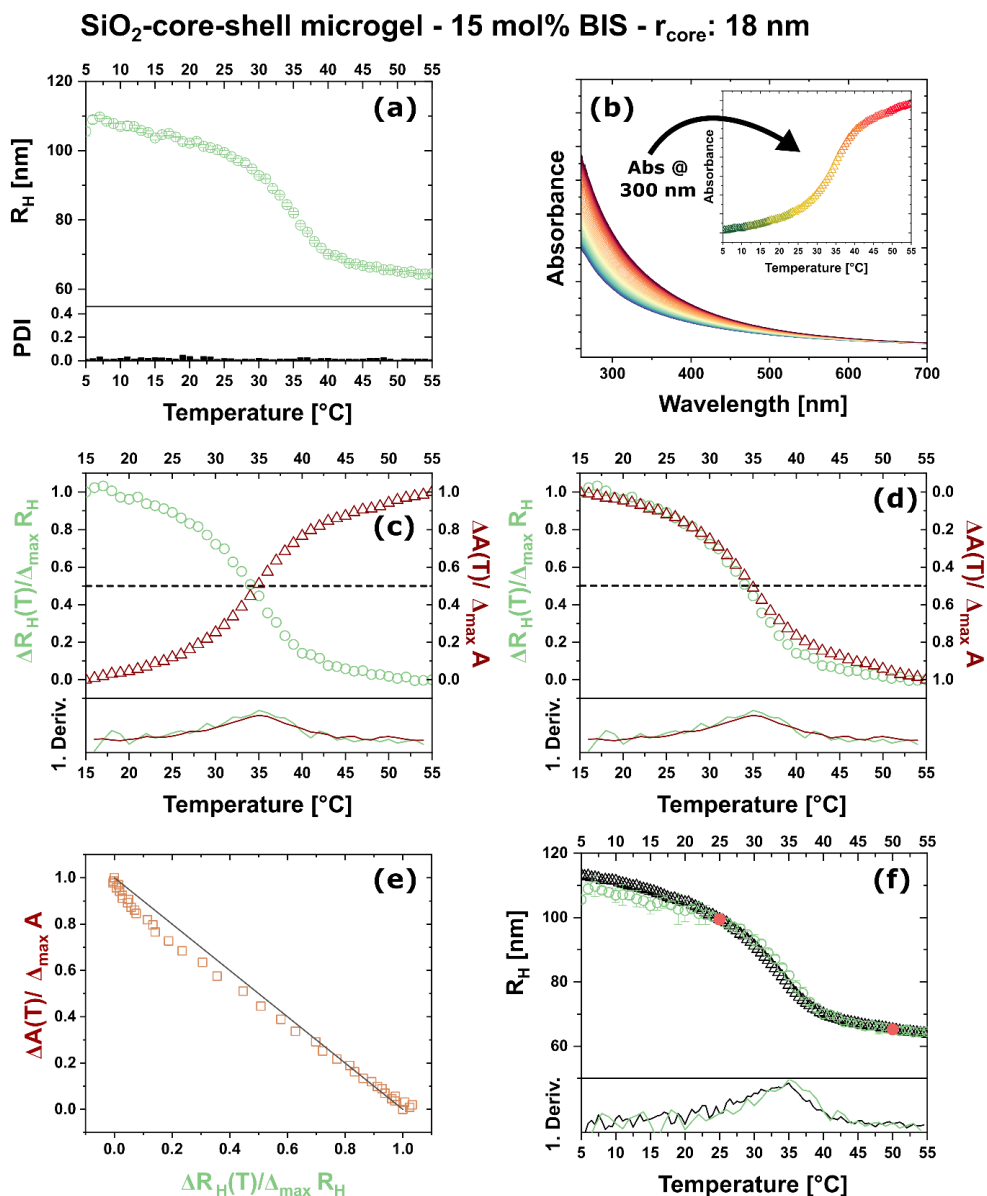


**Figure S5.28:** Overview of the characterization and processing of the measurement data for a core-shell microgel with a SiO<sub>2</sub> core. The microgel shell is crosslinked with 15 mol% BIS and the encapsulated silica core has a radius of  $18 \pm 2$  nm. Temperature-dependent DLS measurements including the polydispersity indices (PDI) and temperature dependent UV-Vis absorbance measurements are presented in (a) and (b) respectively. The inset in (b) shows the plot of the absorbance values at 300 nm against the respective temperature. (c) Plot of the normalized data from (a) in green and (b) in red against the temperature. (d) Alternative representation of the plot in (c). The y-axis that shows the normalized absorbance data is inverted to simplify the comparison of the normalized data. Both plots (c) and (d) include the first derivatives of the functions in the respective color. (e) Plot of the normalized absorbance against the normalized hydrodynamic radii. The black line indicates a slope of -1. (f) Comparison of the DLS data (green) and the calculated hydrodynamic radii by use of the absorbance data (black). Red dots represent the reference points from DLS at 25 and 50 °C which are needed for the calculation. Additionally presented is the first derivative of both functions in the respective color.

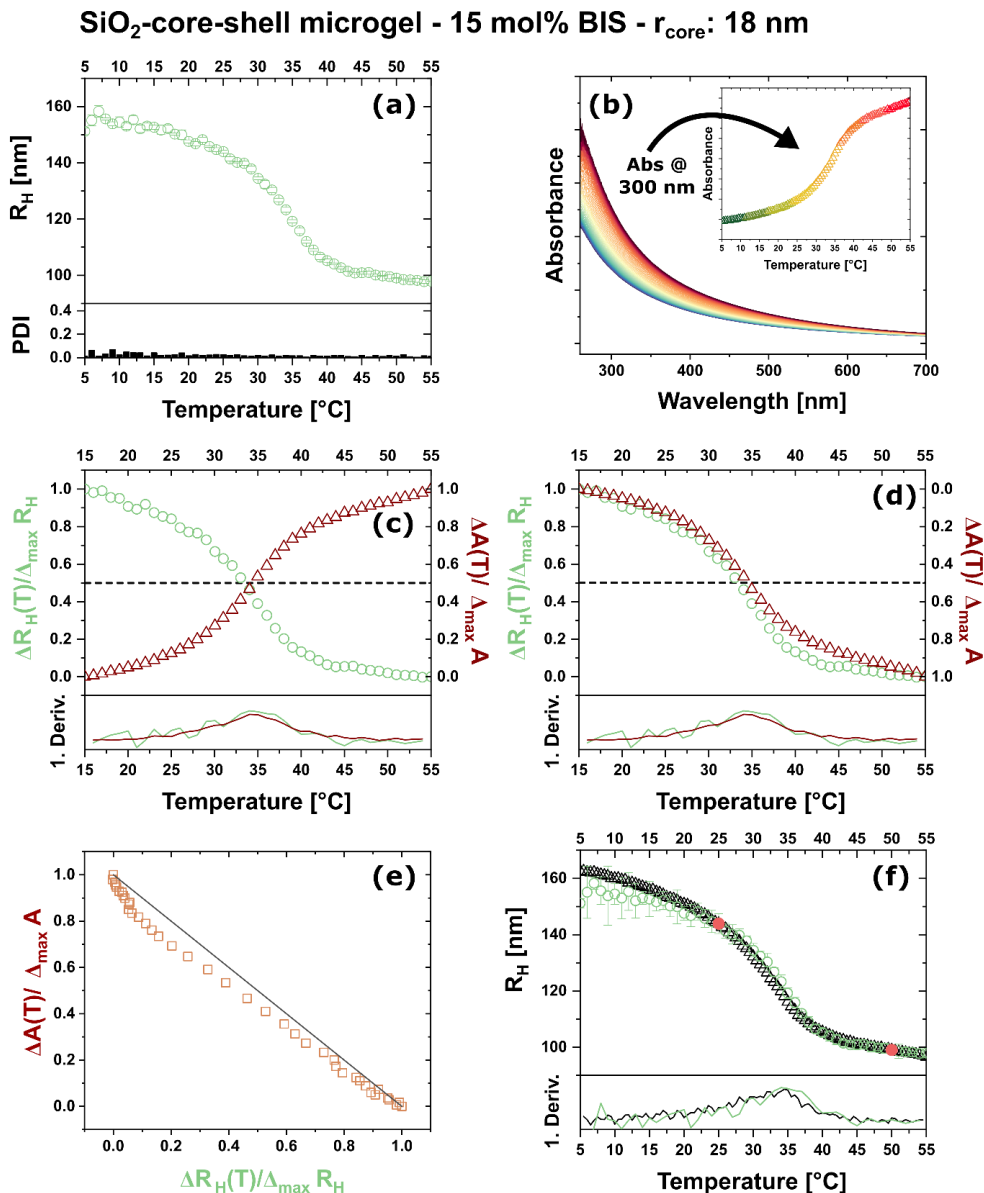


**Figure S5.29:** Overview of the characterization and processing of the measurement data for a core-shell microgel with a SiO<sub>2</sub> core. The microgel shell is crosslinked with 15 mol% BIS and the encapsulated silica core has a radius of  $18 \pm 2$  nm. Temperature-dependent DLS measurements including the polydispersity indices (PDI) and temperature dependent UV-Vis absorbance measurements are presented in (a) and (b) respectively. (c) Plot of the normalized data from (a) in green and (b) in red against the temperature. (d) Alternative representation of the plot in (c). The y-axis that shows the normalized absorbance data is inverted to simplify the comparison of the normalized data. Both plots (c) and (d) include the first derivatives of the functions in the respective color. (e) Plot of the normalized absorbance against the normalized hydrodynamic radii. The black line indicates a slope of -1. (f) Comparison of the DLS data (green) and the calculated hydrodynamic radii by use of the absorbance data (black). Red dots represent the reference points from DLS at 25 and 50 °C which are needed for the calculation. Additionally presented is the first derivative of both functions in the respective color.

**SiO<sub>2</sub>-core-shell microgel - 15 mol% BIS -  $r_{\text{core}}$ : 18 nm - 1 mol% AMPS**

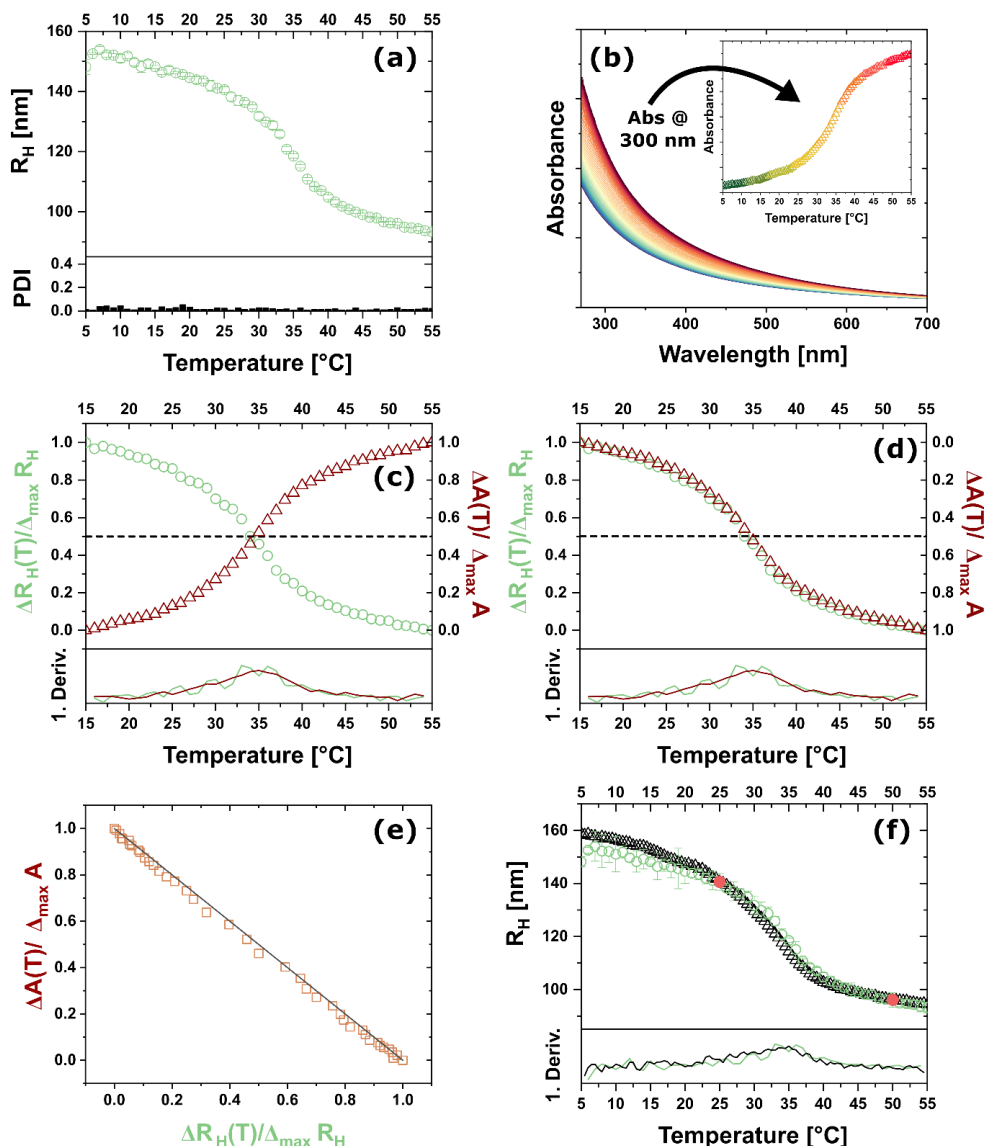


**Figure S5.30:** Overview of the characterization and processing of the measurement data for a core-shell microgel with a SiO<sub>2</sub> core. The microgel shell is crosslinked with 15 mol% BIS and the encapsulated silica core has a radius of  $18 \pm 2$  nm. During the encapsulation of the silica core 1 mol% AMPS were added to the reaction. Temperature-dependent DLS measurements including the poly dispersity indices (PDI) and temperature dependent UV-Vis absorbance measurements are presented in (a) and (b) respectively. The inset in (b) shows the plot of the absorbance values at 300 nm against the respective temperature. (c) Plot of the normalized data from (a) in green and (b) in red against the temperature. (d) Alternative representation of the plot in (c). The y-axis that shows the normalized absorbance data is inverted to simplify the comparison of the normalized data. Both plots (c) and (d) include the first derivatives of the functions in the respective color. (e) Plot of the normalized absorbance against the normalized hydrodynamic radii. The black line indicates a slope of -1. (f) Comparison of the DLS data (green) and the calculated hydrodynamic radii by use of the absorbance data (black). Red dots represent the reference points from DLS at 25 and 50 °C which are needed for the calculation. Additionally presented is the first derivative of both functions in the respective color.

SiO<sub>2</sub>-core-shell microgel - 15 mol% BIS - r<sub>core</sub>: 18 nm - 2.5 mol% AMPS

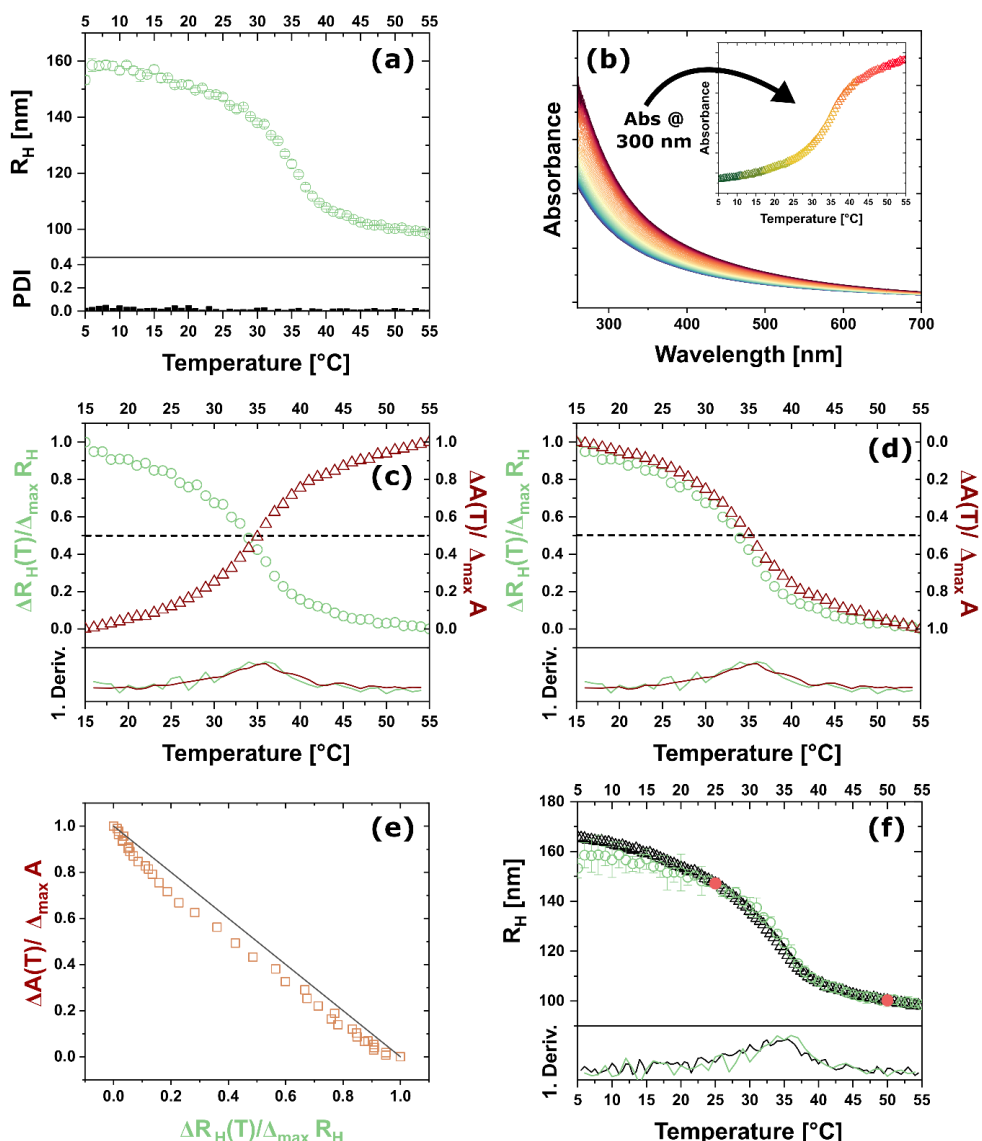


**Figure S5.31:** Overview of the characterization and processing of the measurement data for a core-shell microgel with a SiO<sub>2</sub> core. The microgel shell is crosslinked with 15 mol% BIS and the encapsulated silica core has a radius of  $18 \pm 2$  nm. During the encapsulation of the silica core 2.5 mol% AMPS were added to the reaction. Temperature-dependent DLS measurements including the polydispersity indices (PDI) and temperature dependent UV-Vis absorbance measurements are presented in (a) and (b) respectively. The inset in (b) shows the plot of the absorbance values at 300 nm against the respective temperature. (c) Plot of the normalized data from (a) in green and (b) in red against the temperature. (d) Alternative representation of the plot in (c). The y-axis that shows the normalized absorbance data is inverted to simplify the comparison of the normalized data. Both plots (c) and (d) include the first derivatives of the functions in the respective color. (e) Plot of the normalized absorbance against the normalized hydrodynamic radii. The black line indicates a slope of -1. (f) Comparison of the DLS data (green) and the calculated hydrodynamic radii by use of the absorbance data (black). Red dots represent the reference points from DLS at 25 and 50 °C which are needed for the calculation. Additionally presented is the first derivative of both functions in the respective color.

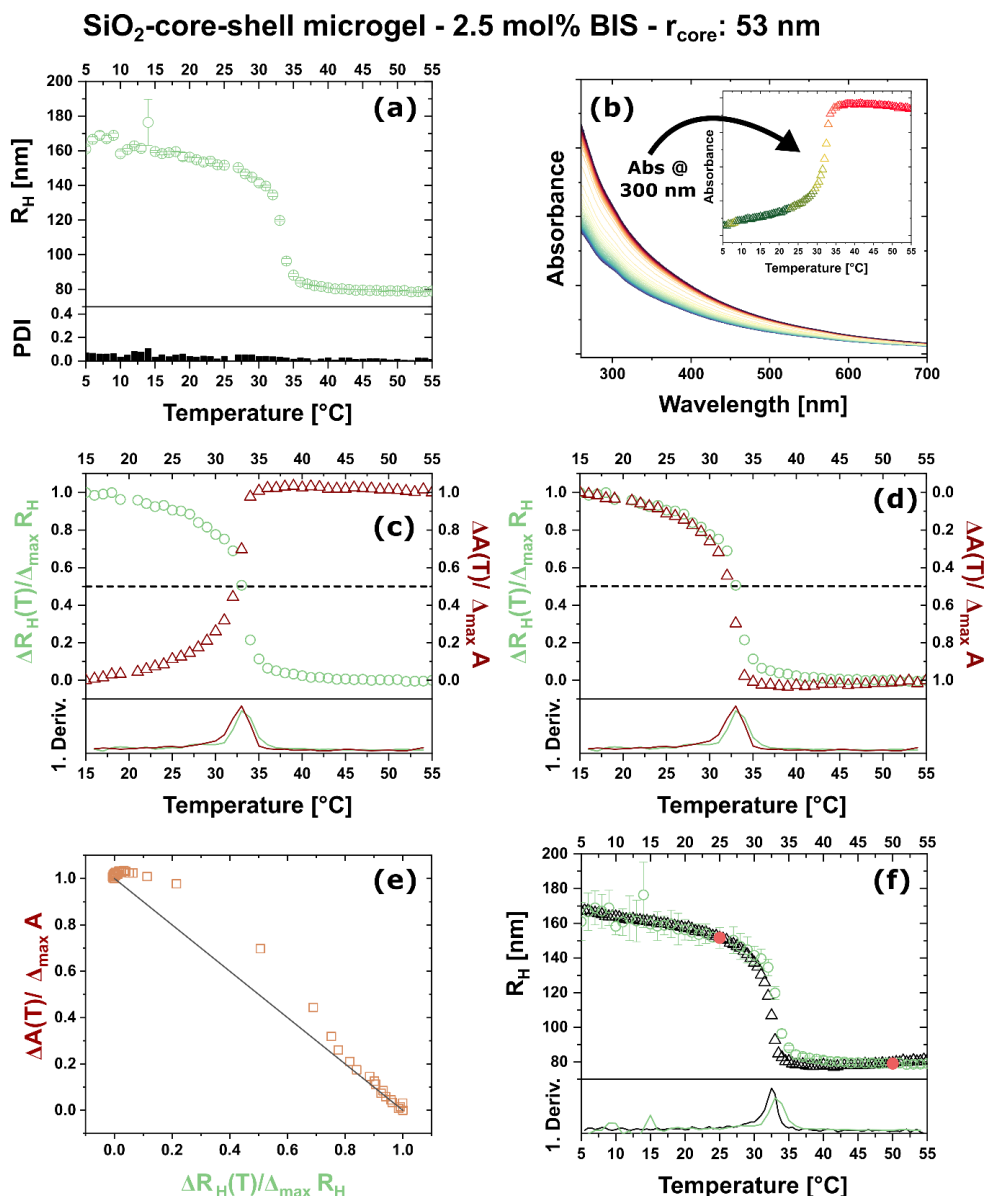


**Figure S5.32:** Overview of the characterization and processing of the measurement data for a core-shell microgel with a SiO<sub>2</sub> core. The microgel shell is crosslinked with 2.5 mol% BIS and the encapsulated silica core has a radius of  $53 \pm 3$  nm. Temperature-dependent DLS measurements including the polydispersity indices (PDI) and temperature dependent UV-Vis absorbance measurements are presented in (a) and (b) respectively. The inset in (b) shows the plot of the absorbance values at 300 nm against the respective temperature. (c) Plot of the normalized data from (a) in green and (b) in red against the temperature. (d) Alternative representation of the plot in (c). The y-axis that shows the normalized absorbance data is inverted to simplify the comparison of the normalized data. Both plots (c) and (d) include the first derivatives of the functions in the respective color. (e) Plot of the normalized absorbance against the normalized hydrodynamic radii. The black line indicates a slope of -1. (f) Comparison of the DLS data (green) and the calculated hydrodynamic radii by use of the absorbance data (black). Red dots represent the reference points from DLS at 25 and 50 °C which are needed for the calculation. Additionally presented is the first derivative of both functions in the respective color.

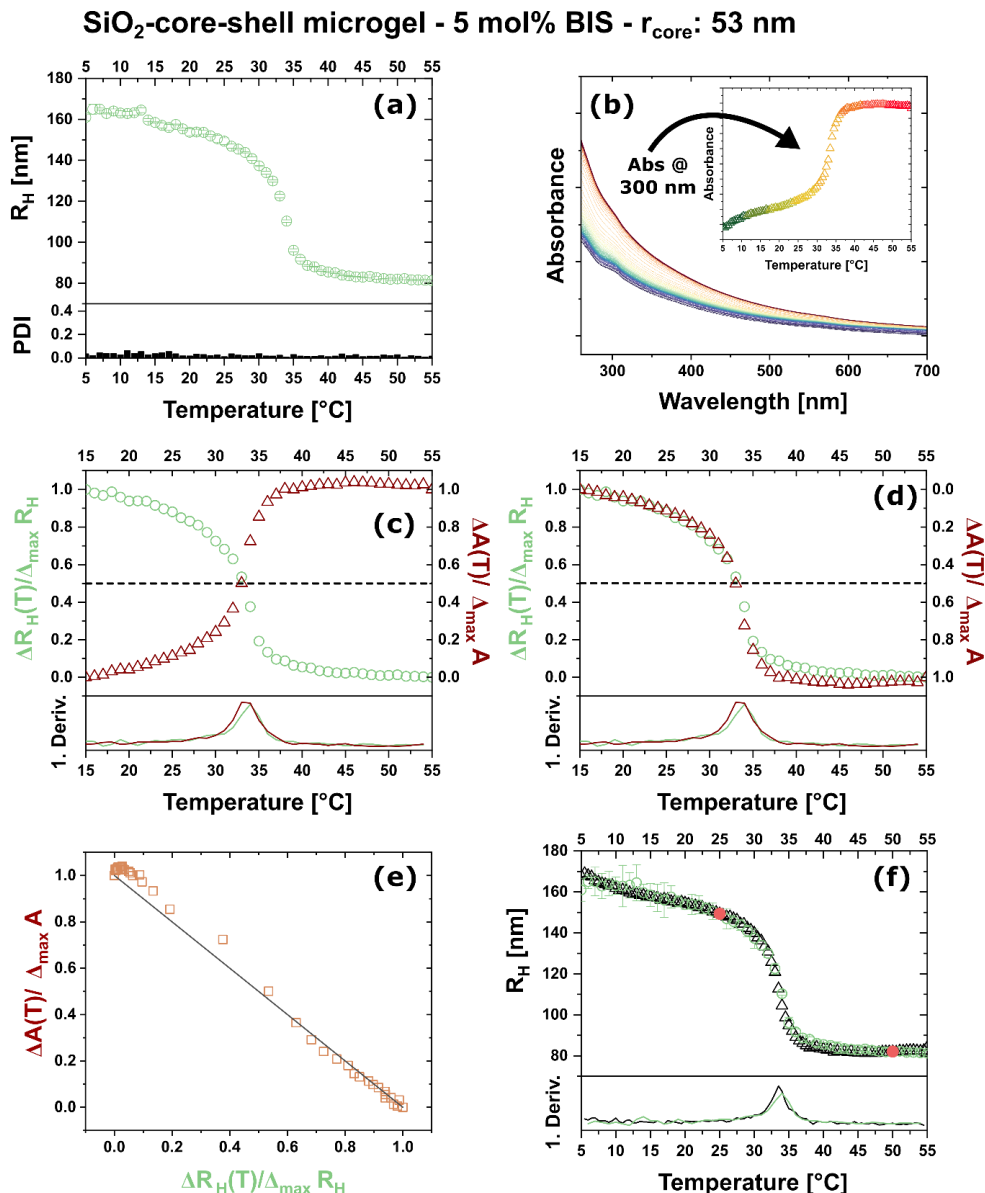


**Figure S5.33:** Overview of the characterization and processing of the measurement data for a core-shell microgel with a SiO<sub>2</sub> core. The microgel shell is crosslinked with 5 mol% BIS and the encapsulated silica core has a radius of  $53 \pm 3$  nm. Temperature-dependent DLS measurements including the polydispersity indices (PDI) and temperature dependent UV-Vis absorbance measurements are presented in (a) and (b) respectively. The inset in (b) shows the plot of the absorbance values at 300 nm against the respective temperature. (c) Plot of the normalized data from (a) in green and (b) in red against the temperature. (d) Alternative representation of the plot in (c). The y-axis that shows the normalized absorbance data is inverted to simplify the comparison of the normalized data. Both plots (c) and (d) include the first derivatives of the functions in the respective color. (e) Plot of the normalized absorbance against the normalized hydrodynamic radii. The black line indicates a slope of -1. (f) Comparison of the DLS data (green) and the calculated hydrodynamic radii by use of the absorbance data (black). Red dots represent the reference points from DLS at 25 and 50 °C which are needed for the calculation. Additionally presented is the first derivative of both functions in the respective color.

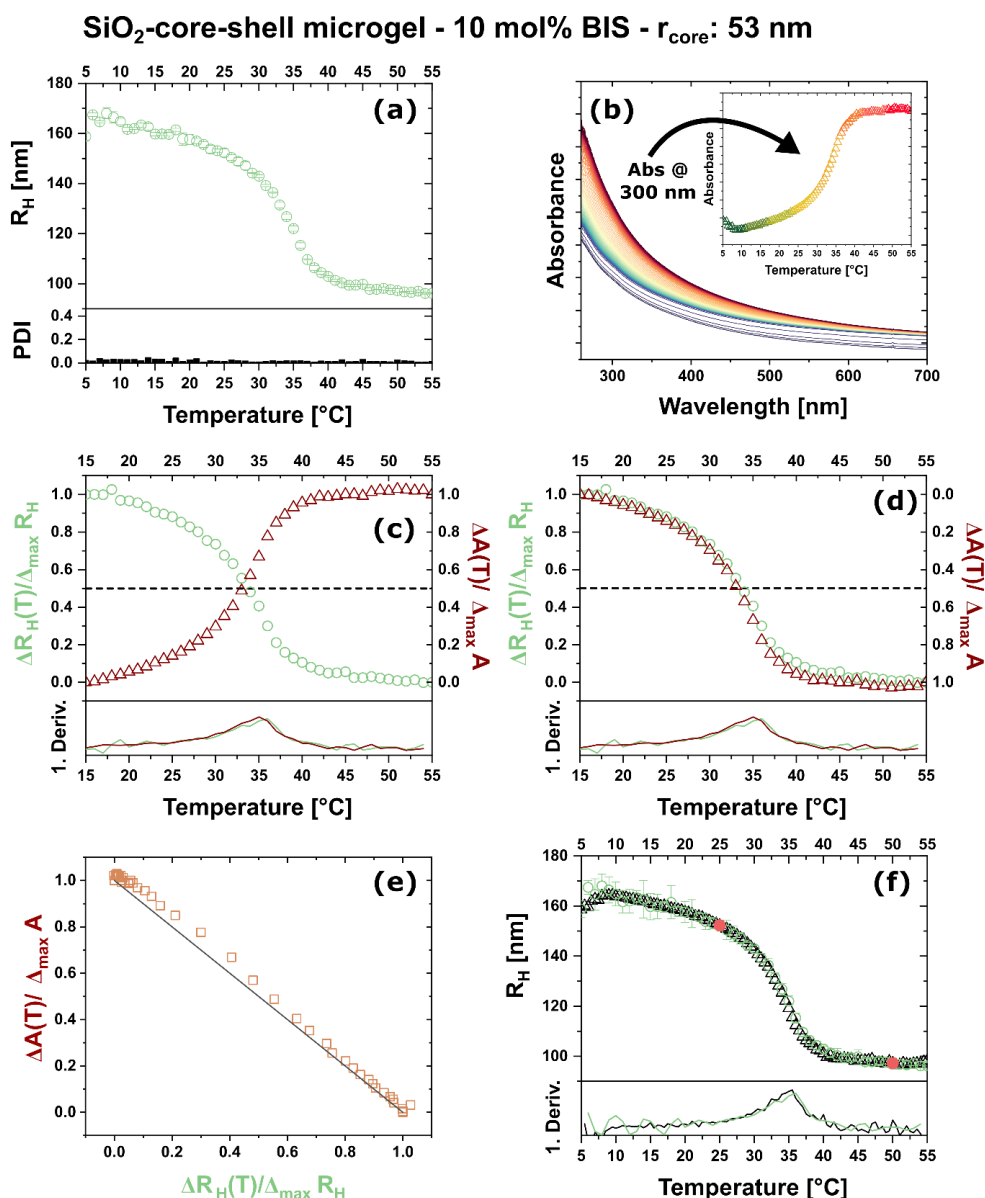


**Figure S5.34:** Overview of the characterization and processing of the measurement data for a core-shell microgel with a SiO<sub>2</sub> core. The microgel shell is crosslinked with 10 mol% BIS and the encapsulated silica core has a radius of  $53 \pm 3$  nm. Temperature-dependent DLS measurements including the polydispersity indices (PDI) and temperature dependent UV-Vis absorbance measurements are presented in (a) and (b) respectively. The inset in (b) shows the plot of the absorbance values at 300 nm against the respective temperature. (c) Plot of the normalized data from (a) in green and (b) in red against the temperature. (d) Alternative representation of the plot in (c). The y-axis that shows the normalized absorbance data is inverted to simplify the comparison of the normalized data. Both plots (c) and (d) include the first derivatives of the functions in the respective color. (e) Plot of the normalized absorbance against the normalized hydrodynamic radii. The black line indicates a slope of -1. (f) Comparison of the DLS data (green) and the calculated hydrodynamic radii by use of the absorbance data (black). Red dots represent the reference points from DLS at 25 and 50 °C which are needed for the calculation. Additionally presented is the first derivative of both functions in the respective color.

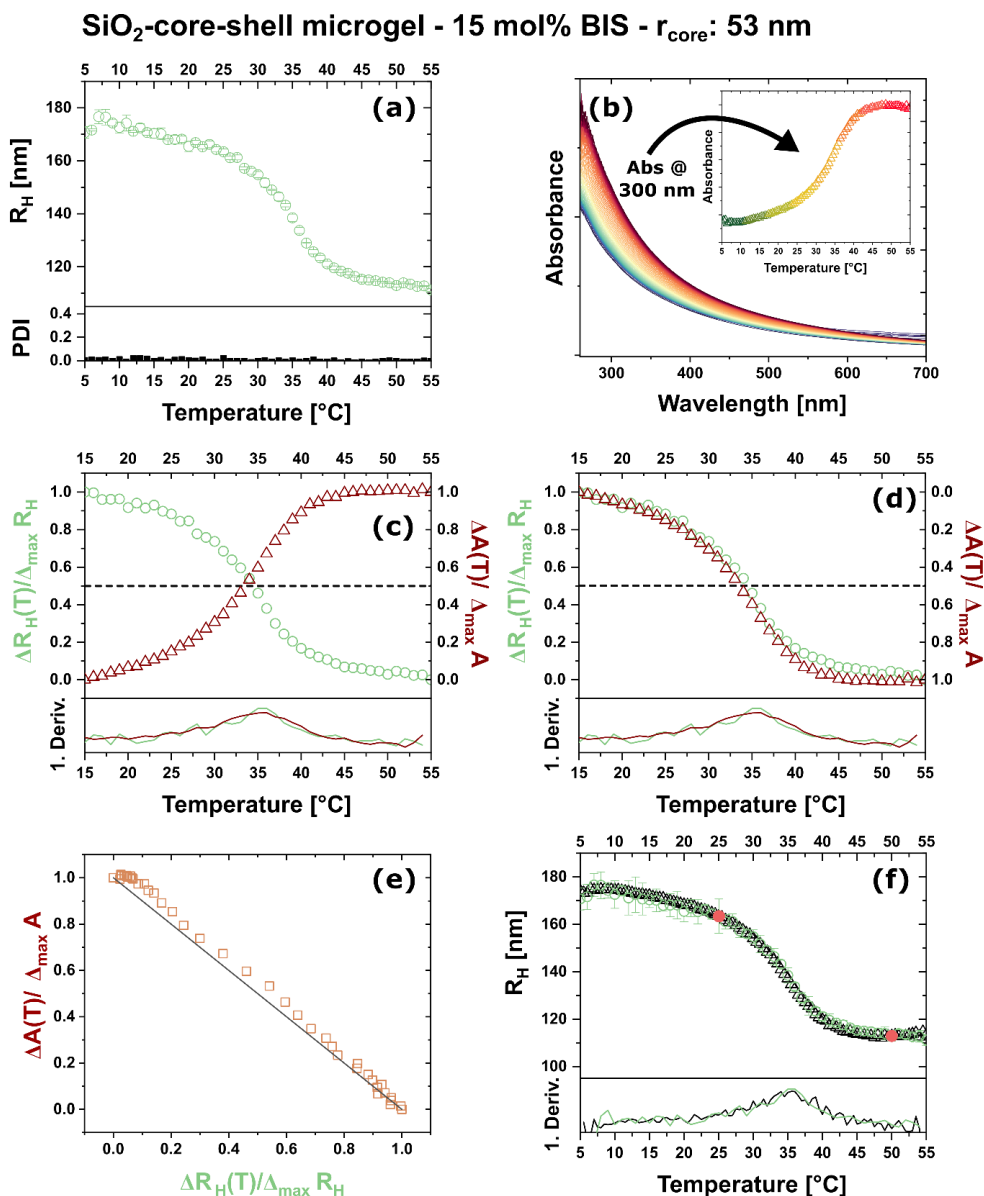


**Figure S5.35:** Overview of the characterization and processing of the measurement data for a core-shell microgel with a SiO<sub>2</sub> core. The microgel shell is crosslinked with 15 mol% BIS and the encapsulated silica core has a radius of  $53 \pm 3$  nm. Temperature-dependent DLS measurements including the poly dispersity indices (PDI) and temperature dependent UV-Vis absorbance measurements are presented in (a) and (b) respectively. The inset in (b) shows the plot of the absorbance values at 300 nm against the respective temperature. (c) Plot of the normalized data from (a) in green and (b) in red against the temperature. (d) Alternative representation of the plot in (c). The y-axis that shows the normalized absorbance data is inverted to simplify the comparison of the normalized data. Both plots (c) and (d) include the first derivatives of the functions in the respective color. (e) Plot of the normalized absorbance against the normalized hydrodynamic radii. The black line indicates a slope of -1. (f) Comparison of the DLS data (green) and the calculated hydrodynamic radii by use of the absorbance data (black). Red dots represent the reference points from DLS at 25 °C and 50 °C which are needed for the calculation. Additionally presented is the first derivative of both functions in the respective color.

5. Following the volume phase transition of thermoresponsive microgels by dynamic light scattering and turbidity: Correlations depend on microgel homogeneity

**Table S5.3:** Determined hydrodynamic radii below the VPTT at 25 °C and above the VPTT at 50 °C, VPTT by DLS and absorbance measurements and important components of the investigated core-shell microgels with SiO<sub>2</sub> cores.

Microgel	Crosslinker [mol%]	Comonomer [mol%]	R <sub>SiO<sub>2</sub>-Core</sub> [nm]	R <sub>H@25 °C</sub> [nm]	R <sub>H@50 °C</sub> [nm]	VPTT DLS [°C]	VPTT Abs. [°C]
C <sub>18</sub> S <sub>65</sub> -15	15	-	18 ± 2	64 ± 2	43 ± 1	37.0	35.0
C <sub>18</sub> S <sub>100</sub> -15	15	-	18 ± 2	99 ± 2	65 ± 0	35.0	35.0
C <sub>18</sub> S <sub>155</sub> -15	15	-	18 ± 2	144 ± 4	99 ± 1	35.5	35.0
C <sub>18</sub> S <sub>155</sub> -15-co-AMPS <sub>1mol%</sub>	15	2.5 (AMPS)	18 ± 2	141 ± 3	96 ± 3	35.0	35.0
C <sub>18</sub> S <sub>163</sub> -15-co-AMPS <sub>2.5mol%</sub>	15	2.5 (AMPS)	18 ± 2	147 ± 1	100 ± 2	35.5	35.0
C <sub>53</sub> S <sub>154</sub> -2.5	2.5	-	53 ± 3	152 ± 6	79 ± 1	33.0	33.0
C <sub>53</sub> S <sub>152</sub> -5	5	-	53 ± 3	149 ± 1	82 ± 2	34.0	33.5
C <sub>53</sub> S <sub>158</sub> -10	10	-	53 ± 3	152 ± 2	97 ± 2	35.5	35.0
C <sub>53</sub> S <sub>152</sub> -15	15	-	53 ± 3	163 ± 7	113 ± 2	35.0	35.0



## 6. Conclusion and Perspectives

This thesis focused on the synthesis and characterization of complex copolymer microgels. First, an in situ approach for the formation of gold nanoparticles within PNIPAM-based copolymer microgels was introduced. This approach represents a promising alternative to established encapsulation protocols to obtain hybrid core-shell microgels in a controlled manner. However, the successful formation of single gold nanoparticles raised new questions about the internal structure of complex copolymer microgels and an inhomogeneous distribution of individual components in the network. Then, initiated by these findings, a novel analytical methodology that could provide insights into inhomogeneities of the inner structure of microgels was evaluated. This methodology is based on the combination of temperature-dependent DLS and temperature-dependent UV-Vis absorbance measurements. In the following the main findings of this thesis are shortly summarized and concluded.

In the first part of this work, a protocol to perform in situ synthesis and overgrowth of single gold nanoparticles within PNIPAM-based microgels was established. The resulting hybrid microgel systems were characterized with various methods including DLS, SAXS and TEM measurements. In a systematic approach, microgels solely based on PNIPAM were first investigated followed by the successive increase in complexity and functionality by incorporation of additional monomers into the system. In this context, the effects on the in situ synthesis as well as physicochemical properties like the hydrodynamic radius, the electrophoretic mobility of the particles and the swelling behavior were studied.

Microgels that are solely based on PNIPAM were found to be unsuitable to form gold nanoparticles within the polymer network by in situ reduction. It turned out that the key component for the controlled reduction of gold ions within the microgels are functional groups that can selectively complex and gather gold ions in certain domains in the microgels. For the microgels in this work, the monomer AAEM was incorporated which introduces  $\beta$ -diketone functionalities into the polymer chains. The introduction of AAEM into the microgels comes with the disadvantage of a bad colloidal stability towards higher temperatures due to the hydrophobic character of the monomer. Performing in situ experiments with PNIPAM-based microgels with incorporated AAEM groups (P(NIPAM-co-AAEM)), the uncontrolled formation of multiple gold

nanoparticles within the microgels could be observed. The amount of gold nanoparticles formed, that were about 7 nm in diameter, could be varied in part by the added amount of chloroauric acid during the synthesis. As a consequence, an increased amount of chloroauric acid resulted in a higher amount of gold nanoparticles formed. However, it was not possible to achieve the formation of only single gold nanoparticles within the microgels, independent on the ratio between chloroauric acid and the microgels.

To increase the affinity between gold ions and the microgel network and achieve a better control over the formation of gold nanoparticles, small contents of AAc (2.5 mol%) were incorporated into the polymer chains of the microgel resulting in the formation of negatively charged P(NIPAM-co-AAEM-co-AAc) microgels. The introduction of AAc not only restored the colloidal stability of microgels above the VPTT but also improved the controllability of the in situ formation of gold nanoparticles. After introduction of negative charges, the controlled formation of single, monodisperse gold nanoparticles was achieved successfully. The nanoparticles showed a diameter of approximately 10 nm which makes them directly comparable to gold nanoparticles synthesized by the well-established Turkevich protocol which exhibit diameters between 10 nm and 19 nm.<sup>119, 219</sup> SAXS measurements validated the size range with a determined mean diameter of 7.5 nm for a larger assembly of hybrid microgels. Furthermore, the overgrowth of the formed gold nanoparticles by (surfactant-supported) growth protocols was successfully accomplished. In the past, similar results have been reported for the overgrowth of Turkevich particles which suggest a similar facet structure for gold nanoparticles formed during the in situ synthesis. This observation further highlights the potential of the newly introduced hybrid microgel system. Similar to the P(NIPAM-co-AAEM) microgels, the number of gold nanoparticles formed could be increased to a certain extent by variation of the ratio between microgels and gold ions added to the system. The increase in the ratio between ions and microgels initially led to a growth of the particle diameter to about 14 nm. Introduction of additional gold ions showed no further growth in size but instead lead to the formation of multiple gold nanoparticles. The observation indicated the existence of AAEM rich domains in the microgel that presumably favor and cause the accumulation of gold ions in these regions of the microgels.

The exact interplay between AAc and AAEM monomers in the polymer chains and the influence on the formation of the microgel network as well as the influence on the formation of gold nanoparticles need further investigation in future experiments. Nevertheless, the successful in situ formation of gold nanoparticles in complex microgels showed that the combination of multiple monomers can allow for new and unique properties and applications that cannot be realized with microgels based only on a single monomer. At the same time, the complexity of the architecture and the interplay between individual monomers becomes even more difficult to understand with each additional incorporated monomer.

The second part of this work dealt with the characterization of different microgel systems using a combination of temperature-dependent DLS and UV-Vis absorbance spectroscopy measurements. The combination of both techniques results in a novel analytical methodology to study the swelling behavior of microgel systems and thereby gain deeper insight into structural inhomogeneities caused by distributions of monomers in microgel networks. To cover a broad range of microgel systems with different properties, 30 PNIPAM-based microgels were synthesized divided in three types of systems. The microgel systems covered the “classical” NIPAM-based microgels without comonomers or inorganic cores, copolymer microgels with different comonomers and core-shell microgels with SiO<sub>2</sub> cores.

“Classical” NIPAM-based microgels were further varied by different degrees of crosslinking and initiators which have an influence on the charge without drastically altering the composition of the microgels.

A total of four types of copolymer microgels have been synthesized and characterized. For this reason, the respective comonomer with concentrations of 2.5 mol% was added during the microgel synthesis. AMPS and AAc were incorporated into the microgel networks to provide negative charges, while APTAC and 2-VP were incorporated to provide positive charges. A further classification can be made as AAc and 2-VP show an additional pH responsiveness while AMPS and APTAC hold a permanent charge. The comonomers were chosen to cover a variety of microgels with different swelling properties.

Moreover, core-shell microgels with different sizes of SiO<sub>2</sub> cores, crosslinking degrees and shell sizes were synthesized. In addition, by incorporation of AMPS as comonomer in the shell, hybrid microgel systems with distinct swelling behaviors and properties could be achieved.

Temperature-dependent DLS and UV-Vis spectroscopy measurements were conducted in the range from 5 °C to 55 °C for all 30 microgel systems. For the temperature-dependent DLS measurements it was found that all microgel systems show the expected VPT behavior. The exact temperature and temperature interval at which the microgels transition from swollen into the collapsed state strongly depends on the amount of crosslinker and the composition of the microgels, more precisely, the incorporated comonomer or amount of initiator used. For the UV-Vis absorbance spectroscopy measurements it was shown that the absorbance increases with increasing temperature. In case of microgels, measured absorbance represents the scattering as the microgels do not absorb visible light. From a scattering theory perspective, a decrease in the scattering intensity (and therefore absorbance) would be expected due to the decrease in size when the microgels collapse. Nevertheless, the observed behavior can be attributed to the transition from the fuzzy sphere structure (or similar architectures with an inhomogeneous distribution of crosslinker and monomers) to a rather homogenous sphere. In the swollen state, the loosely crosslinked fuzzy parts of the microgel do not significantly contribute to the measured scattering based on the low refractive index. Upon transition to the collapsed state, the polymer material from the fuzzy parts collapses onto the rather homogenous, inner core region resulting in a decrease of the effective size of the microgel but an increase in size of the core region. The rise in polymer volume fraction of the inner core is accompanied with an increase in the refractive index contrast which together result in the increase of the absorbance.

For the correlation of the absolute change in the normalized absorbance and the absolute change in the size, a linear correlation for the “classical” PNIPAM microgels and the core-shell microgels was found while deviations from the linear behavior were observed for the copolymer microgels. The linear dependency is suggested to exist when the transition of the microgel from a fuzzy sphere structure in the swollen state to a homogenous sphere in the collapsed state happens homogeneously on the global and local scale. Furthermore, this allows for the direct translation from absolute changes in the effective size to absolute changes in the absorbance. For copolymer

microgels the deviations from the linear correlation indicate a heterogenous structure e.g., distribution of different monomers in the microgel network. The formation of subdomain-like structures during the synthesis of the microgels, that have been discussed in the Introduction (**Chapter 1**) of this work, could be the reason for the inhomogeneous (de-)swelling on a local scale which would also directly influence the refractive index. In consequence, absolute changes in the absorbance differ from absolute changes in hydrodynamic radius as DLS only provides access to the changes in the effective size of the microgel while changes in absorbance obtained by UV-Vis measurements can be based on local changes in the refractive index contrast.

Such inhomogeneous network structures could also be visualized by TEM imaging of negative stained “classical” microgels presented in the Introduction (**Chapter 1**) of this work. The imaging of the microgels suggested that heavy metal ions (e.g., uranyl ions) can diffuse into the networks to varying degrees dependent on the crosslinker density. This observation is particular interesting as it leads to the question if the diffusion of gold ions during the in situ synthesis is also dependent on the incorporated amount of crosslinker. At the same time the studies showed the potential of TEM imaging to visualize microgels and gain additional information about the structure of the networks.

For “classical” PNIPAM microgels and core-shell microgels the linear dependency given by the novel methodology allowed for the calculation of theoretical swelling curves based on the temperature-dependent absorbances using only two reference points from size determination by DLS. The calculated swelling curves were in good agreement with the experiments and therefore the UV-Vis absorbance measurements could potentially be used for characterization of microgel systems with an even higher throughput compared to DLS and without additional data processing. Furthermore, the method could allow for the investigations of microgel systems which cannot be measured by DLS e.g. hybrid microgel systems with heavy inorganic cores. Depending on the system, gravity can influence the movement and therefore impede the correlation of the time-dependent scattering intensity that requires random Brownian motion. Absorbance measurements do not rely on the random movement of the microgels and therefore influences by gravity can be circumvented for example by stirring of the particle dispersion.

In future studies, it might be possible to fully automate measurements of both methods and the subsequent processing of data. DLS and UV-Vis absorbance measurements are particularly interesting due to the wide accessibility, simplicity and low time requirement. The automation could be used to further increase the efficiency of microgel characterization and the identification of trends especially in respect to machine learning.

Moreover, the method seems promising to learn more about the inner structure of the microgels used for the in situ formation of gold nanoparticles in the first part of this work. In combination with temperature-dependent form factor analysis, a better understanding of the inner structure and composition of complex microgels could and needs to be achieved. Also, it would be imaginable to infiltrate the microgels with dye molecules that show affinity to negatively charged carboxy or the complexing  $\beta$ -diketone groups and use dSTORM experiments to visualize domains in the microgel structure.

Until now, reports of hybrid microgels for applications in catalysis were mainly based on the uncontrolled immobilization or formation of nanoparticles within the microgel. The controlled in situ formation of single nanoparticles in multifunctional copolymer microgels presented in this work could potentially open novel pathways towards an enhanced efficiency and new possibility of complex microgels as nanoreactors. Detailed investigations of the internal structure of microgels containing unique functionalities play a crucial role as they allow to further adjust the systems in regard to required application and properties respectively.

Overall, this work underlined the complexity of microgel systems especially when (multiple) comonomers are added to the system. The systematic study of the systems is inevitable to gain a deeper knowledge about the inner structure, distribution of components and interplay of functional groups. However, this work also showed that the use of supposedly simple methods can be a new starting point for ideas and perspectives. Especially, correlative approaches, in combination with microscopic methods, show a tremendous potential to address open questions about microgel systems.

## 7. References

1. Pelton, R. Temperature-sensitive aqueous microgels. *Adv. Colloid Interface Sci.* **2000**, *85* (1), 1-33.
2. Meng, Z.; Smith, M. H.; Lyon, L. A. Temperature-programmed synthesis of micron-sized multi-responsive microgels. *Colloid and Polymer Science* **2009**, *287*, 277-285.
3. Tanaka, T.; Ishiwata, S. i.; Ishimoto, C. Critical Behavior of Density Fluctuations in Gels. *Physical Review Letters* **1977**, *38* (14), 771-774.
4. Wu, C.; Zhou, S. Volume Phase Transition of Swollen Gels: Discontinuous or Continuous? *Macromolecules* **1997**, *30* (3), 574-576.
5. Pankasem, S.; Thomas, J. K.; Snowden, M. J.; Vincent, B. Photophysical Studies of Poly(N-isopropylacrylamide) Microgel Structures. *Langmuir* **1994**, *10* (9), 3023-3026.
6. Shibayama, M.; Tanaka, T.; Han, C. C. Small-angle neutron scattering study on weakly charged temperature sensitive polymer gels. *The Journal of Chemical Physics* **1992**, *97* (9), 6842-6854.
7. Shibayama, M.; Tanaka, T.; Han, C. C. Small angle neutron scattering study on poly(N-isopropyl acrylamide) gels near their volume-phase transition temperature. *The Journal of Chemical Physics* **1992**, *97* (9), 6829-6841.
8. Shibayama, M.; Tanaka, T. Small-angle neutron scattering study on weakly charged poly(N-isopropyl acrylamide-co-acrylic acid) copolymer solutions. *The Journal of Chemical Physics* **1995**, *102* (23), 9392-9400.
9. Hoare, T.; Pelton, R. Titrametric Characterization of pH-Induced Phase Transitions in Functionalized Microgels. *Langmuir* **2006**, *22* (17), 7342-7350.
10. Hoare, T.; Pelton, R. Highly pH and Temperature Responsive Microgels Functionalized with Vinylacetic Acid. *Macromolecules* **2004**, *37* (7), 2544-2550.
11. Kratz, K.; Hellweg, T.; Eimer, W. Influence of charge density on the swelling of colloidal poly(N-isopropylacrylamide-co-acrylic acid) microgels. *Colloids Surf. A Physicochem. Eng. Asp.* **2000**, *170* (2), 137-149.
12. Kratz, K.; Hellweg, T.; Eimer, W. Effect of connectivity and charge density on the swelling and local structural and dynamic properties of colloidal PNIPAM microgels. *Berichte der Bunsengesellschaft für physikalische Chemie* **1998**, *102* (11), 1603-1608.
13. Fernández-Nieves, A.; Fernández-Barbero, A.; Vincent, B.; De Las Nieves, F. Charge controlled swelling of microgel particles. *Macromolecules* **2000**, *33* (6), 2114-2118.
14. Karg, M.; Pastoriza-Santos, I.; Rodriguez-González, B.; von Klitzing, R.; Wellert, S.; Hellweg, T. Temperature, pH, and Ionic Strength Induced Changes of the Swelling Behavior of PNIPAM-Poly(allylactic acid) Copolymer Microgels. *Langmuir* **2008**, *24* (12), 6300-6306.
15. Shibayama, M.; Ikkai, F.; Inamoto, S.; Nomura, S.; Han, C. C. pH and salt concentration dependence of the microstructure of poly(N-isopropylacrylamide-co-acrylic acid) gels. *The Journal of Chemical Physics* **1996**, *105* (10), 4358-4366.
16. Bergman, M. J.; Pedersen, J. S.; Schurtenberger, P.; Boon, N. Controlling the morphology of microgels by ionic stimuli. *Soft Matter* **2020**, *16* (11), 2786-2794, 10.1039/C9SM02170A.
17. Snowden, M. J.; Chowdhry, B. Z.; Vincent, B.; Morris, G. E. Colloidal copolymer microgels of N-isopropylacrylamide and acrylic acid: pH, ionic strength and temperature effects. *Journal of the Chemical Society, Faraday Transactions* **1996**, *92* (24), 5013-5016, 10.1039/FT9969205013.
18. Hofmann, C. H.; Plamper, F. A.; Scherzinger, C.; Hietala, S.; Richtering, W. Cononsolvency revisited: solvent entrapment by N-isopropylacrylamide and N, N-diethylacrylamide microgels in different water/methanol mixtures. *Macromolecules* **2013**, *46* (2), 523-532.
19. Hüther, A.; Xu, X.; Maurer, G. Swelling of n-isopropyl acrylamide hydrogels in water and aqueous solutions of ethanol and acetone. *Fluid Phase Equilibria* **2004**, *219* (2), 231-244.
20. Liétor-Santos, J. J.; Fernández-Nieves, A. Motion of microgels in electric fields. *Advances in Colloid and Interface Science* **2009**, *147-148*, 178-185.
21. Fernández-Nieves, A.; Márquez, M. Electrophoresis of ionic microgel particles: From charged hard spheres to polyelectrolyte-like behavior. *The Journal of Chemical Physics* **2005**, *122* (8).
22. Kato, E. Pressure-induced volume phase transition of polyacrylamide gels in acetone-water mixtures. *The Journal of Chemical Physics* **2000**, *113* (3), 1310-1314.
23. Liétor-Santos, J. J.; Gasser, U.; Vavrin, R.; Hu, Z. B.; Fernandez-Nieves, A. Structural changes of poly(N-isopropylacrylamide)-based microgels induced by hydrostatic pressure and temperature studied by small angle neutron scattering. *The Journal of Chemical Physics* **2010**, *133* (3).
24. Liétor-Santos, J.-J.; Sierra-Martin, B.; Vavrin, R.; Hu, Z.; Gasser, U.; Fernandez-Nieves, A. Deswelling Microgel Particles Using Hydrostatic Pressure. *Macromolecules* **2009**, *42* (16), 6225-6230.
25. Bekir, M.; Jelken, J.; Jung, S.-H.; Pich, A.; Pacholski, C.; Kopyshv, A.; Santer, S. Dual responsiveness of microgels induced by single light stimulus. *Applied Physics Letters* **2021**, *118* (9).

26. Jelken, J.; Jung, S.-H.; Lomadze, N.; Gordievskaya, Y. D.; Kramarenko, E. Y.; Pich, A.; Santer, S. Tuning the Volume Phase Transition Temperature of Microgels by Light. *Advanced Functional Materials* **2022**, *32* (2), 2107946.
27. Sharma, A.; Gordievskaya, Y. D.; Lomadze, N.; Bekir, M.; Jung, S.-H.; Pich, A.; Santer, S. Making microgels photo-responsive by complexation with a spiropyran surfactant. *Soft Matter* **2023**, *19* (22), 4088-4098, 10.1039/D3SM00580A.
28. Suzuki, A.; Tanaka, T. Phase transition in polymer gels induced by visible light. *Nature* **1990**, *346* (6282), 345-347.
29. Schimka, S.; Lomadze, N.; Rabe, M.; Kopyshv, A.; Lehmann, M.; von Klitzing, R.; Romyantsev, A. M.; Kramarenko, E. Y.; Santer, S. Photosensitive microgels containing azobenzene surfactants of different charges. *Physical Chemistry Chemical Physics* **2017**, *19* (1), 108-117, 10.1039/C6CP04555C.
30. Karg, M.; Pich, A.; Hellweg, T.; Hoare, T.; Lyon, L. A.; Crassous, J. J.; Suzuki, D.; Gumerov, R. A.; Schneider, S.; Potemkin, I. I.; et al. Nanogels and Microgels: From Model Colloids to Applications, Recent Developments, and Future Trends. *Langmuir* **2019**, *35* (19), 6231-6255.
31. Das, M.; Zhang, H.; Kumacheva, E. MICROGELS: Old Materials with New Applications. *Annual Review of Materials Research* **2006**, *36* (1), 117-142.
32. Agrawal, G.; Agrawal, R.; Pich, A. Dual Responsive Poly(N-vinylcaprolactam) Based Degradable Microgels for Drug Delivery. *Particle & Particle Systems Characterization* **2017**, *34* (11), 1700132.
33. Hoare, T. R.; Kohane, D. S. Hydrogels in drug delivery: Progress and challenges. *Polymer* **2008**, *49* (8), 1993-2007.
34. Bromberg, L.; Temchenko, M.; Hatton, T. A. Dually Responsive Microgels from Polyether-Modified Poly(acrylic acid): Swelling and Drug Loading. *Langmuir* **2002**, *18*, 4944-4952.
35. Nolan, C. M.; Serpe, M. J.; Lyon, L. A. Thermally modulated insulin release from microgel thin films. *Biomacromolecules* **2004**, *5* (5), 1940-1946.
36. Richtering, W.; Potemkin, I. I.; Rudov, A. A.; Selge, G.; Trautwein, C. Could multiresponsive hollow shell-shell nanocontainers offer an improved strategy for drug delivery? *Future Medicine*: 2016; Vol. 11, pp 2879-2883.
37. Islam, M. R.; Ahiabu, A.; Li, X.; Serpe, M. J. Poly (N-isopropylacrylamide) Microgel-Based Optical Devices for Sensing and Biosensing. *Sensors* **2014**, *14* (5), 8984-8995.
38. Gao, Y.; Li, X.; Serpe, M. J. Stimuli-responsive microgel-based etalons for optical sensing. *RSC Advances* **2015**, *5* (55), 44074-44087, 10.1039/C5RA02306H.
39. Keskin, D.; Mergel, O.; van der Mei, H. C.; Busscher, H. J.; van Rijn, P. Inhibiting Bacterial Adhesion by Mechanically Modulated Microgel Coatings. *Biomacromolecules* **2019**, *20* (1), 243-253.
40. Bridges, A. W.; Singh, N.; Burns, K. L.; Babensee, J. E.; Andrew Lyon, L.; García, A. J. Reduced acute inflammatory responses to microgel conformal coatings. *Biomaterials* **2008**, *29* (35), 4605-4615.
41. Nussbaum, N.; Bergfreund, J.; Vialetto, J.; Isa, L.; Fischer, P. Microgels as globular protein model systems. *Colloids and Surfaces B: Biointerfaces* **2022**, *217*, 112595.
42. Stieger, M.; Pedersen, J. S.; Lindner, P.; Richtering, W. Are Thermoresponsive Microgels Model Systems for Concentrated Colloidal Suspensions? A Rheology and Small-Angle Neutron Scattering Study. *Langmuir* **2004**, *20* (17), 7283-7292.
43. Karg, M. Multifunctional inorganic/organic hybrid microgels. *Colloid and Polymer Science* **2012**, *290* (8), 673-688.
44. Welsch, N.; Ballauff, M.; Lu, Y. Microgels as Nanoreactors: Applications in Catalysis. In *Chemical Design of Responsive Microgels*, Pich, A., Richtering, W. Eds.; Springer Berlin Heidelberg, **2011**; pp 129-163.
45. Mei, Y.; Lu, Y.; Polzer, F.; Ballauff, M.; Drechsler, M. Catalytic Activity of Palladium Nanoparticles Encapsulated in Spherical Polyelectrolyte Brushes and Core-Shell Microgels. *Chemistry of Materials* **2007**, *19* (5), 1062-1069.
46. Lu, Y.; Mei, Y.; Drechsler, M.; Ballauff, M. Thermosensitive Core-Shell Particles as Carriers for Ag Nanoparticles: Modulating the Catalytic Activity by a Phase Transition in Networks. *Angew. Chem. Int. Ed.* **2006**, *45* (5), 813-816.
47. Contreras-Cáceres, R.; Sánchez-Iglesias, A.; Karg, M.; Pastoriza-Santos, I.; Pérez-Juste, J.; Pacifico, J.; Hellweg, T.; Fernández-Barbero, A.; Liz-Marzán, L. M. Encapsulation and Growth of Gold Nanoparticles in Thermoresponsive Microgels. *Adv. Mater.* **2008**, *20* (9), 1666-1670.
48. Gorelikov, I.; Field, L. M.; Kumacheva, E. Hybrid Microgels Photoresponsive in the Near-Infrared Spectral Range. *Journal of the American Chemical Society* **2004**, *126* (49), 15938-15939.
49. Das, M.; Sanson, N.; Fava, D.; Kumacheva, E. Microgels Loaded with Gold Nanorods: Photothermally Triggered Volume Transitions under Physiological Conditions. *Langmuir* **2007**, *23* (1), 196-201.
50. Karg, M.; Pastoriza-Santos, I.; Pérez-Juste, J.; Hellweg, T.; Liz-Marzán, L. M. Nanorod-Coated PNIPAM Microgels: Thermoresponsive Optical Properties. *Small* **2007**, *3* (7), 1222-1229.
51. Schmidt, A. M. Thermoresponsive magnetic colloids. *Colloid and Polymer Science* **2007**, *285* (9), 953-966.

52. Ge, J.; Huynh, T.; Hu, Y.; Yin, Y. Hierarchical Magnetite/Silica Nanoassemblies as Magnetically Recoverable Catalyst-Supports. *Nano Letters* **2008**, *8* (3), 931-934.
53. Wong, J. E.; Gaharwar, A. K.; Müller-Schulte, D.; Bahadur, D.; Richtering, W. Dual-stimuli responsive PNIPAM microgel achieved via layer-by-layer assembly: magnetic and thermoresponsive. *J Colloid Interface Sci* **2008**, *324* (1-2), 47-54.
54. Bhattacharya, S.; Eckert, F.; Boyko, V.; Pich, A. Temperature-, pH-, and magnetic-field-sensitive hybrid microgels. *Small* **2007**, *3* (4), 650-657.
55. Ménager, C.; Sandre, O.; Mangili, J.; Cabuil, V. Preparation and swelling of hydrophilic magnetic microgels. *Polymer* **2004**, *45* (8), 2475-2481.
56. Kratz, K.; Eimer, W. Swelling properties of colloidal poly(N-Isopropylacrylamide) microgels in solution. *Berichte der Bunsengesellschaft für physikalische Chemie* **1998**, *102* (6), 848-854.
57. Brändel, T.; Dirksen, M.; Hellweg, T. Tuning the Swelling Properties of Smart Multiresponsive Core-Shell Microgels by Copolymerization. *Polymers* **2019**, *11* (8), 1269.
58. Das, M.; Kumacheva, E. From polyelectrolyte to polyampholyte microgels: comparison of swelling properties. *Colloid and Polymer Science* **2006**, *284* (10), 1073-1084.
59. Hertle, Y.; Hellweg, T. Thermoresponsive copolymer microgels. *J. Mater. Chem. B* **2013**, *1* (43), 5874-5885, 10.1039/C3TB21143F.
60. Varga, I.; Gilányi, T.; Mészáros, R.; Filipcsei, G.; Zrínyi, M. Effect of Cross-Link Density on the Internal Structure of Poly(N-isopropylacrylamide) Microgels. *The Journal of Physical Chemistry B* **2001**, *105* (38), 9071-9076.
61. Kyrey, T.; Witte, J.; Feoktystov, A.; Pipich, V.; Wu, B.; Pasini, S.; Radulescu, A.; Witt, M. U.; Kruteva, M.; von Klitzing, R.; et al. Inner structure and dynamics of microgels with low and medium crosslinker content prepared via surfactant-free precipitation polymerization and continuous monomer feeding approach. *Soft Matter* **2019**, *15* (32), 6536-6546, 10.1039/C9SM01161G.
62. Acciaro, R.; Gilányi, T.; Varga, I. Preparation of Monodisperse Poly(N-isopropylacrylamide) Microgel Particles with Homogenous Cross-Link Density Distribution. *Langmuir* **2011**, *27* (12), 7917-7925.
63. Scheffold, F. Pathways and challenges towards a complete characterization of microgels. *Nature Communications* **2020**, *11* (1), 4315.
64. Pelton, R. H.; Chibante, P. Preparation of aqueous latices with N-isopropylacrylamide. *Colloids Surf.* **1986**, *20* (3), 247-256.
65. Wu, X.; Pelton, R. H.; Hamielec, A. E.; Woods, D. R.; McPhee, W. The kinetics of poly(N-isopropylacrylamide) microgel latex formation. *Colloid Polym. Sci.* **1994**, *272* (4), 467-477.
66. Witt, M. U.; Hinrichs, S.; Möller, N.; Backes, S.; Fischer, B.; von Klitzing, R. Distribution of CoFe<sub>2</sub>O<sub>4</sub> Nanoparticles Inside PNIPAM-Based Microgels of Different Cross-linker Distributions. *The Journal of Physical Chemistry B* **2019**, *123* (10), 2405-2413.
67. Still, T.; Chen, K.; Alsayed, A. M.; Aptowicz, K. B.; Yodh, A. G. Synthesis of micrometer-size poly(N-isopropylacrylamide) microgel particles with homogeneous crosslinker density and diameter control. *Journal of Colloid and Interface Science* **2013**, *405*, 96-102.
68. Sierra-Martin, B.; Retama, J. R.; Laurenti, M.; Fernández Barbero, A.; López Cabarcos, E. Structure and polymer dynamics within PNIPAM-based microgel particles. *Advances in Colloid and Interface Science* **2014**, *205*, 113-123.
69. Stieger, M.; Richtering, W.; Pedersen, J. S.; Lindner, P. Small-angle neutron scattering study of structural changes in temperature sensitive microgel colloids. *J. Chem. Phys.* **2004**, *120* (13), 6197-6206.
70. Gnan, N.; Rovigatti, L.; Bergman, M.; Zaccarelli, E. In Silico Synthesis of Microgel Particles. *Macromolecules* **2017**, *50* (21), 8777-8786.
71. Ninarello, A.; Crassous, J. J.; Paloli, D.; Camerin, F.; Gnan, N.; Rovigatti, L.; Schurtenberger, P.; Zaccarelli, E. Modeling Microgels with a Controlled Structure across the Volume Phase Transition. *Macromolecules* **2019**, *52* (20), 7584-7592.
72. Keerl, M.; Pedersen, J. S.; Richtering, W. Temperature Sensitive Copolymer Microgels with Nanophase Separated Structure. *Journal of the American Chemical Society* **2009**, *131* (8), 3093-3097.
73. Ponomareva, E.; Tadgell, B.; Hildebrandt, M.; Krüsmann, M.; Prévost, S.; Mulvaney, P.; Karg, M. The fuzzy sphere morphology is responsible for the increase in light scattering during the shrinkage of thermoresponsive microgels. *Soft Matter* **2022**, *18* (4), 807-825, 10.1039/D1SM01473K.
74. Karanastasis, A. A.; Zhang, Y.; Kenath, G. S.; Lessard, M. D.; Bewersdorf, J.; Ullal, C. K. 3D mapping of nanoscale crosslink heterogeneities in microgels. *Materials Horizons* **2018**, *5* (6), 1130-1136, 10.1039/C8MH00644J.
75. Siemes, E.; Nevskiy, O.; Sysoiev, D.; Turnhoff, S. K.; Oppermann, A.; Huhn, T.; Richtering, W.; Wöll, D. Nanoscopic Visualization of Cross-Linking Density in Polymer Networks with Diarylethene Photoswitches. *Angewandte Chemie International Edition* **2018**, *57* (38), 12280-12284.
76. Bergmann, S.; Wrede, O.; Huser, T.; Hellweg, T. Super-resolution optical microscopy resolves network morphology of smart colloidal microgels. *Physical Chemistry Chemical Physics* **2018**, *20* (7), 5074-5083, 10.1039/C7CP07648G.

77. Otto, P.; Bergmann, S.; Sandmeyer, A.; Dirksen, M.; Wrede, O.; Hellweg, T.; Huser, T. Resolving the internal morphology of core-shell microgels with super-resolution fluorescence microscopy. *Nanoscale Advances* **2020**, *2* (1), 323-331, 10.1039/C9NA00670B.
78. Watanabe, T.; Nishizawa, Y.; Minato, H.; Song, C.; Murata, K.; Suzuki, D. Hydrophobic Monomers Recognize Microenvironments in Hydrogel Microspheres during Free-Radical-Seeded Emulsion Polymerization. *Angewandte Chemie International Edition* **2020**, *59* (23), 8849-8853.
79. Gelissen, A. P. H.; Oppermann, A.; Caumanns, T.; Hebbeker, P.; Turnhoff, S. K.; Tiwari, R.; Eisold, S.; Simon, U.; Lu, Y.; Mayer, J.; et al. 3D Structures of Responsive Nanocompartmentalized Microgels. *Nano Letters* **2016**, *16* (11), 7295-7301.
80. Rodríguez-Fernández, J.; Pérez-Juste, J.; García de Abajo, F. J.; Liz-Marzán, L. M. Seeded growth of submicron Au colloids with quadrupole plasmon resonance modes. *Langmuir* **2006**, *22* (16), 7007-7010.
81. Nehl, C. L.; Hafner, J. H. Shape-dependent plasmon resonances of gold nanoparticles. *Journal of Materials Chemistry* **2008**, *18* (21), 2415-2419, 10.1039/B714950F.
82. Ponomareva, E.; Volk, K.; Mulvaney, P.; Karg, M. Surface Lattice Resonances in Self-Assembled Gold Nanoparticle Arrays: Impact of Lattice Period, Structural Disorder, and Refractive Index on Resonance Quality. *Langmuir* **2020**, *36* (45), 13601-13612.
83. Kelly, K. L.; Coronado, E.; Zhao, L. L.; Schatz, G. C. The Optical Properties of Metal Nanoparticles: The Influence of Size, Shape, and Dielectric Environment. *J. Phys. Chem. B* **2003**, *107* (3), 668-677.
84. Hoare, T.; Pelton, R. Characterizing charge and crosslinker distributions in polyelectrolyte microgels. *Curr. Opin. Colloid Interface Sci.* **2008**, *13* (6), 413-428.
85. Thorne, J. B.; Vine, G. J.; Snowden, M. J. Microgel applications and commercial considerations. *Colloid and Polymer Science* **2011**, *289* (5), 625-646.
86. Seiffert, S.; Weitz, D. A. Microfluidic fabrication of smart microgels from macromolecular precursors. *Polymer* **2010**, *51* (25), 5883-5889.
87. Tumarkin, E.; Kumacheva, E. Microfluidic generation of microgels from synthetic and natural polymers. *Chemical Society Reviews* **2009**, *38* (8), 2161-2168, 10.1039/B809915B.
88. Mueller, E.; Alsop, R. J.; Scotti, A.; Bleuel, M.; Rheinstädter, M. C.; Richtering, W.; Hoare, T. Dynamically Cross-Linked Self-Assembled Thermoresponsive Microgels with Homogeneous Internal Structures. *Langmuir* **2018**, *34* (4), 1601-1612.
89. Pich, A.; Richtering, W. *Chemical Design of Responsive Microgels*; Springer Berlin Heidelberg, **2010**.
90. McPhee, W.; Tam, K. C.; Pelton, R. Poly(N-isopropylacrylamide) Latices Prepared with Sodium Dodecyl Sulfate. *Journal of Colloid and Interface Science* **1993**, *156* (1), 24-30.
91. Heskins, M.; Guillet, J. E. Solution Properties of Poly(N-isopropylacrylamide). *J. Macromol. Sci. A* **1968**, *2* (8), 1441-1455.
92. Flory, P. J.; Rehner Jr, J. Statistical mechanics of cross-linked polymer networks I. Rubberlike elasticity. *The journal of chemical physics* **1943**, *11* (11), 512-520.
93. Flory, P. J. *Principles of Polymer Chemistry*; Cornell University Press, **1953**.
94. Kratz, K.; Hellweg, T.; Eimer, W. Structural changes in PNIPAM microgel particles as seen by SANS, DLS, and EM techniques. *Polymer* **2001**, *42* (15), 6631-6639.
95. Guillermo, A.; Cohen Addad, J. P.; Bazile, J. P.; Duracher, D.; Elaissari, A.; Pichot, C. NMR investigations into heterogeneous structures of thermosensitive microgel particles. *Journal of Polymer Science Part B: Polymer Physics* **2000**, *38* (6), 889-898.
96. Di Lorenzo, F.; Seiffert, S. Nanostructural heterogeneity in polymer networks and gels. *Polymer Chemistry* **2015**, *6* (31), 5515-5528, 10.1039/C4PY01677G.
97. Hertle, Y.; Zeiser, M.; Hasenöhrl, C.; Busch, P.; Hellweg, T. Responsive P(NIPAM-co-NtBAM) microgels: Flory-Rehner description of the swelling behaviour. *Colloid and Polymer Science* **2010**, *288* (10), 1047-1059.
98. Zhou, S.; Chu, B. Synthesis and volume phase transition of poly (methacrylic acid-co-N-isopropylacrylamide) microgel particles in water. *The Journal of Physical Chemistry B* **1998**, *102* (8), 1364-1371.
99. Höfl, S.; Zitzler, L.; Hellweg, T.; Herminghaus, S.; Mugele, F. Volume phase transition of "smart" microgels in bulk solution and adsorbed at an interface: A combined AFM, dynamic light, and small angle neutron scattering study. *Polymer* **2007**, *48* (1), 245-254.
100. Saunders, B. R.; Vincent, B. Thermal and osmotic deswelling of poly(NIPAM) microgel particles. *J. Chem. Soc., Faraday Trans.* **1996**, *92* (18), 3385-3389, 10.1039/FT9969203385.
101. Xu, W.; Rudov, A. A.; Schroeder, R.; Portnov, I. V.; Richtering, W.; Potemkin, I. I.; Pich, A. Distribution of Ionizable Groups in Polyampholyte Microgels Controls Interactions with Captured Proteins: From Blockade and "Levitation" to Accelerated Release. *Biomacromolecules* **2019**, *20* (4), 1578-1591.
102. Wong, J. E.; Gaharwar, A. K.; Müller-Schulte, D.; Bahadur, D.; Richtering, W. Dual-stimuli responsive PNIPAM microgel achieved via layer-by-layer assembly: Magnetic and thermoresponsive. *Journal of Colloid and Interface Science* **2008**, *324* (1), 47-54.
103. Phua, D. I.; Herman, K.; Balaceanu, A.; Zakrevski, J.; Pich, A. Reversible size modulation of aqueous microgels via orthogonal or combined application of thermo-and phototriggers. *Langmuir* **2016**, *32* (16), 3867-3879.

104. Meeks, A.; Lerch, M. M.; Schroeder, T. B. H.; Shastri, A.; Aizenberg, J. Spiropyran Photoisomerization Dynamics in Multiresponsive Hydrogels. *Journal of the American Chemical Society* **2022**, *144* (1), 219-227.
105. Li, C.; Iscen, A.; Palmer, L. C.; Schatz, G. C.; Stupp, S. I. Light-driven expansion of spiropyran hydrogels. *Journal of the American Chemical Society* **2020**, *142* (18), 8447-8453.
106. Lin, S.; Wang, W.; Ju, X.-J.; Xie, R.; Liu, Z.; Yu, H.-R.; Zhang, C.; Chu, L.-Y. Ultrasensitive microchip based on smart microgel for real-time online detection of trace threat analytes. *Proceedings of the National Academy of Sciences* **2016**, *113* (8), 2023-2028.
107. Wang, F.; Liu, Z.; Xie, R.; Ju, X.-J.; Wang, W.; Pan, D.-W.; Chu, L.-Y. Poly(N-isopropylmethacrylamide-co-4-acrylamidobenzo-18-crown-6) microgels with expanded networks for excellent adsorption of lead(II) ions. *Particuology* **2023**, *77*, 105-115.
108. Karg, M. Functional Materials Design through Hydrogel Encapsulation of Inorganic Nanoparticles: Recent Developments and Challenges. *Macromolecular Chemistry and Physics* **2016**, *217* (2), 242-255.
109. Pich, A.; Karak, A.; Lu, Y.; Ghosh, A. K.; Adler, H. J. Tuneable catalytic properties of hybrid microgels containing gold nanoparticles. *J Nanosci Nanotechnol* **2006**, *6* (12), 3763-3769.
110. Juarez, B. H.; Liz-Marzán, L. M. Microgels and Nanoparticles: Where Micro and Nano Go Hand in Hand. *Zeitschrift für Physikalische Chemie* **2015**, *229* (1-2), 263-282.
111. Pelton, R.; Hoare, T. Microgels and Their Synthesis: An Introduction. In *Microgel Suspensions*, **2011**; pp 1-32.
112. Karg, M.; Lu, Y.; Carbó-Argibay, E.; Pastoriza-Santos, I.; Pérez-Juste, J.; Liz-Marzán, L. M.; Hellweg, T. Multiresponsive Hybrid Colloids Based on Gold Nanorods and Poly(NIPAM-co-allylactic acid) Microgels: Temperature- and pH-Tunable Plasmon Resonance. *Langmuir* **2009**, *25* (5), 3163-3167.
113. Gawlitza, K.; Turner, S. T.; Polzer, F.; Wellert, S.; Karg, M.; Mulvaney, P.; Klitzing, R. v. Interaction of gold nanoparticles with thermoresponsive microgels: influence of the cross-linker density on optical properties. *Phys. Chem. Chem. Phys.* **2013**, *15* (37), 15623-15631, 10.1039/C3CP51578H.
114. Fernández-López, C.; Polavarapu, L.; Solís, D. M.; Taboada, J. M.; Obelleiro, F.; Contreras-Cáceres, R.; Pastoriza-Santos, I.; Pérez-Juste, J. Gold Nanorod-pNIPAM Hybrids with Reversible Plasmon Coupling: Synthesis, Modeling, and SERS Properties. *ACS Applied Materials & Interfaces* **2015**, *7* (23), 12530-12538.
115. Qian, Z.; Guye, K. N.; Masiello, D. J.; Ginger, D. S. Dynamic Optical Switching of Polymer/Plasmonic Nanoparticle Hybrids with Sparse Loading. *The Journal of Physical Chemistry B* **2017**, *121* (5), 1092-1099.
116. Karg, M.; Pastoriza-Santos, I.; Liz-Marzán, L. M.; Hellweg, T. A Versatile Approach for the Preparation of Thermosensitive PNIPAM Core-Shell Microgels with Nanoparticle Cores. *ChemPhysChem* **2006**, *7* (11), 2298-2301.
117. Contreras-Cáceres, R.; Pacífico, J.; Pastoriza-Santos, I.; Pérez-Juste, J.; Fernández-Barbero, A.; Liz-Marzán, L. M. Au@pNIPAM Thermosensitive Nanostructures: Control over Shell Cross-linking, Overall Dimensions, and Core Growth. *Advanced Functional Materials* **2009**, *19* (19), 3070-3076.
118. Dulle, M.; Jaber, S.; Rosenfeldt, S.; Radulescu, A.; Förster, S.; Mulvaney, P.; Karg, M. Plasmonic gold-poly(N-isopropylacrylamide) core-shell colloids with homogeneous density profiles: a small angle scattering study. *Phys. Chem. Chem. Phys.* **2015**, *17* (2), 1354-1367, 10.1039/C4CP04816D.
119. Turkevich, J.; Stevenson, P. C.; Hillier, J. A study of the nucleation and growth processes in the synthesis of colloidal gold. *Discussions of the Faraday Society* **1951**, *11* (0), 55-75, 10.1039/DF9511100055.
120. Rauh, A.; Honold, T.; Karg, M. Seeded precipitation polymerization for the synthesis of gold-hydrogel core-shell particles: the role of surface functionalization and seed concentration. *Colloid and Polymer Science* **2016**, *294* (1), 37-47.
121. Karg, M.; Jaber, S.; Hellweg, T.; Mulvaney, P. Surface Plasmon Spectroscopy of Gold-Poly-N-isopropylacrylamide Core-Shell Particles. *Langmuir* **2011**, *27* (2), 820-827.
122. Suzuki, D.; Kawaguchi, H. Hybrid Microgels with Reversibly Changeable Multiple Brilliant Color. *Langmuir* **2006**, *22* (8), 3818-3822.
123. Hüntzschel, N.; Hund, R.-D.; Hund, H.; Schrinner, M.; Lück, C.; Pich, A. Hybrid Microgels with Antibacterial Properties. *Macromolecular Bioscience* **2009**, *9* (5), 444-449.
124. Shi, S.; Wang, Q.; Wang, T.; Ren, S.; Gao, Y.; Wang, N. Thermo-, pH-, and Light-Responsive Poly(N-isopropylacrylamide-co-methacrylic acid)-Au Hybrid Microgels Prepared by the in Situ Reduction Method Based on Au-Thiol Chemistry. *The Journal of Physical Chemistry B* **2014**, *118* (25), 7177-7186.
125. Agrawal, G.; Schürings, M. P.; van Rijn, P.; Pich, A. Formation of catalytically active gold-polymer microgel hybrids via a controlled in situ reductive process. *J. Mater. Chem A* **2013**, *1* (42), 13244-13251, 10.1039/C3TA12370G.
126. Zhang, J.; Xu, S.; Kumacheva, E. Polymer Microgels: Reactors for Semiconductor, Metal, and Magnetic Nanoparticles. *Journal of the American Chemical Society* **2004**, *126* (25), 7908-7914.

127. Wunder, S.; Polzer, F.; Lu, Y.; Mei, Y.; Ballauff, M. Kinetic Analysis of Catalytic Reduction of 4-Nitrophenol by Metallic Nanoparticles Immobilized in Spherical Polyelectrolyte Brushes. *The Journal of Physical Chemistry C* **2010**, *114* (19), 8814-8820.
128. Sabadasch, V.; Fandrich, P.; Annegarn, M.; Hellweg, T. Effect of Methacrylic Acid in PNNPAM Microgels on the Catalytic Activity of Embedded Palladium Nanoparticles. *Macromolecular Chemistry and Physics* **2022**, *223* (11), 2200045.
129. Sabadasch, V.; Dirksen, M.; Fandrich, P.; Hellweg, T. Multifunctional Core-Shell Microgels as Pd-Nanoparticle Containing Nanoreactors With Enhanced Catalytic Turnover. *Frontiers in Chemistry* **2022**, *10*, Original Research.
130. Thies, S.; Simon, P.; Zelenina, I.; Mertens, L.; Pich, A. In Situ Growth and Size Regulation of Single Gold Nanoparticles in Composite Microgels. *Small* **2018**, *14* (51), 1803589.
131. Borsali, R.; Pecora, R. *Soft matter characterization*; Springer, **2008**.
132. Finsy, R. Particle sizing by quasi-elastic light scattering. *Advances in Colloid and Interface Science* **1994**, *52*, 79-143.
133. Zemb, T.; Lindner, P. *Neutron, X-rays and light. Scattering methods applied to soft condensed matter*; North Holland, **2002**.
134. Stetefeld, J.; McKenna, S. A.; Patel, T. R. Dynamic light scattering: a practical guide and applications in biomedical sciences. *Biophys Rev* **2016**, *8* (4), 409-427.
135. Siegert, A. J. F.; Massachusetts Institute of Technology Radiation, L. *On the fluctuations in signals returned by many independently moving scatterers*; Radiation Laboratory, Massachusetts Institute of Technology, **1943**.
136. Koppel, D. E. Analysis of Macromolecular Polydispersity in Intensity Correlation Spectroscopy: The Method of Cumulants. *The Journal of Chemical Physics* **2003**, *57* (11), 4814-4820.
137. Provencher, S. W. A constrained regularization method for inverting data represented by linear algebraic or integral equations. *Computer Physics Communications* **1982**, *27* (3), 213-227.
138. Provencher, S. W. CONTIN: a general purpose constrained regularization program for inverting noisy linear algebraic and integral equations. *Computer Physics Communications* **1982**, *27* (3), 229-242.
139. Perkampus, H.-H. *UV-VIS Spectroscopy and its Applications*; Springer Science & Business Media, **2013**.
140. Kerker, M.; Loebel, E. M. *The Scattering of Light and Other Electromagnetic Radiation*; Elsevier Science, **2016**.
141. Hulst, H. C.; van de Hulst, H. C. *Light Scattering by Small Particles*; Dover Publications, **1981**.
142. Ruska, E. The development of the electron microscope and of electron microscopy. *Bioscience Reports* **1987**, *7* (8), 607-629.
143. Thomas, J.; Gemming, T. *Analytische Transmissionselektronenmikroskopie - Eine Einführung für den Praktiker*; **2013**. DOI: 10.1007/978-3-7091-1440-7.
144. Williams, D. B.; Carter, C. B. *Transmission Electron Microscopy: A Textbook for Materials Science*; Springer, **2009**.
145. Graef, M. *Introduction to Conventional Transmission Electron Microscopy*; **2003**. DOI: 10.1016/S0025-5408(03)00178-8.
146. Goodhew, P. J.; Humphreys, J.; Beanland, R. *Electron Microscopy and Analysis, Third Edition*; Taylor & Francis, **2000**.
147. Brydson, R. *Aberration-corrected analytical transmission electron microscopy*; Wiley Online Library, **2011**.
148. Reimer, L. Scanning Electron Microscopy: Physics of Image Formation and Microanalysis, Second Edition. *Measurement Science and Technology* **2000**, *11* (12), 1826.
149. Hayat, M. E. *Basic techniques for transmission electron microscopy*; Elsevier, **2012**.
150. Parthasarathy, M. V. Transmission Electron Microscopy: Chemical Fixation, Freezing Methods, and Immunolocalization. In *The Maize Handbook*, Freeling, M., Walbot, V. Eds.; Springer New York, **1994**; pp 118-134.
151. Bradley, D. E. A Study of the Negative Staining Process. *Microbiology* **1962**, *29* (3), 503-516.
152. De Carlo, S.; Harris, J. R. Negative staining and cryo-negative staining of macromolecules and viruses for TEM. *Micron* **2011**, *42* (2), 117-131.
153. Zhou, Z.; Hollingsworth, J. V.; Hong, S.; Wei, G.; Shi, Y.; Lu, X.; Cheng, H.; Han, C. C. Effects of particle softness on shear thickening of microgel suspensions. *Soft Matter* **2014**, *10* (33), 6286-6293, 10.1039/C4SM01181C.
154. Frank, J. Introduction: Principles of Electron Tomography. In *Electron Tomography: Methods for Three-Dimensional Visualization of Structures in the Cell*, Frank, J. Ed.; Springer New York, **2006**; pp 1-15.
155. Baker, W. O. Microgel, A New Macromolecule. *Industrial & Engineering Chemistry* **1949**, *41* (3), 511-520.
156. Kundu, S.; Pal, A.; Ghosh, S. K.; Nath, S.; Panigrahi, S.; Praharaj, S.; Pal, T. A New Route to Obtain Shape-Controlled Gold Nanoparticles from Au(III)- $\beta$ -diketonates. *Inorganic Chemistry* **2004**, *43* (18), 5489-5491.

157. Gibson, D.; Johnson, B. F. G.; Lewis, J. Metal  $\beta$ -diketone complexes. Part VI. Some  $\beta$ -diketone complexes of copper(I), silver(I), and gold(I). *Journal of the Chemical Society A: Inorganic, Physical, Theoretical* **1970**, (0), 367-369, 10.1039/J19700000367.
158. Tollan, C. M.; Echeberria, J.; Marcilla, R.; Pomposo, J. A.; Mecerreyes, D. One-step growth of gold nanorods using a  $\beta$ -diketone reducing agent. *Journal of Nanoparticle Research* **2009**, *11* (5), 1241-1245.
159. Plamper, F. A.; Richtering, W. Functional Microgels and Microgel Systems. *Acc. Chem. Res.* **2017**, *50* (2), 131-140.
160. Richtering, W.; Potemkin, I. I.; Rudov, A. A.; Sellge, G.; Trautwein, C. Could multiresponsive hollow shell-shell nanocontainers offer an improved strategy for drug delivery? *Nanomed. J.* **2016**, *11* (22), 2879-2883.
161. Smeets, N. M. B.; Hoare, T. Designing responsive microgels for drug delivery applications. *J. Polym. Sci.* **2013**, *51* (14), 3027-3043.
162. Uhlig, K.; Wegener, T.; He, J.; Zeiser, M.; Bookhold, J.; Dewald, I.; Godino, N.; Jaeger, M.; Hellweg, T.; Fery, A.; et al. Patterned Thermoresponsive Microgel Coatings for Noninvasive Processing of Adherent Cells. *Biomacromolecules* **2016**, *17* (3), 1110-1116.
163. Pich, A.; Karak, A.; Lu, Y.; Ghosh, A. K.; Adler, H.-J. P. Preparation of Hybrid Microgels Functionalized by Silver Nanoparticles. *Macromol. Rapid Commun.* **2006**, *27* (5), 344-350.
164. Suzuki, D.; Kawaguchi, H. Modification of Gold Nanoparticle Composite Nanostructures Using Thermosensitive Core-Shell Particles as a Template. *Langmuir* **2005**, *21* (18), 8175-8179.
165. Siirilä, J.; Karesoja, M.; Pulkkinen, P.; Malho, J.-M.; Tenhu, H. Soft poly(N-vinylcaprolactam) nanogels surface-decorated with AuNPs. Response to temperature, light, and RF-field. *Eur. Polym. J.* **2019**, *115*, 59-69.
166. Kumar, V. R. R.; Samal, A. K.; Sreeprasad, T. S.; Pradeep, T. Gold Nanorods Grown on Microgels Leading to Hexagonal Nanostructures. *Langmuir* **2007**, *23* (17), 8667-8669.
167. Zhang, Y.; Liu, K.; Guan, Y.; Zhang, Y. Assembling of gold nanorods on P(NIPAM-AAPBA) microgels: a large shift in the plasmon band and colorimetric glucose sensing. *RSC Adv.* **2012**, *2* (11), 4768-4776, 10.1039/C2RA20466E.
168. Zhang, Q. M.; Berg, D.; Mugo, S. M.; Serpe, M. J. Lipase-modified pH-responsive microgel-based optical device for triglyceride sensing. *ChemComm* **2015**, *51* (47), 9726-9728, 10.1039/C5CC02853A.
169. Müller, M.; Tebbe, M.; Andreeva, D. V.; Karg, M.; Alvarez Puebla, R. A.; Pazos Perez, N.; Fery, A. Large-Area Organization of pNIPAM-Coated Nanostars as SERS Platforms for Polycyclic Aromatic Hydrocarbons Sensing in Gas Phase. *Langmuir* **2012**, *28* (24), 9168-9173.
170. Jones, C. D.; Lyon, L. A. Photothermal Patterning of Microgel/Gold Nanoparticle Composite Colloidal Crystals. *J. Am. Chem. Soc.* **2003**, *125* (2), 460-465.
171. Sharma, B.; Striegler, S. Crosslinked Microgels as Platform for Hydrolytic Catalysts. *Biomacromolecules* **2018**, *19* (4), 1164-1174.
172. Dell'Anna, M. M.; Mastroianni, P.; Rizzuti, A.; Suranna, G. P.; Nobile, C. F. Synthesis and copolymerization of rhodium(I) and palladium(II) complexes with the deprotonated form of 2-(acetoacetoxy)ethyl methacrylate. *Inorganica Chimica Acta* **2000**, *304* (1), 21-25.
173. Homola, J. Surface Plasmon Resonance Sensors for Detection of Chemical and Biological Species. *Chem. Rev.* **2008**, *108* (2), 462-493.
174. Ritchie, R. H. Plasma Losses by Fast Electrons in Thin Films. *Physical Review* **1957**, *106* (5), 874-881.
175. Barnes, W. L.; Dereux, A.; Ebbesen, T. W. Surface plasmon subwavelength optics. *Nature* **2003**, *424* (6950), 824-830.
176. Bradley, M.; Ramos, J.; Vincent, B. Equilibrium and Kinetic Aspects of the Uptake of Poly(ethylene oxide) by Copolymer Microgel Particles of N-Isopropylacrylamide and Acrylic Acid. *Langmuir* **2005**, *21* (4), 1209-1215.
177. Sabadasch, V.; Wiehemeier, L.; Kottke, T.; Hellweg, T. Core-shell microgels as thermoresponsive carriers for catalytic palladium nanoparticles. *Soft Matter* **2020**, *16* (23), 5422-5430, 10.1039/D0SM00433B.
178. Khan, A.; El-Toni, A. M.; Alrokayan, S.; Alsalhi, M.; Alhoshan, M.; Aldwayyan, A. S. Microwave-assisted synthesis of silver nanoparticles using poly-N-isopropylacrylamide/acrylic acid microgel particles. *Colloids Surf. A Physicochem. Eng. Asp.* **2011**, *377* (1), 356-360.
179. Lu, Y.; Yuan, J.; Polzer, F.; Drechsler, M.; Preussner, J. In Situ Growth of Catalytic Active Au-Pt Bimetallic Nanorods in Thermoresponsive Core-Shell Microgels. *ACS Nano* **2010**, *4* (12), 7078-7086.
180. Lu, Y.; Proch, S.; Schrinner, M.; Drechsler, M.; Kempe, R.; Ballauff, M. Thermosensitive core-shell microgel as a "nanoreactor" for catalytic active metal nanoparticles. *J. Mater. Chem.* **2009**, *19* (23), 3955-3961, 10.1039/B822673N.
181. Lange, H.; Juárez, B. H.; Carl, A.; Richter, M.; Bastús, N. G.; Weller, H.; Thomsen, C.; von Klitzing, R.; Knorr, A. Tunable Plasmon Coupling in Distance-Controlled Gold Nanoparticles. *Langmuir* **2012**, *28* (24), 8862-8866.

182. Mastrorilli, P.; Nobile, C. F.; Marchese, G. Cobalt(II) and iron(III) complexes with 2-(acetoacetoxy)ethylmethacrylate: potential precursors of hybrid catalysts. *Inorganica Chim. Acta* **1995**, *233* (1), 65-69.
183. Honold, T.; Volk, K.; Rauh, A.; Fitzgerald, J. P. S.; Karg, M. Tunable plasmonic surfaces via colloid assembly. *J. Mater. Chem. C* **2015**, *3* (43), 11449-11457, 10.1039/C5TC02115D.
184. Schild, H. G. Poly(N-isopropylacrylamide): experiment, theory and application. *Prog. Polym. Sci.* **1992**, *17* (2), 163-249.
185. Girardot, R.; Viguier, G.; Pérez, J.; Ounsy, M. FOXTROT: A JAVA-based application to reduce and analyse SAXS and WAXS piles of 2D data at synchrotron SOLEIL. *Proceedings of the 8th canSAS Meeting, Tokai, Japan* **2015**, 14-16.
186. <http://www.sasview.org/>.
187. Nayak, S.; Gan, D.; Serpe, M. J.; Lyon, L. A. Hollow Thermo-responsive Microgels. *Small* **2005**, *1* (4), 416-421.
188. Rodríguez-Fernández, J.; Pérez-Juste, J.; García de Abajo, F. J.; Liz-Marzán, L. M. Seeded Growth of Submicron Au Colloids with Quadrupole Plasmon Resonance Modes. *Langmuir* **2006**, *22* (16), 7007-7010.
189. Saunders, B. R.; Vincent, B. Microgel particles as model colloids: theory, properties and applications. *Adv. Colloid Interfaces Sci.* **1999**, *80* (1), 1-25.
190. Brijitta, J.; Schurtenberger, P. Responsive hydrogel colloids: Structure, interactions, phase behavior, and equilibrium and nonequilibrium transitions of microgel dispersions. *Curr. Opin. Colloid Interface Sci.* **2019**, *40*, 87-103.
191. Karg, M.; Hellweg, T. New "smart" poly(NIPAM) microgels and nanoparticle microgel hybrids: Properties and advances in characterisation. *Curr. Opin. Colloid Interface Sci.* **2009**, *14* (6), 438-450.
192. Shibayama, M.; Tanaka, T. Volume phase transition and related phenomena of polymer gels. In *Responsive Gels: Volume Transitions I*, Dušek, K. Ed.; Springer Berlin Heidelberg, **1993**; pp 1-62.
193. Wedel, B.; Zeiser, M.; Hellweg, T. Non NIPAM Based Smart Microgels: Systematic Variation of the Volume Phase Transition Temperature by Copolymerization. *Z. Phys. Chem.* **2012**, *226* (7-8), 737-748.
194. Holderer, O.; Maccarrone, S.; Pasini, S.; Appavou, M. S.; Gelissen, A. Raspberry structures in microgel-silica nanoparticle composite systems. *Results Phys.* **2021**, *21*, 103805.
195. Watanabe, T.; Kobayashi, C.; Song, C.; Murata, K.; Kureha, T.; Suzuki, D. Impact of Spatial Distribution of Charged Groups in Core Poly(N-isopropylacrylamide)-Based Microgels on the Resultant Composite Structures Prepared by Seeded Emulsion Polymerization of Styrene. *Langmuir* **2016**, *32* (48), 12760-12773.
196. Horigome, K.; Ueki, T.; Suzuki, D. Direct visualization of swollen microgels by scanning electron microscopy using ionic liquids. *Polym. J.* **2016**, *48* (3), 273-279.
197. Mourran, A.; Wu, Y.; Gumerov, R. A.; Rudov, A. A.; Potemkin, I. I.; Pich, A.; Möller, M. When Colloidal Particles Become Polymer Coils. *Langmuir* **2016**, *32* (3), 723-730.
198. Horecha, M.; Senkovskyy, V.; Synytska, A.; Stamm, M.; Chervanyov, A. I.; Kiriy, A. Ordered surface structures from PNIPAM-based loosely packed microgel particles. *Soft Matter* **2010**, *6* (23), 5980-5992, 10.1039/C0SM00634C.
199. Burmistrova, A.; Richter, M.; Eisele, M.; Üzüüm, C.; Von Klitzing, R. The Effect of Co-Monomer Content on the Swelling/Shrinking and Mechanical Behaviour of Individually Adsorbed PNIPAM Microgel Particles. *Polymers* **2011**, *3* (4), 1575-1590.
200. Wiedemair, J.; Serpe, M. J.; Kim, J.; Masson, J.-F.; Lyon, L. A.; Mizaikoff, B.; Kranz, C. In-Situ AFM Studies of the Phase-Transition Behavior of Single Thermo-responsive Hydrogel Particles. *Langmuir* **2007**, *23* (1), 130-137.
201. Reufer, M.; Diaz-Leyva, P.; Lynch, I.; Scheffold, F. Temperature-sensitive poly(N-Isopropyl-Acrylamide) microgel particles: A light scattering study. *Eur. Phys. J. E* **2009**, *28* (2), 165-171.
202. Berne, B. J.; Pecora, R. *Dynamic Light Scattering: With Applications to Chemistry, Biology, and Physics*; Dover Publications, **2013**.
203. Aragón, S. R.; Pecora, R. Theory of dynamic light scattering from polydisperse systems. *J. Chem Phys.* **1976**, *64* (6), 2395-2404.
204. Scotti, A.; Liu, W.; Hyatt, J. S.; Herman, E. S.; Choi, H. S.; Kim, J. W.; Lyon, L. A.; Gasser, U.; Fernandez-Nieves, A. The CONTIN algorithm and its application to determine the size distribution of microgel suspensions. *J. Chem Phys.* **2015**, *142* (23), 234905.
205. Koppel, D. E. Analysis of Macromolecular Polydispersity in Intensity Correlation Spectroscopy: The Method of Cumulants. *J. Chem Phys.* **1972**, *57* (11), 4814-4820.
206. Barnett, C. Some applications of wave-length turbidimetry in the infrared. *J. Phys. Chem.* **1942**, *46* (1), 69-75.
207. Tadjell, B.; Ponomareva, E.; Karg, M.; Mulvaney, P. Scattering of Visible Light by Au-PNIPAM Core-Shell Microgels. *J. Phys. Chem. C* **2022**, *126* (36), 15336-15347.
208. Hoogenboom, R. Chapter 2 - Temperature-Responsive Polymers: Properties, Synthesis, and Applications. In *Smart Polymers and their Applications (Second Edition)*, Aguilar, M. R., San Román, J. Eds.; Woodhead Publishing, **2019**; pp 13-44.

209. Hartlen, K. D.; Athanasopoulos, A. P. T.; Kitaev, V. Facile Preparation of Highly Monodisperse Small Silica Spheres (15 to >200 nm) Suitable for Colloidal Templating and Formation of Ordered Arrays. *Langmuir* **2008**, *24* (5), 1714-1720.
210. Stöber, W.; Fink, A.; Bohn, E. Controlled growth of monodisperse silica spheres in the micron size range. *J. Colloid Interface Sci.* **1968**, *26* (1), 62-69.
211. Eckert, T.; Richtering, W. Thermodynamic and hydrodynamic interaction in concentrated microgel suspensions: Hard or soft sphere behavior? *J Chem Phys* **2008**, *129* (12).
212. Harrer, J.; Rey, M.; Ciarella, S.; Lowen, H.; Janssen, L. M. C.; Vogel, N. Stimuli-Responsive Behavior of PNIPAm Microgels under Interfacial Confinement. *Langmuir* **2019**, *35* (32), 10512-10521.
213. Tadgell, B.; Ponomareva, E.; Karg, M.; Mulvaney, P. Temperature-Jump Spectroscopy of Gold-Poly(N-isopropylacrylamide) Core-Shell Microgels. *J Phys Chem C* **2022**, *126* (8), 4118-4131.
214. Dubbert, J.; Honold, T.; Pedersen, J. S.; Radulescu, A.; Drechsler, M.; Karg, M.; Richtering, W. How Hollow Are Thermoresponsive Hollow Nanogels? *Macromolecules* **2014**, *47* (24), 8700-8708.
215. Yanase, K.; Buchner, R.; Sato, T. Microglobule formation and a microscopic order parameter monitoring the phase transition of aqueous poly(N-isopropylacrylamide) solution. *Phys Rev Mater* **2018**, *2* (8).
216. Nishizawa, Y.; Matsui, S.; Urayama, K.; Kureha, T.; Shibayama, M.; Uchihashi, T.; Suzuki, D. Non-Thermoresponsive Decanano-sized Domains in Thermoresponsive Hydrogel Microspheres Revealed by Temperature-Controlled High-Speed Atomic Force Microscopy. *Angew Chem Int Edit* **2019**, *58* (26), 8809-8813.
217. Wiehemeier, L.; Brandel, T.; Hannappel, Y.; Kottke, T.; Hellweg, T. Synthesis of smart dual-responsive microgels: correlation between applied surfactants and obtained particle morphology. *Soft Matter* **2019**, *15* (28), 5673-5684.
218. Kuk, K.; Gregel, L.; Abgarjan, V.; Croonenbrock, C.; Hansch, S.; Karg, M. Micron-Sized Silica-PNIPAM Core-Shell Microgels with Tunable Shell-To-Core Ratio. *Gels-Basel* **2022**, *8* (8).
219. Honold, T.; Skrybeck, D.; Wagner, K. G.; Karg, M. Fully Reversible Quantitative Phase Transfer of Gold Nanoparticles Using Bifunctional PNIPAM Ligands. *Langmuir* **2017**, *33* (1), 253-261.